Experimental Study of Cavitation Inception During Vortex-Vortex Interaction and Investigation of Constrained Volumetric Velocimetry Methods

by

Daniel J. Knister

A dissertation submitted in partial fulfillment
of the requirements for the degree of
Doctor of Philosophy
(Mechanical Engineering)
in the University of Michigan
2024

Doctoral Committee:

Interim Dean Steven L. Ceccio, Co-Chair
Associate Research Scientist Harish Ganesh, Co-Chair
Professor David R. Dowling
Associate Professor Eric Johnsen
Professor Robert Krasny

Daniel J. Knister

dknister@umich.edu

ORCID iD: 0009-0000-0137-5363

© Daniel J. Knister 2024

DEDICATION

This work is dedicated to God, who has given us the three harps for revelation - the third of which is nature.

The Word of the Most High came down and put on

A weak body with hands,

And He took two harps

In His right and left hands.

The third He set up before Himself

To be a witness to the [other] two,

For the middle harp taught

That their Lord is playing them.

St. Ephrem the Syrian, Hymn 29

English translation by Kathleen McVey (Ephrem the Syrian: Hymns, 1989)

ACKNOWLEDGEMENTS

First, I would like to thank my thesis committee for their comments. Their collective knowledge of fluid mechanics is immense, and my work has benefited greatly from their insightful questions. I greatly appreciate my committee chairs, Dean Steven L. Ceccio and Dr. Harish Ganesh for their guidance and support over the years. You've taught me a great deal, from fundamental experimental principles to a learned cynicism while reading papers. I am thankful for Prof. David Dowling serving on my committee with his deep knowledge of experiments and fluids and acoustics. I am thankful for Prof. Eric Johnsen who mentored me in my incipient research career as an undergrad – a rather formative opportunity – and now contributed to the committee as a cavitation expert. I am thankful for Prof. Robert Krasny serving as the cognate member and lending his expertise on vortex dynamics.

Outside the committee, I would also like to thank Dr. Douglas Neal and the other staff at LaVision who graciously allowed me to borrow hardware and software that I used in this thesis. I look forward to joining LaVision and having you all as my colleagues.

I appreciate all my labmates and the Dowling lab members that I've worked with and learned from during my time here. I especially thank Dr. Elizabeth Callison, who taught me most of what I know about the particulars of the experimental methods we use in the lab. She also was a welcome taste tester for my varied culinary endeavors and a delightfully fun person to joke around with when we perhaps should have been working harder. I also thank Dr. Anubhav Bhatt as he also taught me a good deal about doing experiments in the lab. I appreciate Nick

Lucido, who was a rather good conference travel buddy, but I would like to encourage him to expand his unfortunately limited repertoire of jokes.

Thank you additionally to all the staff in Mechanical Engineering and the Marine Hydrodynamics Lab without whose help these experiments would not be possible. Kent Pruss and Bill Kirkpatrick were critical in manufacturing the system and components I used. Jason Bundoff and Jim Smith were very helpful in working in the MHL. Nicole Cheesman would do whatever it took to get the components I needed.

Beyond my professional life, I would like to acknowledge my family and friends who have supported me. It's been nice living only a few hours away from my parents, making it easy to go rock climbing or water skiing with them and taking a break from work. I appreciate my sisters' support, primarily by sharing about the dogs they've seen, and for being tour guides while visiting the PNW.

Thanks also to the boys: Chris, Brian, Alex, and Paul. Most of the tomfoolery in my life is with you guys, and it's been a real pleasure getting away from the lab and going about with you all. Thank you especially to Chris as my long time roommate and instigator of a great deal. Thank you to Alex H. for being a real fun friend with whom I talk about fluids and climb. I appreciate you pretending that I understood wave turbulence theory and the significance of your work.

Thanks to my fellow cooking nerds, Zach and Brian. I'm proud of the range of beers and cured meats we've made together. I know we can hold our own against anything I've bought in a store. These cooking times were of course made much more fun by our discussions and jokes about fluids and Fourier transforms. Some of the most enjoyable times I've had in grad school

were around the table with you guys. Thanks also to M: I'm glad you finally appreciate my tiramisu and capicola.

Thank you also to the Episcopal community I've had at St. Clare's and Canterbury House. I appreciate the welcoming that I've felt especially at St. Clare's despite the continual questions about when I would graduate.

Finally, for those who led me to pursue the wonderfully beautiful field of fluid mechanics, whether directly or indirectly, I owe a great deal of thanks. Mr. Dave VonEhr, my high school chemistry teacher, introduced us to Bernoulli's principle which initially struck my curiosity in fluids. Peter Fitchen got me to take ME 520 with him our junior year of undergrad. And of course, the Good Lord who has created this difficult field that nevertheless often leaves me awestruck – gladly have I strummed the third harp, as St. Ephrem calls it in the quoted epigraph.

This work was funded by ONR under MURI MURI Grant Number N00014-17-1-2676 supervised by Dr. Ki-Han Kim and Dr. Julie Young as well as by the Naval Nuclear Lab under Dr. Alex Mychkovsky.

TABLE OF CONTENTS

DEDICATION ii
ACKNOWLEDGEMENTS iii
LIST OF FIGURES x
LIST OF TABLES xvi
NOMENCLATURE xvii
ABSTRACT xxi

CHAPTER

I. **Motivation and Background** 1

1. Study of Artificially Constrained Velocimetry as a Proxy for Coaxial Measurements 1
2. Study of Vortex Interaction Leading to Cavitation Inception 6

II. Experimental Methods 15

1. mLCC Facility Overview 15
2. High-Speed Videography 19
3. Acoustic Measurements 19
4. Nuclei Measurements 20

III. Particle Based Velocimetry Methods 30

1. Velocimetry Apparatus 30

2. Choice of Seeding 31
3. Outline of Velocimetry Algorithms 36
4. Stereoscopic Particle Image Velocimetry 38
5. Tomographic Particle Image Velocimetry 40
6. Shake the Box Particle Tracking Velocimetry 42
7. Comparison of Methods 44
8. Freestream Turbulence Measurements in mLCC 45

IV. Study of Artificially Constrained Velocimetry as a Proxy for Coaxial Velocimetry 49

1. Overview 49
2. Test Model and Configuration 49
3. Comparison of Volumetric Reconstructions of Particles 54
4. Comparison of Instantaneous Fields 57
5. Comparison of Statistical Quantities 59
6. Discussion 64
7. Conclusions 67

V. Study of Interaction of Counter Rotating Vortex Pairs 90

1. Overall Evolution of the Vortex Pair 90
2. Test Models and Experimental Setup 91
3. Experimental Test Conditions 93
4. Cavitation Visualization of Vortical Interaction 97

5. Discussion 101

VI. Linear Instability of Counter Rotating Vortex Pairs 123

1. Vortex Properties Upstream of Interaction 123
2. Importance of Averaging Choice 127
3. Scaling of Vortex Behavior 128
4. Linear Stability Analysis 129
5. Discussion 132
6. Conclusions 134

VII. Non-Linear Regime of Counter Rotating Vortex Pair Interaction 148

1. Topology of Non-Linear Interactions 148
2. Approach for Vortex Analysis 148
3. Vortex Motion and Topology 150
4. Core Reduction and Straining in the Secondary Vortex 151
5. Estimation of Pressure in the Vortex Cores 153
6. Vortex Strain-Out Leading to Cavitation Suppression in the Primary Vortex 155
7. Discussion 158
8. Conclusions 161

VIII. Cavitation Inception in the Interaction of a Pair of Counter-Rotating Vortices 181

1. Characterization of Freestream Nuclei 181

2. Combined High-Speed Video and Acoustic Characterization of Inception 182
3. Relating Nuclei Content to Observed Cavitation Event Rate 186
4. Nuclei Content, Vortex Minimum Pressure, and Acoustic Emission 189
5. Conclusions 193

IX. Contributions 218
1. Study of Artificially Constrained Velocimetry as a Proxy for Coaxial Measurements 218
2. Study of Vortex Interaction Leading to Cavitation Inception 219

APPENDIX 222

BIBLIOGRAPHY 227

LIST OF FIGURES

FIGURE

1. Chapter 1

1.1. Camera and Illumination Positioning for Ideal and Coaxial Systems 11

1.2. Coordinate System of Wedge Study 12

1.3. Example of Cavitation Streamers and Rollers 13

1.4. Example of Cavitation Inception in Two Vortex Interaction 13

1.5. Coordinate System of Two Vortex Interaction 14

2. Chapter 2

2.1. Pictures of the mLCC Test Section and Contraction 25

2.2. Pictures of mLCC and Test Support Structure 26

2.3. Diagram and Image of Cavitation Susceptibility Meter 27

2.4. Shifting Nuclei Distribution 28

2.5. Change in Concentration of Nuclei Over Time 29

4. Chapter 4

4.1. Schematic of Experimental Setup for Wedge Experiments 69

4.2. Instantaneous Velocity and Vorticity Fields 70

4.3. Averaged Tomographic Particle Reconstruction Intensity 71

4.4. Averaged Tomographic Particle Reconstruction with Both Laser Cavities 72

4.5. Reconstructed Particles Comparing MTE and Disuse 73

4.6. Tomographic Reconstruction of Particles with and without Constraint 74

4.7. Close Comparison of Particle Reconstruction 75

4.8. Comparison of Particle Reconstructions 76

4.9. Velocity Field Comparison with and without MTE 77

4.10. Velocity Field Comparison with and without Constraint 77

4.11. Velocity Field Comparison with Time Series Data 78

4.12. STB-VIC# Time Series Velocity Field Comparison 78

4.13. STB-VIC# Frame Straddled Velocity Field Comparison 79

4.14. Vorticity Field Comparison with and without MTE 79

4.15. Vorticity Field Comparison with and without Constraint 80

4.16. Vorticity Field Comparison for Time Series Data 80

4.17. STB-VIC# Time Series Vorticity Field Comparison 81

4.18. STB-VIC# Frame Straddled Vorticity Field Comparison 81

4.19. Comparison of Time Series Data Over Time 82

4.20. Comparison of Time Series Data Over Time 83

4.21. Location of Averaged Quantity Comparison Points 84

4.22. Mean Flow Fields at Various Location 85

4.23. Reynolds Stresses with Time Series Data 86

4.24. Reynolds Stresses with Frame Straddled Data 87

4.25. Reynolds Stresses with Frame Straddled Data, MTE Comparison 88

4.26. Reynolds Stresses, Comparing Frame Straddled and Time Series 89

5. Chapter 5

5.1. Schematic of Test Geometry 102

5.2. Schematic of Test Geometry 103

5.3. Cartoon of Vortex Interaction 103

5.4. Cavitation Visualization of Case N.0 104

5.5. Cavitation Visualization of Case N.2 107

5.6. Cavitation Suppression in Case N.2 110

5.7. Cavitation Visualization of Case N.4 111

5.8. Cavitation Visualization of Case M.4 114

5.9. Cavitation Visualization of Case N.P2 117

5.10. Cavitation Visualization of Case N.P4 117

5.11. Location of Case N.0 118

5.12. Location of Case N.2 119

5.13. Location of Case N.4 120

6. Chapter 6

6.1. Instant of Upstream Measurement of Case N.0 with STB 135

6.2. Instant of Upstream Measurement of Case N.2 with STB 136

6.3. Instantaneous and Averaged 2-D Fields 137

6.4. Circulation Ratio with Angle of Attack 138

6.5. Circulations with Angle of Attack 138

6.6. Radii of Vortices with Angle of Attack 139

6.7. Reynolds Number Scaling of Secondary Radius 139

6.8. Reynolds Number Scaling of Primary Radius 140

6.9. Reynolds Number Scaling of Vortex Circulations 140

6.10. Reynolds Number Scaling of Vortex Circulations 141

6.11. Reynolds Number Scaling of Circulation Ratio 141

6.12. Reynolds Number Scaling of Circulation Ratio 142

6.13. Reynolds Number Scaling of Maximum Vorticity 142

6.14. Reynolds Number Scaling of Maximum Vorticity 143

6.15. Estimated and Observed Instability Growth Rate 143

7. Chapter 7

7.1. Topography of the Secondary Vortex 162

7.2. Depiction of Process of Analysis of Vortices 163

7.3. Separation of Vortices Over Time 164

7.4. Vertical Component of Vorticity Over Time 165

7.5. Axial Velocity in Secondary Vortex Legs 165

7.6. Strain Rate Projected Along Vortex Legs 166

7.7. Estimate of Vortex Pressure Drop for Case N.2 167

7.8. Estimate of Vortex Pressure Drop for Case N.0 167

7.9. Estimate of Vortex Pressure Drop for Case N.4 168

7.10. Estimate of Vortex Pressure Drop for Case M.4 169

7.11. Pressure Drop in the Legs of Case N.2 170

7.12. Pressure Drop in the Legs of Case N.0 171

7.13. Pressure Drop in the Legs of Case N.4 172

7.14. Pressure Drop in the Legs of Case M.4 173

7.15. Vortex Strain-out for Case N.2 174

7.16. Top View of Vortex Strain-out for Case N.2 176

7.17. Eccentricity of Vortex Components 179

8. Chapter 8.

8.1. Non-Matched Foil Nuclei Concentration 194

8.2. Matched Foil Nuclei Concentration 195

8.3. Example Inception Event 196

8.4. Example Inception Event 198

8.5. Example Inception Event with Acoustics and Video 200

8.6. Example Pop Event 202

8.7. Example Chirp Event 203

8.8. Example Chirpy Pop Event 204

8.9. Example Chirpy Pop Event 205

8.10. Inception Event Rates for Case N.0 206

8.11. Inception Event Rates for Case N.2 207

8.12. Inception Event Rates for Case N.4 208

8.13. Inception Event Rates for Case M.4 209

8.14. Nuclei Capture Radius 210

8.15. Estimated Inception Rates for Case N.0 211

8.16. Estimated Inception Rates for Case N.2 212

8.17. Estimated Inception Rates for Case N.4 213

8.18. Likelihood of Popping for Case N.2 214

8.19. Likelihood of Popping for Case N.4 215

8.20. Likelihood of Popping for Case M.4 215

8.21. Likelihood of Popping for All Cases 216

8.22. Low DO Chirp Duration for All Cases 216

8.23. Chirp Duration for Case M.4 217

8.24. High DO Chirp Duration for All Cases 217

Appendix

A.1 Large Foil Schematic 223

A.2 Small Foil Schematic 224

A.3 Water Tunnel Layout Drawing 225

A.4 Water Tunnel Layout Drawing 226

LIST OF TABLES

TABLE

3. Chapter 3

    3.1. Comparison of Velocimetry Methods 47

    3.2. Benefits and Drawbacks of Velocimetry Methods 48

5. Chapter 5

    5.1. Location and Extent of Measurement Domains 121

    5.2. Configurations of Geometry for Different Cases 122

6. Chapter 6

    6.1. Vortex Properties with Angle of Attack 144

    6.2. Vortex Properties with Freestream Speed 145

    6.3. Vortex Properties with Freestream Speed at Upstream Point 146

    6.4. Vortex Properties for Different Cases at Midstream Point 147

7. Chapter 7

    7.1. Radius of the Secondary Vortex at Different Locations and Cases 180

    7.2. Circulation of the Secondary Vortex at Different Locations and Cases 180

    7.3. Radius of the Secondary Throughout the Topography 180

NOMENCLATURE

Greek Symbols

α – angle of attack

Γ – vortex circulation (m^2/s)

Δx – grid spacing of PIV

ε – eccentricity of the vortex

θ – swirling direction of a vortex

κ – concentration of nuclei ($1/cm^3$)

λ – eigenvalue of a matrix

μ – dynamic viscosity (kg/m s)

ν – kinematic viscosity (m^2/s)

ρ – fluid density (kg/m^3)

σ – cavitation number

τ – non-dimensional time

υ – random uncertainty

χ – concentration of dissolved gas (kg/m^3)

φ – image moment

ω – vorticity (1/s)

Latin Symbols

b – vortex separation distance (mm)

c – foil chord (mm)

d – foil tip thickness (mm)

d_p – particle diameter (μm)

e – inception event rate (1/s)

f – image moment index

g – image moment index

h – wedge base height (mm)

l – position vector (mm)

$n_{effective}$ – number of independent samples

p – denotes primary vortex

q – flux of nuclei (1/s)

r_c – vortex radius (mm)

s – denotes secondary vortex

u – streamwise velocity (m/s)

v – vertical velocity (m/s)

w – spanwise velocity (m/s)

x – streamwise direction (mm)

y – vertical direction (mm)

z – spanwise direction (mm)

Acronyms and Upper Case Latin Symbols

CVV – Coaxial Volumetric Velocimetry

IPR – Iterative Particle Reconstruction

LPT – Lagrangian Particle Tracking

MTE – Motion Tracking Enhancement

N_I – particle image density

N_S – image source density

R – correlation coefficient

Re – Reynolds Number

P – pressure

PIV – Particle Image Velocimetry

PTV – Particle Tracking Velocimetry

SMTE – Sequential Motion Tracking Enhancement

STB – Shake-the-Box

TKE – Turbulent Kinetic Energy

Tomo-PIV – Tomographic Particle Image Velocimetry

U_0 – freestream velocity

VIC# - Vortex-in-Cell #

ABSTRACT

This work is comprised of two topics: a study of artificially constrained volumetric velocimetry and cavitation during the interaction of a pair of counter-rotating vortices.

Often, an experimentalist may not have sufficient access to achieve an ideal illumination of a volumetric velocimetry measurement domain. Instead, illumination that is coaxial to the cameras' lines of sight may be necessary, which is believed to hinder accurate tomographic reconstruction (used in tomographic particle image velocimetry, Tomo-PIV) as it precludes a sharp cutoff in brightness over the depth of field. To probe this difficulty, data is taken in the wake of a triangular wedge (18 mm base height, 15 degree opening angle) placed in a recirculating water channel at 6 m/s. Volumetric velocimetry and planar velocimetry data are taken with a Photonics DM-100 laser (dual cavity laser with 100 mJ/pulse per cavity at 10 kHz) and four Phantom v1212 cameras at a seeding density of 0.03 ppp with sharp cutoffs of laser intensity with depth (greater than 4 to 1). These data are then processed in typical fashion as well as in by artificially constraining the depth to less than half to mimic the effects of coaxial illumination on the signal to noise ratio of the data (going from 4:1 to 1:1). It was expected that tomographic reconstruction would fail in such a case, but the study found that while the tomographic reconstruction was affected, the eventual velocity fields had relatively small error compared to other sources of error such as misalignment of the cavities. These results suggest that coaxial illumination may be feasible for Tomo-PIV in some cases.

Separately, in many hydrodynamic turbulent shear flows, the weaker, stream-wise oriented vortices will cavitate before the stronger, span-wise vortices. This occurs due to stretching of the weaker vortices by the stronger vortices, which leads to a reduction in the core pressures of the weaker vortices. The stretching leads to reduced vortex core diameters and axial flow, but the relative interplay of these was previously unclear. This study experimentally examines a canonical case of this vortex interaction and inception process by looking at a pair of initially parallel line vortices undergoing the Crow instability. The vortices are generated by hydrofoils (modified NACA 66 profiles with chord 167 mm and varying span) whose relative arrangement can be adjusted to vary the flow properties. The vortices were characterized over a range of speeds, from 1 to 10 m/s, with Shake-the-Box particle tracking velocimetry (STB) using the same laser and cameras as above. STB measurements at 3 m/s throughout the downstream region were used to infer pressure drops in the cores of the vortices, with typical pressure drops in excess of 100 kPa found. Reduction in core radius of the stretched vortex and not axial jetting was found to cause the pressure drop. Inception experiments with acoustic measurements over a range of freestream pressures (70 to 150 kPa absolute) at fixed speed of 10 m/s were then done to find inception event rates (approximately 0.01 – 10 events/sec). The inception event rates were predicted reasonably by combination of pressure drops from STB and measurements of nuclei in the water. The acoustic emissions of inception are related to the nuclei and vortex flow properties.

CHAPTER I

Motivation and Background

Study of Artificially Constrained Velocimetry as a Proxy for Coaxial Measurements

A wide array of velocimetry techniques is available to investigate complex turbulent flows. Choosing an appropriate method to investigate a given flow may be constrained by a variety of potential factors, such as the topology and complexity of the flow, the parameters of the flow (i.e. the maximum velocity and size scales), and the usually finite resources available to perform the measurement (primarily financial cost and time required). For optically-based measurements like particle image velocimetry (PIV) and Lagrangian particle tracking velocimetry (LPT), these constraints include the illumination, seeding, and cameras available for measurement as well as constraints on the experimental apparatus such as optical access. Limited optical and illumination access may force the experimentalist to use a coaxial arrangement of cameras and illumination, resulting in the depth direction (Z-direction) being oriented in the direction of propagation of the laser. As an example, if the flow in a particular pipe amongst a network of pipes is to be measured, there may only be a particular location suited for optical access where the measurement can be made. Bends in the pipes above or below the measurement location could then inhibit illumination along the axis of the pipe and force a coaxial arrangement of cameras. Figure 1.1(a) and (b) shows a mockup of such a case, where the cameras are looking in coaxially to the illuminating laser (b), as well as an arrangement with

ideal illumination shown in Figure 1.1 (a) (with the cameras' lines of sight cutting through the thinnest extent of the illumination). The Z direction is generally considered in volumetric PIV to be the thinnest direction of the measurement domain, which is the "depth" direction when considering all cameras' focal planes.

Mapping of a measurement volume to 3-D space affects the estimated 3-D velocity field for correlation based estimation methods such as Tomographic Particle Image Velocimetry (Tomo-PIV) (Scarano, 2013). Tomo-PIV is a volumetric, correlation based velocimetry technique that uses multiple cameras to tomographically reconstruct particles in 3 dimensional space and correlate their motion between successive frames. This technique and other PIV techniques are explained in greater detail in Chapter 3. However, the requirement for clear Z extents is evidently less strict for shake-the-box particle tracking velocimetry (STB) as (Schneiders et al., 2018) demonstrated with coaxial volumetric velocimetry (CVV). In that case, the light source illuminated the measurement volume from a point directly in the center of the cameras. While they were successful with that measurement, and later used such technology to measure the flow around a model of a cyclist (Jux et al., 2018), a comparable approach has not been studied with Tomo-PIV.

Despite the popularity and several advantages of STB based measurements, Tomo-PIV is still sought to measure statistical flow quantities such as Reynolds stresses. This is due to the limited number of samples and acquisition requirements of frame-straddled measurements (compared with time-resolved STB) to estimate such quantities. Frame straddled measurements take independent samples arbitrarily spaced in time where each sample consists of two image frames. The time between samples is generally much greater than the time between the two image frames. The motion of particles between these frames can then be correlated (PIV) or

tracked (PTV) to find velocity fields. Each double frame set yields a velocity field independent of every other double frame set if the time between sets is sufficient. In contrast, time series measurements take image frames equally spaced in time. The motion of particles between successive frames can then be correlated (PIV) or tracked (PTV) to find velocity fields and acceleration fields. However, these velocity fields are correlated in time and no longer independent. Depending on whether the user desires statistical flow field quantities or time-resolved properties, the user may choose whether to use time series or frame straddled methods. Generally, time-resolved measurements are correlated, so the effective number of independent samples of a flow field for finding mean properties typically runs much lower than the number of samples taken (Smith et al., 2018). As convergence of statistical quantities requires independent samples, the number of time-resolved measurement samples required for convergence is significantly higher than for frame straddled measurements. In the study of the wedge flow in this thesis, time series measurements require approximately two orders of magnitude more samples as frame straddled measurements to achieve an equivalent number of independent samples. Thus, for mean flow properties, taking frame-straddled data is preferable to time-resolved data due to data storage and processing requirements. On applications where frame-straddled measurements are strongly preferred (e.g., for statistical flow quantities), Tomo-PIV may perform better than STB. While STB can be calculated with frame-straddled data (Novara et al., 2023), it lacks the acceleration and time history information that aids the prediction of future steps, reducing the number of particles that STB can track and increasing the likelihood of false tracks. This process of STB is explained in greater detail in Chapter 3.

Techniques such as Tomo-PIV and STB can provide all velocity and velocity gradient information in a volume while Stereoscopic-PIV (Stereo-PIV) can provide all three components

of velocity in a plane. Depending on the flow features of interest, the velocity on a plane may be sufficient. However, as several researchers have noted, starting with (Michaelis & Wieneke, 2008), volumetric methods such as Tomo-PIV often provide higher quality velocity field data than Stereo-PIV. The loss of particles due to out of plane motion is often a primary cause of low correlations and poor data with Stereo-PIV while volumetric PIV suffers from this effect less due to a higher proportion of particles staying within the measurement region between successive frames. While this is a notable advantage of volumetric measurements, Stereo-PIV can be done with a significantly less powerful light source, and the processing time is also significantly less. For applications where all three components of velocity are necessary, but not the full velocity gradient tensor, Stereo-PIV is a viable candidate.

A systematic study on the performance of Tomo-PIV in a co-axial configuration had not been performed before. Also, less focus has been on comparing volumetric methods with regards to statistical flow quantities of interest such as TKE or Reynolds stresses. More attention has been paid to instantaneous comparisons, but in some cases, it may be the statistical flow quantities that are of interest. For instance, in validating a computational study against an experimental study, an instantaneous flow comparison cannot realistically be made, but statistical quantities can be compared.

This work examines some of the questions and choices described above. First, in a case where coaxial illumination is necessary, what effect does such a poorly defined illumination volume have on Tomo-PIV and STB? Another query is whether two-camera Stereo-PIV can give measurements of second-order statistics (e.g., TKE and Reynolds stress) comparable to volumetric velocimetry methods or are volumetric velocimetry methods necessary to determine statistical quantities relating to out-of-plane (Z-direction) motion?

The constraint of a sharply defined volume is weaker for STB, as was shown by (Schneiders et al., 2018) with their CVV system. Since the method for volumetrically reconstructing particles in STB, iterative particle reconstruction (IPR, which is discussed in detail in Chapter 3), can effectively ignore a particle if it cannot reconstruct it within the volume, STB is expected to perform well in such situations. In contrast, Tomo-PIV is expected to force all pixel intensities recorded in the cameras to be reconstructed within the measurement volume resulting in increased disparities for coaxial configurations. Accordingly, the general recommendation for a Tomo PIV measurement is that the mean reconstructed particle intensity inside the illuminated volume be at least 1.5 times the intensity outside the illuminated volume. The intensity outside the volume is considered to be representative of ghost particle intensity and the noise floor of the measurement for calculating a signal-to-noise ratio.

To study the performance of these methods in a coaxial configuration, measurements are taken in a relatively thick volume (8.5 mm) and then processed with Tomo PIV and Shake-the-Box PTV at the full thickness and at an artificially constrained thinner depth (3.5 mm). The goal of this is to mimic the effects of a poorly cut-off illumination volume (for Tomo-PIV) as encountered in a coaxially illuminated measurement. With the full thickness, the reconstructed particle intensity profile has ideal levels with the difference between the illuminated region and the exterior of the volume generally greater than 4. In contrast, for the partially constructed volume, with the artificial depth constraint, the ratio of particle intensity in the reconstructed region in the illuminated volume to the non-reconstructed region (that still lies within the illuminated volume) approaches one, replicating the effects of coaxial measurements.

These questions are first approached with a canonical case of the flow in the wake of a wedge with PIV and PTV. Several different acquisition regimes were used and compared using

the several processing methods noted above – Stereo-PIV, Tomo-PIV, and STB with VIC# and binning all with frame-straddled and time series data. These measurements are repeated in the immediate near wake of the wedge including the stagnation region as well as approximately ten base heights downstream. The coordinate system of these measurements is shown in Figure 1.2. The x-direction is streamwise, increasing with freestream direction and starting at the base of the wedge. The y-direction is vertical, with the midpoint of the wedge serving as 0. As a right handed coordinate system, the z-direction is in the span of the tunnel.

Study of Vortex Interaction Leading to Cavitation Inception

For many hydrodynamic flows, cavitation is undesirable and regions most likely to cavitate are those around the lifting surfaces and in the passages and wakes of propulsors. These regions are characterized by turbulent free shear flows with a complicated web of vortical structures of varied strength and orientation. In such flows, inception is expected to first occur in the cores of stronger "streamwise" vortices. However, inception usually occurs in weaker "secondary" vortices as has been noted in several studies (Katz and O'hern (1986), O'hern (1990)). An example of these interacting vortices for a turbulent shear flow is in Figure 1.3, for a wedge. Similarly, (Belahadji et al., 1995) found cavitation in weaker vortical structures in the wake of a wedge while (Ran and Katz, 1994) also noted this phenomenon in a turbulent jet. It is hypothesized that the stretching of the weaker vortices by the stronger vortices leads to rapid transient pressure drops in these weaker vortices, causing inception. Chesnakas and Jessup (2003) examined interacting vortices and inception in weaker vortex structures in the context of a propulsor. Several previous studies have examined this phenomenon from an experimental and computational point of view.

Agarwal et al. (2023) examined a turbulent backward facing step with experimental measurements of 3-D velocity fields. They observed good agreement between inferred low pressure regions from PIV measurements to the observed cavitation inception locations. They also demonstrated that the weaker vortices present in the flow (Quasi-Streamwise Vortices in their nomenclature) were the corresponding vortical structures that first cavitated in the flow. Prior experiments by (Choi & Ceccio, 2007) and (Chang et al., 2012) examined a simplified system of two counter-rotating vortices produced by a pair of hydrofoils at various attack angles, and the present study follows especially their efforts. This configuration is shown in Figure 1.4. The two vortices undergo the long wavelength Crow instability which leads to strong stretching and pressure drop in the core of the weaker vortex. These studies measured the flow field in the upstream regions before substantial instability occurred. Downstream measurements were performed with high-speed video and hydrophones as the PIV hardware of the time did not allow high-speed three-component velocity measurements over a volume. Due to lack of availability of velocity fields, they were not able to relate observed inception events in secondary vortices to rapid pressure drop.

Examining the single-phase flow that drives the vortex instability and stretching, Crow (1970) originally gave the mathematical derivation of the long wavelength instability for a set of Rankine vortices. Though originally derived for equal strength counter-rotating vortices, others expanded on this work to consider other vortex configurations (Jimenez, 1975) showed that co-rotating vortices of a similar configuration do not experience this instability. Work by (Widnall, 1975) included the effects of vortex core properties like axial and azimuthal velocity distributions to predict the onset and location of the instability. (Tsai & Widnall, 1976) and Moore and Saffman (1975) considered the effects of external strain fields and vortices with an

elliptic cross section as opposed to the assumed circular cross section of (Crow, 1970) and Jimenez (1975). Such elliptically shaped vortices have internal strain fields that interact nonlinearly with the external strain field imposed by a nearby vortex resulting in amplified strain rates. This can lead to growth rates of the instability that are several times the external strain field. Klein *et al.* (1995) considered instabilities for a large but finite number of nearly parallel vortices, demonstrating that all counter-rotating vortex pairs are unstable and all co-rotating vortex pairs are stable with respect to the Crow instability, although the elliptic instability may still be possible. Given the relevance of this problem for aircraft trailing vortices at busy airports, other studies considered systems of two pairs of unequal strength, counter-rotating vortices. In this case, within each pair, one vortex represents the wingtip vortex while the other represents the vortex from the flaps. The two vortices within the pair are co-rotating and unequal strength while the pairs are equal and opposite to each other. (Crouch, 1997) derived a set of equations governing their dynamics and showed the transient growth they experienced due to the nonnormality of the linear stability operator. This configuration was considered experimentally in (Ortega et al., 2003) and numerically in (Bristol et al., 2004). The experiments used dye injection and PIV downstream of a towed flapped wing device. They showed, in some cases, the breakdown of the weaker vortices (within each pair) into vortex rings and showed good agreement with the predictions of their analytical and numerical models. They also noted and named the so-called "Ω loop" structures that occur in flows of unequal strength counter rotating vortices. Later experiments by (Leweke & Williamson, 2011) used PIV to examine equal-strength counter-rotating vortices and the long-time development of vortex breakdown and reconnection. More recently Brandao et al. (n.d.) has computed the interaction of a pair of counter-rotating vortices. This study demonstrated several long-term behaviors of this

interaction at high Reynolds number, namely that the larger, stronger vortex is strained out by the weaker vortex before the weaker vortex itself eventually breaks down. A previous numerical study by (Marshall et al., 2001) demonstrated somewhat similar results, but at a vortex circulation-based Reynolds number of 1500.

Notably, most studies have examined equal-strength pairs of vortices. While the underlying physical mechanism remains the same, the behavior of unequal-strength vortices differs substantially. Equal strength vortices often have the most unstable wavelengths of around 10 times the separation distance of the vortices. In contrast, unequal-strength vortices can have unstable wavelengths about the length of the separation distance. Similarly, unequal strength vortices typically experience higher growth rates of instability in the weaker vortex with dramatically reduced instability growth in the stronger vortex. This situation of unequal strength vortices is most relevant to us and accordingly the focus of our study on inception occurring due to vortex stretching.

This study focuses on the canonical case of two nearly parallel, counter-rotating (sometimes referred to as an anti-parallel configuration), unequal strength vortices produced by a pair of hydrofoils in a water channel. The weaker vortex experiences substantial stretching as it undergoes the long wavelength Crow instability. As this vortex interaction develops, the dynamics of the interaction are examined at several locations with cavitation visualization of the vortices and detailed high-speed volumetric velocimetry. The vortex interaction is initially found to be well governed by the linear dynamics of the Crow instability. In the downstream region (streamwise distance, x, is much greater than initial vortex separation, b), the nonlinear vortex interaction shows non-intuitive straining patterns in the stronger vortex. Scaling of the vortices over a single decade of Reynolds number is shown, and this is used in conjunction with time-

resolved velocimetry measurements to estimate the development of pressure in the secondary vortex. These estimates of pressure are then used in the following chapter to make estimates of cavitation inception (based on a given nuclei distribution) and compared with acoustic measurements of inception.

As in the wedge, the x-direction is in the streamwise direction, starting at the tail of the hydrofoils. The y-direction is vertical, starting at the tip of the larger hydrofoil. The z-direction is in the spanwise direction of the tunnel as shown in Figure 1.5.

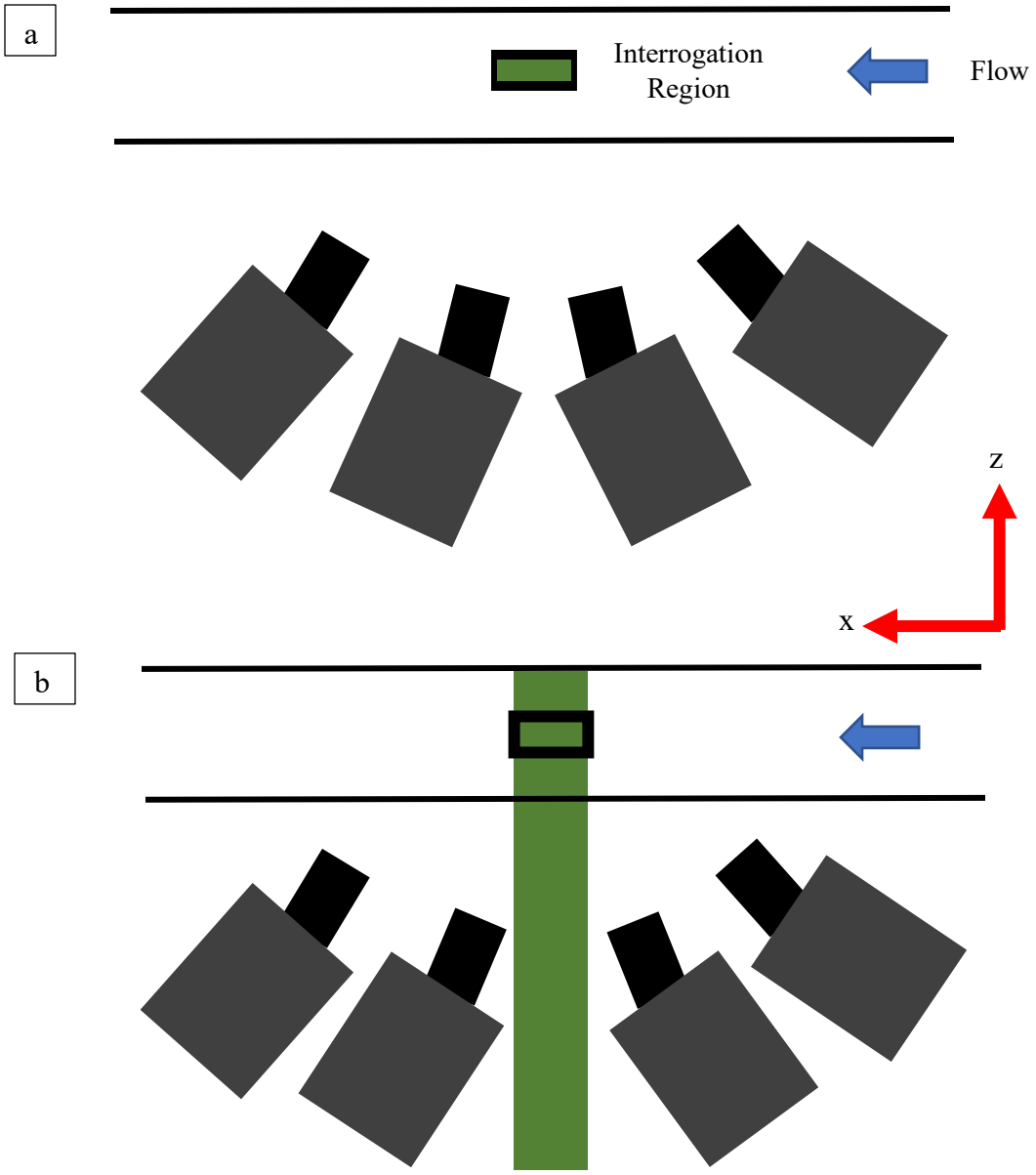


Figure 1.1 Camera and Illumination Positioning for Ideal and Coaxial Systems. (a) The upper image shows a typical ideal case of a volumetric velocimetry setup with the cameras outside some flow channel (outlined in black) and the illumination from below (green box). (b) The lower image shows a case where coaxial velocimetry may be necessary. Here a pipe with flow out of the page cannot readily be illuminated from below, so the light (green box representing a laser) must propagate from roughly the same direction as the cameras' view (coaxial with the cameras). The intended measurement volume is the black box in the middle of the green light sheet. As the illumination propagates through this region, it does not have clear extents in Z.

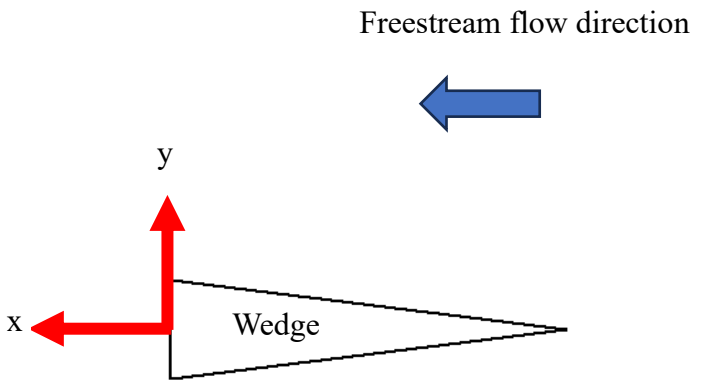


Figure 1.2 Coordinate System of Wedge Study. The flow considered in the artificially constrained study of Tomo-PIV is the near wake of a wedge. A drawing showing the coordinate system relative to the wedge is shown here. The flow goes from right to left, and the x direction has its origin at the base of the wedge and increases in the streamwise direction. The y direction is vertical and has its origin at the midpoint of the wedge base. The z direction is into the plane of the page.

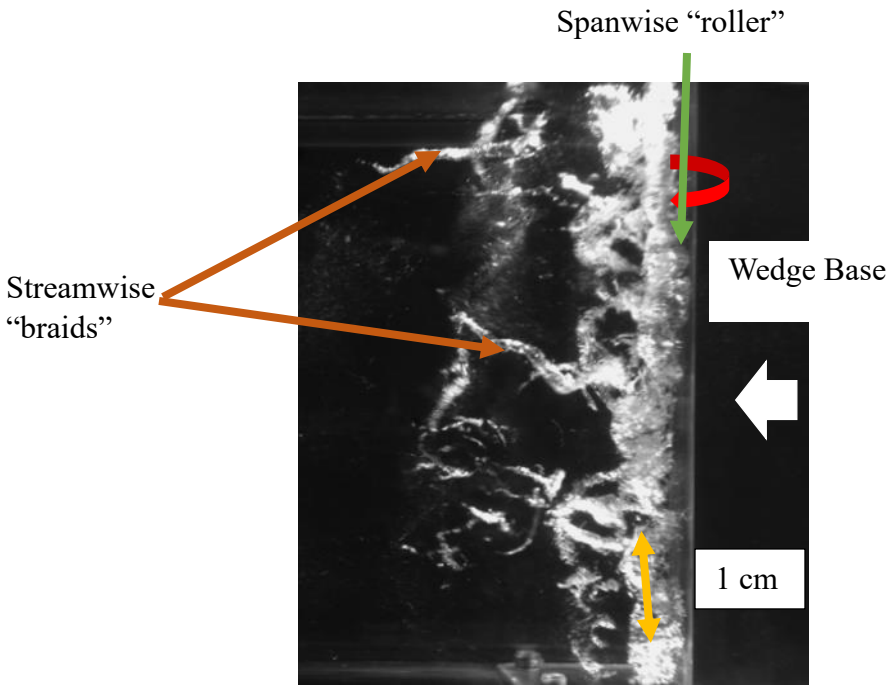


Figure 1.3 Example of Cavitation Streamers and Rollers. The cavitation in the wake of wedge shows the interaction between stronger, spanwise oriented rollers and weaker, streamwise oriented braids. Photo courtesy of Anubhav Bhatt.

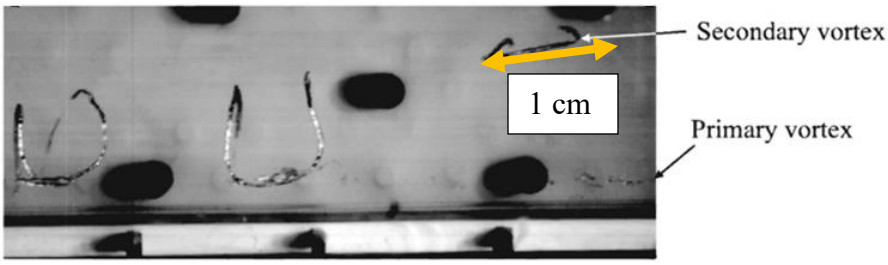


Figure 1.4 Example of Cavitation Inception in Two Vortex Interaction. Cavitation during the interaction of a pair of counter-rotating vortices undergoing the Crow instability is shown here. The weaker, secondary vortex wraps around the stronger, primary vortex and can incept more readily than the primary vortex. Photo from Chang *et al*. (2012).

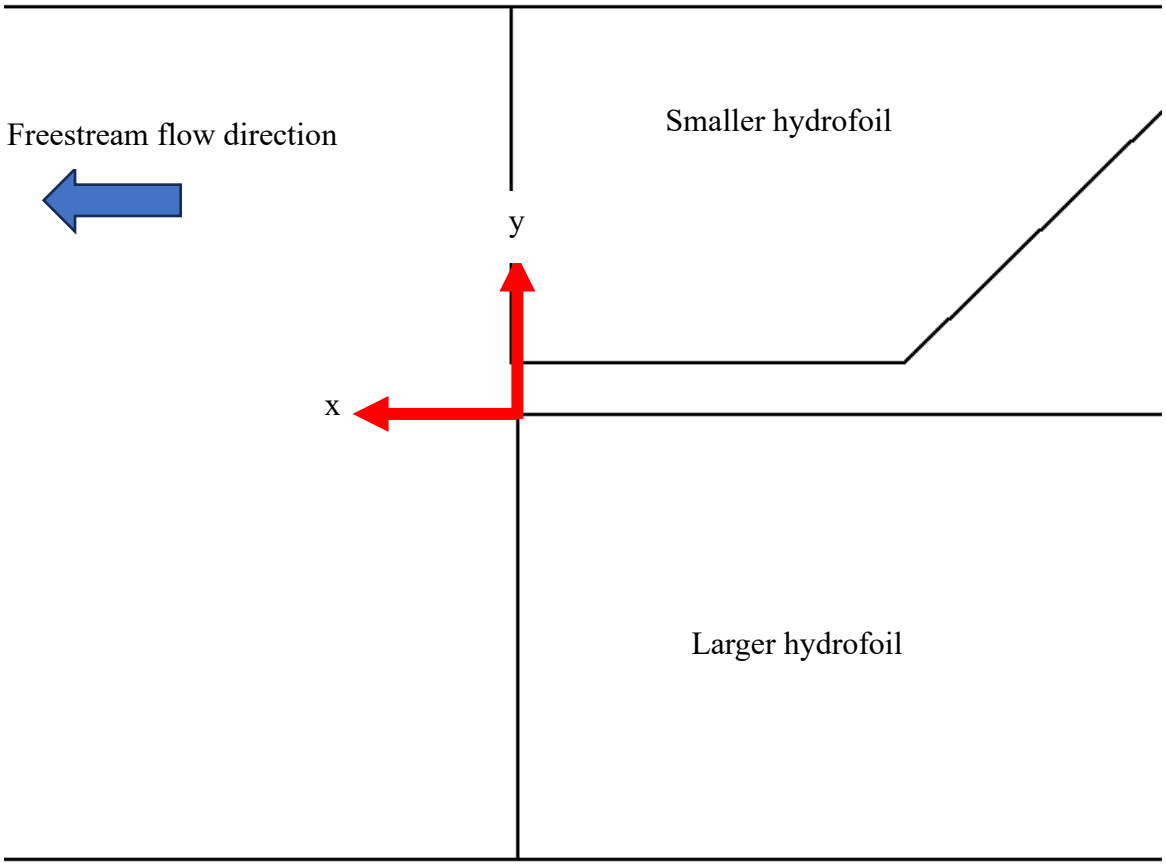


Figure 1.5 Coordinate System of Two Vortex Interaction. The flow considered in the study of the interaction of vortices. A drawing showing the coordinate system relative to the hydrofoils is shown here. The flow goes from right to left, and the x direction has its origin at the tail of the larger hydrofoil and increases in the streamwise direction. The y direction is vertical and has its origin at the tip of the larger hydrofoil. The z direction is into the plane of the page.

CHAPTER II

Experimental Methods

The experimental apparatus and methods used in both experimental programs are in described in this chapter. In both studies, the flow facility employed was the Miniature Large Cavitation Channel (mLCC), a recirculating water flow facility. Each study also employed volumetric particle imaging velocimetry. Additional measurements taken as part of the cavitation study are described here.

mLCC Facility Overview

The mLCC is a recirculating cavitation channel that is a $1/14^{th}$ scale model of the U.S. Navy's William B. Morgan Large Cavitation Channel in Memphis, TN (Etter et al., 2005). The mLCC has a 22.5 by 22.5 cm square test section (with chamfered corners) with removable, clear acrylic windows on all four sides. The test section flow can operate at a range of speeds from 1 to 25 m/s, but in this work, only speeds between 1 and 10 m/s were employed. Upstream of the test section is a 6.4 to 1 contraction. Separate rings of tubing around the inlet and outlet of this contraction each connect four pressure taps on the tunnel walls. The rings port into the tunnel top, bottom, and both tunnel sides and provide averaged measurements of pressure at those streamwise locations. Given the known contraction ratio, the pressure differential between these pressure measurements is used to estimate the flow velocity in the channel using the Bernoulli pressure change. The downstream ring, immediately upstream of the test section, is also used to

measure the freestream pressure in the test section. An Omega PX409 differential pressure transducer with ±0.08% accuracy was used to measure the pressure difference across the contraction, giving an uncertainty in velocity of ±0.06%. An Omega PX419 transducer with ±0.08% accuracy was used to measure static pressure immediately upstream of the test section, giving an uncertainty of ±0.08% in static pressure. Figure 2.1 shows the locations of these pressure taps. Figure 2.1 also shows the test section in relation to the contraction.

Upstream of the contraction, a flow straightener and screen are used to break up large vortices generated by the impeller and turning vanes and leave low turbulence in the test section, and the flow is strained as it moves through the contraction, reducing the small-scale turbulent fluctuations. PIV was used to estimate the freestream turbulence in the test section. With an empty test section, the freestream turbulence level (RMS of u'/U_0 where u' is the fluctuating streamwise velocity component and U_0 is the mean freestream velocity) was measured with stereoscopic particle image velocimetry (Stereo-PIV) to be less than 0.25%. The particulars of the freestream turbulence measurements are detailed in the following chapter on velocimetry measurements.

As a cavitation channel, the pressure in the test section, P_0, can be varied between 20 and 200 kPa (absolute). A head tank is connected above the mLCC to allow this pressure variation either by applying a vacuum pump or pressurized air supply to accomplish reduced or raised pressure. A deaeration loop is connected to the channel and can be used to modify the dissolved and free gas content. In this loop, water from the tunnel is sprayed into a vacuum tank held to low (absolute) pressure before being returned to the tunnel. The vacuum tank is separately connected to a vacuum pump to maintain a low pressure (typically greater than 90 kPa below atmospheric pressure) in the tank. As the water sprays into the tank, dissolved gases are drawn

out of solution due to the low pressure. The water leaving the vacuum tank has a lower dissolved gas content. This deaeration loop runs in parallel to the tunnel, so not all the water in the tunnel passes through the deaeration section for every passage of a particular bolus of water through the test section. Accordingly, it takes hours to reach desirable levels of nuclei for inception. For low nuclei concentrations in this study (corresponding to 13-15% of dissolved saturation concentration of gas at atmospheric pressure), this generally took around 15-20 hours to reach. For higher nuclei concentrations (~30-35% of dissolved saturation concentration), this generally took around 5 hours to achieve.

The dissolved gas content was measured using a Thermo Scientific Orion 083005MD dissolved oxygen (DO) probe with Thermo Scientific Orion Star A113 meter with a combined uncertainty of ±2% in dissolved oxygen saturation concentration. DO content is used as a proxy for total dissolved gas content. Setting an arbitrary distribution of nuclei is not possible, but the power law distribution of natural nuclei can be shifted and estimated by the dissolved oxygen (DO) content of the water. Additionally, the deaeration loop contains a sub-loop with a filter that allows the water to be filtered for particulates down to 1 to 5 microns. This filtering allows the addition and removal of particles for PIV. It is worth noting that the presence of the uniformly sized PIV particles does not lead to a noticeable spike in nuclei at a particular critical pressure (or size corresponding to the particle size), so it was not necessary to remove the PIV particles to have a reasonable power law distribution of nuclei in the tunnel. Dissolved gas content remained close to constant during the inception experiments as the tunnel was sealed from outside air being ingested. Measured DO content varied less than 2% across a day of measurements, and if left undisturbed, the tunnel could hold a similarly consistent DO for weeks. However, DO is a single value and does not give the concentrations of nuclei of various sizes. That information

requires a different tool, such as the cavitation susceptibility meter (CSM) described at the end of this chapter.

As most of the velocity measurements in this thesis were taken with a four camera volumetric velocimetry system, it is imperative that a steady base is available for the cameras and illumination. To this end, a new platform was constructed over and around the lower return of the mLCC, as shown in Figure 2.2. This platform, containing approximately one literal ton of steel, has an optical table mounted on rails so that it can be slid spanwise along the width of the test section. A separate platform for users to walk on surrounds the measurement platform so that the weight of the users will not disturb the measurement system. Together, these design features ensure that the vibration of the cameras and illumination is minimal. More importantly, for volumetric velocimetry, it is important that any minimal shifts (i.e. sub-pixel shifts) that occur are uniform across the cameras so that a good volume self-calibration can be obtained. Vibrations should be reduced as much as possible, and any remaining vibrations must involve the cameras shaking together (though not necessarily together with the test section). In general, volume self-calibration on the data sets in this thesis had mean disparities of less than 0.05 voxels, indicative of minimal vibrations.

For pressure measurements away from the walls of the tunnel, the pressure field is calculated from velocity fields measured with PIV. This avoids perturbing the flow which would happen if pressure were measured by a probe immersed in the flow field. However, integration of the velocity field only yields a pressure field solution up to a constant. To obtain absolute pressures, a boundary condition must be placed on the pressure field. To this end, a modified Pitot tube was inserted into the tunnel at the edge of volumes of flow field measurements where pressure would be measured. The Pitot tube had its center filled with epoxy such that only the

surrounding static pressure was measured. It was connected to an Omega PX419 static pressure transducer with ±0.08% accuracy, the same as the above model. This was used to determine the pressure change from the wall of the tunnel to the edge of the velocimetry volume and thus the absolute pressure at the edge of the volume relative to the freestream pressure in the tunnel. The velocimetry volume was made large enough such that the pressure at the boundary did not change significantly as the vortices studied transited through it so that a steady pressure boundary condition could be assumed. It was not possible to measure the unsteady pressure in the middle of the flow field at the same time as the velocimetry measurements as a pressure probe would perturb the flow. This necessitated the determination of the steady pressure boundary condition.

High-Speed Videography

High-speed video was taken with two Phantom v1212 cameras with 50 mm AF Nikkor or 105 mm AF Micro-Nikkor lenses. While these lenses have autofocus, the Phantom cameras do not, so camera focusing was performed manually. The cameras can be placed to view the tunnel from the side. In some cases, when a top-down view was needed, a mirror was placed on top of the tunnel as there is not enough space for a camera above or below the tunnel. The camera length scales were found by calibration from a simple ruler, allowing some quantitative information to be derived from the high-speed videos. An Arrilux Pocketpar 200 backlit the tunnel while an Arrilux Pocketpar 400 illuminated the tunnel from the same side as the cameras. The backlight was necessary to prevent shadows from appearing behind the cavitating vortices.

Acoustic Measurements

As cavitation inception generates a range of acoustic emissions, a hydrophone can record them and allow distinguishing between varied types of acoustics and the underlying cavitation.

A Bruel and Kjaer Type 8103 hydrophone was placed above the tunnel in a water-filled pocket. The hydrophone was held by a piece of foam to reduce reflections. A Type 2635 Bruel and Kjaer charge amplifier fed the hydrophone signal into a National Instruments 6361 DAQ. Data was acquired at 500 kHz. The data was filtered digitally in Matlab after acquisition and this processing is detailed in Chapter 8.

Nuclei Measurements

While zero or negative pressures in the liquid are necessary for cavitation inception, a nucleus is needed to initiate inceptions given the magnitude of tensions occurring in the flows studied here (i.e. these flows undergo heterogeneous nucleation). It is therefore necessary to measure the concentration and critical pressure of the freestream nuclei population. Various methods, such as interferometric Mie imaging and long-range microscopic shadowgraphy, have been developed for measuring small bubbles that often serve as nuclei (see a discussion in (Brandner, n.d.). Such optical methods, however, are ineffective for small nuclei such as those in natural nuclei populations that were present during the present experiments. In the range of nuclei size distributions (~O(10μm)) that are relevant here, a Cavitation Susceptibility Meter (CSM) is the ideal tool.

Originally developed by Oldenziel (1982), the CSM runs the channel water through a venturi such that the pressure drops to negative absolute pressures (tensions). A picture and representative diagram are shown in Figure 2.3. As the liquid runs through the tension, the nuclei incept and make a sharp acoustic emission which is detected by a small piezoelectric element. By varying the flow rate, the tension in the throat of the venturi can be varied and measured indirectly by measuring the flow rate and the static pressure upstream. The CSM is swept through a range of tensions, and at each tension, the number of inception events detected

up by the piezoelectric is recorded. As the tension is known and the flow rate and time of acquisition are known, the number of nuclei at that critical tension in a given fluid volume is determined. For a given critical tension or pressure, $P_{critical}$, a corresponding critical radius, $r_{critical}$, can be found by treating nuclei as spheres of contaminant gas following

$$P_{critical} = P_{vap} - \frac{4S}{3r_{critical}}$$

where S is the surface tension. This is known as the Blake critical radius and this relation can be used to determine the size of nuclei that incept at a given critical pressure. However, it is important to note that the nuclei may not be clean gas bubbles but may be the result of any inclusion in the liquid that has a gas pocket (e.g. a Harvey nucleus).

Some subtleties are important in operating the CSM. First, the CSM must draw water from upstream of the contraction, slightly below the wall of the tunnel, so that the water flowing through represents the water flowing through the test section without altering the flow in the test section with the wake of the inlet tube. The inlet tube should gently curve forward into the direction of the flow, and the velocity in the inlet of the CSM loop should match the velocity of the water it is drawing from. Additionally, ideally there should be minimal pressure change for the CSM until it reaches the throat of the venturi. This is to prevent any change in the nuclei from occurring between the channel and the CSM measurement location. Related to that necessity, to ensure that the water in the channel during the CSM measurement has the same nuclei distribution as during cavitation measurements, it is best to run the tunnel at full speed and the lowest pressure used in the cavitation study to allow the nuclei distribution to equilibrate.

Yet, running the water through the channel for a cavitation measurement has the unfortunate tendency to shift the nuclei distribution up (i.e. larger nuclei in higher

concentrations) as nuclei can be drawn out of solution as the water experiences low pressures during the dynamic flow in the test section. Given the length of time that is necessary to run a CSM measurement, shifts in nuclei concentration during the CSM measurement itself are also possible. Figure 2.4 shows several runs of the CSM used in this study on the mLCC water. These runs were conducted across 2 days and the tunnel was sealed during this time. The tunnel was running at a minimal speed to circulate the water. While the amount of air in the tunnel should not have changed in this time, the nuclei distribution measured did change. Note that not only does the typical concentration of the nuclei vary between nearly one order of magnitude, the slope of the nuclei distribution changes substantively as well.

As noted above and shown by Figure 2.4, the nuclei distribution of a particular filling of the channel is not necessarily a fixed quantity even if no outside air is ingested or dissolved air is drawn out during deaeration. The nuclei distribution should be regarded as a dynamic equilibrium between the dissolved gases and the nuclei, and the balance of this equilibrium can shift over time depending especially on the pressure applied to the water. Figure 2.5 shows the shift in concentration at a fixed level of tension over time. These measurements were taken immediately by first allowing a hydrofoil to cavitate for 10 minutes. Following that cavitation, the drift of nuclei concentration over time was recorded. Given the length of time of measuring a full nuclei distribution curve, only the concentration at a single critical tension was measured. There is a noticeable drift in the first few minutes. It then proceeds to drift slower after this stage. As such, the largest uncertainty in relating the nuclei measurement to the eventual cavitation inception measurements derives from the shift in the nuclei distribution over time. The underlying assumption of the CSM is that the water passing through the CSM has the same nuclei distribution as the water in the channel during the inception experiments. This assumption

relies on the equilibrium of the nuclei not shifting between the CSM measurements and the inception measurements as well as the CSM being properly set up such that no changes to the nuclei distribution occur between the CSM and the tunnel during the CSM measurement. This last assumption cannot be directly tested, but the length of time the water spends running between the channel and the CSM is orders of magnitude smaller than the length of the inception measurements. Further, the pressure changes are more extreme in the channel than between the channel and the CSM. As such, the largest uncertainty related to the actual nuclei distribution comes from the changes between the CSM and inception measurements. In initial testing, done by running the CSM before and after inception measurements, the difference between the CSM measurements varied between a factor of 2 and 4.

If the channel was run at conditions corresponding to the inception measurements before the initial CSM measurement, the new nuclei distribution equilibrium could be reached, and the difference between initial and final CSM measurements was only as much as 3. To better account for these effects, before inception measurements, the channel was run at the same speed as the inception measurements and comparable pressures for approximately 10 minutes. After this, an initial CSM measurement was taken and following the inception measurements, a final CSM measurement was taken. Nevertheless, the CSM measurement would noticeably change during the duration of the CSM measurement as the nuclei shifted yet again (as suggested by Figure 2.5), again by a factor as much as 2 to 3. Mitigating these shifts was done by first allowing the tunnel to cycle at a low speed for approximately 10 minutes before beginning the CSM measurement. In all cases in this work, the initial and final CSM measurements were averaged, and as a conservative estimate, the CSM measurements are assumed to be within a factor of 4 of the actual nuclei distribution.

Beyond the uncertainties discussed above, bias errors must be accounted for. (Yakushiji, 2010) used a high-speed camera in combination with the CSM to evaluate over and under counting of nuclei for the exact CSM used in this study and found that the CSM generally overcounted at high tensions and undercounted at low tensions and that this tendency led to CSM measured nuclei densities between 10 and 150% of the actual density. Additionally, (Yakushiji, 2010) used numerical models to estimate sources of bias errors. Bias errors in nuclei density due to bubble slip velocity and the static pressure difference were found to be around 10 and 5% respectively.

(Khoo et al., 2020) discusses the dramatic variability of nuclei measurements typical of cavitation measurements, even in facilities with more elaborate deaeration and nuclei control systems than that used here (such as the Cavitation Research Laboratory Tunnel at the Australian Maritime College).

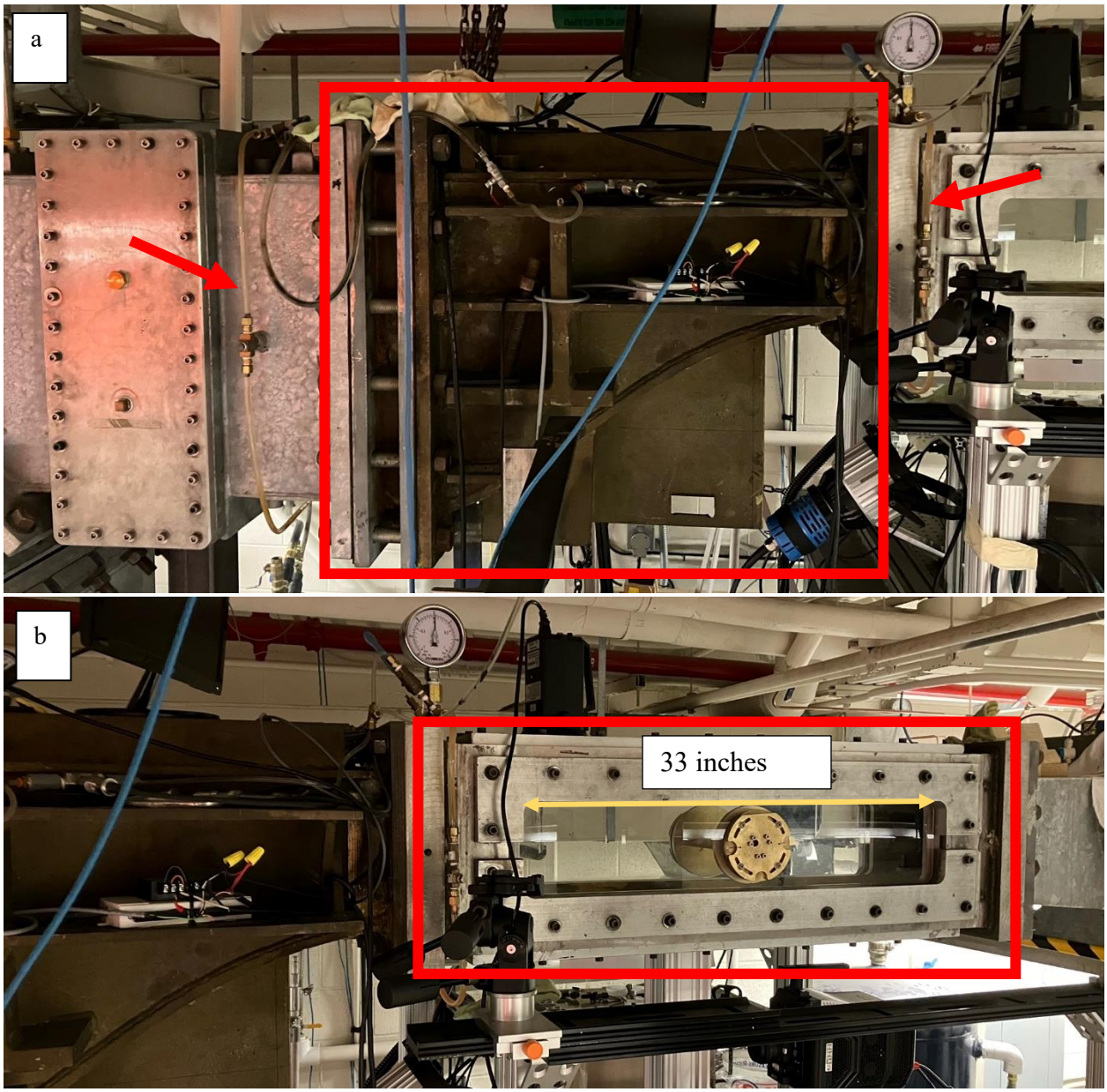


Figure 2.1 Pictures of the mLCC Test Section and Contraction. The upper image (a) shows the contraction of the mLCC in the red box. It is an asymmetric contraction top to bottom. The red arrows denote the rings where pressure is taken upstream and downstream of the contraction to measure average velocity. The lower image (b) shows slightly downstream of (a) where the test section with acrylic windows is in the red square.

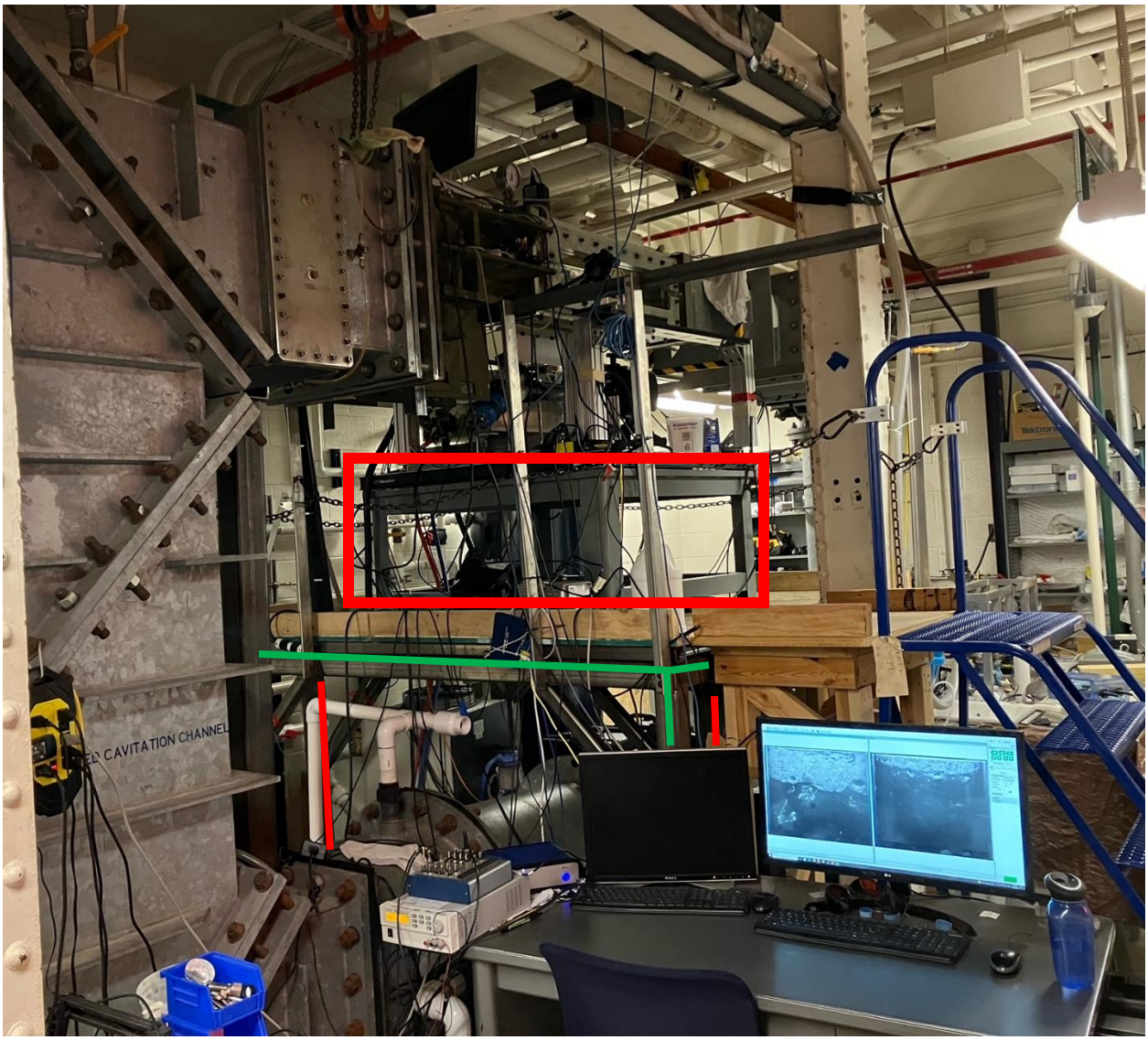


Figure 2.2 Pictures of mLCC and Test Support Structure. The cavitation channel used in this study, the mLCC, has multiple platforms in the middle of it. The inner platform, isolated from the outer platform, holds the laser and cameras and consists of approximately 1 ton of steel. The portions visible in this photo are boxed and highlighted in red. The outer platform is intended for personnel to walk on while not disturbing the inner platform and is outlined in green where visible in this photo.

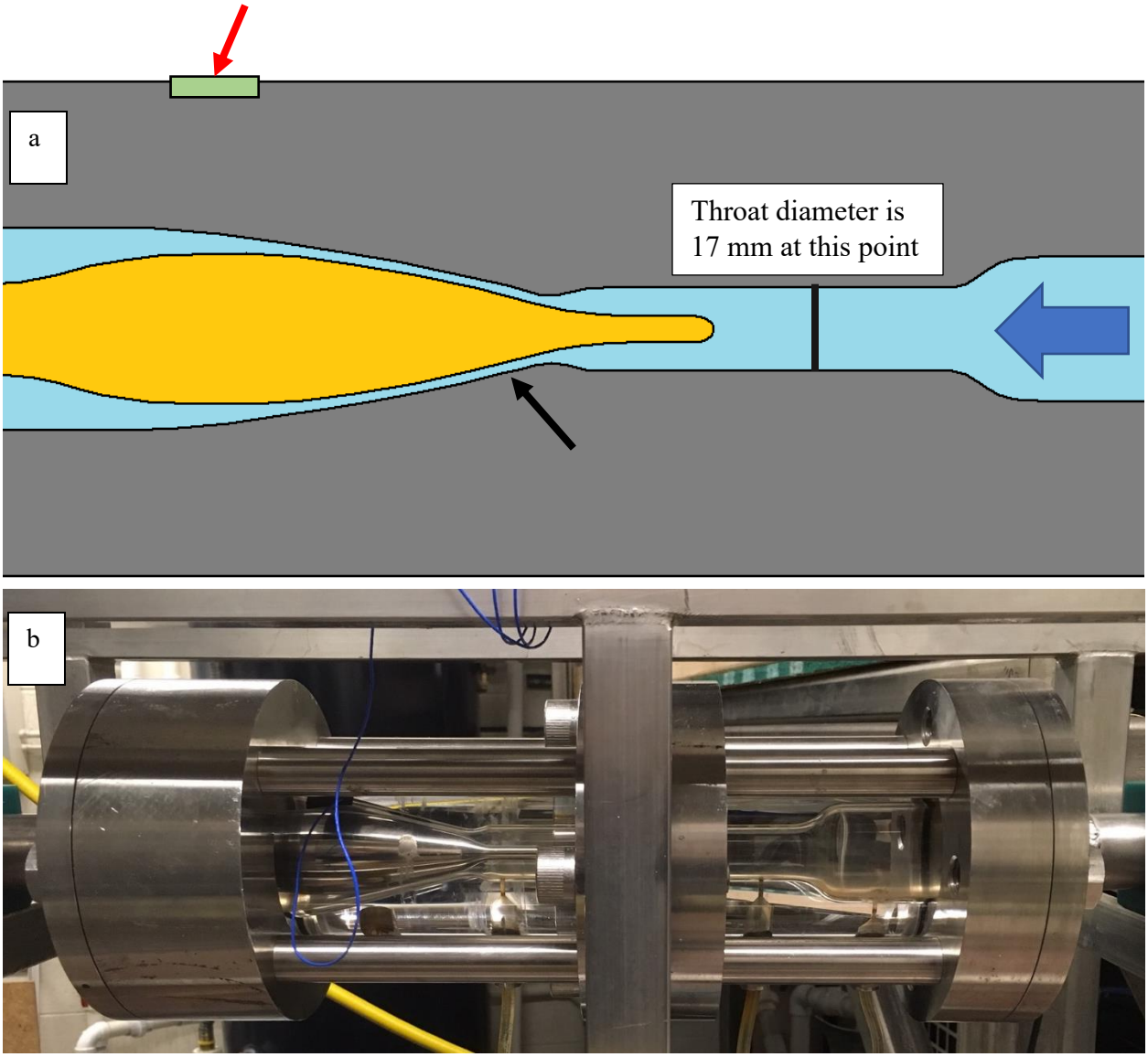


Figure 2.3 Diagram and Image of Cavitation Susceptibility Meter. (a) The cavitation susceptibility meter (CSM) has flow coming from the right as denoted by the blue arrow. It reaches an axisymmetric contraction where it encounters an annulus of tension, indicated by the black arrow. The brass centerbody, shown in orange here, helps prevent the occurrence of the region of tension from choking when it cavitates. "Pops" from the cavitation events are measured by the piezoelectric, denoted by the red arrow. (b) shows the particular CSM used in this study, lent by the Naval Surface Warfare Center-Carderock Division.

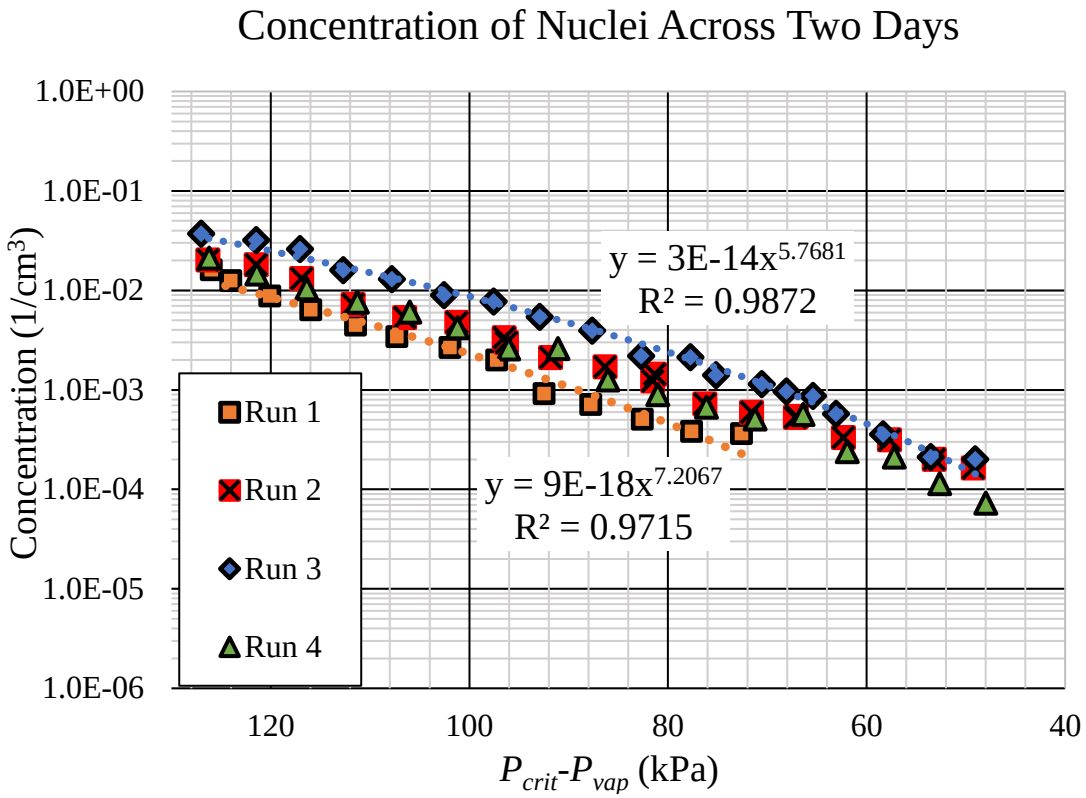


Figure 2.4 Shifting Nuclei Distribution. The CSM was run 4 times over 2 days with the same water, sealed in to prevent addition or loss of contaminant gas. Despite the quantity of contaminant gas being fixed, the different runs give different nuclei populations. The differences between various runs can be as much as an order of magnitude, and the slope of the nuclei distribution curves can vary substantially as well.

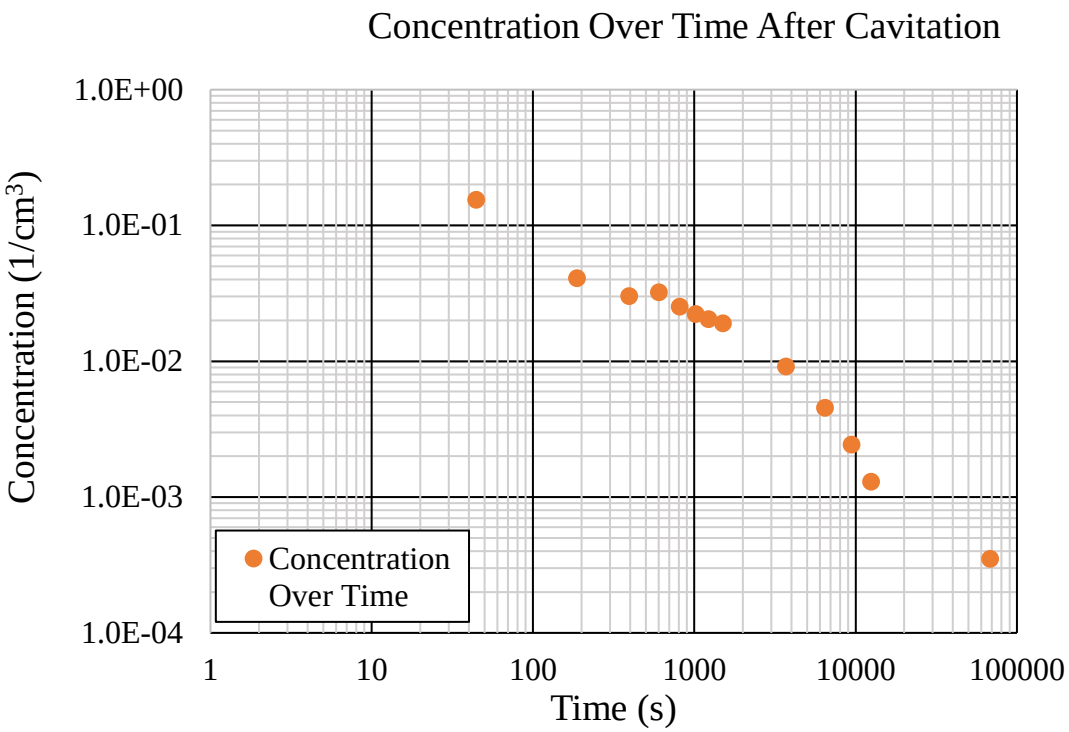


Figure 2.5 Change in Concentration of Nuclei Over Time. To demonstrate the shift in nuclei concentration over time, the tunnel was set to cavitate over a hydrofoil. After this cavitation, with the tunnel circulating at low speed, the concentration at a fixed critical pressure was measured repeatedly from almost immediately after and up to the next morning. As can be seen above, the concentration dropped massively even within the first few minutes. Over the course of an hour, which is not quite enough time to fully measure a whole nuclei distribution with the CSM, the change is over an order of magnitude.

CHAPTER III

Particle Based Velocimetry Methods

For detailed characterization of instantaneous flow structures, it is advantageous to directly measure velocity field data. Such measurements can be achieved through the visualization of particle motions in the flow domain. This thesis makes use of several related but distinct particle based velocimetry methods. In general, these methods involve illuminating and imaging a region of a flow seeded with small particles that closely track the surrounding flow. From two or more recordings of the particle images, velocity fields can be inferred. Various algorithms and techniques are used in particle based velocimetry and several algorithms may be applied to the same set of imaged data. This section provides some background as these details pertain to this thesis, and (Raffel et al., n.d.) is recommended for detailed coverage on all aspects of this topic.

Velocimetry Apparatus

All the particle based velocimetry measurements in this thesis share the same set of hardware. A Photonics Dual Head DM-100 high-speed laser with a maximum power of 10 mJ/pulse at 10 kHz for each cavity was used to illuminate the measurement domains. The laser cavities are placed in parallel within the laser, and the beams are polarized. The two beams are merged within the laser unit using incoherent polarization combining. In this, the two different laser cavities have different polarizations, so when one laser strikes the beam combiner, it is reflected as if striking a mirror, while the other laser passes through it. For frame-straddled data

(discussed later), the heads are fired sequentially with arbitrary time separation, *dt*, between frames. Thus, for frame-straddled data, the two lasers can illuminate the same volume twice with an arbitrary time separation. For time series data, both heads can be fired simultaneously to approximately double the illumination.

Four Phantom v1212 cameras with a 1280 x 800 pixel images at 12,600 frames per second with 12 bit depth dynamic range were used. Correspondingly, frame-straddled data can be taken at 6,300 frames per second. Higher frame rates can be achieved if only a portion of the camera sensor is used. LaVision Scheimpflug adapters were used to view non-orthogonally into the test section. Four 105 mm Micro-Nikkor macro lenses were used, sometimes in combination with Nikon TC-201 2X and Tele Plus 1.4X DGX teleconverters. Auto focus, while built into these lenses, was not used as the cameras had Scheimpflug adapters that are not compatible with this feature. A LaVision High Speed PTU X commanded the devices and controlled the system timing.

Choice of Seeding

Inherent to all particle based techniques is the assumption that the particles represent the underlying fluid motion (i.e. they are true Lagrangian tracers). This is an ideal circumstance, given that the particles are of finite size and may have a specific gravity that differs from the surrounding fluid. In the range of flow media, length, and velocity scales experimentalists encounter, this makes choice of particles a non-trivial decision. A further limitation is that the particle tracking velocimetry (PTV) algorithm used here, Shake-the-Box (STB), assumes uniform particle shape and size as part of the iterative particle reconstruction (IPR).

The particles employed for this experiment were selected due to their good tracking with the flow. While ideal particles perfectly trace the flow, in practice, the particles used in this study have some slip velocity relative to the surrounding liquid flow. The extent of this slip is governed by the density difference and size of the particles as well as the speed of the liquid flow, a fact which has been appreciated, if not understood, since Theophrastus, who noted that "because of their smallness… So too in the same way dust [particles] sometimes remain[s] hanging in the air for a long time and does not descend." Twenty micron diameter LaVision Polyamide HQ (1.03 g/cc) particles were incorporated in all experiments in this thesis. To ensure that the particles seeding the flow have such uniformity, before running experiments, the water in the tunnel ran through a 1 micron filter in series with the deaeration loop for approximately 15 hours. After this, only a few stray particles remained in the illuminated volume (<50).

The Stokes number of the particles can be estimated by relating the response time of the particle to the time scale of the flow,

$$St = \frac{\tau_p}{\tau_f}$$

where τ_f is the flow time scale, and for nearly neutrally buoyant particles we can estimate the particle time scale, τ_p, as

$$\tau_p = \frac{d_p^2 \Delta\rho}{18\mu}$$

where d_p is the particle diameter, $\Delta\rho$ is the density difference, and μ is the dynamic viscosity of the water (Raffel *et al*. 2018). This gives a time scale of around $7 \cdot 10^{-7}$s for the particles. We estimate the flow time scale for the wedge flow ($\tau_{f,w}$) as

$$\tau_{f,w} = \frac{h}{U_0}$$

with h as the wedge base height and U_0 as the freestream velocity. We then estimate the time scale for the two vortex flow ($\tau_{f,v}$) as

$$\tau_{f,v} = r_c^2/\Gamma$$

where r_c is a typical core radius of the vortex and Γ is the typical vortex strength. For the wedge, the flow time scale then is $3 \cdot 10^{-3}$s. The vortices are considered at a range of Reynolds number, and the flow time scale for the vortical flow ranges from $1.5 \cdot 10^{-3}$ to $5 \cdot 10^{-5}$s. Thus, for the highest speed vortical flow case, we can estimate the Stokes number to be as high as 0.01 (at a flow speed of 10 m/s). The usual threshold for suitable particles is a Stokes number of 0.1, and a value of 0.01 indicates that the bias error due to the particle lag is negligible. At the lower speeds in the vortical flow study and in the wedge study, the Stokes number is even lower, so provided even distribution of particles throughout the flow structures studied, particle slip should be a negligible contribution to bias error in those cases as well.

However, vortices tend to eject PIV particles from their cores, making the assumption of even distribution of particles throughout flow structures invalid (Raffel *et al*. 2018). Measuring the cores of vortices is a principal aim of this work, so using particles that stay in the vortex cores is critical. This tendency towards ejecting the particles happens as the particles continue to orbit the vortices. In other words, this is due to the time integrated slip velocity of particles in the vortices which, while negligible over the flow time scales above (relevant for estimating bias errors in resolving vortical structures), but it is <u>not</u> negligible when integrated over the lifetime of the vortices in the two vortex case. This slip velocity can be estimated as

$$U_s = d_p^2 \frac{\Delta\rho}{18\mu} \frac{u_\theta^2}{r_c}$$

where u_θ is the swirl velocity of the vortex. Considering just the two vortex problem (the measurements in the wedge flow are not taken as far downstream), as the vortex radius is larger at lower speeds and the swirl velocity is lower at lower speeds (with the slip velocity even having a quadratic dependence on the swirl velocity), the effect of this particle slip is substantially reduced by reducing the freestream speed of the tunnel. Estimating the slip velocity with the above formula and data taken in this thesis, the scaled slip velocity U_s/U_0 is 5 times greater for the highest speed case (10 m/s) than the lower speed case that is accordingly studied more in this thesis (3 m/s). In practice, the particle density in the vortex core is visually reduced when the freestream velocity is 10 m/s as compared to when it is 3 m/s. Accordingly, due to the difficulties of acquiring adequately seeded data when the tunnel is at 10 m/s, the detailed single-phase measurements of the downstream interaction of the vortices were taken at 3 m/s. This will be discussed further below.

Cost and availability also constrain the choice of particles. With the total volume of the water tunnel around 1000 gallons, a substantial amount of seeding particles was required for flood seeding. Approximately 300-500 g of seeding particles were added. Prior experiments in Knister *et al*. (2020) used fluorescent Cospheric particles with a density of 1.0 g/cc and even some slightly buoyant fluorescent particles with a density of 0.995 g/cc. Besides the benefits fluorescence offers for signal to noise ratio in particle images, the density matches that of water more closely, so the particles stay in the cores of the vortices for longer. However, the amount of seeding necessary to adequately resolve the structures we desired to measure throughout this thesis was not available with these Cospheric particles due to shortages and delays in manufacturing.

Depending on the different volumes considered, different seeding densities were used. The maximum seeding density that can be used was found empirically for each measurement volume. From experience, this upper limit is the concentration such that the STB algorithm can track only half the particles that it detects. Adding additional seeding past this point will generally not lead to a higher absolute number of particles tracked (i.e. higher density data), and it will likely lead to more false tracks. Small trial datasets were acquired and calculated with STB to tune the parameters and find this empirical limit. This maximum seeding is generally quoted in terms of particles per pixel (ppp) which is the particle image density, N_I. In the various volumes measured in this study, that was generally around 0.03 ppp. However, this metric presents an incomplete picture as the ability to track particles depends on their size and thus potential for occluding viewing of each other in a camera's view. To account for this, the image source density, N_S, a different parameter, is found with

$$N_s = N_I \cdot \frac{\pi}{4}\left(d_{particle}\right)^2$$

(Scarano 2013) where N_I is particle image density ((Schröder & Schanz, 2022) and $d_{particle}$ is the typical particle diameter measured in pixels. If $d_{particle}$ is larger, the particles are more likely to overlap, and N_S captures this. Given the typical diameter of particles in the images in this thesis, N_S is about 0.4-0.6, which for a four camera setup is close to the limit of what can be successfully reconstructed via tomography (Raffel *et al*. 2018). Thus, even though N_I is somewhat low, the measurements in this work are still at relatively high seeding density for MART reconstruction approaches. For a four camera system, N_S of about 0.5 is considered the limit of tomographic reconstruction before ghost particles cause failure of the reconstruction.

Nevertheless, N_I conveys the important detail that optical velocimetry necessarily projects all the particles in the illuminated volume onto the 2-D measurement plane of the camera sensor. For a constant size of the particles on the sensor plane, this means that thickening the volume will lead to a higher N_I. In other words, when comparing volumes of different thicknesses, to maintain a similar N_I, different seeding densities in the tunnel must be used. Seeding density can be increased by mixing in additional particles. It can also be removed by running the water in the tunnel through the deaeration and filter loop. By these tools, we can achieve the highest seeding that STB can track for a given measurement volume.

Outline of Velocimetry Algorithms

For the given set of cameras and laser and particles described above, a broad outline of the different velocimetry approaches used in this thesis is provided below. Table 3.1 summarizes the differences between the different techniques, and Table 3.2 provides a comparison of their relative benefits and drawbacks. First, stereoscopic PIV (Stereo-PIV), which is a planar measurement that measures all three components of velocity is used. Stereo-PIV uses multiple cameras to estimate out of plane motion after first computing the in-plane components separately for each camera. Subsequently, tomographic PIV (Tomo-PIV), which is a volumetric measurement that delivers all three components of velocity and their spatial gradients is used. While both Stereo-PIV and Tomo-PIV methods use correlations, Tomo-PIV differs in that it first tomographically reconstructs the particle intensities into the measurement volume. Afterward, correlation is done over a subregion in the measurement space instead of a correlation window as in two-dimensional PIV (e.g., Stereo-PIV in this thesis).

Shake-the-Box particle tracking velocimetry (STB) is a volumetric particle tracking velocimetry method that finds velocity and acceleration from individual particle tracks, not based

on using correlation of images. Tomo-PIV and STB can be performed on the same sets of images. STB is a Lagrangian measurement which can then be converted into an Eulerian frame with either a binning algorithm or a data assimilation tool, Vortex-in-Cell# (VIC#). Binning is a simple spatially weighted averaging of particle data. VIC# is instead a data assimilation tool that constrains the field to minimize the divergence of velocity (as the flows considered here are incompressible) and to minimize the curl of the acceleration field.

The three above methods can all be used as either time series (or single pulse) or frame-straddled measurements (double pulse). Time series measurements have the particle images recorded at instances equally spaced in time. Within this larger dataset, successive images can be used to find velocity, and from successive velocity fields, temporal acceleration can also be found. In contrast, frame-straddled measurements rely on independent sets of double-frame images. In each double frame set, the time separation of the images can be set arbitrarily short as colinear laser heads are used to illuminate the flow. The two images can then be used to estimate the velocity field. However, the time separation between each double-frame image set is usually much larger than the time separation within the image set, so temporal acceleration cannot be found with frame-straddled measurements. Thus, frame-straddled measurements are generally useful in developing independent samples of a velocity field. Depending on the spacing in time between double frame sets, frame straddled measurements can also be used to capture time evolution of flow structures. By default, time resolved measurements can capture the time evolution of flow structures. To capture the motion of particles in a flow (whether via correlation as in PIV or by directly tracking as in STB), the temporal resolution must be higher than that required to capture the dynamics of flow structures. As an example, in the wedge flow study

considered in this thesis, the shedding frequency is around 90 Hz, but tracking the particles in the wake requires recording images at 20 kHz, which is much higher than the Nyquist frequency.

Stereoscopic Particle Image Velocimetry

Stereoscopic particle image velocimetry (Stereo-PIV) is a PIV method that yields all three components of velocity in a single plane of the imaged flowfield. A detailed description of the technique is given in Raffel *et al*. (2018). The flow is illuminated with a thin collimated light sheet. The light sheet must be thin enough to ensure gradients across its thickness (defined as the z-direction of the flow) are negligible as Stereo-PIV treats the region as a plane, not a thin volume. However, the light sheet must also be thick enough that any out of plane motion does not cause an excessive number of particles to move into and out of the light sheet between successive frames. Another parameter to consider is that the minimum width of the PIV interrogation window should be at least the thickness of the light sheet. Stereo-PIV requires viewing the same flow region from at least two cameras. A two camera Stereo-PIV system is most common, but four camera Stereo-PIV also exists and gives lower uncertainties. The cameras must have independent lines of sight, and the angle between them governs the relative uncertainty between the different velocity components. Given the requirement of different viewing angles, at least one camera must view the field at an angle relative to the measurement domain. As the lens plane and camera sensor plane (image plane) will no longer be parallel to the plane of the measurement, an angular adjustment between lens and image planes is necessary to achieve the Scheimpflug condition. Additionally, since in the flows considered here there is a change in index of refraction (from water to acrylic to air), the non-orthogonality of the cameras relative to the measurement plane yields another complication as this change should be accounted for and corrected. This necessitates the use of prisms or water filled boxes on the

outside of the acrylic windows so that the cameras' lines of sight pass orthogonally into the prism or water filled box. This corrects for the change in index of refraction but not for the Scheimpflug condition.

As noted above, in Stereo-PIV, the in-plane velocity components are first found independently for each camera. The results are then used to calculate all three components of velocity, given knowledge of the angles between the cameras (which can be found during calibration). This calibration is performed by placing a calibration target (either with two planes built into it or by translating a single plane target) and acquiring calibration images. It is advisable that this calibration target is coincident with the light sheet, but planar self-calibration (PSC) based on particle images means this is not a strict requirement when infeasible. As there will always be some angular misalignment and displacement offset between calibration target and light sheet plane, PSC is always advisable. PSC uses the disparity between where a point occurs and space and where it occurs in the multiple cameras to correct the calibration mapping. After calibration, particle images can be recorded in frame straddled or time series mode and velocity fields calculated.

A benefit of Stereo-PIV is that there is a generally accepted method for uncertainty quantification. (Sciacchitano et al., 2015), using a range of experiments for comparison as documented in the database in (Neal et al., 2015), compared the uncertainty surface method ((Timmins et al., 2012)), the particle disparity approach ((Sciacchitano et al., 2013)), the peak ratio criterion ((Charonko & Vlachos, 2013), and the correlation statistics method ((Wieneke, 2015)) and found correlation statistics to most accurately estimate the uncertainty of the measurement. This method uses the correlations underlying a given Stereo-PIV velocity field, so for each field,

the uncertainty at each spatial point can be estimated and therefore propagated through subsequent calculations.

Tomographic Particle Image Velocimetry

Tomo-PIV employs a measurement domain that is a three-dimensional volume which is thicker than a single interrogation volume. In a volumetric measurement domain, particles are more likely to stay within the volume between successive images. However, determining volumetric information from several planar images requires use of volumetric reconstruction before any cross-correlation can be done to find velocity fields. Tomographic reconstruction takes the image intensities from the sensor planes and maps them into the 3-D space of the measurement domain. Accomplishing this is dependent on having several independent lines of sight, akin to Stereo-PIV, along with sub-pixel accuracy in the calibration. This sub-pixel accuracy constraint necessitates use of Volume Self-Calibration (VSC).

However, with the increased thickness of the volume, particles are more likely to overlap and occlude view of each other during imaging. Accordingly, generally use of 3 cameras is considered the minimum necessary for Tomo-PIV as opposed to 2 cameras for Stereo-PIV. Use of 4 cameras is typical as a balance between accuracy with achievable particle seeding densities and cost. Also, the concentration of particles in particles per unit volume must be lower for volumetric measurements than for Stereo-PIV as looking across a thickness means a higher particle image density, N_I (in particles per pixel), for the same concentration. As noted in the particle section above, this N_I is not the final say in how dense a flow may be seeded and still be accurately reconstructed as particle diameter must be considered as well (leading to N_S).

Assuming a reasonable seeding density, such as an N_S of less than 0.5, and adequately illuminated images, tomographic reconstruction can be approached with variants of algebraic

reconstruction techniques (ART). These are generally initiated with something like multiplicative line of sight (MLOS) followed by several iterations of multiplicative ART (MART). The results of this analysis can be improved by use of motion tracking enhancement (MTE) or sequential motion tracking enhancement (SMTE, which differs from MTE only in that it is applied to time series data as opposed to frame-straddled data). MTE makes use of the reconstructions of successive fields to remove or reduce the intensity of false or "ghost" particles and increase the brightness of real particles, since ghost particles should not convect like the surrounding flow. Thus, MTE can therefore noticeably improve a particle reconstruction and subsequent vector calculation.

After tomographically reconstructing particles in the measurement domain, 3-D motion calculation follows. The domain is divided into box shaped interrogation volumes. A windowing operation via a Gaussian kernel is then applied followed by cross correlation (usually performed by FFT) of the volume with corresponding volumes in successive images. Amid several cross-correlation iterations, a volumetric deformation algorithm handles the 3-D deformation of the interrogation volumes. In the correlation domain, the correlation peak is found and scaling the displacement of the peak by optical magnification and the time difference between successive images gives the local velocity. The resulting velocity field may then be used for MTE (or SMTE). From the velocity field, spatial gradients can then be found.

As Tomo-PIV is a more recently developed technique, there is not a generally accepted approach for estimating uncertainty a posteriori from recorded images like there is for Stereo-PIV. Several researchers have used the divergence of the resulting flow field as a tool to estimate the random error in their measurements as for incompressible flows, as the divergence should be

zero within the single flow domain. (Lynch & Scarano, 2014) follow (Atkinson et al., 2011) and use

$$v_{u_i} = \sigma_{Dev}\left(\frac{\partial u_i'}{\partial x_i}\right)\frac{1}{\sqrt{\frac{3}{2\Delta x^2}}}$$

where σ_{Dev} indicates standard deviation of the divergence and Δx is the grid spacing of vectors. Using this approach, uncertainty can be estimated where Tomo-PIV is applied. Tomo-PIV is used is the chapter examining the wake of a wedge, and this uncertainty estimate varies from between 1-5% of freestream velocity for time series data and 2-8% with frame straddled data, with noticeable spatial variation. Higher uncertainty is in the immediate near wake region of the flow while lower uncertainty is in regions where the flow is nearly parallel. These uncertainty estimates are in line with the prior studies. Bias errors due to mistiming of the illumination is assumed to be negligible. Misalignment of the planes is negligible due to the self-calibration procedure used throughout this thesis.

Shake the Box Particle Tracking Velocimetry

The Tomo-PIV algorithm above uses correlations between particle containing interrogation volumes to find velocity. In contrast, PTV tracks particles on an individual basis and calculates velocity for the (presumably) Lagrangian tracer particles. Historically, volumetric PTV was limited to low seeding densities. Accurate estimation of particle location between the multiple cameras requires sub-pixel accuracy (and thus VSC), which becomes especially difficult if the particles overlap much due to higher seeding densities. Reconstruction of particle locations in 3-D can be done with epipolar geometry or tomographic reconstruction of the

particles, but in either case, the seeding density is limited, which correspondingly limits the spatial resolution of the measurement.

A major advance in PTV was the development of "shake the box" (STB). STB takes one of the developments enabling Tomo-PIV, VSC, and uses it to achieve the sub-pixel accuracy that previously evaded tomographic PTV and other prior PTV methods. Also critical to STB was the development of Iterative Particle Reconstruction (IPR), which allows particle position reconstruction at higher seeding by subtracting out particles and then iterating on the residuals left behind after the subtraction. The particles subtracted out are estimated with a calibrated optical transfer function (OTF), which is a (typically Gaussian) model for the size and brightness a particle should have in a particular camera in a particular location. Given this OTF, it is important that the particles are uniform, whereas a tomographic reconstruction is less sensitive to uniformity. As we can effectively filter the water in the cavitation channel and seed with particles of our choice, this particle uniformity is not a significant constraint for the studies presented here. IPR also has superior sub-pixel accuracy as it does not need 3-D peak detection like tomography and "shakes" the particles in 3-D space to accurately locate them. Additionally, IPR is much faster and requires less memory than tomography.

Another key to STB is heavy use of prior timesteps (or timestep in the case of Two Pulse STB or TP-STB). STB uses this information in the IPR step by predicting a particle cloud for future time steps (for time resolved STB) or by iterating between reconstruction and tracking (TP-STB). This essentially reverses the order for PTV in that tracks are predicted before reconstruction begins. The accuracy of the tracks and the power of IPR is such that these predictions can then be used as the initialization for IPR and the errors of the predicted locations of particles can be easily corrected during the image matching and IPR process. In contrast,

traditional PTV would reconstruct particles then attempt to match pairs between successive images. Prior PTV methods did use predicted particle locations, but mainly as a tool to limit the search radius for particle pairing. Given the OTF and iteration with residual images, STB suppresses ghost particles effectively, allowing substantially higher seeding densities with faster processing times than prior PTV algorithms.

As STB and accompanying methods of calculating Eulerian fields from it are more recent than Tomo-PIV, there is also no generally accepted way of estimating the uncertainty of the measurements a posteriori. While estimation based on the standard deviation of divergence could be used here as in Tomo-PIV, the VIC# algorithm uses a divergence free assumption as an optimization constraint, so using that approach here as well is suspect. A detailed examination of errors in a benchmark comparison ((Sciacchitano, 2019)) of STB and data assimilation algorithms showed that the mean bias error for velocity was within 1% while random error was around 5-10% depending on seeding density for the VIC# algorithm. Using VIC# to estimate pressure found mean bias errors between 7 and 13% with smaller random errors of 3-7%, again depending on seeding density. (Jeon et al., 2022) found similar results for velocity, but higher bias errors, around 15%, for pressure. At the seeding densities used herein, we then expect bias errors of less than 1% and random errors of approximately 5% in velocity and bias errors of 15% and random errors of 3-4% in pressure. As with the Tomo-PIV, bias errors due to mistiming of the illumination is assumed to be negligible. Similarly, misalignment of the planes is negligible due to the self-calibration procedure used throughout this thesis.

Comparison of Methods

A brief comparison of the different velocimetry methods above is given in Table 3.2 and described here. Because of the correlation windows or subregions used in PIV methods, sharp

spatial gradients are generally poorly captured as the averaging in a window or subregion operates as a low pass filter. In contrast, STB, as it tracks particles on an individual level, does not cause spatial filtering. Individual particle data is generally then converted to an Eulerian field, but even a simple spatially weighted technique such as binning weights nearer particles more heavily, tending to lead to less spatial filtering. With VIC#, the capture of spatial gradients is further improved. Further, STB, even with VIC# computes much faster than Tomo-PIV in the cases considered here. These lead to the choice of VIC# for the measurements of the counter rotating vortices in the latter portion of this work.

Freestream Turbulence Measurements in mLCC

The prior chapter noted that the freestream turbulence in the mLCC was measured to be approximately 0.25% the freestream velocity. For these freestream turbulence measurements, frame straddled Stereo-PIV data (or double frame data, i.e. independent measurements with two successive frames were used with the interframe time arbitrarily set) were taken at a range of speeds, from 1 to 10 m/s and this turbulence level was consistent across this range. Critically, that data was taken with particle displacements of around 80 to 100 pixels. It is necessary to use such large displacements to measure the fluctuations because using smaller displacements (8-12 pixels would be typical values in Stereo-PIV) will lead to a high relative uncertainty in the measurements, which artificially inflates the fluctuations measured. Indeed, at a fixed speed, by altering the interframe time to vary the particle displacement by an order of magnitude, the calculated turbulence intensity was found to be inversely related to the particle displacement, down to a turbulence intensity of 0.25% at the greatest displacements. This inverse relation demonstrates the importance of picking the appropriate choice of acquisition parameters with PIV. Estimation of uncertainty in Stereo-PIV measurements with correlation statistics is now

generally accepted (Neal *et al*. 2015), and with the large displacements used, the estimated uncertainty was negligible compared to the velocity fluctuations, suggesting that the measured turbulence level reflects the physical fluctuations of the flow and not inflation of the turbulence level due to uncertainty. A separate measurement technique for finding the freestream turbulence (e.g. hot wire anemometry) was not available, but laser doppler anemometry (LDA) measurements were taken in the a geometrically similar water channel, the William B. Morgan Large Cavitation Channel ((Park et al., n.d.)), which had comparable levels of turbulence at around 0.2% to 0.5% depending on freestream velocity. Therefore, our measured level of freestream turbulence in the mLCC tunnel is similar and is consistent with the level of turbulence expected for a tunnel with modest contraction ratios (Barlow *et al*. (1999)).

	Stereo-PIV (SPIV)	Tomographic-PIV (TPIV)	Shake the Box (STB)
Velocity Field	2 dimensions 3 velocity components	3 dimensions, 3 velocity components	3 dimensions, 3 velocity and acceleration components
Reconstruction Method	N/A	Algebraic Reconstruction Technique (ART)	Iterative Particle Reconstructive (IPR)
Velocity Calculation	Correlation of particle groups in interrogation windows	Correlation of particle groups in interrogation regions	Derivatives of individual particle trajectories
Post-Processing	Vector validation and anisotropic denoising	Motion tracking enhancement	Vortex-in-Cell# (data assimilation for Eulerian fields)

Table 3.1 Comparison of Velocimetry Methods. The different particle based velocimetry algorithms used are compared here. While Tomo-PIV and STB can be performed on the same recorded images of an illuminated volume, the algorithms differ at every step. Tomo-PIV and STB can be done on recorded images appropriate for Stereo-PIV (i.e. a thin light sheet), but the reverse is not true. Tomo-PIV and Stereo-PIV both rely on similar velocity calculation approaches but are otherwise distinct.

	Stereo-PIV (SPIV)	Tomographic-PIV (TPIV)	Shake the Box (STB)
Costs	Inexpensive with respect to hardware and processing	Expensive with respect to hardware and processing	Expensive with respect to hardware
Seeding Density (ppp)	ppp ~ 0.2 across a plane	ppp ~ 0.2 across a volume	ppp ~ 0.1 across a volume (high compared to other PTV)
3-D Motion Analysis	Performs poorly with out-of-plane velocity component	Performs well with all three velocity components	Performs well with all three velocity components
Uncertainty Quantified	Correlation statistics	No agreed upon method	No agreed upon method
Spatial Gradients	Correlations filter spatial velocity gradients	Correlations filter spatial velocity gradients	STB produces sharper spatial velocity and acceleration gradients

Table 3.2 Benefits and Drawbacks of Velocimetry Methods. The different particle based velocimetry algorithms used have various benefits and drawbacks as note here.

CHAPTER IV

Study of Artificially Constrained Velocimetry as a Proxy for Coaxial Velocimetry

Overview

Due to experimental constraints, a region of flow may only be measurable with a coaxial arrangement of cameras and illumination. This leads to poorly defined *Z* extents in the volumetric domain. To study the effect of this coaxial illumination on volumetric reconstruction and velocimetry, we study an ideal volumetric velocimetry setup and artificially constrain it to approximate the effects of coaxial illumination. The wake of a wedge is examined here as an exemplary case.

Test Model and Configuration

A Photonics Dual Head DM-100 high speed laser with a maximum power of 10 mJ/pulse at 10 kHz for each head was used in combination with four Phantom v1212 cameras which can take 1280 x 800 pixel images at 12,600 frames per second. As is common, all four cameras were used for volumetric velocimetry measurements. For Stereo-PIV measurements, all four cameras were used to enable the option of four camera Stereo-PIV. The seeding was LaVision's Polyamide HQ with 20 micron typical diameter and a density of 1.03 g/cc to come close to the density of the working fluid, which is water for all these cases.

All measurements were taken in the test section of the Miniature Large Cavitation Channel (mLCC) at the University of Michigan Marine Hydrodynamics Lab. In all cases, water filled boxes sealed against the sides of the water channel helped correct for the change of index

of refraction as the cameras viewed from outside the acrylic windows as shown in Figure 4.1. The wake of a wedge is measured both in the immediate near wake recirculation zone and approximately 10 base heights downstream. The symmetric wedge has an opening angle (total) of 15 degrees and a base height, h, of 18 mm. This wedge has an identical 2-D shape to that of Wu (2021) and similarly the freestream velocity, U_0, was 6 m/s. The water temperature was not controlled but was measured to be between 21 and 24 Celsius. Accordingly, the Reynolds number based on wedge base height is approximately 110,000. The experiments differ here in that this wedge was not allowed to cavitate as that would preclude the use of optical techniques such as Tomo-PIV. Additionally, the blockage ratio is much lower here and the spanwise extent of the wedge is 22.5 cm as the facility used was the mLCC as opposed to the X-Ray equipped cavitation channel used by Wu (2021). A schematic of the test section and a side view are shown in Figure 4.1. In the near wake region, three cameras were placed on one side of the tunnel and a fourth on the other side of the tunnel, as shown in Figure 4.1. An "arc" array of cameras is common for volumetric PIV experiments, but not feasible in this situation as the wedge would block the view of a camera placed on the upstream side of the wedge and looking at the wedge's wake. Space constraints due to the size of the cameras led to the placement of the fourth camera on the other side of the tunnel. This arrangement, governed by available space near the test section is not ideal and unavoidably the four cameras had somewhat different focal distances. Both the upstream and downstream measurements had the cameras in roughly equivalent positions relative to their respective measurement volumes. For both the upstream and downstream measurements, the illuminated volume measured was approximately 35 x 35 x 8.5 mm, though part of the upstream field of view was blocked by the presence of the wedge. An

example image of an instantaneous velocity and vorticity field from the near wake region of the wedge is shown in Figure 4.2.

Before data was acquired, the cameras were calibrated with a two-plane plate with a regular grid of dots. After image acquisition, Planar Self Calibration (PSC) (Wieneke 2006) was used to center the illuminated volume on $z = 0$. This PSC was used for the Stereo PIV calculations. For Tomo PIV and STB calculations, the PSC was followed by Volumetric Self Calibration (VSC) ((Wieneke, 2008)). The VSC ensured an average disparity of less than 0.1, generally around 0.03, and a maximum disparity of less than 0.2, generally less than 0.1. With the optical setup used, the particles were in the diffraction limited regime, and the particle diameter was around 4-5 pixels which is unfortunately higher than ideal. A typical metric to assess the seeding density is the particle image density, N_I, which is the number of particles in the camera view, divided by the area of the camera sensor, giving units of particles per pixel, often abbreviated ppp (Schroder and Schanz 2023). As the intention was to use Tomo-PIV and STB processing on the same data, the seeding density was constrained somewhat by the limits of STB to about 0.025-0.04 ppp for the upstream cases and 0.04-0.07 ppp for the downstream cases, with some variation between the cameras. Increasing above this, the STB tracking performance worsened. This is admittedly lower than what other researchers have used for STB, but in this case the larger particle diameter increases particle overlap making the particles harder to track. To quantify this density, we note the source density, N_S, to be

$$N_s = N_I \cdot \frac{\pi}{4}\left(d_{particle}\right)^2$$

(Scarano 2013) where N_I is particle image density (Schroder and Schanz 2023) and $d_{particle}$ is the typical particle diameter measured in pixels. Generally, researchers report N_I, but this metric

only offers part of the information needed to quantify how difficult the tomographic reconstruction problem is. If particles are larger, they are more likely to overlap, and N_S captures this. Given the typical diameter of particles in the images (about 4 pixels in the upstream and about 3 pixels in the downstream), N_S is about 0.4-0.6, which for a four camera setup is close to the limit of what can be successfully reconstructed (Raffel *et al*. 2018). Thus, even though N_I is somewhat low, these measurements are still at relatively high seeding density, where reconstruction becomes more difficult.

To compare between volumetric and planar measurements, the illumination volume was set up and the cameras calibrated for volumetric measurement. After acquiring the volumetric data, the volume was thinned by adjusting the physical aperture to a thickness appropriate for Stereo-PIV (about 1.5 mm) in a plane parallel to the freestream direction. Additional seeding was added to achieve a comparable seeding density to the volumetric case then planar data was acquired. This procedure was used for both the upstream and downstream measurements. In between the upstream and downstream measurement acquisition days, the water was filtered to remove seeding particles and allow starting with the volumetric measurements.

The image data was then processed with DaVis 10.2. Prior to any velocimetry calculations, the images were preprocessed by subtracting a local minimum, applying a Gaussian smoothing kernel of 1x1 pixel, and generally applying a constant field subtraction to ensure the background of the images is precisely zero in pixels with no particles for noise elimination. The Tomo-PIV processing is done both with and without Motion Tracking Enhancement (MTE) for the artificially constrained reconstruction and compared to the full reconstruction (with MTE). This comparison between full and partial reconstruction is done for both time series and frame-straddled data. As the immediately prior velocity field is known in time series Tomo-PIV, MTE

can be calculated with minimal cost by Sequential Motion Tracking Enhancement (SMTE, Lynch and Scarano, 2015). Therefore, for all time-series Tomo-PIV measurements, MTE (specifically, SMTE) is used by default. Partial and full depth processing of the data is then done with STB followed by VIC and binning, again for time series and frame-straddled data. To compare the partial and full reconstructions with each other and with the planar measurement (Stereo-PIV), after all data processing was completed (i.e. after computing mean flow quantities), the data was interpolated onto a regular grid at $Z = 0$ (the center of the volume). The Stereo-PIV is calculated on the $Z = 0$ plane by default, yet this still was interpolated onto the same x-y grid as the Tomo-PIV and STB results. This interpolation was necessary as the various calculations were done on a grid size ideal for each calculation. Stereo-PIV specifically had to be calculated on a coarser grid than was ideal for the Tomo-PIV and Eulerian calculations from STB as the grid size for Stereo-PIV should be wider than the light sheet is thick (Raffel *et al*. 2018). Tomo-PIV and VIC# were done on the University of Michigan's computing cluster, Great Lakes, with the distributed module of DaVis. Stereo-PIV and STB were processed on a desktop. For the frame-straddled data, 10,000 independent, double-frame sets were processed. For the time series data, 30,000 images were processed, across approximately 140 flow cycles.

In many comparative studies of volumetric velocimetry methods, the results are compared on an instantaneous basis. Less attention has focused on the ensembles of the fluctuations of these instantaneous observations, such as those compiled in Reynolds stresses. Here, the primary emphasis will be on the statistics of such data as, in many cases, a CFD simulation will be compared to experiments on this basis since a CFD simulation cannot exactly model a given instant measured experimentally.

Comparison of Volumetric Reconstruction of Particles

Before any volumetric velocimetry calculations can start, the particles must be reconstructed. With Tomo-PIV, this is initiated with Multiplicative Line-of-Sight (MLOS), followed by several iterations of Multiplicative Algebraic Reconstruction Technique (MART). These algorithms take the intensity information from the sensor planes of the four cameras and reconstruct that intensity in the volume. After this, correlation for Tomo-PIV starts. Separately, for STB, IPR reconstructs the particle locations within the volume. This method functions rather differently than the tomographic reconstruction, using epipolar geometry to triangulate the particle positions within the volume by matching particle candidates across cameras. IPR does this iteratively and corrects the particle location after each iteration. IPR also uses an Optical Transfer Function (OTF), which allows it to find and fit particles that don't appear as circular Gaussian blobs. The appearance of particles as oblong shapes as opposed to circles (their physical shape) happens often in deep volumes with changes of index of refraction in the line-of-sight, by identifying an appropriate size and shape for each region in the volume. If particles do not fit the OTF particle shape for their location, or if they are insufficiently bright, then the particle is deleted. Due to the triangulation approach, IPR should suffer less from using poorly defined and unevenly illuminated volumes. Indeed, the author has noted that STB (using IPR) will often track particles in regions that do not appear illuminated in the tomographic particle reconstructions. Therefore, we only examine the effects of partial and full reconstruction on the tomographic reconstructions, not the STB particle reconstructions.

First, we compare the averaged intensity profiles of the particle reconstructions from each laser head (for frame-straddled measurements) as well as from both heads fired together (for time series measurements). These comparisons are done with the downstream data, as the presence of

the wedge leaves a portion of the flow without particles to reconstruct. The situation in the upstream is approximately the same, so we do not present equivalent figures from the upstream to avoid redundancy. Figure 4.3 comes from the frame-straddled measurements and shows the difference between the two laser heads, which fire in sequence during frame-straddled measurements. While the illuminated extents are almost the same, the brightest regions of each laser head are slightly misaligned, despite the repeated efforts of the author to align them perfectly. This unfortunately could not be corrected via normalization of the frames to one another, and it causes some lower correlations than would otherwise occur between frames. This also shows that the ratio between outside the illuminated volume and within the illuminated volume is approximately 3.5 to 5. This metric relates the signal of the particles in the volume to the noise level of the ghost particles and thus stands in as a signal to noise ratio. A ratio of 1.5 is generally considered the minimum necessary for Tomo-PIV. Figure 4.4 shows the averaged intensity profile of the time series measurements, when both the laser heads fire together. As expected, the resulting images are brighter, and the reconstructed intensities have higher brightness as well. This also results in a more even illumination across the volume and the ratio between illuminated volume and outside the volume is about 5 to 6. The more even illumination across the volume and higher SNR leads to better correlations for the time series measurements than the frame-straddled measurements.

Figure 4.5 shows the reconstructed intensities of the first frame of an arbitrarily chosen instant. The tomographic reconstructions with and without MTE and the difference between them is shown below for comparison. The reconstructions with and without MTE do not differ appreciably and this is likely due to the quality of the measurements and reasonable seeding density, making MTE less necessary.

Figure 4.6 shows the same first frame of the same arbitrary instant, but here, the difference between the full and partial reconstruction is shown. The partial reconstruction is substantially brighter than the full reconstruction in the region that the partial reconstruction was calculated. The difference then, from subtracting the partially reconstructed region from the fully reconstructed region, is not clear when viewed on the same scale as the prior panels. Thus, the fourth panel shows this difference rescaled to show the negative values resulting from the larger magnitude in the partial reconstruction. The brightness difference between the constrained and full reconstruction cannot be related to a simple scalar across the field. Instead, it varies spatially.

Figure 4.7 shows a small region from the center of the reconstructed area with and without MTE for both the partial and fully reconstructed cases. Again, the bright particle regions appear brighter in the partial reconstruction and thus end up negative in the difference. The differences between using MTE and not using MTE are relatively minor in comparison. In conclusion, from comparing the tomographic reconstructions, we see that the particles appear brighter in the partial reconstruction than in the full reconstruction, but their locations are not substantively different. Additionally, the partial reconstruction has “clouds” of reconstructed intensity that do not correspond to any particles in the full reconstruction volume. Lesser differences appear when comparing the use or non-use of MTE.

The same patterns are found when examining the tomographic reconstructions for the time series data. (S)MTE is used by default for time series Tomo-PIV, so the comparison is only made between complete and partial reconstructions of the particles. However, the comparison is still worth noting as the illumination across the volume is quite even, unlike in the frame straddled data where there is some misalignment of the laser heads. As can be seen in Figure

4.8, even with even illumination of the volume between varying images, the partial reconstruction of the flow leads to brighter particles in the reconstructed region compared to that same region in the full reconstruction region, just as in the case of frame straddled data.

Overall, some clear differences appear in between the various computational cases when examining the tomographic reconstructions of the particles. In both time series and frame-straddled data, artificially constraining the reconstruction leads to notable differences in the intensity of the reconstructed particles. As in the typical explanation of the tomographic reconstruction, the algorithm does what it can to place the recorded intensities into the specified volume, even if they do not physically exist there. This leads to increased brightness of particles physically within the volume as well as some likely false particles and clouding around those particles. The occurrence of increased brightness for both time series and frame-straddled data shows that it cannot be attributed to the slight misalignment of the two laser heads. We shall now examine how those differences translate into velocity fields after the correlation phase of the calculation.

Comparison of Instantaneous Fields

As is typical for PIV methods comparisons, the various methods are compared first on an instantaneous basis. In Figure 4.9, Tomo-PIV is compared with and without MTE and in Figure 4.10, Tomo-PIV is compared with full and partial reconstructions (both with MTE on). The results shown are from the immediate near wake region with frame-straddled data. The Tomo-PIV computations do not differ noticeably to the eye when comparing the use of MTE or not. Differences are clearer when comparing the full and partial reconstruction. As an additional comparison, time series data is shown in Figure 4.11. Here, the difference between the full and partial reconstruction data is minimal. This stands in contrast to the frame-straddled data, which

shows substantive differences. The frame-straddled data likely suffers more from the slight misalignment of the two lasers heads that fire for each frame, as seen in Figures 4.4 and 4.5. This misalignment causes the correlation to be worse for the partially reconstructed Tomo-PIV data than for the full reconstruction data, leading to a worse velocity field. The time series data does not suffer from such misalignment, so it is less affected when considering full and partial reconstruction. In contrast to the frame-straddled Tomo-PIV data, the STB-VIC# fields do not differ visually when comparing the full and partial thickness, as shown in Figure 4.12. This is as expected since the IPR method at the core of STB matches particles between camera views using epipolar geometry and can reconstruct particles regardless of whether the entire region is reconstructed or not. Comparing the Tomo-PIV to the STB-VIC# fields in Figure 4.13, the different processing methods appear somewhat different. Likely some patches of velocity in the Tomo-PIV data are unphysical (i.e. a high velocity region surrounded by low velocity areas) which leads to the difference.

As another instantaneous comparison of the different methods, the Z-direction (or spanwise oriented) vorticity fields are shown. Since vorticity is computed from gradients of the velocity field, its calculation tends to amplify the noise present in the original data, so minor differences should be magnified. As above, the differences between the Tomo-PIV fields with and without MTE are minimal, as shown in Figure 4.14. In comparing the full and partial reconstruction data in Figure 4.15, the differences are much more notable with the frame-straddled data. However, in Figure 4.16, the difference between full and partial thickness reconstruction is again substantially less for time series data. In the case of STB-VIC#, the difference between the full and partial reconstructions is again relatively minimal, as shown in Figure 4.17. Finally, Figure 4.18 shows that there are some differences in comparing the STB-

VIC# with the Tomo-PIV. This is especially clear in the shear layer at the bottom of the wedge around Y = -0.5. The magnitude of vorticity is higher in the STB-VIC# calculation likely due to Tomo-PIV functioning as a low pass filter. This filtering effect from Tomo-PIV leads to poorer resolution of sharp gradients and should reduce the magnitude of the vorticity there as observed. Other patches where there are differences generally occur nearer to the boundaries of the measurements, where there is likely poorer camera overlap, and not all cameras may see a particular set of particles, so the quality of the measurements is lesser in those regions.

The above comparisons were done by noting similarities and differences between velocity and vorticity fields chosen at arbitrary instants. We now compare the full and partial field reconstructions of Tomo-PIV over time at an arbitrary location (chosen to be near the shear layer at the bottom of the wedge) in the measurement volume as shown in Figure 4.19 and Figure 4.20. The frame-straddled measurements show good agreement at this point. Similarly, the time series measurements also show good agreement. Comparing Figure 4.9, where the spatial field is shown at an instance, and Figure 4.14, where a particular time instance is shown over a whole plane, the agreement is better in the comparison over time. This implies that the differences between full and partial reconstruction occur randomly in space and time, so an arbitrary location may not show substantive difference for all time instances, just some sporadic instances.

Comparison of Statistical Quantities

As the above fields do have some small differences, the cumulative effects of those differences are now examined by comparing the time-averaged quantities. For this section, both the time series and frame-straddled data are compared. To adequately estimate the averaged quantities, independent observations should be used and compiled into averaged and averages of fluctuations.

Each frame-straddled observation is independent from that preceding and succeeding it as the measurements were taken to allow that. In contrast, the time series data must allow STB to follow the motion of individual particles through time or Tomo-PIV to have correlations between successive images. In high acceleration regions such as small vortices, this requires high temporal resolution. While the minimum displacement of a particle in PTV should be at least 1.5 times its diameter, the ability of STB to track particles limits the maximum displacement to less than 10 voxels in this measurement campaign. The time series data is taken at 20 kHz based on this. This is almost 200 times the frequency of the dominant structures in the wedge wake, so unsurprisingly, the time series data are not independent. Therefore, while there are 30,000 samples in the time series comparisons and only 10,000 samples in the frame-straddled comparisons, the number of effective samples in the time series data is less than that of the frame-straddled data. While this number of effective samples can be estimated by examining the correlation of successive observations, this correlation varies spatially throughout the measurement volume. In the worst-case location, the effective number of samples drops down to around 500 samples (out of the 30,000 taken). It was not feasible to take and process an order of magnitude more time series data to accordingly get a similar number of independent samples between time series and frame-straddled data, so we will use the results from the 30,000 fields while keeping in mind that they represent less than 1,000 independent observations.

For these data, the bias errors of the measurements themselves (e.g. due to mis-timing of the acquisition or misalignment of the illumination planes to the cameras) are assumed to be small. The relative random uncertainty for flow quantities can be estimated based on statistics of those flow quantities. For the mean flow,

$$v_{\overline{u_i}} = \sigma_{Dev}(u_i)/\sqrt{n_{effective}}$$

where $v_{\overline{u_i}}$ is the uncertainty of the i-th mean flow component, $\sigma_{Dev}(u_i)$ is the standard deviation of the velocity component and $n_{effective}$ is the effective number of independent snapshots. For the Reynolds shear stress, the estimate is

$$v_{\overline{u_i'u_j'}} = \frac{\sqrt{1 + R_{ij}^2}\sigma_{Dev(u_i)}\sigma_{Dev(u_j)}}{\sqrt{n_{effective} - 1}}$$

where $v_{\overline{u_i'u_j'}}$ is the relative uncertainty of the Reynolds shear stress, and R_{ij} is the correlation coefficient between u_i and u_j. Both the above estimates of uncertainty overestimate the actual uncertainty because they accrue from both the physical variation of the flow as well as the random error of the measurements. Nevertheless, in the following measurements, the number of effectively independent samples is sufficiently high to reduce these quantities to manageable levels. For frame straddled data, the relative uncertainties are generally a fraction of a percent of their respective quantities of interest. For time series data, they are approximately 2-3% of the measured quantities of interest.

First, the average quantities of the upstream are presented. To compare the various volumetric methods with each other and the planar Stereo-PIV measurement, the velocity field at Z = 0 is interpolated. At this spanwise location, multiple vertical cuts are examined at several streamwise locations. The multiple streamwise locations are examined due to the rapid change in the flow features in the streamwise direction. The locations of these streamwise cuts relative to the wedge are shown in Figure 4.21. The mean velocity fields are then shown in Figure 4.22 and exhibit good agreement between the various methods. This holds whether in the high speed, nearly unidirectional flow below the wedge, the recirculating stagnation region behind the wedge, or in the transitional region between them. The mean Reynolds stress fields are then

shown in Figure 4.23, Figure 4.24, and Figure 4.25 at one of the streamwise locations. Other streamwise locations show similar trends but are not shown for brevity. First, Figure 4.23 shows the time series data which shows good agreement between the full and partial width Tomo-PIV data. This agrees slightly worse with the Stereo-PIV data and the STB-VIC# and STB-binning data. Notably, the planar, Stereo-PIV measurement likely to overestimate the out-of-plane component in the recirculation region. This likely results from the higher uncertainty of the measurements in this region, as can be seen in the correlations. The notable jump in the STB-binning data (and less noticeable in the other calculations) is at the transition between the low-speed recirculation region and high-speed free stream region. As binning at the used resolution is based on a relatively small number of particles, weighted by distance from the centroid of the bin, this is perhaps unsurprising as sometimes particles enter the binned volume while at other times low speed particles enter the binned volume. As it alternates between these two, the mean squared fluctuation rises dramatically. Due to the sharp weighting, biasing towards particles nearest the centroid, binning does not use as many particles as a comparably sized Tomo-PIV interrogation volume. In the sense that the measurements taken here are all particle based, binning then does not have as many samples as Tomo-PIV. Binning accordingly does not have quite the low-pass effect of a correlation-based method, though it is commendably faster. The effects of the shear layer are observed in the correlations of the PIV methods. A notable “kink” occurs in the correlation plots at this location. While PIV methods effectively average over a set of particles and low-pass filter the data, with the sharp difference in speed across the shear layer, the correlations suffer accordingly.

Figure 4.24 shows the same quantities of interest at the same location, but with frame straddled data as opposed to time series data. Similar trends are noted with the time series data

in Figure 4.23, though the out-of-plane component of Stereo-PIV results is much different than with the time series data. Figure 4.25 only shows the Tomo-PIV results to demonstrate the difference between full and artificially constrained reconstructions of the volume. The artificially constrained reconstructions show higher Reynolds stresses than the full reconstruction. This demonstrates that the constrained reconstruction, which translates into low level noise in the instantaneous fields, inflates the Reynolds stress when taken as an ensemble. Figure 4.26 compares the time series and frame-straddled data. There are some differences between the frame-straddled and times series data, which likely result from two causes. First, the time series data does not have nearly as many independent samples as the frame-straddled data, so those results are not truly converged to the same extent as the frame-straddled data. Second, the misalignment of the laser beams does lead to lower correlations in the frame-straddled data than in the time series data, potentially worsening the frame-straddled results.

Considering the freestream turbulence, we would expect that the freestream turbulence value should approach zero as we move down in the y direction, away from the wedge. However, this generally does not occur with these measurements. Since the computation of Reynolds stress components from experimental data captures both the fluctuation of the flow and the effects of the uncertainty of the measurement (Wilson and Smith, 2013), this quantity can depend more strongly on the uncertainty of the measurement than the actual physical fluctuation. To mitigate this, when attempting to measure freestream turbulence with a PIV system, it is necessary to allow a much longer than normal displacement (i.e. around 80-100 pixels as opposed to a more typical 8-10 pixels) to reduce the relative uncertainty of the measurement (Neal *et al*. 2015). This is not feasible with the present measurements as that would prevent tracking and correlation of the bulk of the flow. As such, a high relative uncertainty artificially

inflates the computed Reynolds stresses in regions where the physical velocity fluctuations should be much lower than documented here. For brevity, only the results at a single streamwise location in the upstream region are shown here.

Discussion

As part of the tomographic reconstruction of particles, some false particles, termed "ghost particles", will be reconstructed within the volume. This results from lines of sight, occluded behind real particles, intersecting from multiple cameras, which can appear as a particle in the reconstruction. Adding more cameras helps reduce the level of ghosting as does lower seeding densities or smaller particles. These changes to the experimental configuration itself can either drive up cost (adding cameras) or result in less dense data. Hence, MTE was implemented to help remove ghost particles from the reconstruction to prevent them from affecting the correlation calculations for velocity. The original expectation was that Tomo-PIV would perform poorly without MTE, and likely even with MTE, for the partially reconstructed data as over half the particles would not physically exist within the reconstructed volume. This artificially constrained reconstruction leads to higher ghost levels as particle intensities cannot be reconstructed where they physically exist, an effect that is seen in the reconstruction comparisons in Figures 7, 8, and 9. However, the reconstruction of these false particles did not lead to substantively different statistics of fluctuating quantities. They also did not lead to noticeably different instantaneous fields in the case of time series data. The differences between full and artificially constrained frames-straddled Tomo-PIV appear to result from the slight mismatch of the laser beam heads.

Noticeably, the above effects are true independent of MTE. That MTE did not have a significant effect could result from the use of high signal-to-noise ratio images. Another

possibility is that the seeding density was not high enough for MTE to be needed to remove ghost particles. As noted above, the present measurement should be around the threshold where a tomographic reconstruction with four cameras should fail ($N_S \sim 0.5$, Raffel *et al*. 2018), but the situation is somewhat different when only reconstructing a partial volume. Conversely, STB was expected to perform adequately when only calculated in a partially reconstructed volume since IPR uses epipolar geometry to place particles in the volume. However, in practice, the Tomo-PIV results were indistinguishable from each other in the mean, regardless of whether a partial or full reconstruction was used or whether MTE was used or not. The instantaneous results also appeared identical for the time series data in comparing full and partial reconstruction. This is likely due to the operation of the MART technique in reconstructing the particle intensities. Scarano (2013) notes that it functions akin to an AND operator and will not add intensity to a given voxel unless all lines of sight intersecting that point also have intensity there. In practice, this technique is not perfect, and a close examination of a region with partial and full reconstruction shows that the partially reconstructed volume will have intensities that do not exist in the fully reconstructed volume. Additionally, the intensities that occupy the same location in both partial and full reconstructions (and therefore are likely true particles) are substantially brighter in the partial reconstruction. The average integrated particle intensity across the partial volume is thus brighter than for the full volume. However, regardless of the details of the tomographic reconstruction, the subsequent vector calculation does not show significant differences between full and artificially constrained cases. The resulting instantaneous and averaged fields indicate that the partial and full reconstruction depths perform equivalently when in time series mode or when considering mean flow properties (for both frame straddled and time series mode).

These results suggest that Tomo-PIV may be feasible in coaxially illuminated measurements. Even with the relatively high source density for four cameras ($N_S \sim 0.5$) and the artificial constraint of only the partial depth reconstruction, the tomographic reconstruction is robust enough to produce data comparable to the full reconstruction. However, it is worth noting that the high source density is true for the entire thickness of the volume. If we only consider the partial volume that we reconstructed, the particle density through this portion of the volume only accounts for less than half of the total particle density. Therefore, the effective particle concentration is lower than stated above ($N_I \sim 0.025$ to 0.040). It should be emphasized that thickening a volume will lead to a higher N_I on the camera sensor. Thus, thickening a volume, or as suggested by the results here, using a coaxially illuminated measurement and massively increasing the illuminated depth, will illuminate more particles and thus require a lower seeding density in terms of particles per physical volume to maintain the same proportion of particles per pixel. Alternatively, if an experiment can use a rake of seeding as opposed to global seeding, the particles can largely transit through the desired measurement volume and not other paths through the illumination, so this concern lessens. These considerations on seeding should be kept in mind while considering the above results.

The performance of STB with binning suggests that care must be taken when considering shear layers and unsurprisingly, VIC# performs better at producing Eulerian measurements from particle track data. Also notably underperforming, Stereo-PIV significantly overpredicts the magnitude of out-of-plane velocity fluctuations. This can be attributed to several causes. First, the slight misalignment of the two laser sheets brightest regions in frame-straddled mode worsens the correlations relative to the time series mode. Second, the loss of particles due to out-of-plane motion worsens the correlations between successive images, which also hinders the

ability of Stereo-PIV to accurately find the out-of-plane velocity as it increases noise in the measurement. Volumetric methods such as Tomo-PIV and STB largely mitigate this issue because particles can displace in the z -direction (out-of-plane) and still correlate or track with the prior frame. Third, the use of only two cameras worsens the correlations relative to a four camera system used in volumetric measurements.

Conclusions

This study examined several questions regarding volumetric and planar velocimetry. In some cases, optical access for cameras and illumination may constrain the experimentalist so that only a coaxial arrangement of cameras and illumination is possible. Illuminating in the same direction as the cameras' lines of sight makes it infeasible to have sharply cut off extents of the measurement volume. In the case of Tomo-PIV, the tomographic reconstruction is understood to perform poorly when the volume has poorly defined extents. This is less of a concern for STB, where IPR will perform well without sharply defined extents. However, Tomo-PIV may be preferred over STB if, for instance, the seeding particles are non-uniform or frame straddled data for statistical quantities is required, so it is worthwhile to examine Tomo-PIV in all cases and not immediately choose STB in all cases. Using an artificially constrained reconstruction, this study probes the effects of ill-defined extents on Tomo-PIV. To our surprise, Tomo-PIV performed well when artificially constrained to partially reconstruct an illuminated volume. MTE did not appear to be the cause of this success. While limited compared to a true coaxial illumination set up, this result suggests coaxially illuminated measurements, where Tomo-PIV is generally considered inadvisable, may still provide useful Tomo-PIV. In some cases, it performs adequately even without a sharply defined extent of the domain. The limits on this then likely

result from sharpness of particle definition and the dramatically increased N_I that would result from maintaining a high seeding density across a much greater depth of illumination.

While the volumetric velocimetry described above is done with the aim of acquiring all three components of velocity in a three-dimensional volume, in some cases, all three components are only needed on a plane. Stereo-PIV can then be used with some success. However, if statistical quantities, such as the full Reynolds stress tensor, are required, Stereo-PIV cannot be guaranteed to perform adequately. The fluctuations of the out-of-plane component were found to be substantively different than the fluctuations found by Tomo-PIV and STB. Stereo-PIV retains its advantages in its well-documented and agreed upon uncertainty quantification (Sciacchitano *et al*. 2015) as well as its speed of calculation, but these results suggest that if accurate resolution of the out-of-plane velocity fluctuations is important, a volumetric method is necessary. The difference between frame-straddled and time series data also suggests that the exact alignment of the two laser heads is more important in Stereo-PIV than in volumetric measurements.

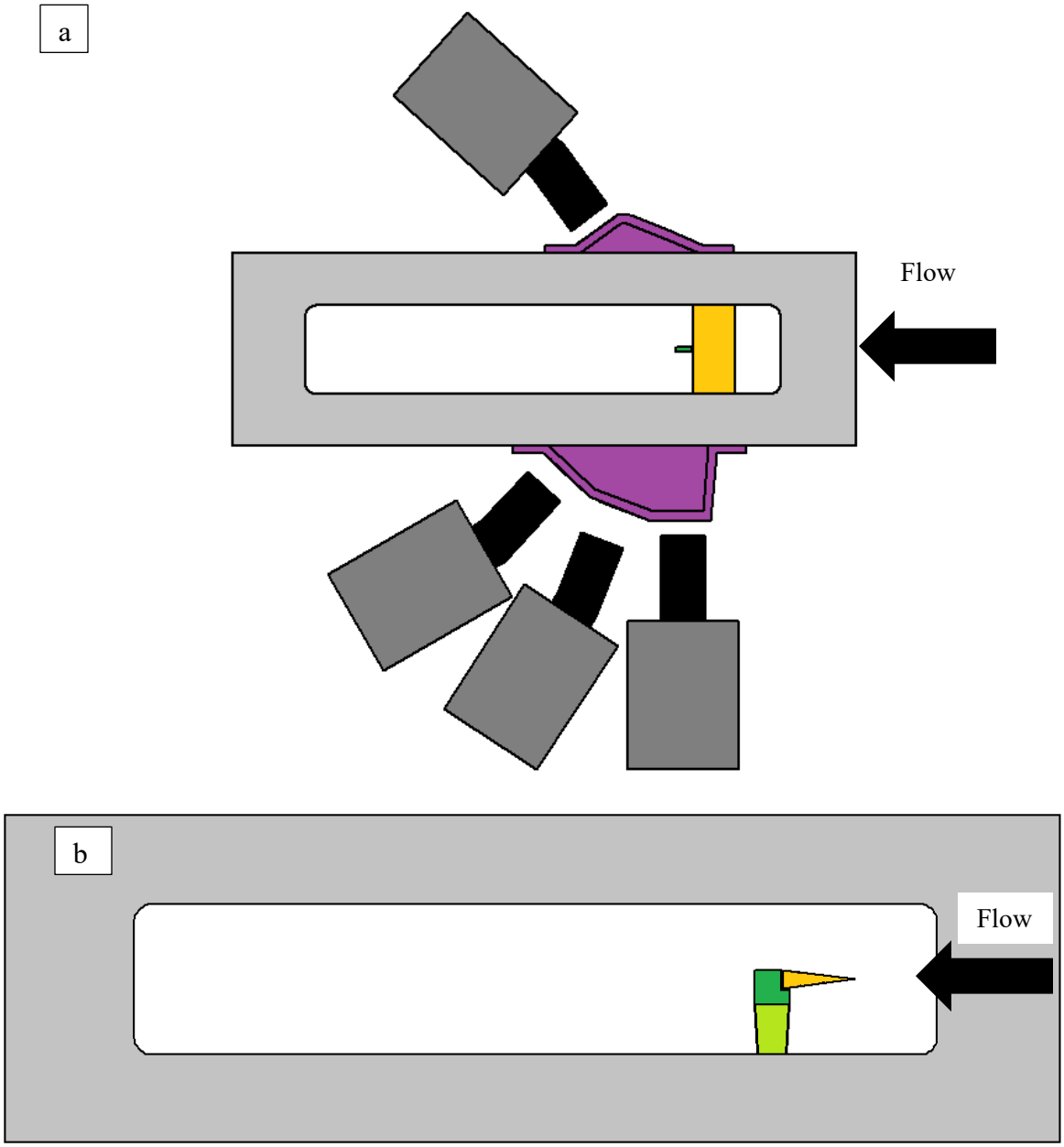


Figure 4.1. Schematic of Experimental Setup for Wedge Experiments. (a) The upper image gives a top down view of the experiment. The upstream measurement region in the wedge wake, the near wake region, is shown in green above, representing the illuminated volume. The wedge, made of brass, is in orange above. The purple structures outside the channel are water filled boxes to accommodate the change of index of refraction from air to acrylic to water. The cameras in gray, with attached lenses and Scheimpflug adapters in black, are set outside of those. (b) A side view shows the size and location of the upstream measurement volume (dark green) relative to the wedge. The illumination comes from below (light green). Flow direction in both images is from right to left.

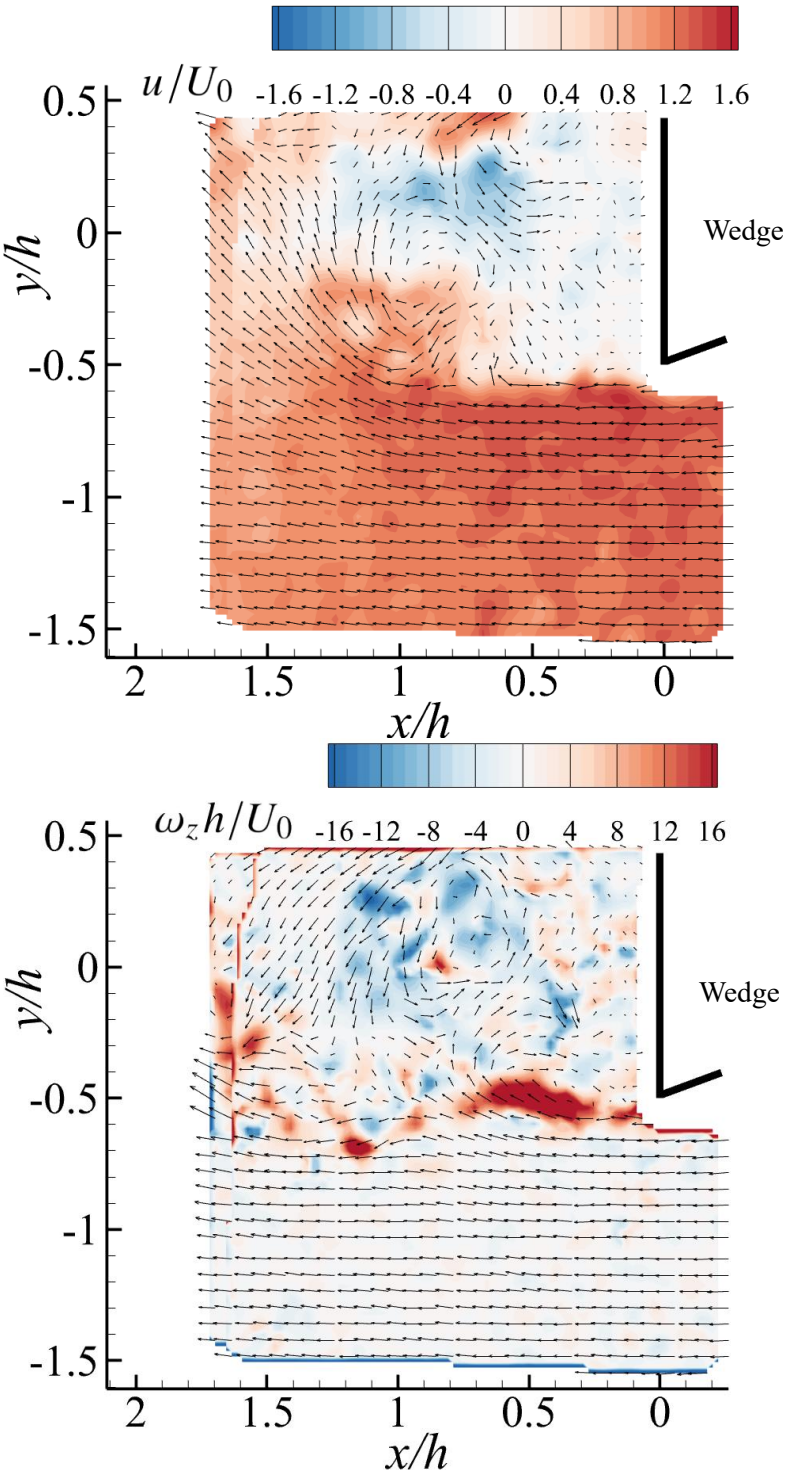


Figure 4.2. Instantaneous Velocity and Vorticity Fields. An instant from the upstream measurement region is shown with the streamwise velocity, u (top) and spanwise vorticity ω_z (bottom), scaled by base height, h, and freestream velocity, U_0. The flow is from right to left, and the wedge base is shown with the black lines. x starts from the base of the wedge while y=0 is at the mid height location of the wedge. Displayed vectors are representative, but they are sparser than the measurement for easier viewing.

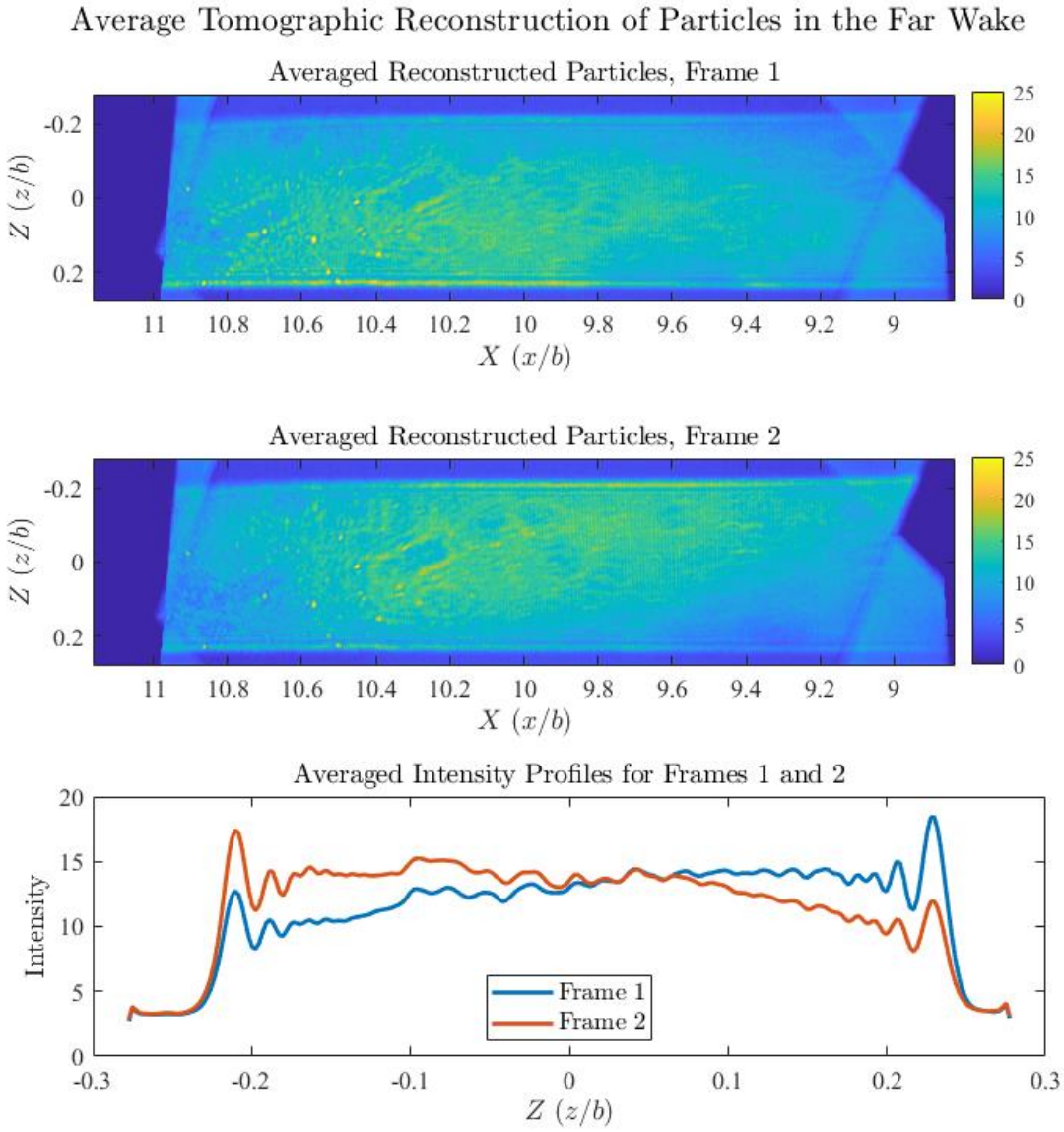


Figure 4.3. Averaged Tomographic Particle Reconstruction Intensity. The tomographic reconstructions of particles for the far wake region in the frame straddled data are integrated over the data set to show the slight differences between the laser alignment of the two beam heads. The illuminated volume shows up as lighter blue and green with the odd angular cuts in the corners coming from limited viewing angles of some of the cameras. The upper image is from the first frame of the data, illuminated by the first laser head while the middle image is from the second laser head. Note that the green region, the most brightly illuminated part, is slightly offset between the two frames. This effect shows up most clearly in the third image, which integrates all particles across the volume from $x/h = 9.8$ to $x/h = 10.2$. This ratio between the illuminated volume (from about $z/h = -0.2$ to $z/h = 0.25$) and non-illuminated volume functions as a proxy for the ghost particle intensity (a noise floor). The ratio here is about 3.5 to 5.

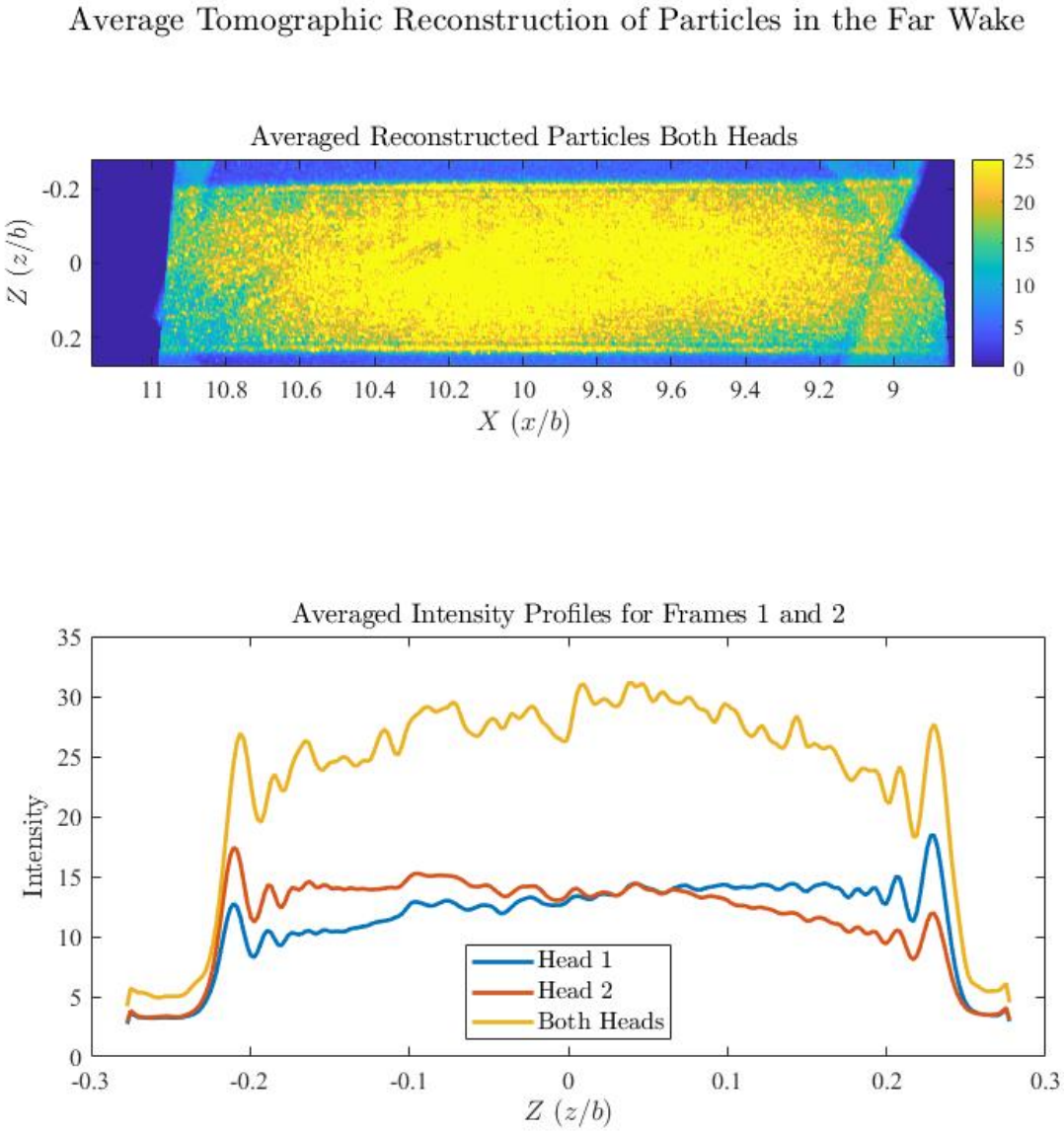


Figure 4.4. Averaged Tomographic Particle Reconstruction with Both Laser Cavities. The tomographic reconstructions of particles for the far wake region for time series data are integrated over time and shown above. Note the much brighter intensity of firing both lasers in tandem as opposed to firing the lasers in a double pulse manner (as in Figure 3 above). The lower image shows, as a comparison, the integrated intensity (from $X = 9.8$ to $X = 10.2$ as well as again integrating over time) for both laser heads individually as well as firing together. This leads to a higher ratio of brightness between illuminated volume (from approximately $Z = -0.2$ to $Z = 0.25$) and non-illuminated volume, a ratio of about 5 to 6.

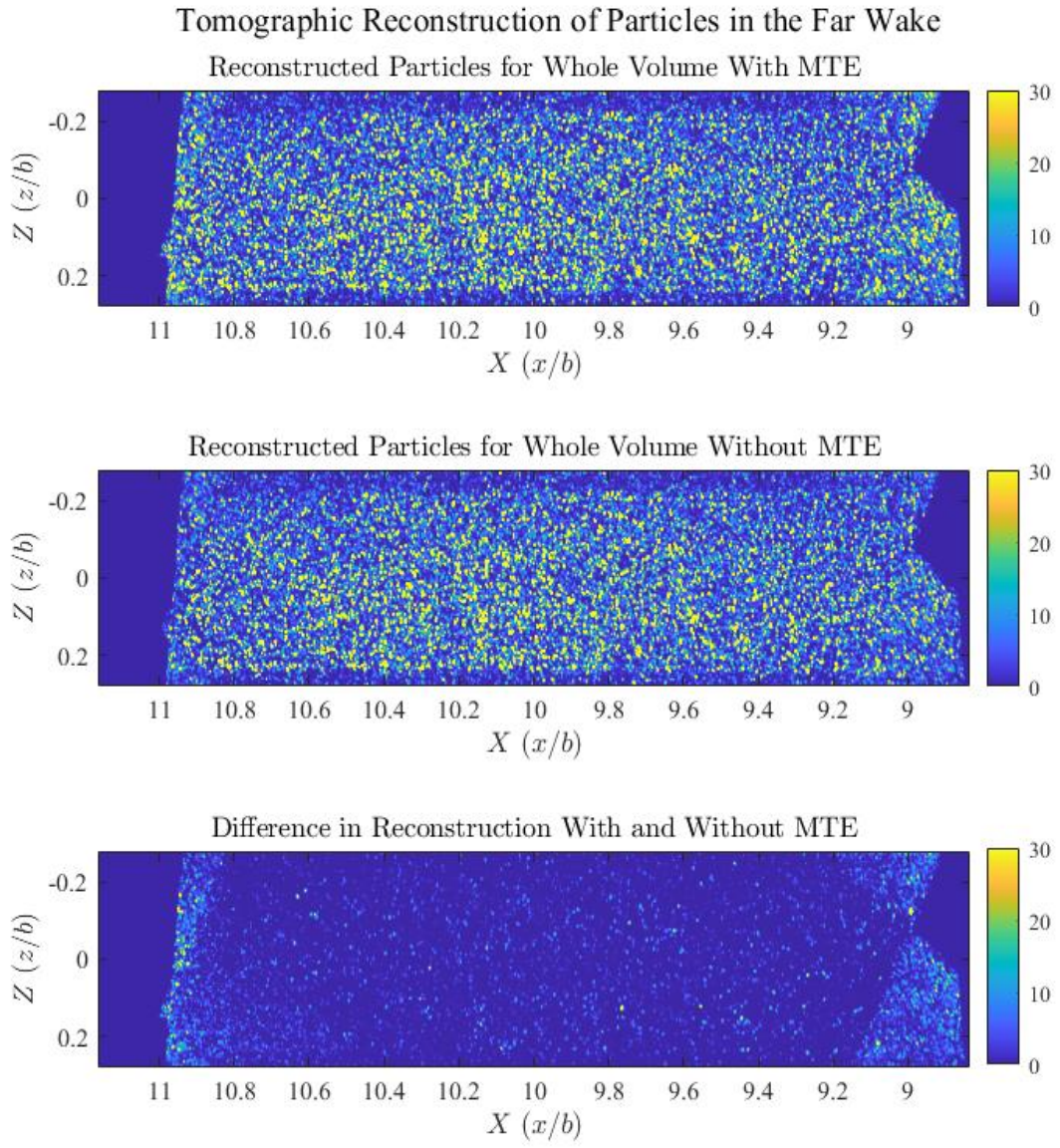


Figure 4.5. Reconstructed Particles Comparing MTE and Disuse. The tomographic reconstruction of particles from an arbitrary instance of the frame straddled data is shown here to demonstrate the effect of MTE. The top panel shows the particles reconstructed with MTE while the middle panel shows the particles reconstructed without MTE. Differences are immediately obvious to the eye, so the bottom panel shows the residual intensity from subtracting the particles reconstructed with MTE from the particles reconstructed without MTE. This shows that by not using MTE, some of the particle energy intensity is missed in the reconstruction.

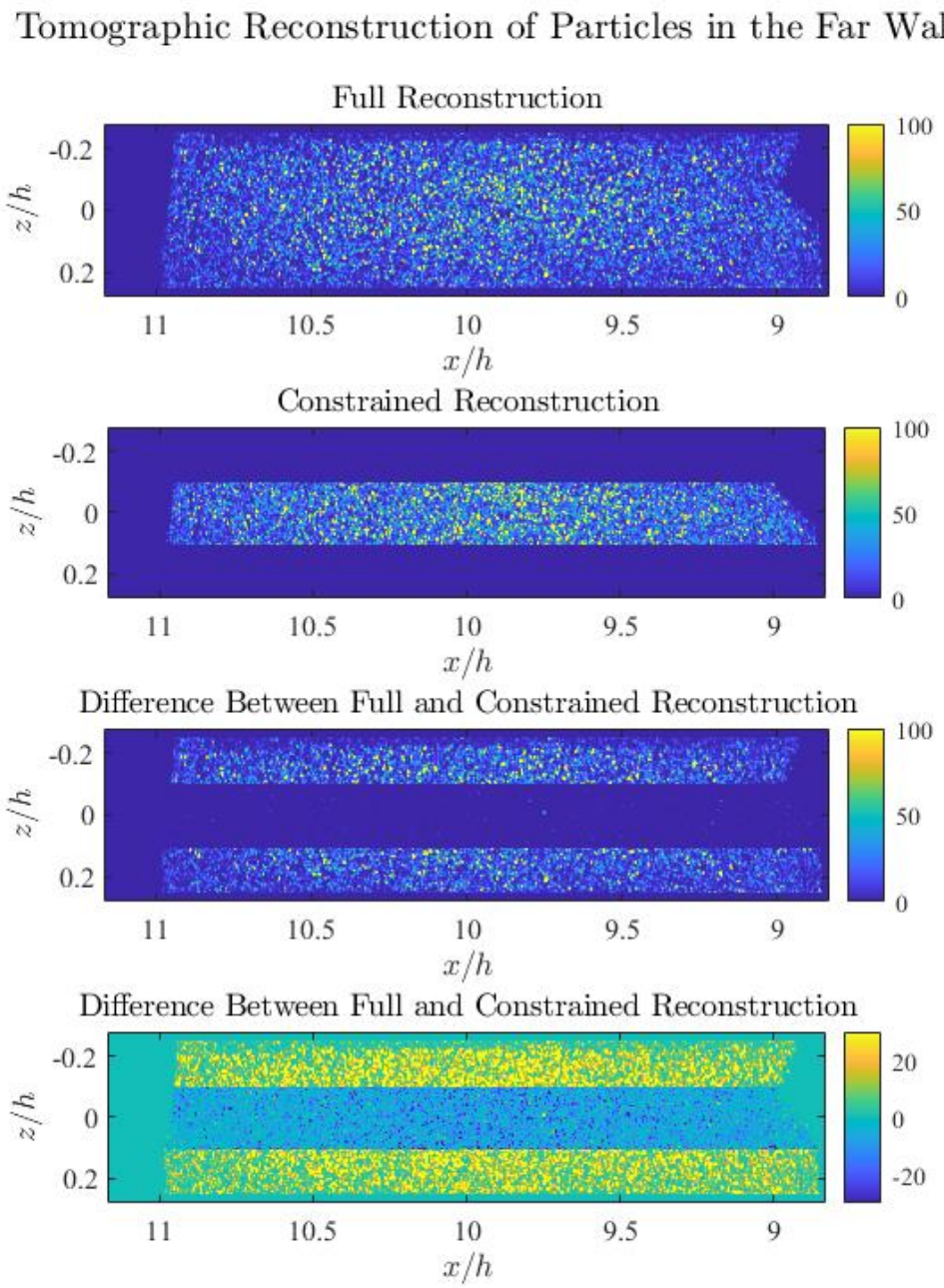


Figure 4.6. Tomographic Reconstruction of Particles with and without Constraint. The tomographic reconstruction of particles from the same arbitrary instance of frame straddled data is shown again but with partial thickness reconstructions as well as full thickness reconstructions. MTE is always used in the data in this image. The top panel shows the full thickness reconstruction of the data while the second panel shows the reconstructed particles of the partial thickness reconstruction. Note the much brighter particles in the partial reconstruction. Thus, when subtracting the partial reconstruction from the full reconstruction (the third and fourth panels), the region has negative intensity. The fourth panel is shown with a different scale to make this negative intensity clear.

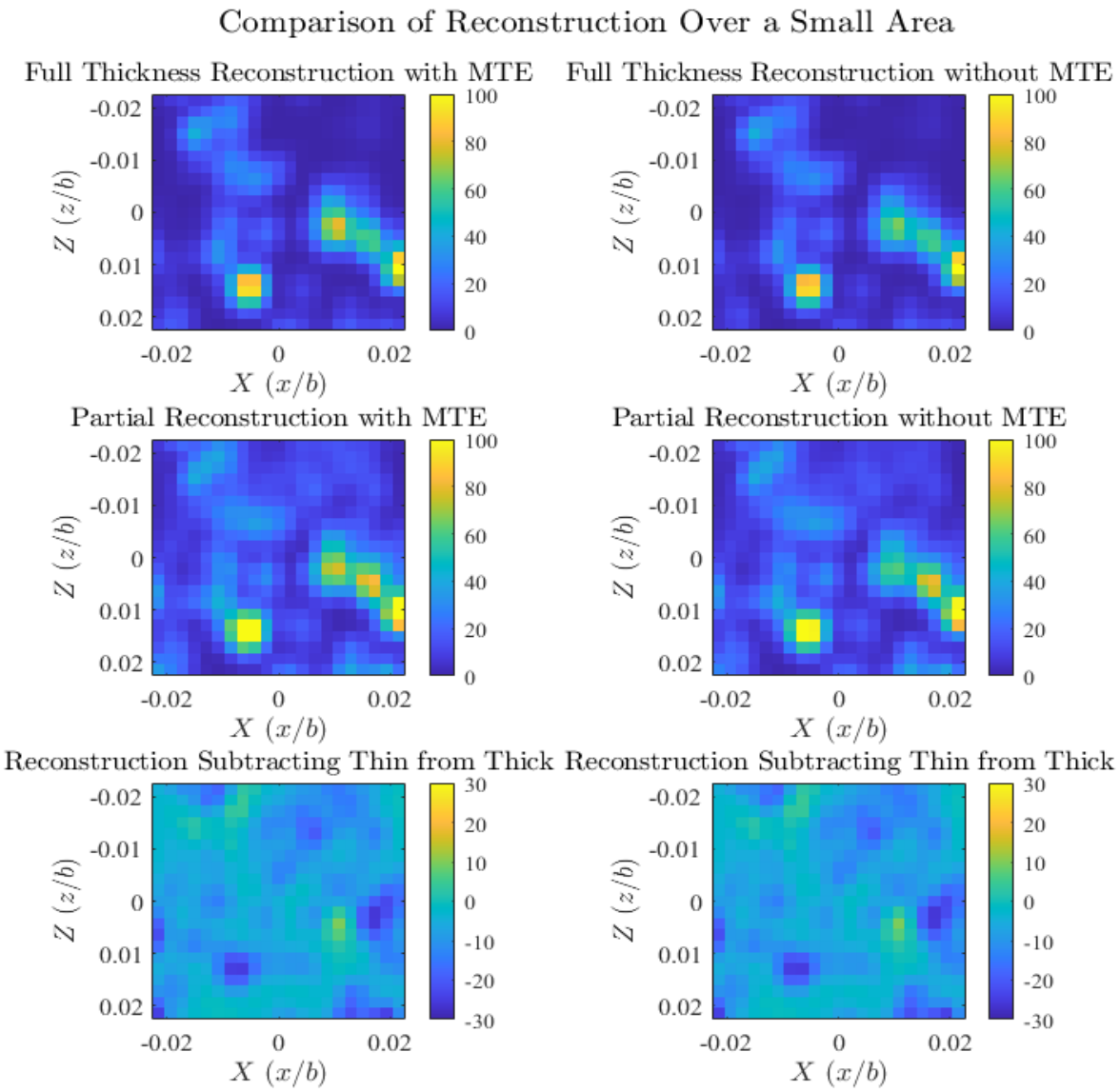


Figure 4.7. Close Comparison of Particle Reconstruction. A small portion of the reconstructed particle volume is reproduced here to more clearly show the differences in reconstructed intensity between different calculation methods. Comparing the top row, the left image has somewhat brighter particles compared to the right image due to the use of MTE for the image on the left. This effect repeats in the middle row, with the MTE aided reconstruction (left) having brighter particles than the non-MTE reconstruction (right). In comparison to the top row, note that the middle row has a sort of cloud of reconstructed intensity throughout that does not appear to form any recognizable particles as well as an overall brighter reconstruction. The last row then shows the difference between the full and partial reconstructions by subtracting the partial reconstruction from the full reconstruction. Again, areas that clearly represent particles have negative intensity due to the partial reconstruction having higher intensity than the full width reconstruction.

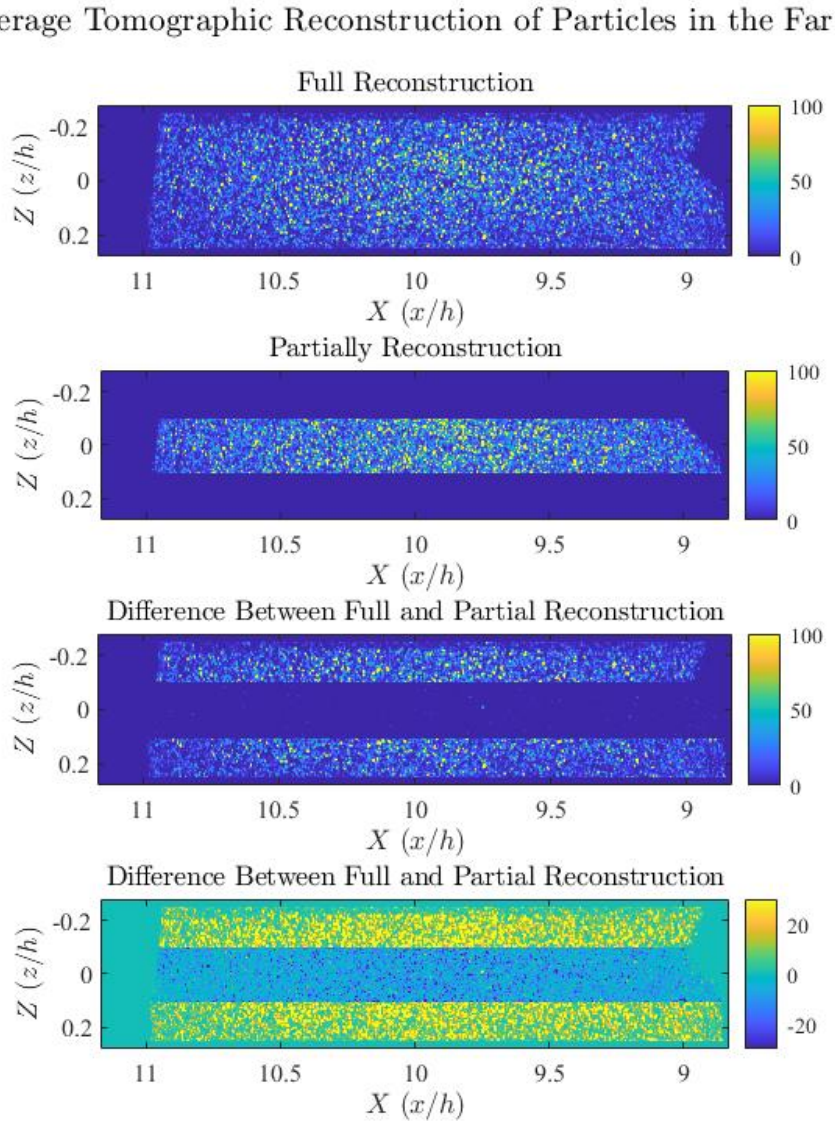


Figure 4.8. Comparison of Particle Reconstructions. An arbitrary instant from the time series data in the far wake of the wedge is compared here between different computations. As in the case of the frame straddled data, the reconstructed particles are brighter in the partial reconstruction case when compared to the full reconstruction case, and close inspection shows that some likely non-physical particles or energy are reconstructed within the artificially constrained volume.

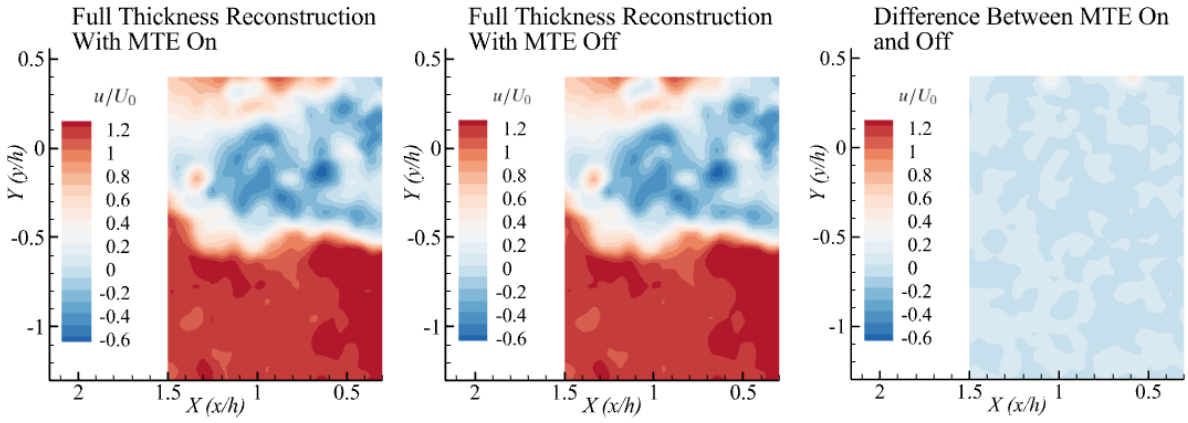


Figure 4.9. Velocity Field Comparison with and without MTE. An arbitrary instant from the frame straddled data in the near wake of the wedge is compared here between different computations. On the left is the velocity field from the Tomo-PIV with the use of MTE while the middle is from Tomo-PIV with no MTE used. The right panel shows the difference between them, which is minimal, indicating that the difference between the use of MTE or not is small in this case.

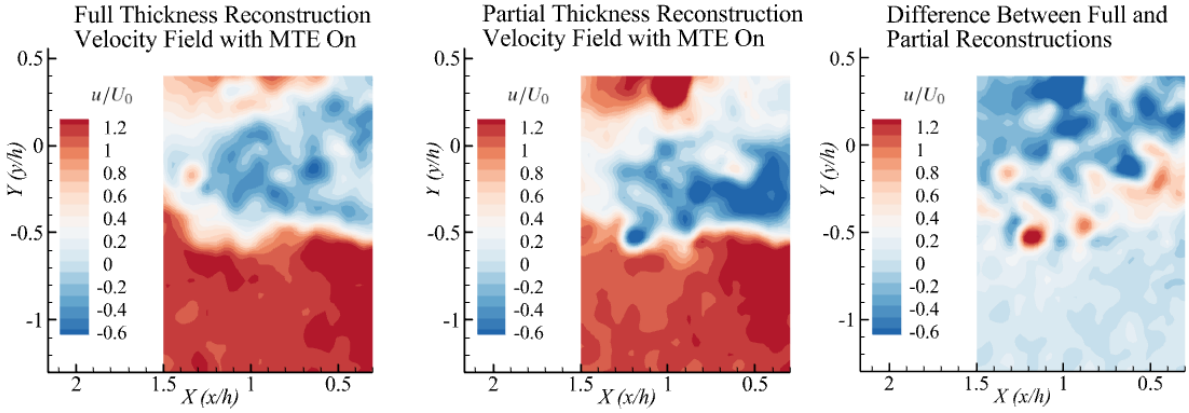


Figure 4.10. Velocity Field Comparison with and without Constraint. An arbitrary instant from the frame straddled data in the near wake of the wedge is compared here between different computations. On the left is the velocity field from the Tomo-PIV with the full thickness reconstructed and computed while the middle has only part of the thickness reconstructed and computed. Both of these calculations used MTE. The right panel shows the difference between the full and partial calculations, showing that at several points, the differences are substantial. It appears that several patches of velocity that do not match their neighboring fields in the partial thickness reconstruction are likely wrong.

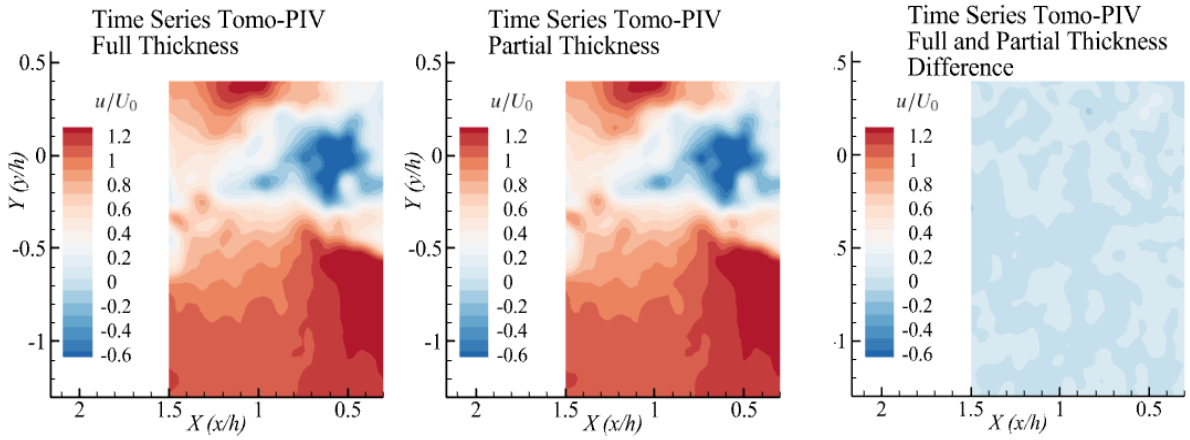


Figure 4.11. Velocity Field Comparison with Time Series Data. An arbitrary instant from the time series data in the near wake of the wedge is compared here between different computations. On the left is the velocity field from the Tomo-PIV with the full thickness reconstructed and computed while the middle has only part of the thickness reconstructed and computed. Both of these calculations used SMTE. The right panel shows the difference between the full and partial calculations, showing minimal differences between the two, especially compared to the frame straddled data above.

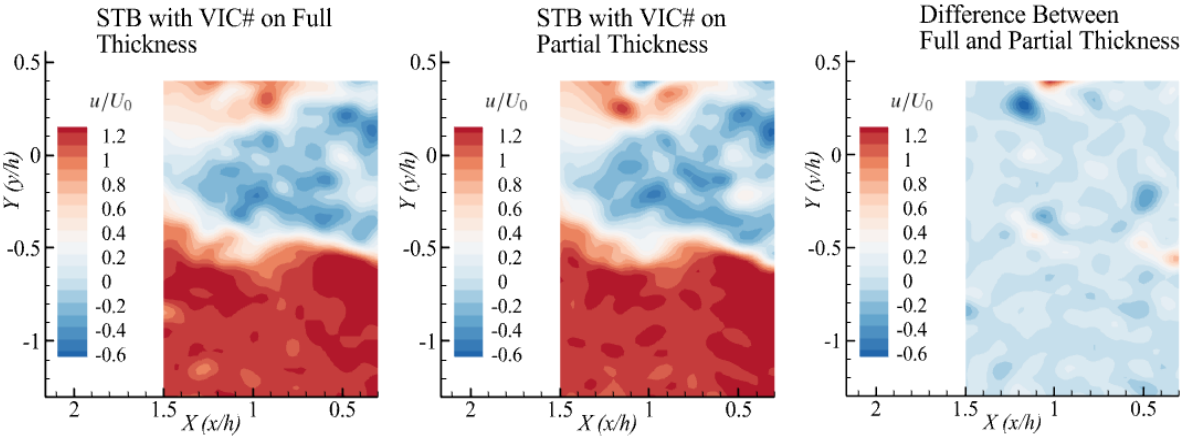


Figure 4.12. STB-VIC# Time Series Velocity Field Comparison. An arbitrary instant from the frame straddled data in the near wake of the wedge is compared here between different computations. On the left is the velocity field from the STB-VIC# calculation over the full thickness. The middle has the STB-VIC# field with only partial thickness. The right has the difference between them, which indicates small differences, mainly near the edges of the field. STB-VIC# is relatively unaffected by the use of partial thickness calculations.

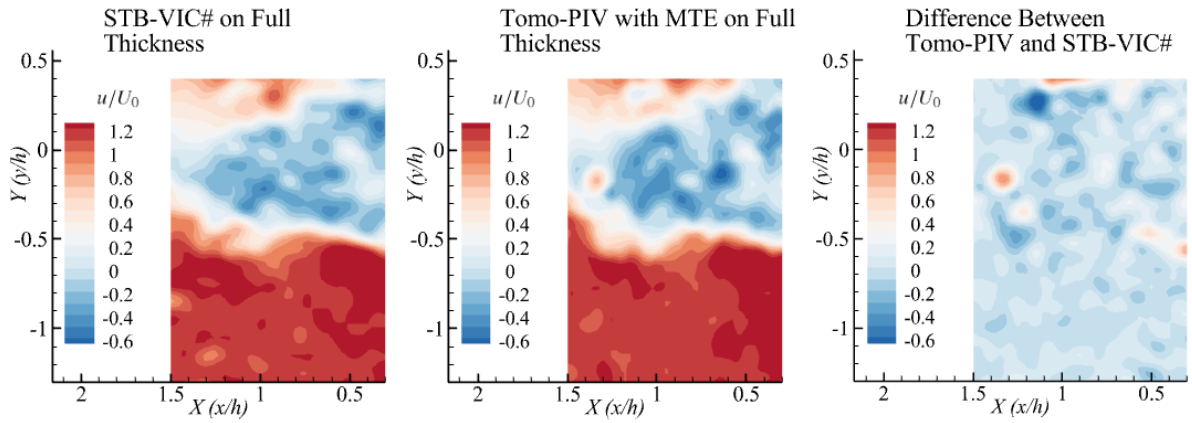


Figure 4.13. STB-VIC# Frame Straddled Velocity Field Comparison. An arbitrary instant from the frame straddled data in the near wake of the wedge is compared here between different computations. On the left is the velocity field from the STB-VIC# calculation over the full thickness. The middle has the Tomo-PIV field with MTE used over the full thickness. The right has the difference between them, which indicates relatively small differences, mainly near the edges of the field.

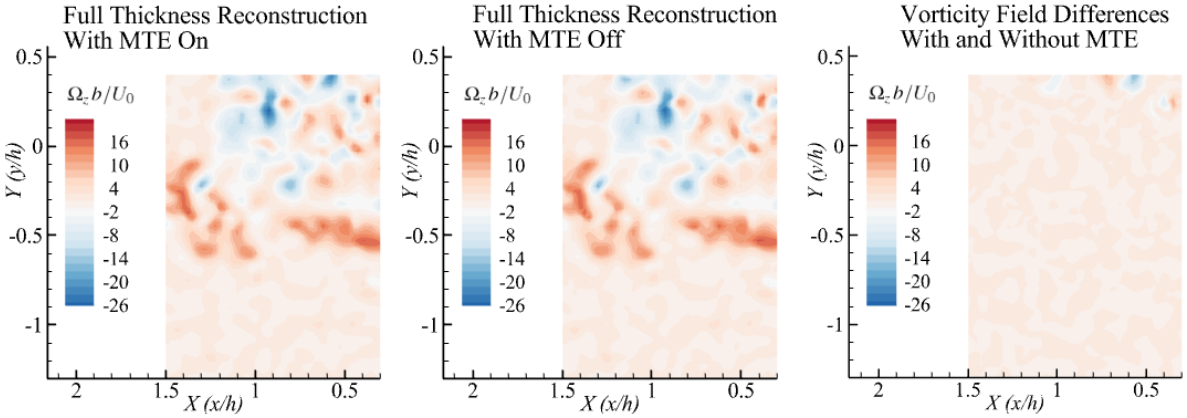


Figure 4.14. Vorticity Field Comparison with and without MTE. An arbitrary instant (the same instant from above) from the frame straddled data in the near wake of the wedge is compared here between different computations, this time with the vorticity field. On the left is the vorticity field from the Tomo-PIV with the use of MTE while the middle is from Tomo-PIV with no MTE used. The right panel shows the difference between them, which is minimal, indicating that the difference between the use of MTE or not is small in this case.

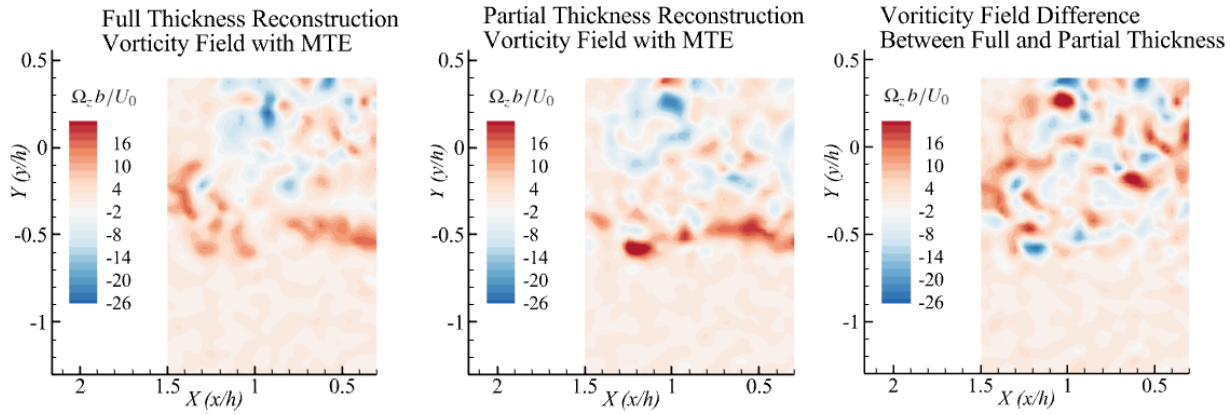


Figure 4.15. Vorticity Field Comparison with and without Constraint. An arbitrary instant (the same instant from above) from the frame straddled data in the near wake of the wedge is compared here between different computations, this time with examination of the vorticity field. On the left is the vorticity field from the Tomo-PIV with the full thickness reconstructed and computed while the middle has only part of the thickness reconstructed and computed. Both of these calculations used MTE. The right panel shows the difference between the full and partial calculations. These differences are greater than in the vorticity field as opposed to the velocity field as the numerical gradients in vorticity amplify noise. Thus, more caution is required when vorticity is the quantity of interest.

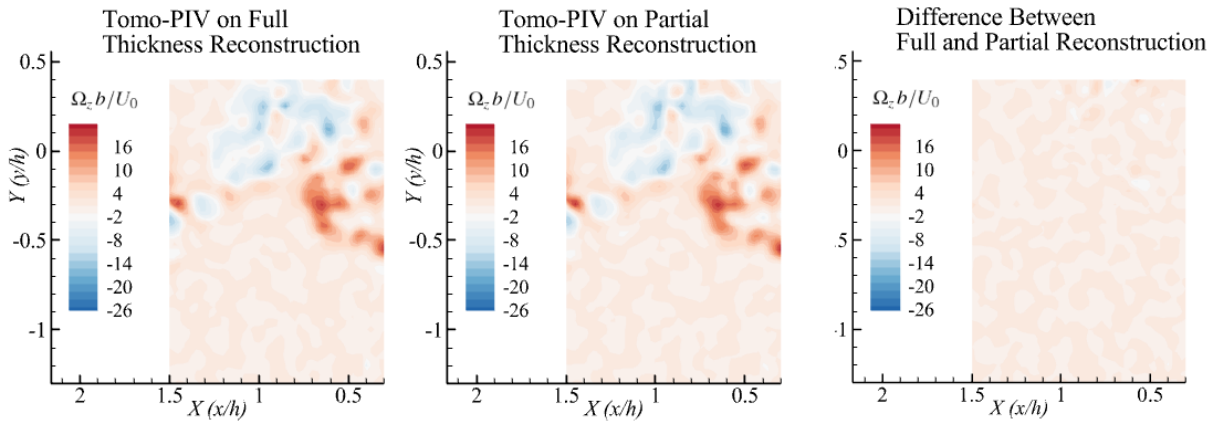


Figure 4.16. Vorticity Field Comparison for Time Series Data. An arbitrary instant (the same instant from above) from the time series data in the near wake of the wedge is compared here between different computations, this time with examination of the vorticity field. On the left is the vorticity field from the Tomo-PIV with the full thickness reconstructed and computed while the middle has only part of the thickness reconstructed and computed. Both of these calculations used SMTE. The right panel shows the difference between the full and partial calculations. The differences between full and partial reconstructed Tomo-PIV are minimal with the time series data.

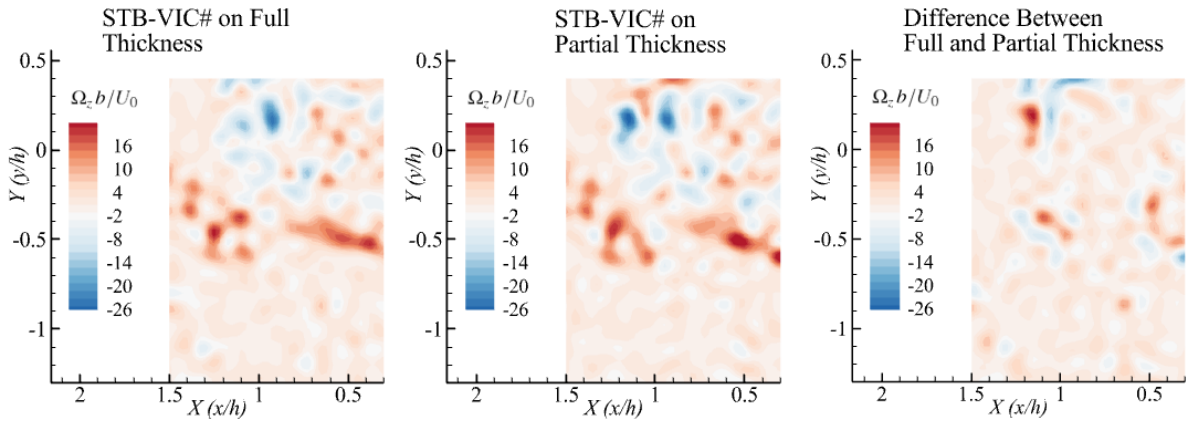


Figure 4.17. STB-VIC# Time Series Vorticity Field Comparison. An arbitrary instant (the same instant from above) from the frame straddled data in the near wake of the wedge is compared here between different computations. On the left is the vorticity field from the STB-VIC# calculation over the full thickness. The middle has the STB-VIC# field with only partial thickness. The right has the difference between them, which indicates some patches of rather different magnitude. STB-VIC# is relatively unaffected by the use of partial thickness calculations as compared to Tomo-PIV calculations.

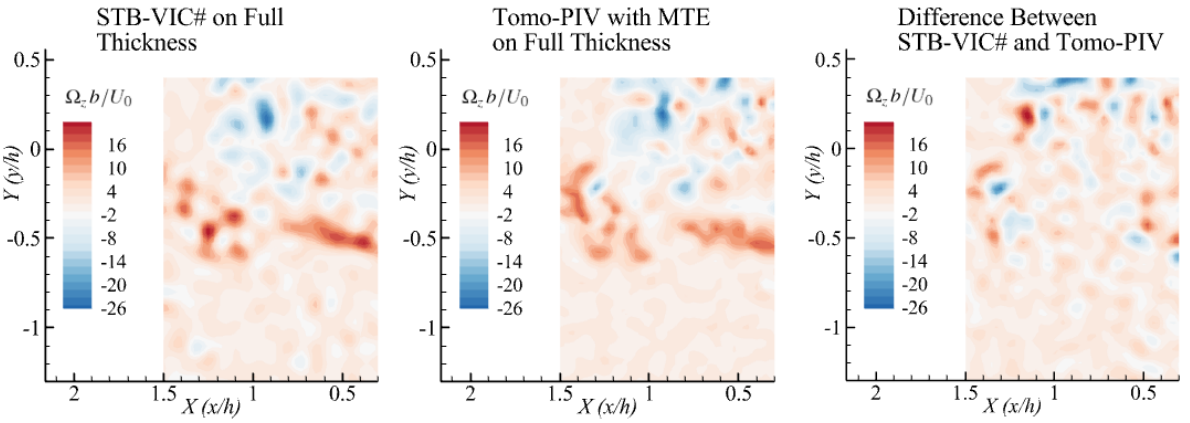


Figure 4.18. STB-VIC# Frame Straddled Vorticity Field Comparison. An arbitrary instant (the same instant from above) from the frame straddled data in the near wake of the wedge is compared here between different computations. On the left is the vorticity field from the STB-VIC# calculation over the full thickness. The middle has the Tomo-PIV field with MTE used over the full thickness. The right has the difference between them. The differences are noticeable, but the features such as the shear layer at $Y = -0.5$ compare well in location. The magnitudes likely differ in this location as Tomo-PIV should act as a low pass filter and

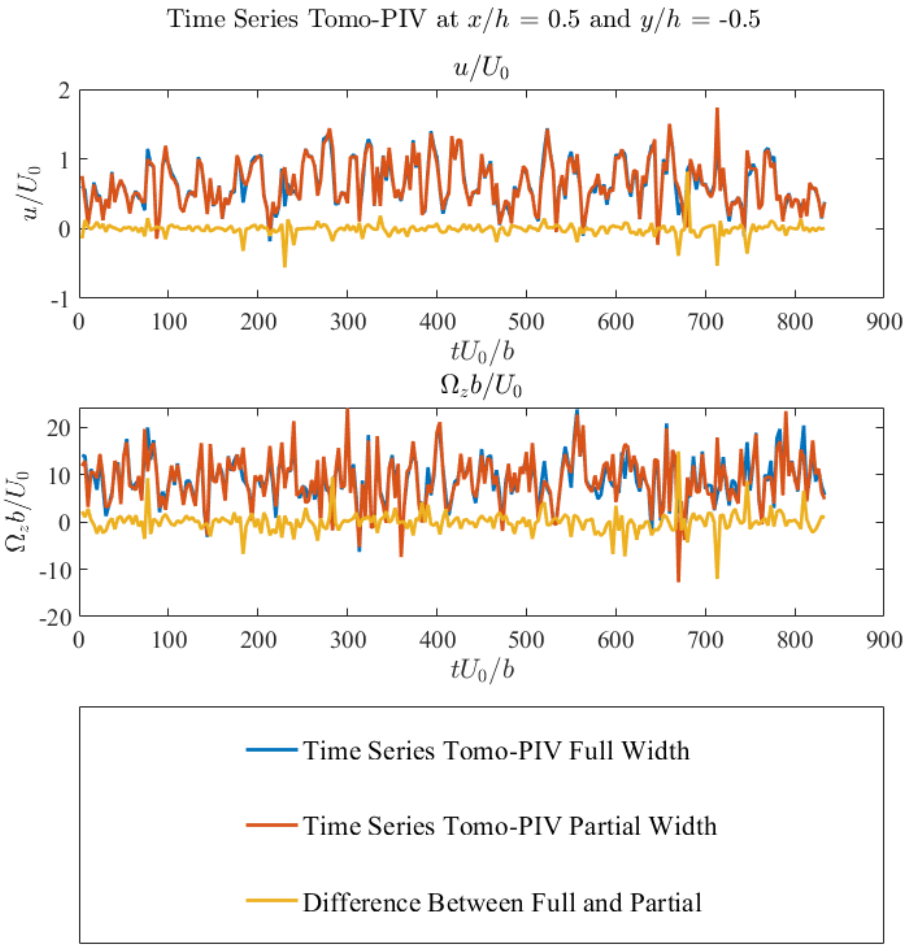


Figure 4.19. Comparison of Time Series Data Over Time. The differences between the full and partial reconstructions of Tomo-PIV at an arbitrary point in the measurement volume are shown for a length of time for frame straddled measurements. At this point in space, the two velocity traces generally track well with one another leading to relatively small differences between them.

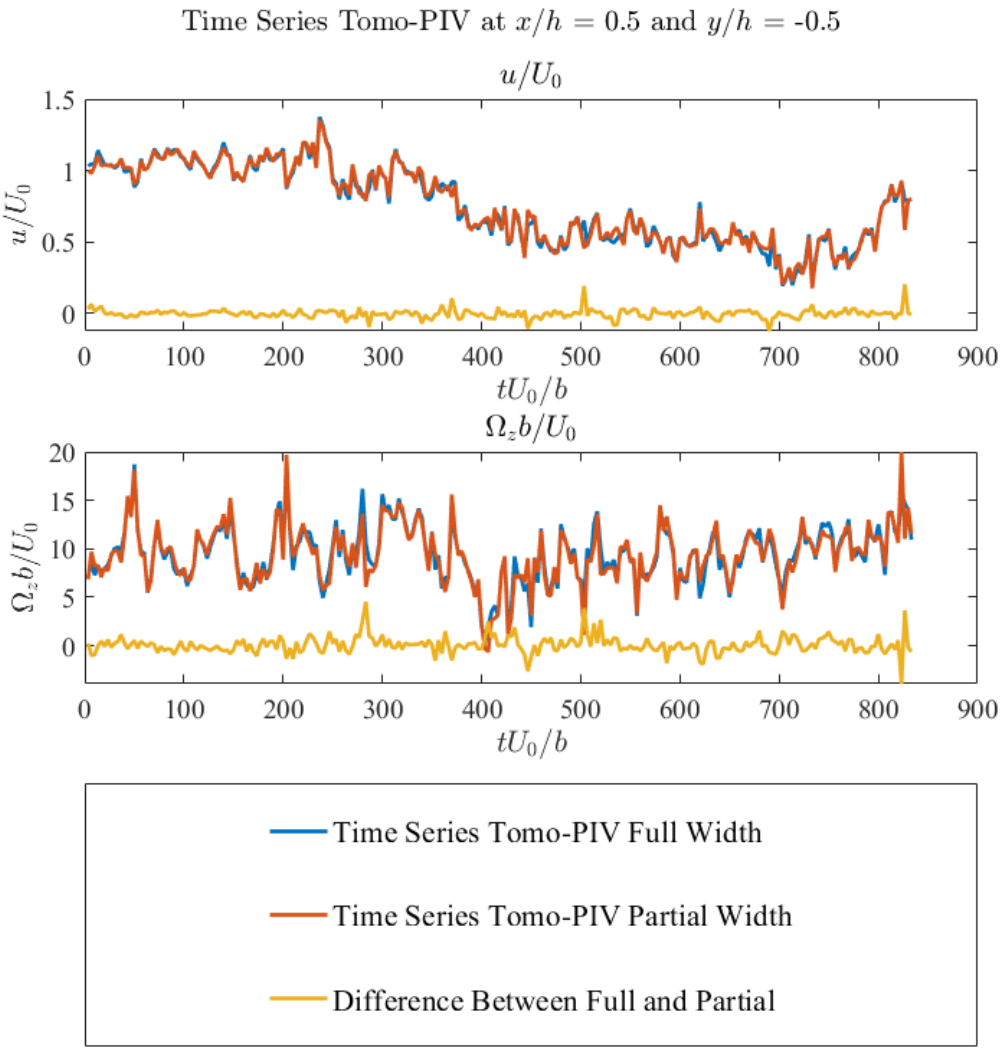


Figure 4.20. Comparison of Time Series Data Over Time. The differences between the full and partial reconstructions of Tomo-PIV at an arbitrary point in the measurement volume are shown for a length of time for time series measurements. The two velocity traces track well with one another leading to relatively small differences between them.

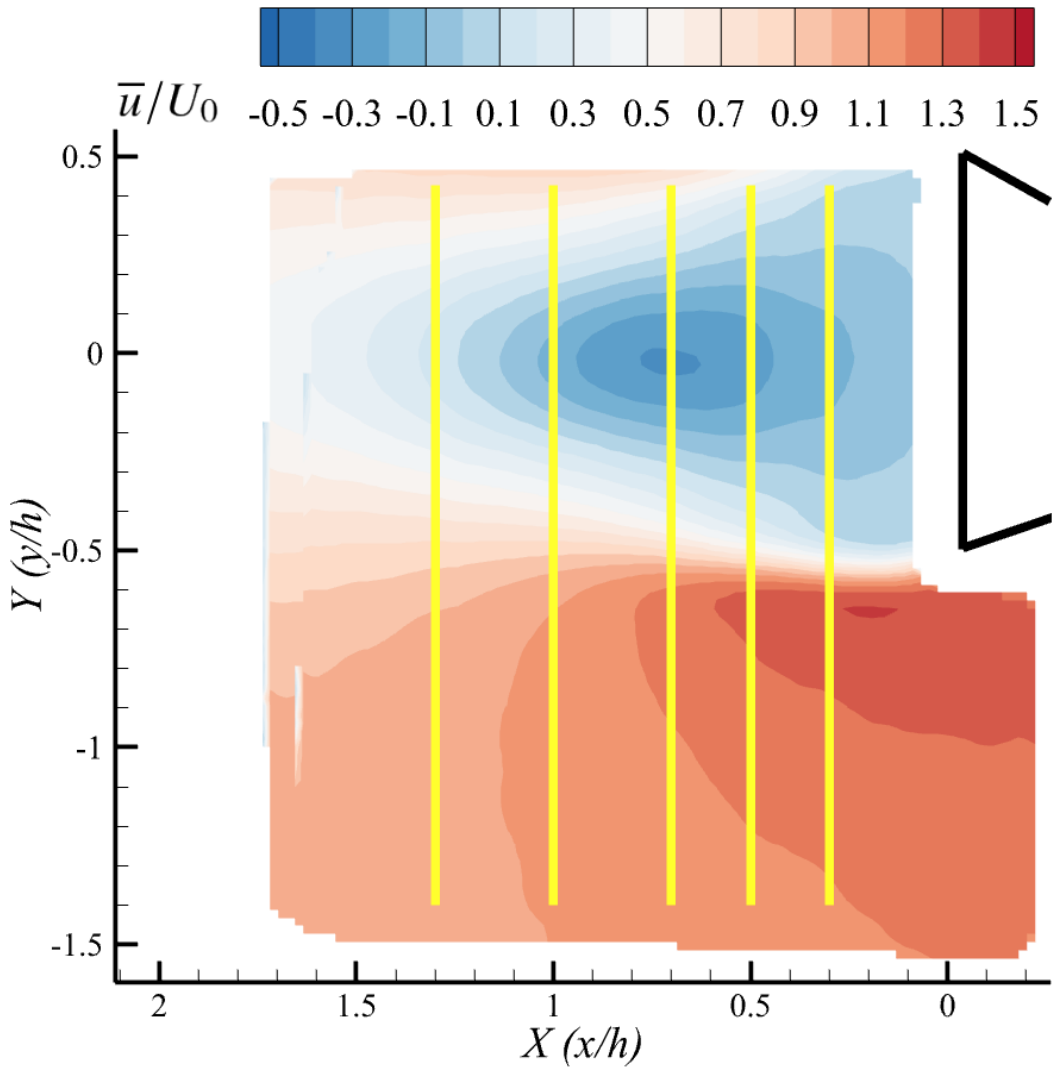


Figure 4.21. Location of Averaged Quantity Comparison Points. In the near wake of the wedge at the spanwise centerline of the volume, five vertical cuts were taken at $X = 0.3$, 0.5, 0.7, 1.0, and 1.3. The different volumetric and planar computational approaches are compared at these X locations and at $Z=0$. The locations of these cuts are represented by the yellow lines above. The wedge is in the upper left corner.

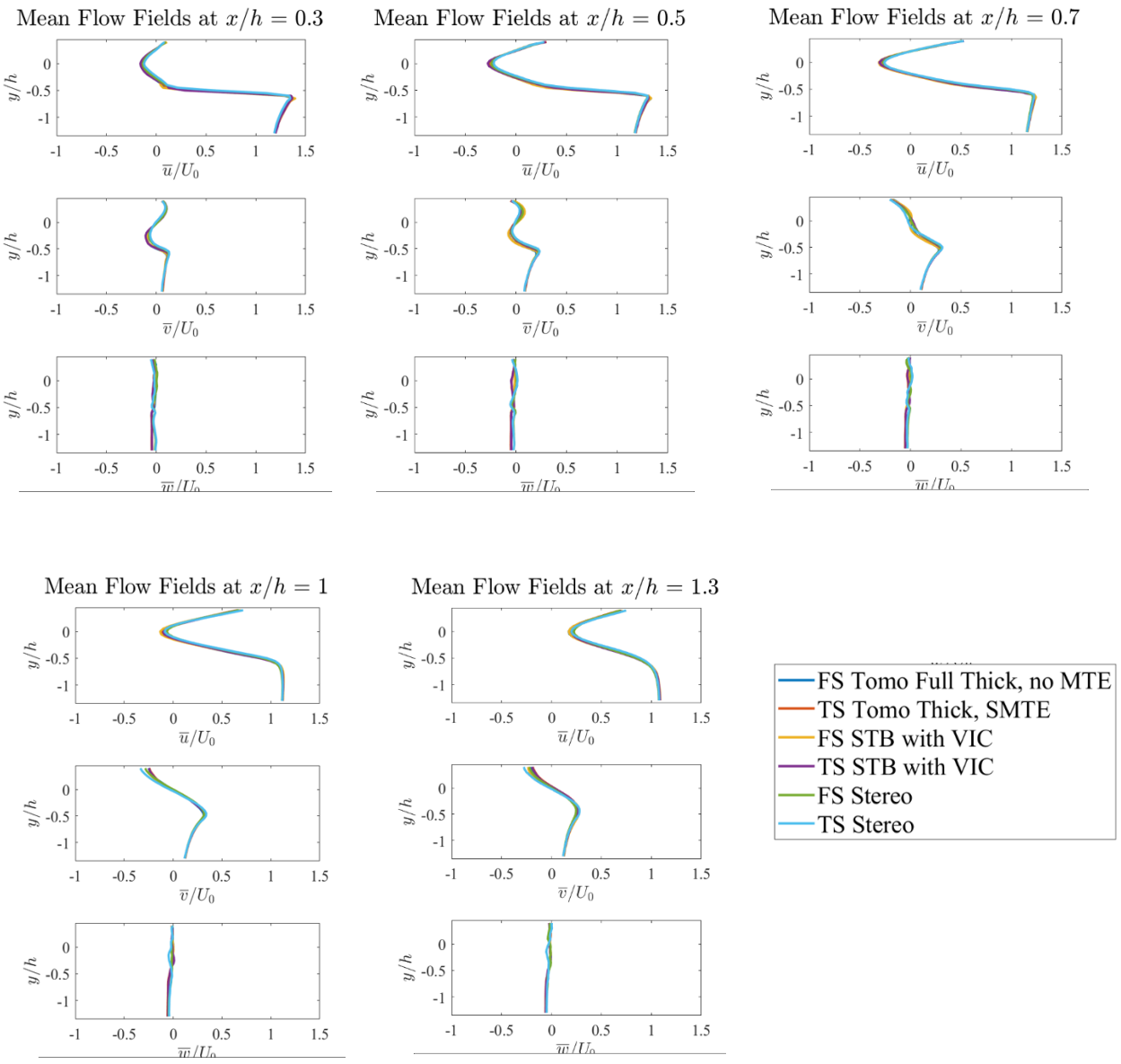


Figure 4.22. Mean Flow Fields at Various Location. The mean flow fields for all three components for the five streamwise locations shown in Figure 20 are shown above. The varied ways of calculating these quantities agree well with each other whether in the recirculation region in the immediate near wake of the wedge or in the freestream below the

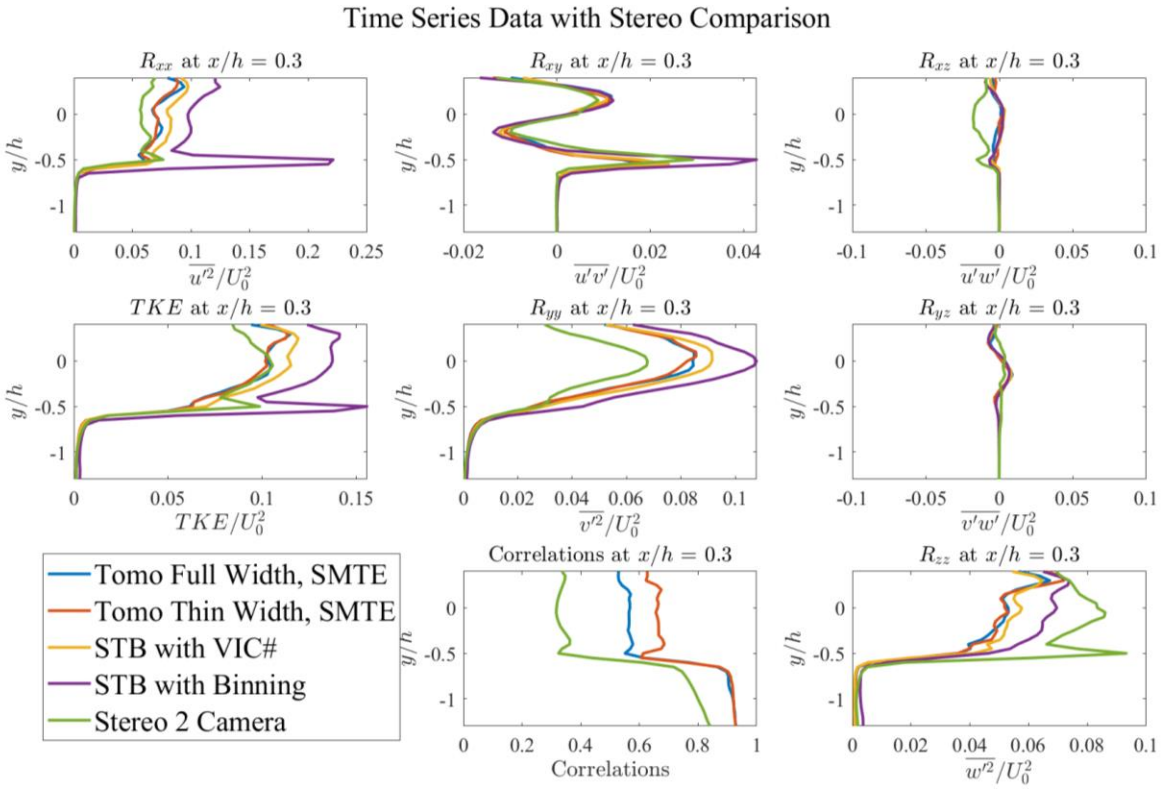


Figure 4.23. Reynolds Stresses with Time Series Data. Time series data, processed in various ways, are shown above. There is good agreement between the planar and volumetric measurements for the in plane components, but the Stereo-PIV is rather different for the out of plane component in the recirculation region. This can be at least partially attributed to the lower correlation of the Stereo-PIV in this region as this indicates higher uncertainty in the measurement.

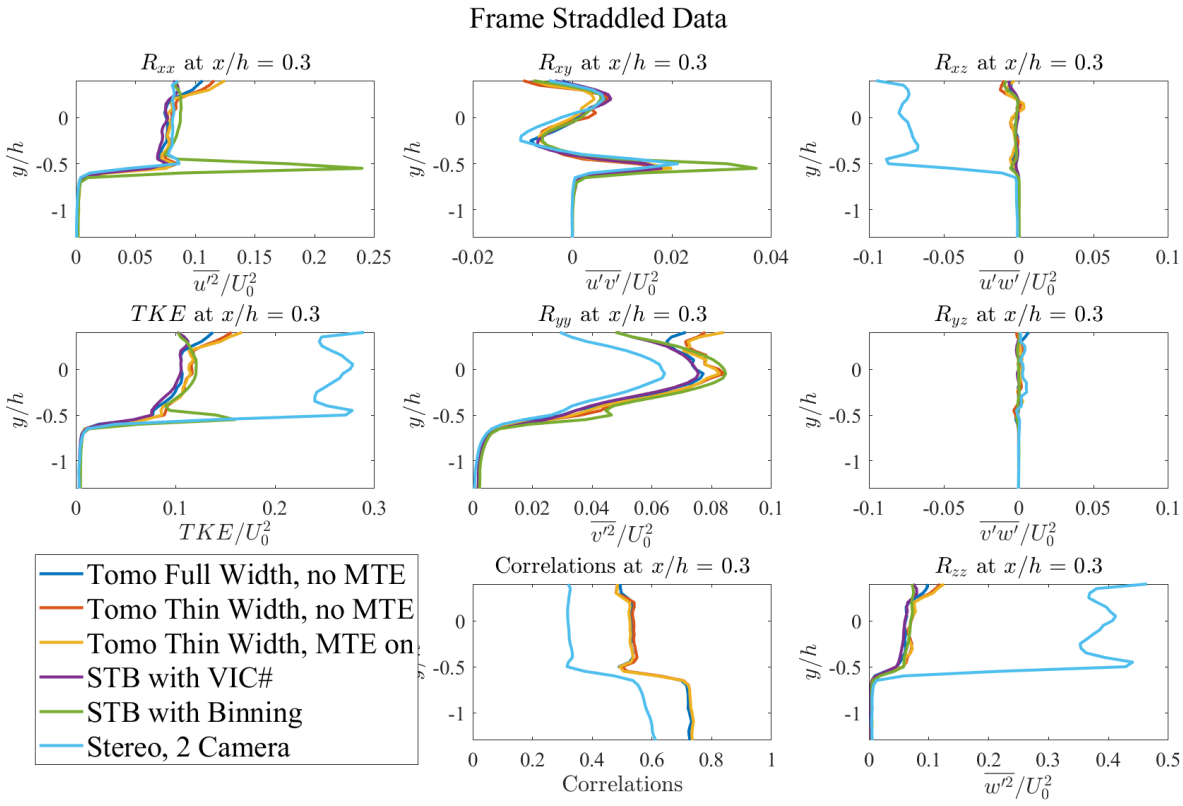


Figure 4.24. Reynolds Stresses with Frame Straddled Data. Frame straddled data, processed in various ways, are shown above. There is good agreement between the planar and volumetric measurements for the in plane components, but the Stereo-PIV is rather different for the out of plane component in the recirculation region. This can be at least partially attributed to the lower correlation of the Stereo-PIV in this region as this indicates higher uncertainty in the measurement. The STB-Binning approach shows a large jump in magnitude at the location of the transition between the recirculation and free stream regions. This is likely due to the binning calculating the velocity based off of relatively few particles and it would be easy for it to alternate between calculating off of low speed (recirculating region) and high speed particles (free stream region), the fluctuations are substantial. Similarly, a comparable kink in the data appears in the correlations as the correlation window there captures both low and high speed particles.

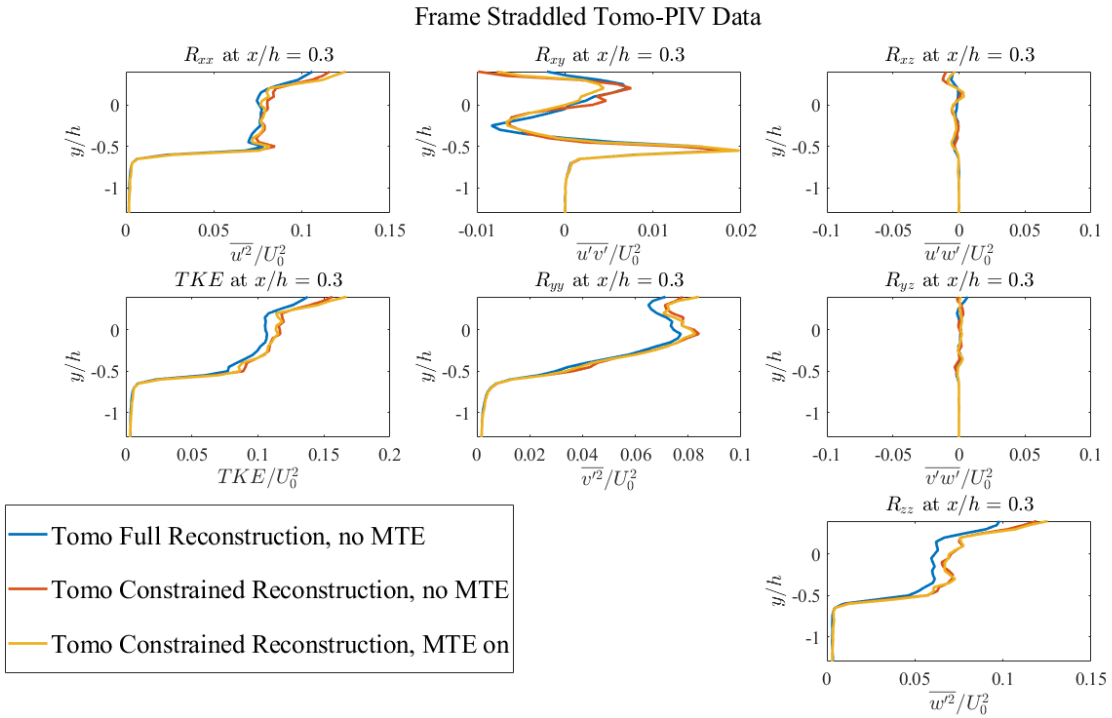


Figure 4.25. Reynolds Stresses with Frame Straddled Data, MTE Comparison. The same frame straddled data as in Figure 24 is shown here, but only with the Tomo-PIV data to show the differences more clearly between full and constrained reconstruction. The full reconstruction generally has lower Reynolds stresses than the artificially constrained reconstructions. As was shown earlier, the artificially constrained reconstructions lead to some artificial fluctuations in the instantaneous velocity fields. When taking the Reynolds average of these fields, these fluctuations translate into higher Reynolds stresses for the ensemble.

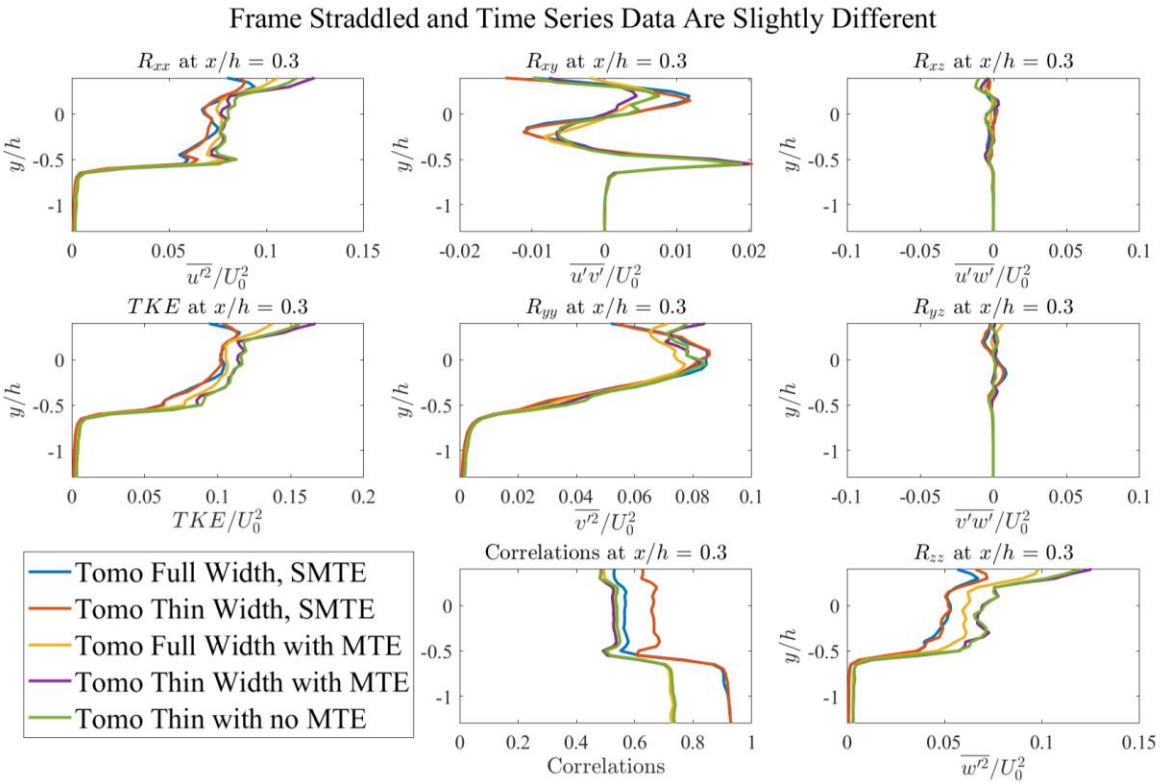


Figure 4.26. Reynolds Stresses, Comparing Frame Straddled and Time Series. Frame straddled data and time series data are compared above indicating slight differences between them. The differences are likely partially due to insufficient samples for the time series data. Another possible cause is a slight misalignment of the two laser heads. In time series mode, the laser heads fire together, giving one more uniform pulse. While in frame straddled mode, the laser heads fire independently, and the brightest parts of each head occur in slightly different locations of the illuminated volume. This likely results in the lower correlations seen in the frame straddled data.

Chapter V

Study of Interaction of Counter Rotating Vortex Pairs

Overall Evolution of the Vortex Pair

As the simplest model system of vortex stretching driving rapid pressure drop and hence cavitation inception, the interactions of a pair of unequal strength, initially parallel, counter-rotating line vortices experiencing Crow instability is considered. Such a vortex pair can be produced by a pair of hydrofoils in a water channel with an arrangement shown by Figures 5.1 and 5.2. First, the vortices rollup in the wake of the foil in an initial configuration where they are parallel in arrangement and have radii of curvature of their centerlines much larger than their separation distance. The weaker ("secondary") vortex begins orbiting the stronger ("primary") counter rotating vortex. As the vortices convect downstream, the secondary experiences substantial stretching as it undergoes the long wavelength Crow instability, and the pressures in the cores of the secondary vortices can be significantly reduced.

The dynamics of this vortex interaction are examined at several locations with cavitation visualization of the vortices and using detailed volumetric velocimetry. The first location for volumetric velocimetry is in the near wake of the foils, here considered the "upstream" region, and serves as a location to measure an initial condition for the interaction. The second location, considered the "midstream" location, is where the vortices are still in the linear stage of the instability development. At this location, the axis of the secondary vortex has a sinusoidal shape while the primary has a gentler curvature as it and the secondary orbit. Downstream of this

location, the instability perturbation in the secondary has a greater amplitude as it stretches out of its previously sinusoidal shape. This is the final “downstream" streamwise location of measurement. Farther downstream than this location, the secondary begins to break from its continuous arcing topology and then reconnect into vortex rings, as shown in Figure 5.3. This chapter focuses on the experimental geometry used and the cavitation visualization of the vortices. Subsequent chapters will focus on the velocimetry measurements of the vortices at the three locations mentioned above.

Test Models and Experimental Setup

To generate the pair of line vortices herein studied, a pair of cambered hydrofoils are arranged in a recirculating cavitation channel. The hydrofoils have a modified NACA 66 section (Shen and Dimotakis 1989). The larger hydrofoil, generating the primary vortex, has a rectangular plan form while the smaller hydrofoil, generating the secondary vortex, has either a tapered plan form or a rectangular plan form of equal chord to the primary foil, depending on the case. To differentiate, values from the cases with the tapered secondary foil are denoted with *n* for non-matching while the rectangular plan form foil case has *m* for matching. The root chord, *c*, for the hydrofoils is 167 mm. The tapered secondary hydrofoil has a rounded tip to encourage roll up of the tip vortex. The rectangular planform hydrofoils for the primary vortex and matching secondary foil have squared off tips. Detailed drawings of the foils used are in Appendix 1. The separation distance between the hydrofoil tips as well as their attack angles were changed. Several different angles of attack of the secondary foil were studied with the tapered foil, though only one angle of attack was studied for the matched hydrofoil.

The pressure in the cores of the vortices is reduced compared to the freestream pressure and, with a significant reduction in the tunnel pressure, the cores may fill with vapor. For the

experiments in this chapter, high-speed video was taken of the vapor filled vortices to observe the full path of the vortices in one field of view, as depicted in Figure 5.1. The cavitating vortices undergo the Crow instability in a fashion very similar to when not cavitating as the instability is relatively insensitive to the radius of the vortices, thus allowing us to use this method to determine the overall flow pattern as well as determine the best locations to visualize the non-cavitating flow. High-speed visualization allows us to chart the large-scale behavior of the vortices over the whole test section as opposed to the limited extents of other measurement techniques. Indeed, the extent of the velocimetry volumes were small enough that the different conditions achieved by varying the secondary foil angle of attack could not be measured by the same volume. The measurement volume had to be moved in the vertical and spanwise directions to measure the different conditions. This motion of the vortices is smallest in the upstream region, when the two vortices are nearly parallel, but it is very large in the downstream region as the secondary vortex wraps around the primary vortex. High-speed cameras were used to obtain a view from the top as well as from the side, a mirror was placed on top of the test section and the cameras focused to look through the mirror down onto the vortices.

While the above high-speed videos offer a qualitative description of the dynamics of the vortex interaction as well as some quantitative information about mean locations and instability perturbation amplitudes, the properties of the vortices themselves cannot be estimated from these visualizations. Accordingly, volumetric velocimetry was used to measure the non-cavitating vortex properties at several locations downstream of the hydrofoils generating the vortices. The upstream volume is approximately 0.7 c downstream of the trailing edge of the primary foil, the midstream volume is approximately 1.2 c, and the downstream volume is approximately 1.7 c. Due to the small extents required to adequately interrogate the velocity fields of the vortices,

three different measurement volumes were used at each of these locations as the vortices were in different locations when changing between the different angles of attack for the several conditions studied. The variations in extents between the three regions used at each downstream location are small (typically less than 5%). The sizes of the different measurement volumes are reported in Table 5.1.

In the upstream region, discussed in Chapter 6, the vortex properties are measured as the vortices are finishing rolling up and while they are initially almost parallel. These properties serve as the initial conditions for the Crow instability that the vortices then undergo. The midstream region captures the linear stage of the instability, where the linear stability analysis for the Crow instability accurately describes the dynamics of the interaction and the instability gives the secondary a modest sinusoidal centerline displacement motion, as also described in Chapter 6. The downstream region measures the nonlinear stage of the interaction and is detailed in Chapter 7. In this area, the secondary is often oriented vertically as it wraps around the primary vortex. Additionally, the secondary tends to break up in this region before it goes on to form vortex rings. Due to this rather different geometry, with the secondary generally not parallel to the primary vortex, a much larger measurement volume must be used. The hardware used for these velocimetry measurements is described in Chapter 3. A schematic of this setup is shown in Figure 5.2. A cartoon of these measurement locations in relation to the vortex instability development is shown in Figure 5.3.

Experimental Test Conditions

With the two hydrofoils used to generate the secondary vortex and several angles of attack of the secondary studied, four foil arrangements are examined in detail. They are denoted by “M” or “N” for a matching or non-matching hydrofoil setup. A digit represents the negative

angle of attack of the secondary foil, and the four conditions are therefore denoted as N.0, N.2, N.4, M.4. Two of these, M.4 and N.4 which have the secondary at -4 degrees angle of attack, were examined over a range flow speeds to examine the effect of chord-based Reynolds number on the formation of the vortices, where

$$Re = \frac{U_0 c}{\nu}$$

where ν is the water's kinematic viscosity. The various conditions studied are listed in Table 5.2 and the reasonings behind the speeds for these conditions are detailed in the following paragraphs.

The cavitation number, σ, is defined as

$$\sigma = \frac{P_0 - P_{vap}}{\frac{1}{2}\rho U_0^2}$$

where P_0 is the far field pressure, P_{vap} is the vapor pressure of the water, and ρ is density. Excessive reduction of far field pressure can result in small amounts of atmospheric air being ingested into the test section, which is undesirable as the ingested air pollutes the tunnel's nuclei population. To keep freestream σ robust for inception measurements, it is therefore preferable to raise freestream velocity, and for cavitation experiments, the freestream speed is 10 m/s.

Obtaining single-phase velocimetry measurements at high flow speeds is physically infeasible for several reasons. First, to adequately track PIV particles in a flow with STB-PTV, they must not travel too far. In unidirectional flow or regions with low accelerations, the author has found that particles may move as much as 20 pixels between successive images and still track in the STB-PTV algorithm. However, in regions with high accelerations, like the cores of vortices, such large displacements make the particles impossible to track. Since measurement of

vortices is the goal here, we must ensure that we limit displacement of the particles to less than 10 pixels. In practice, an increase in the freestream velocity must be matched with an increase in the frame rate of the measurement to keep the displacements low. Similarly, magnifying the measurement domain to allow a higher seeding density and thus spatial resolution increased particle displacements and necessitates higher frame rate. This increased acquisition frequency can result in two main challenges due to hardware limitations in the light output of the laser and resolution of the cameras.

The first challenge is that the power output from the Laser at high speeds. The laser used, a Photonics DM-100, can produce 10 mJ pulses at 10 kHz, the maximum power output it can achieve. Beyond that frequency, the power output remains roughly constant (it declines slightly, but not much), so the energy per pulse drops proportionately. With less energy per pulse, the images dim, reducing the signal-to-noise ratio. Laser beam intensity profiles generally take a close to Gaussian shape, and when setting up the experiment, it is good practice to trim the laser light sheet with a physical aperture. Given that Gaussian intensity profile, this trimming trims off some area that is only dimly illuminated by the laser. Calling this intensity the "cutoff intensity", when we increase the frequency of the laser firing, we reduce the energy per laser pulse. In effect, as the peak intensity drops with this, the radius of the cutoff intensity decreases. Thus, when firing the laser faster, the images dim, and it generally is prudent to trim the illuminated volume down. In addition, the cameras used, Phantom v1212s, can take 1 Megapixel images at only 12.6 kHz. Going beyond this speed requires using only part of the camera sensor, necessitating a reduction in measured area.

Some preliminary experiments were done on the downstream interaction of the vortices at 10 m/s with the velocimetry system operating at 30 or 40 kHz on a region only 3 mm x 3 mm

x 6 mm, such a small volume necessitated due to the restrictions outlined above. This smaller measurement only intermittently captured a portion of the secondary vortex. The primary vortex never passed through that measurement volume. Thus, to measure the entirety of the interaction of the primary and the secondary vortices in the downstream region, a larger interrogation volume is necessary. This larger volume necessitates a lower acquisition frequency to obtain an acceptable illumination level which due to limits on STB-PTV tracking necessitates a lower freestream flow speed. Simultaneously, this larger volume necessitates a lower seeding density to maintain a comparable density of particles on the camera image sensors. This tradeoff cannot be reconciled for the higher flow speeds with the system we currently employ.

A second significant limitation of high-speed velocimetry measurements at high speeds is the particle seeding becomes adversely effected by the stronger vortical flow. An underlying assumption of STB-PTV is that the particles in the flow follow the flow and the particle density remains uniform. In practice, the particles used in this study have some slip velocity relative to the surrounding liquid flow, as discussed in detail in Chapter 3. As mentioned above, the particles in the core of the vortices begin to migrate away from the axis due to the long-lived interaction with the strong centrifugal forces they experience. The particle density in the vortex core is substantially reduced by the time the flow reached the interrogation region when the freestream velocity is 10 m/s as compared to when it is 3 m/s. Hence, detailed measurements were performed at the lower speed and the properties of the vortices at the higher speeds (inception experimental conditions) were inferred using Re scaling.

In the upstream region, where the vortices are close to parallel and the amplitude of the instability is minimal, the measurements were taken from for $U_0 = 1$ to 10 m/s. At this upstream location, there has not been much time for particle slip to cause loss of seeding in the vortex

cores. Also, since the vortices are initially almost parallel, vortex parameters can be measured with measurements of a thin volume (4 mm thick) with the vortex axes cut by this almost planar measurement. With this reduced extent, the laser light sheet does not need to expand as much as for a larger extent, so the energy per pulse per cross sectional area is higher. This means that although the energy per pulse is lower when firing the laser above 10 kHz, it can still be bright enough to take measurements given the reduced illumination volume. As the vortices upstream occupy a relatively small extent compared to downstream, less camera sensor area is needed, so the cameras can acquire images faster than their nominal 12.6 kHz maximum (which is at full Megapixel resolution). Altogether, reduced effects of particle slip, the higher energy intensity of the laser pulse and the reduced extents needing to be measured mean that the upstream region can be measured from inflow velocity range of 1 to 10 m/s while the midstream and downstream regions cannot. *Therefore, the upstream measurements are used to inform the scaling of the downstream measurements and relate the single-phase velocimetry measurements taken at 3 m/s to the cavitation observations taken at 10 m/s.*

Cavitation Visualization of Vortical Interaction

While STB is used to obtain detailed measurements of the vortex interaction, it is helpful to use developed cavitation to see the vortices undergo their interaction. This visualization allows us to note the salient features of the interaction and their evolution as the flow runs downstream.

Figure 5.4 shows Case N.0, with the non-matched secondary foil at zero degrees angle of attack, which has the strongest secondary vortex considered throughout this study. Notably, the radius of the cavitating secondary in Case N.0 is almost comparable to that of the cavitating primary in Case N.0. The secondary has a lower circulation than the primary, so it is a weaker

vortex, but it also has a smaller radius, such that the pressure in its core ends up comparable to that of the primary. Note also that both the vortices convect downwards. Additionally, thin strands of cavitating vortices wrap around both vortices, even very near the foils generating the larger vortices. These strands are not from the secondary vortex but should be considered tertiary vorticity. As the diameter of these strands is small relative to the primary and secondary vortices, these tertiary vortices have a much weaker pressure drop than even the secondary vortex. Since the primary and secondary vortices are roughly anti-parallel and relatively far apart in the upstream region, these tertiary structures cannot be vorticity bridging (as would occur between a pair of co-rotating vortices when their separation, b, is close to the combined radii of the vortices). Instead, it is likely that these result from the rolling up flow between the tips of the hydrofoils.

Figure 5.5 presents several views of Case N.2, with the non-matched secondary foil at -2 degrees angle of attack. The radius of the cavitating secondary is now smaller than the radius of the cavitating primary. Also, the vortices do not convect downward quite so quickly. A fascinating aspect of this case, demonstrated in Figure 5.6, is the local suppression of cavitation in the primary vortex as the secondary vortex draws near it. This suppression of cavitation occurs regularly as portions of the secondary wraps around the primary and the secondary starts to break into vortex rings, as originally noted in Knister *et al*. (2020). While the mechanism is not immediately clear from cavitation alone, in effect, the secondary is straining out the primary vortex, which we will show with STB measurements in Chapter 7.

As the primary vortex experiences the effects of the strain field of the secondary, it loses its circular shape and forms an initially elliptical cross section that eventually starts to curve around the secondary. Within this curved cross section, the primary typically has two patches of

concentrated vorticity, above and below the secondary vortex, connected by a weaker, curved section of vorticity. This upper region persists in cavitation longer than the lower region. It is brought vertically upward substantially and while the interaction cannot be measured in finest detail, as the separation of this upper patch from the secondary drops to zero, some vorticity cancelation likely happens. Simultaneously, spanwise oriented vortical structures are observed. It appears as if this upper portion of the primary vortex is peeled off and turned spanwise, joining the secondary as it breaks apart, though this cannot be shown conclusively with our measurements due to their limited extent and resolution. Farther downstream, with the secondary now broken apart and portions of it oriented spanwise, the secondary moves to reconnect as vortex rings, which then propagate upward due to their own self-induction. When the lower portion of the primary starts to cavitate again after suppression, it is weaker and does not persist.

This straining out of the primary vortex in Case N.2 comports with what was noted by Marshall *et al*. (2002) in Case E of their computations. They considered pairs of unequal strength, counter-rotating vortices with varying circulation ratios. Case E was the only case they considered that also had a smaller core radius in the secondary vortex. In Case E, they noted a straining of the primary akin to what we note here, which they attributed to the higher peak vorticity in the core of the secondary vortex leading to the weaker vortex not straining out as much. Due to the smaller core radii of the secondary vortices in our study, the peak vorticities of the secondary are about equal to or higher than the peak vorticities in the primary vortices in all cases. Simultaneous to this straining out of the primary, the secondary vortex starts to break apart, and it will eventually form vortex rings, those these are not completely formed and visible with cavitation in the length of the test section.

Figure 5.7 considers Case N.4, with the non-matched secondary foil at -4 degrees angle of attack. The cavitating secondary is now of a much smaller radius than that of the primary due to its rather weaker circulation strength. Also, the secondary vortex generally wraps around the primary vortex rather than convecting downward together with the primary vortex again due to its substantially weaker circulation. Figure 5.8 shows Case M.4, with the matched secondary foil at -4 degrees angle of attack. As in Case N.4, the secondary vortex is much weaker than the primary vortex, so the cavitating radius of the primary vortex is much larger than that of the secondary, and the primary vortex does not convect downward much. In these cases, as in Case N.2, there appears to be some amount of cross-axis staining in the primary as the secondary wraps around it. This does not appear to occur in Cases N.4 and M.4 to the same extent that it does in Case N.2. In Cases N.2 and N.4, the primary vortex does not undergo such cavitation suppression as in Case N.2, but it does appear to take a somewhat elongated or stretched form as opposed to a strictly circular cross section.

Several other conditions, with higher angles of attack for the non-matched secondary foil, were briefly considered, as shown in Figures 5.9 and 5.10. Here, the non-matched secondary foil is set to positive 2 and 4 degrees (denoted as Cases N.P2 and N.P4). In these cases, the wrapping up of the vortices interfere substantially with each other, and the vortices do not form downstream of the foils as in cases with negative angles of attack. Due to this, these cases were not considered in the rest of the study, but it is worth noting the behavior of the system over a range of angles of attack. Similarly, setting the non-matching secondary foil to -5 degrees angle of attack lead to such a weak secondary vortex that it could not easily be visualized. Given the relatively short length of the test section, of necessity the foils were placed very near to each other. If more streamwise extent was allowed for the vortex instability to develop and still be

measured, the foils could be moved farther apart and a positive angle of attack for the secondary foil could lead to cleanly forming vortices that then undergo the Crow instability.

The cavitation visualization allows us to note some of the critical features of the vortex interaction with very little experimental cost. A major advantage of the use of high-speed video on the developed cavitation is that the streamwise development of the instability considered can be observed all in the same measurement with two cameras side by side, as in Figure 5.1. This contrasts with the limited measurement domains possible with velocimetry as noted in Table 5.1. Using high-speed videos, calibrated with measurements of distance without the vortices, it is possible to determine the average vertical and spanwise location of both vortices as a function of downstream distance, as shown in Figures 5.11 through 5.13. The data presented here comes from the average of camera recordings over thousands of frames, with the same field of view as the above. These figures display the different rates of relative motion of the vortices. In Case N.0, both vortices are substantially deflected due to their mutual induction and combined rotation. In contrast, Case N.4 shows that only the secondary vortex deflects substantially as it is too weak to shift the primary as much as the primary shifts it.

Discussion

This study examines that Crow instability development over a range of circulation ratios. In one case, N.0, noticeable tertiary vortices wrap around the pair of counter-rotating vortices. To our knowledge, prior studies of the Crow instability have not encountered these structures. Likely they result from the close proximity of the two hydrofoils and the influence they have on each other's roll-up of vorticity.

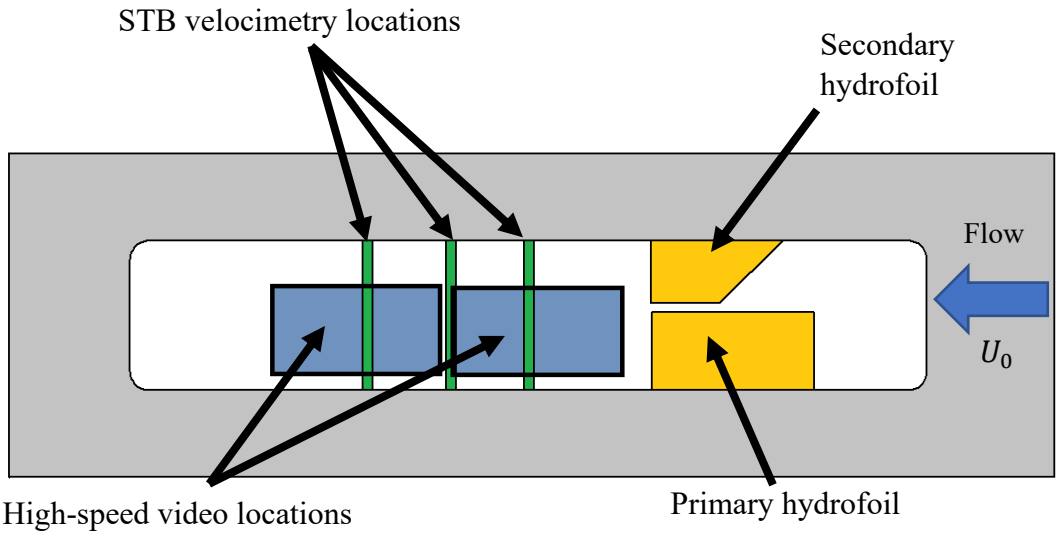


Figure 5.1 Schematic of Test Geometry. A side view of the water channel as used in these experiments. The section in the middle represents the view through the side window. The tunnel extends more vertically above and below, but the corner chamfers occlude viewing these areas. With the flow from right to left (with freestream velocity, U_0), the hydrofoils generate the vortices studied. The top hydrofoil is used to generate the secondary vortex. Shown here is the non-matching hydrofoil, but a hydrofoil that matches the primary hydrofoil (bottom) is also used. The angle of attack of the secondary hydrofoil is swept from -4 to 0 degrees angle of attack. Downstream of the hydrofoils, high-speed video is taken in the regions outlined with blue boxes and used for visualization of developed cavitation as well as observation of incipient cavitation. The STB velocimetry is done at three streamwise locations. The laser comes from below and is shown in green as the laser is 532 nm, but the thicknesses of the illumination volumes have been increased to make the figure more readable.

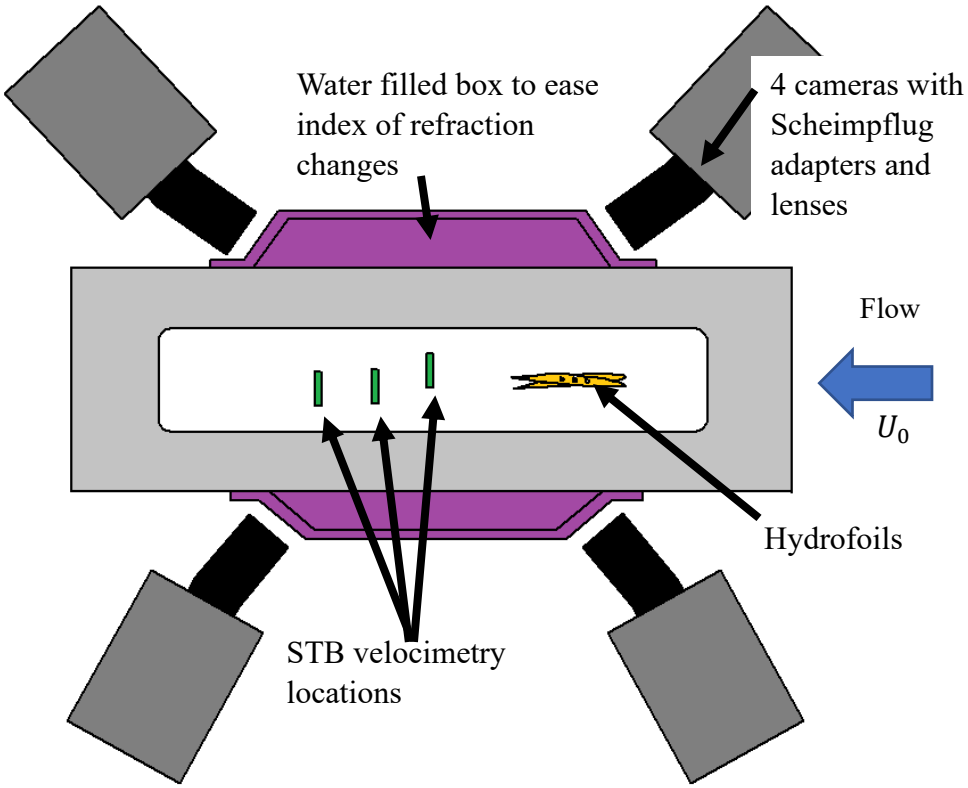


Figure 5.2 Schematic of Test Geometry. The layout of the water channel as set up for volumetric velocimetry measurements and viewed from above. The brass hydrofoils are in orange on the right. Note that the top foil is at a negative angle of attack. The green regions downstream of the foils are the locations of the illuminated volumes for velocimetry. The light purple structures outside the test section are water filled boxes to allow the cameras to interrogate the flow from non-orthogonal views. The four cameras surround the tunnel, with Scheimpflug adapters in place to allow the full illuminated volume to be in focus.

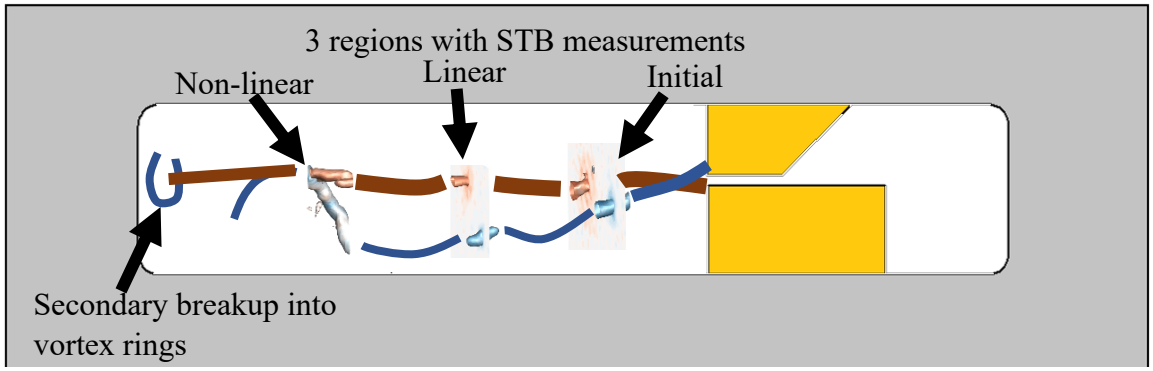
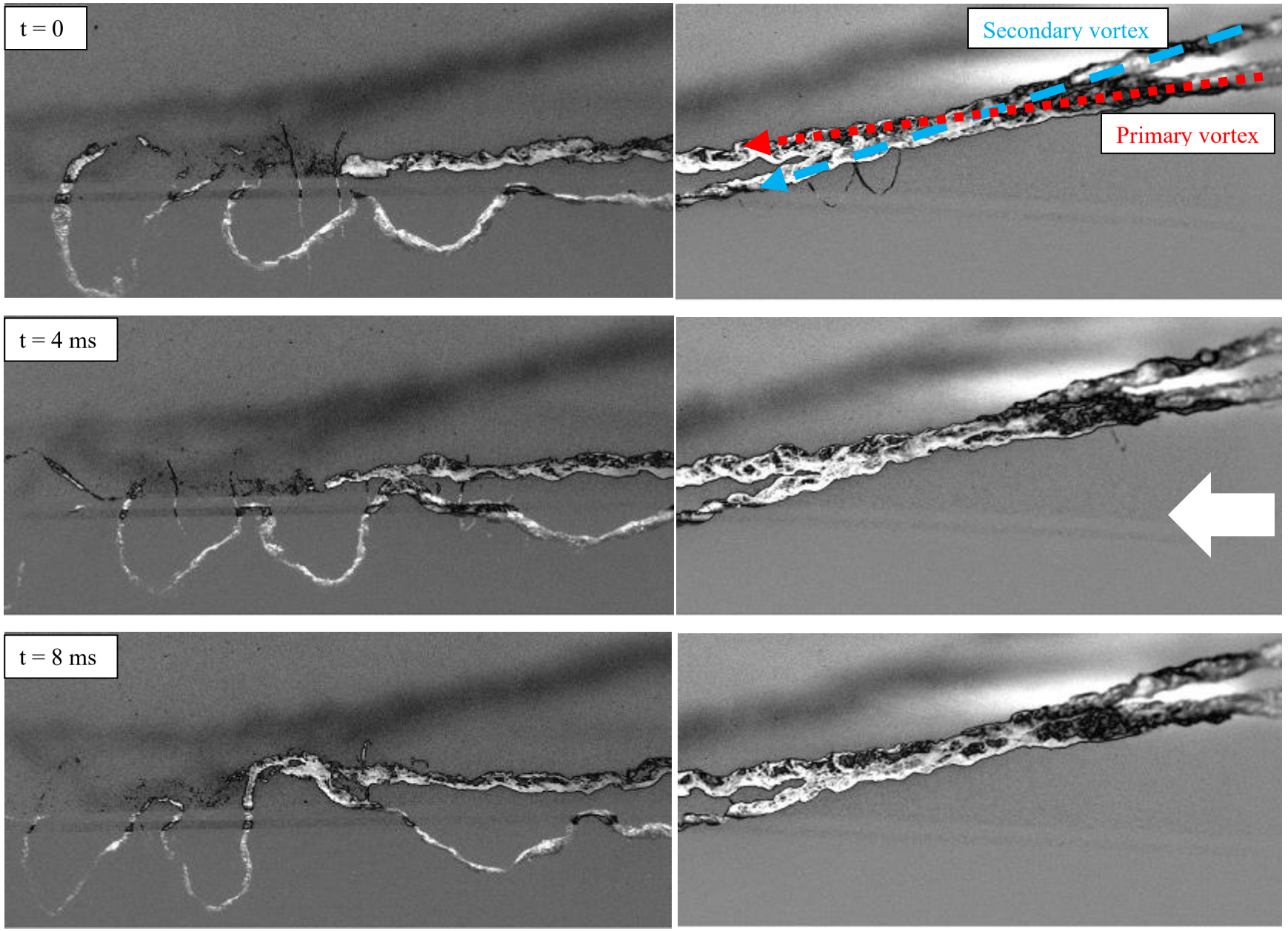


Figure 5.3 Cartoon of Vortex Interaction. A cartoon of the development of the vortex instability studied here. An upstream measurement (0.7 *c*, where *c* is foil chord) is taken for the "initial conditions" of the instability. A midstream measurement is taken in the linear regime of the instability (1.2 *c*). Finally, a measurement is taken in the non-linear regime (1.7 *c* downstream). After this, the secondary breaks up into vortex rings.


t = 0
Secondary vortex
Primary vortex
t = 4 ms
t = 8 ms

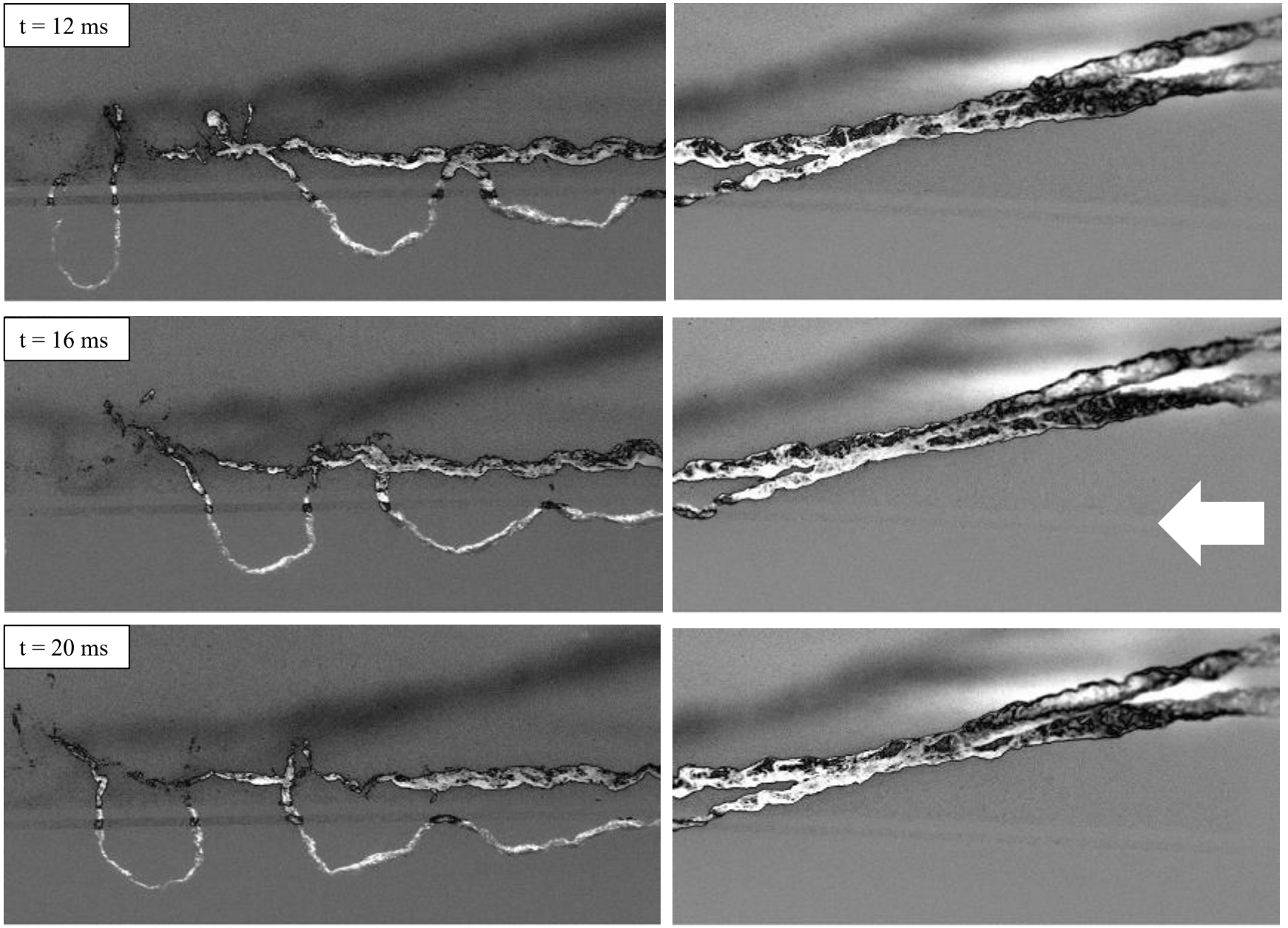
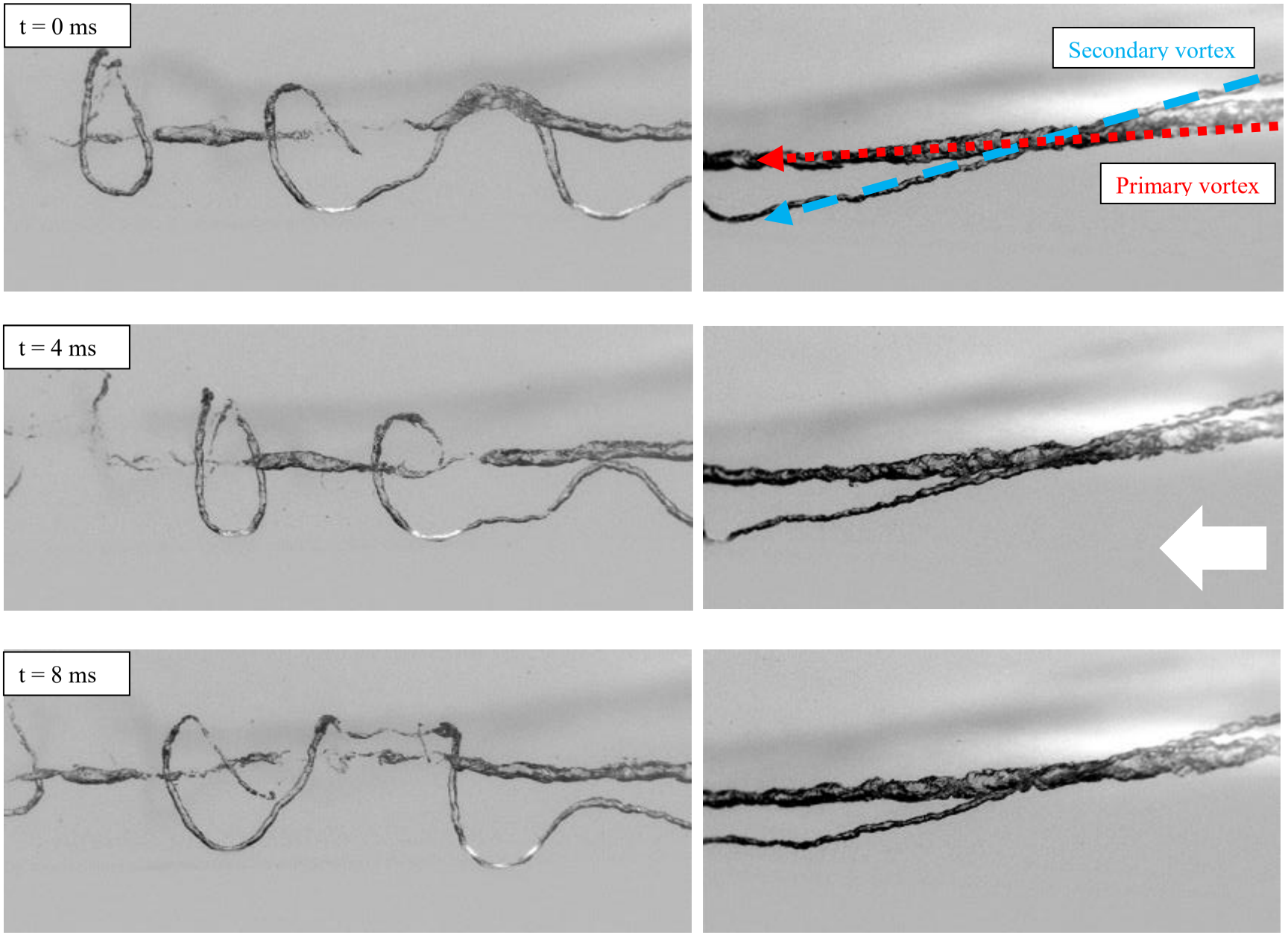

t = 12 ms
t = 16 ms
t = 20 ms

Figure 5.4 Cavitation Visualization of Case N.0. (Preceding pages) Developed cavitation in the vortices in Case N.0 is used to visualize the path of the vortices and their downstream evolution. The flow direction is from right to left, as denoted by the white arrow. The right and left columns of images are from the two cameras. The images are synchronous in time and several time instances are shown, but the fields of view of the cameras do not quite overlap. While the secondary vortex is initially above the primary vortex (right side), it orbits the stronger vortex and ends up below it. Note that both vortices convect downward substantially due to their respective actions on each other, but the secondary vortex does end up lower. While the vortices are both initially close to linear, the secondary vortex develops a sinuous instability and wraps around the primary vortex. In this process, the secondary begins to break apart to form vortex rings and the primary also often breaks down as a vortex. By design, the secondary vortex has a lower circulation than the primary vortex (i.e. it is a weaker vortex), but note that both vortices appear to have comparable diameters when cavitating here. The edge of the cavitating vortices can be assumed to be at the vapor pressure of the water, so the edges of the vortices indicate the distance from their centers where pressure is equal to vapor pressure. Given the lower circulation of the secondary and noting that pressure, $P \sim \Gamma^2 / r_c^2$ (where Γ is vortex circulation and r_c is vortex core radius), this shows that the smaller core size of the secondary leads to pressures in the secondary vortex that are comparable to the pressures in the primary vortex in the upstream region before the secondary vortex is substantially stretched. Note also the presence of "tertiary" vortical structures wrapping around both vortices together.


t = 0 ms
Secondary vortex
Primary vortex
t = 4 ms
t = 8 ms

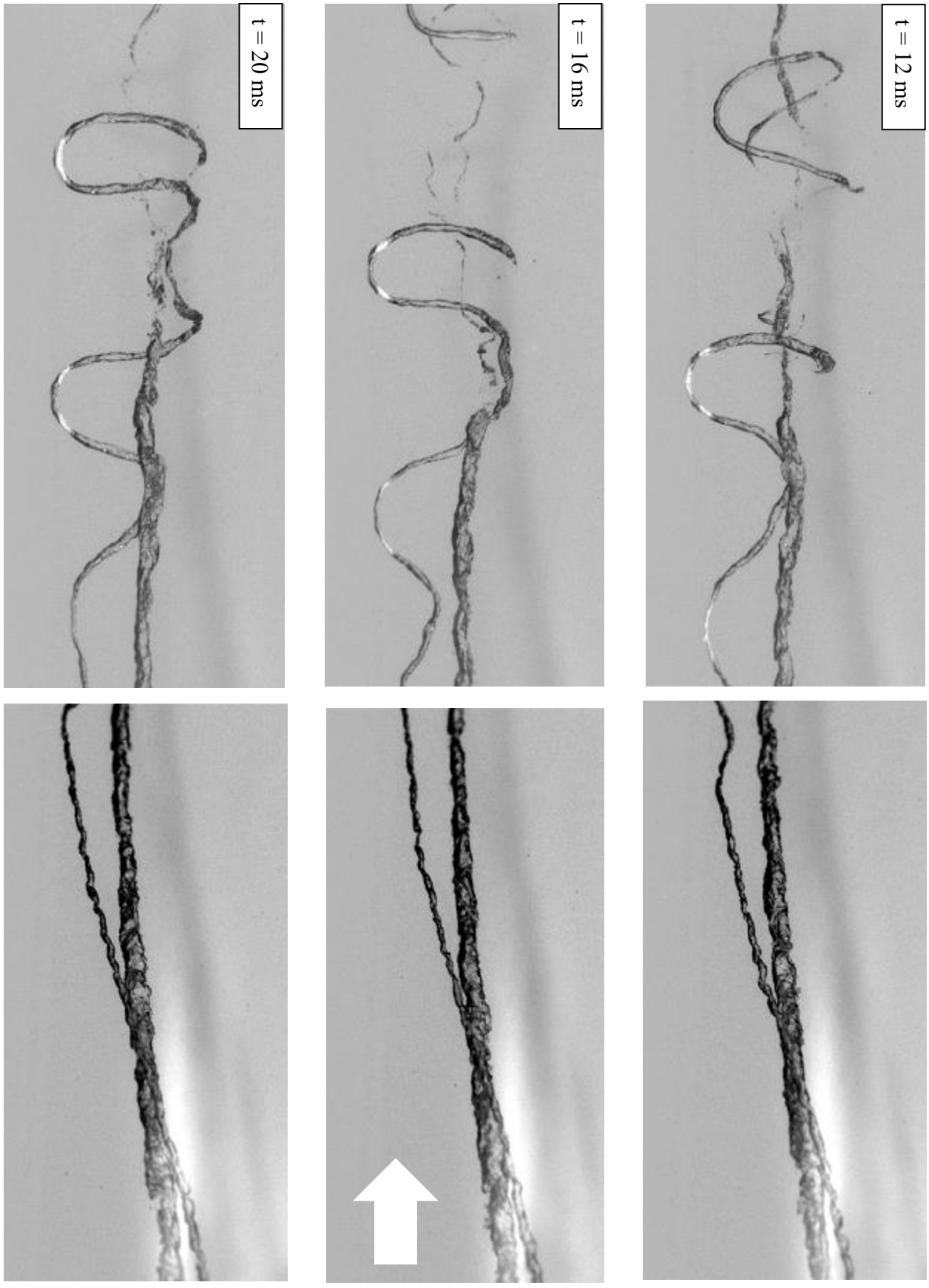

t = 12 ms
t = 16 ms
t = 20 ms

Figure 5.5 Cavitation Visualization of Case N.2. (Preceding pages) Developed cavitation in the vortices in Case N.2 is used to visualize the path of the vortices and their downstream evolution. The flow direction is from right to left, as denoted by the white arrow. The right (upstream) and left (downstream) columns of images are from the two cameras. The images are synchronous in time and several time instances are shown, but the fields of view of the cameras do not quite overlap. While the secondary vortex is initially above the primary vortex, it orbits the stronger vortex and ends up below it. While both vortices convect downward due to their respective actions on each other the primary vortex does not convect downward as much as the secondary vortex in this case nor as much as the primary vortex in Case N.0. This is due to the secondary vortex in Case N.2 being weaker relative to the primary than in Case N.0. While the vortices are both initially close to linear, the secondary vortex develops a sinuous instability and wraps around the primary vortex. In this process, the secondary begins to break apart to form vortex rings. The primary sometimes also breaks down as a vortex. By design, the secondary vortex has a lower circulation than the primary vortex (i.e. it is the weaker vortex), and correspondingly, the secondary has a smaller diameter than the primary when cavitating here.

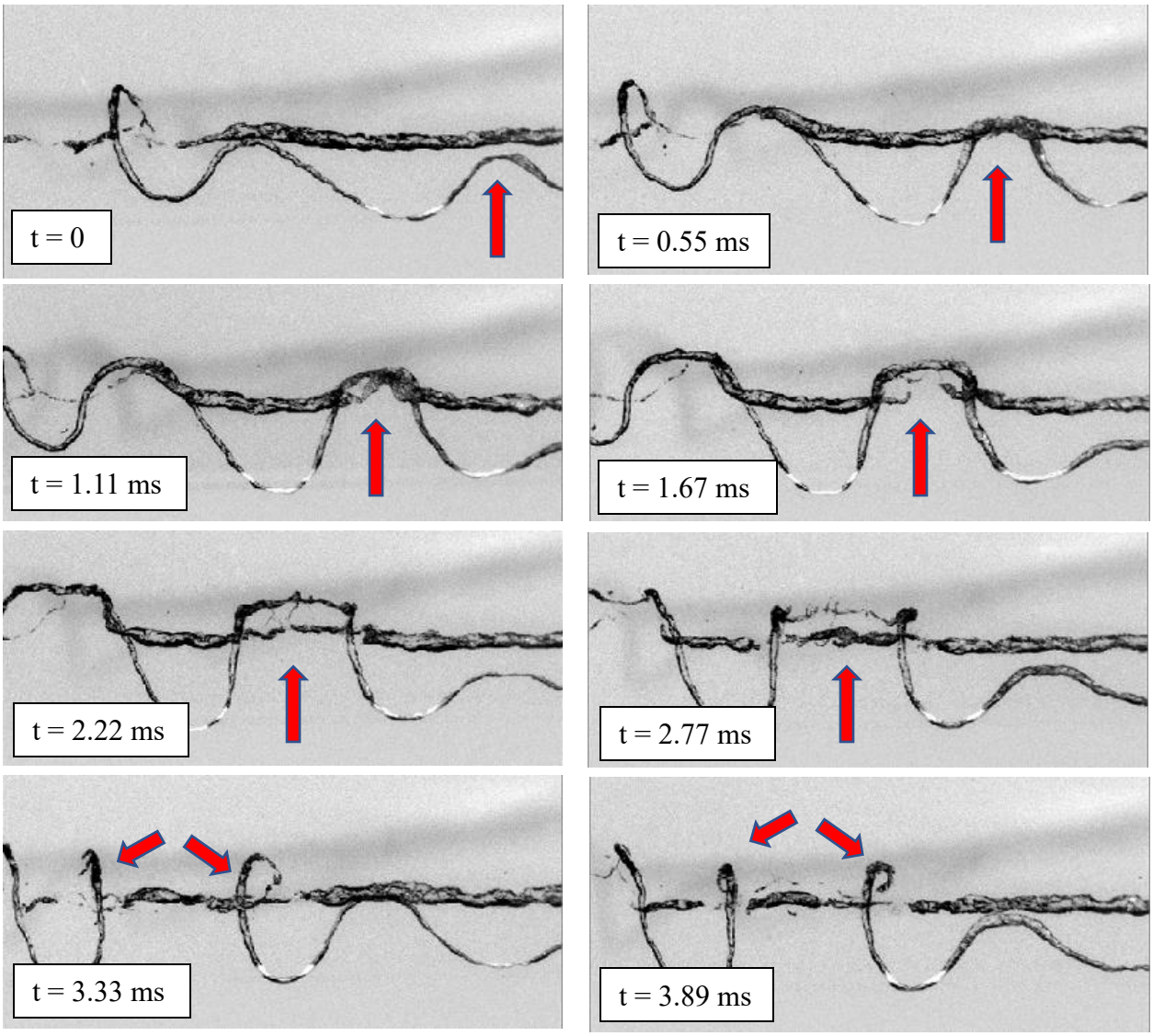
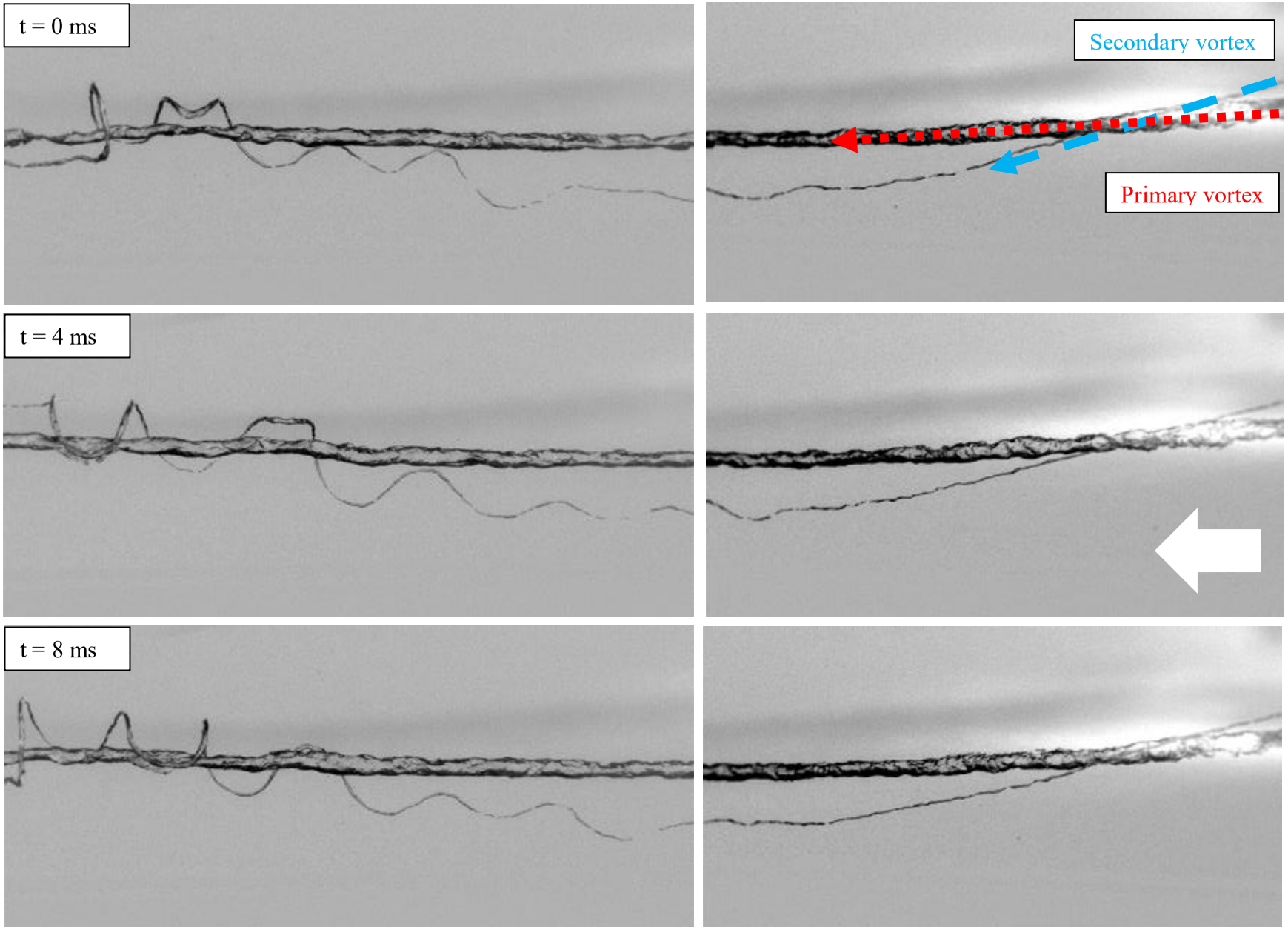


Figure 5.6 Cavitation Suppression in Case N.2. Developed cavitation in the vortices in Case N.2 is used to visualize how the secondary vortex can lead to temporary suppression of cavitation in the primary vortex. The above is a time sequence of images, with the time noted in the lower left of each image. The red arrows denote the structure described in this caption. Initially, a perturbed portion of the secondary vortex is drawn up by the primary vortex. While not visible from this view, the secondary is also moving towards the vortex out of the plane of the page. At t = 1.11 ms, it is near enough to the primary vortex that it causes significant straining in the primary vortex, resulting in elliptical streamlines within the primary vortex. Note that the portion of the primary vortex nearest the secondary at this point is drawn upwards. The strain in the vertical direction is enough that at t = 1.67 ms, cavitation is suppressed in the primary vortex. Some vertically oriented strands of vorticity run between the secondary and the remnants of the primary vortices. A weakened portion at the base of the primary vortex draws together and cavitates at t = 2.22 ms. As this happens, the secondary breaks apart and by t = 3.33 ms, the relevant portion of the secondary is folding away from itself to eventually form vortex rings with neighboring peaks in the secondary.


t = 0 ms
Secondary vortex
Primary vortex
t = 4 ms
t = 8 ms

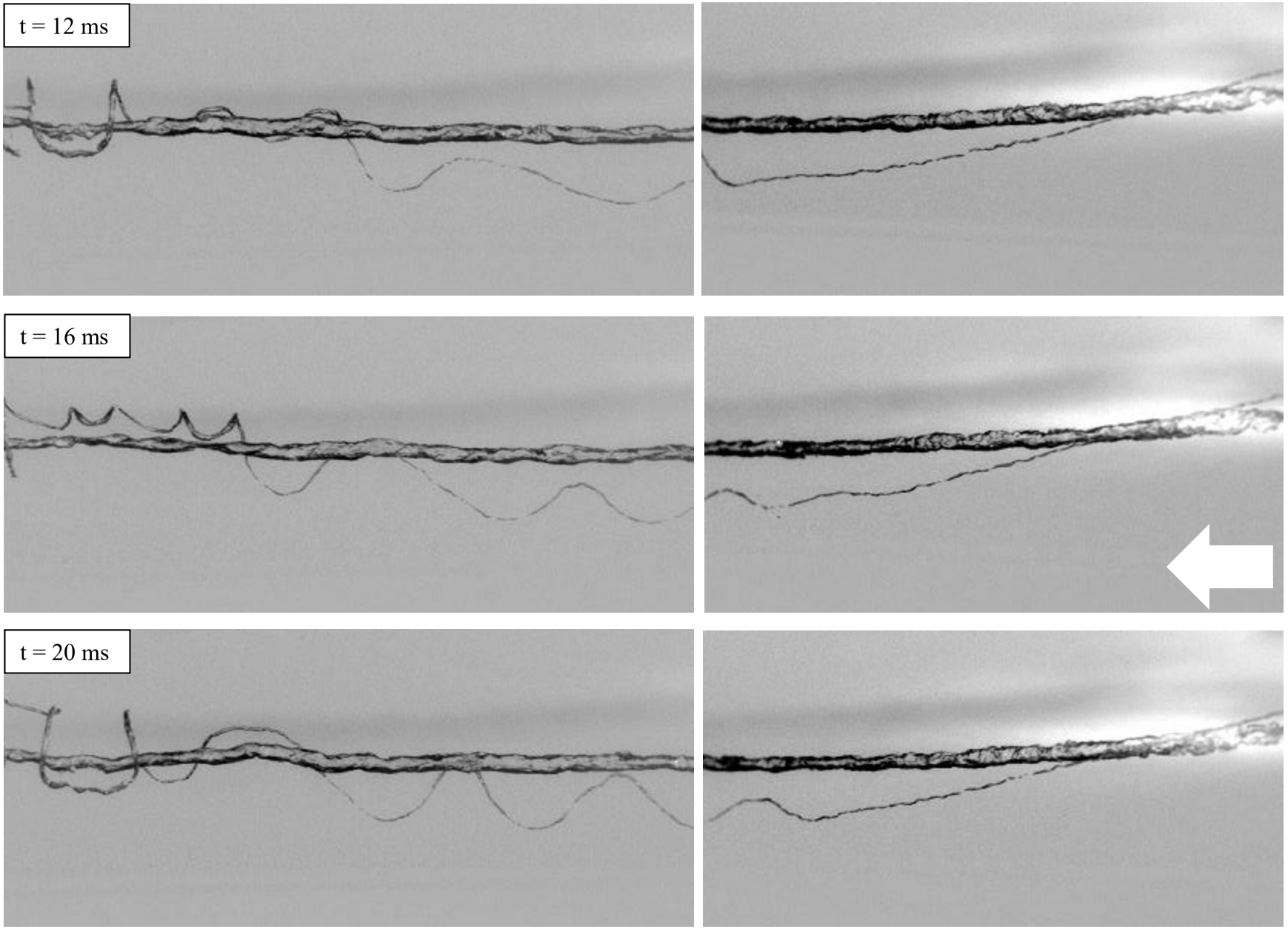
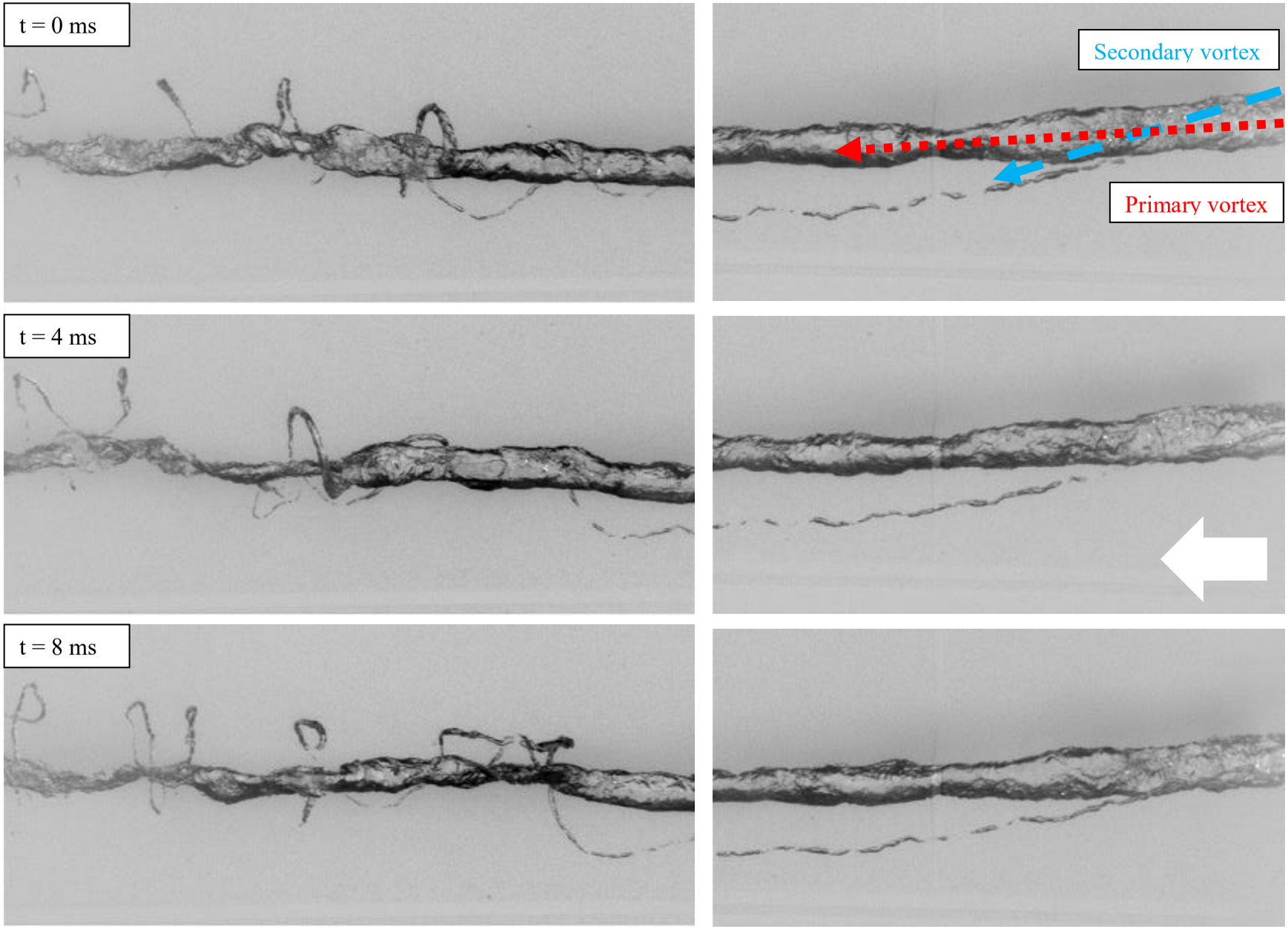

t = 12 ms
t = 16 ms
t = 20 ms

Figure 5.7 Cavitation Visualization of Case N.4. (Preceding pages) Developed cavitation in the vortices in Case N.4 is used to visualize the path of the vortices and their downstream evolution. The flow direction is from right to left, as denoted by the white arrow. The right (upstream) and left (downstream) columns of images are from the two cameras. The images are synchronous in time and several time instances are shown, but the fields of view of the cameras do not quite overlap. While the secondary vortex is initially above the primary vortex, it orbits the stronger vortex and ends up below it. While both vortices convect downward due to their respective actions on each other the primary vortex does not convect downward as much as the secondary vortex in this case nor as much as the primary vortex in Case N.0. This is due to the secondary vortex in Case N.2 being weaker relative to the primary than in Case N.0. While the vortices are both initially close to linear, the secondary vortex develops a sinuous instability and wraps around the primary vortex. In this process, the secondary begins to break apart to form vortex rings. The primary sometimes also breaks down as a vortex. By design, the secondary vortex has a lower circulation than the primary vortex (i.e. it is the weaker vortex), and correspondingly, the secondary has a smaller diameter than the primary when cavitating here.


t = 0 ms
Secondary vortex
Primary vortex
t = 4 ms
t = 8 ms

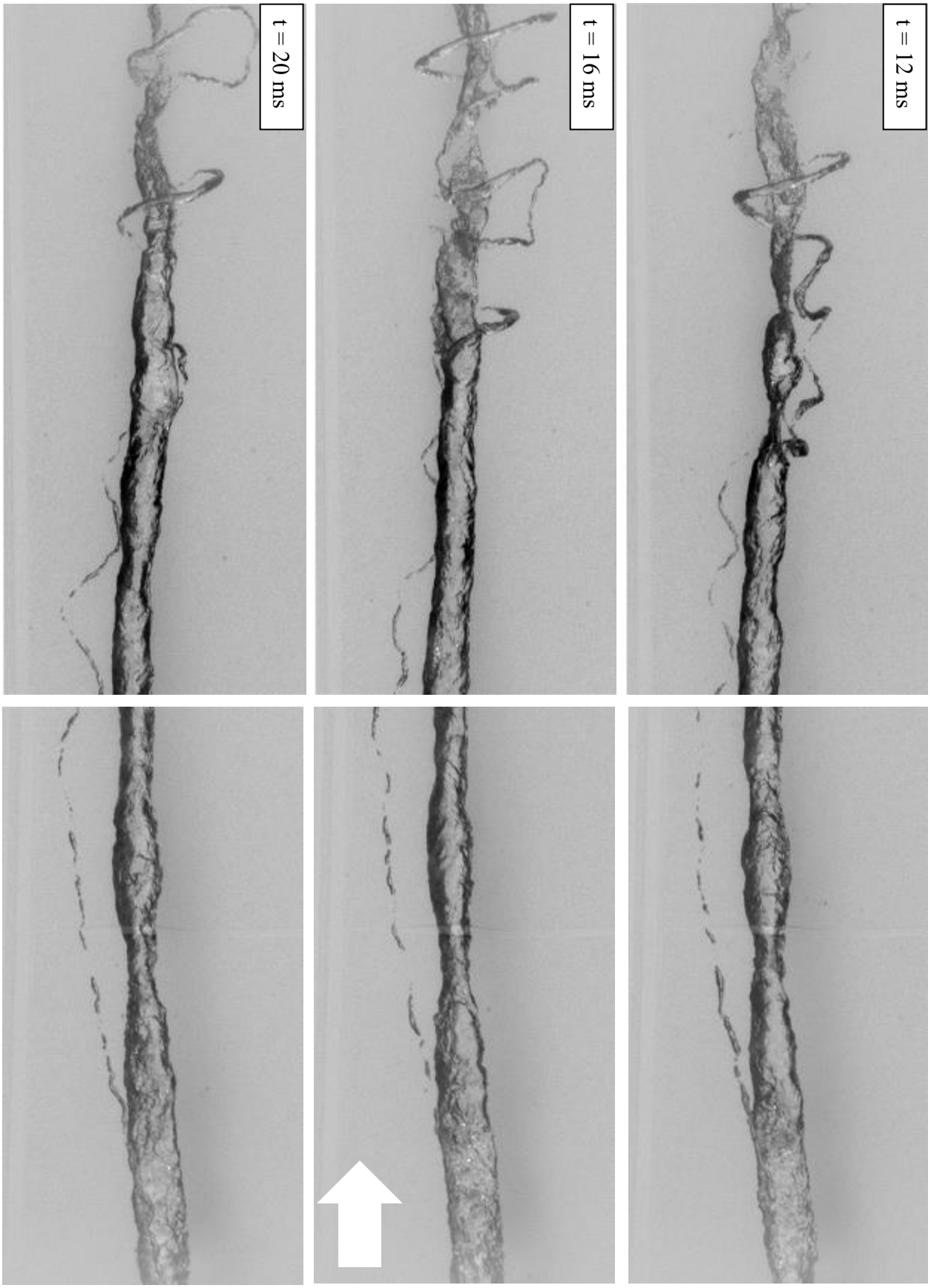

t = 12 ms
t = 16 ms
t = 20 ms

Figure 5.8 Cavitation Visualization of Case M.4. (Preceding pages) Developed cavitation in the vortices in Case M.4 is used to visualize the path of the vortices and their downstream evolution. The flow direction is from right to left, as denoted by the white arrow. The right (upstream) and left (downstream) columns of images are from the two cameras. The images are synchronous in time and several time instances are shown, but the fields of view of the cameras do not quite overlap. While the secondary vortex is initially above the primary vortex, it orbits the stronger vortex and ends up below it. While both vortices convect downward due to their respective actions on each other the primary vortex does not convect downward as much as the secondary vortex in this case nor as much as the primary vortex in Case N.0. This is due to the secondary vortex in Case N.2 being weaker relative to the primary than in Case N.0. While the vortices are both initially close to linear, the secondary vortex develops a sinuous instability and wraps around the primary vortex. In this process, the secondary begins to break apart to form vortex rings. The primary sometimes also breaks down as a vortex. By design, the secondary vortex has a lower circulation than the primary vortex (i.e. it is the weaker vortex), and correspondingly, the secondary has a smaller diameter than the primary when cavitating here.

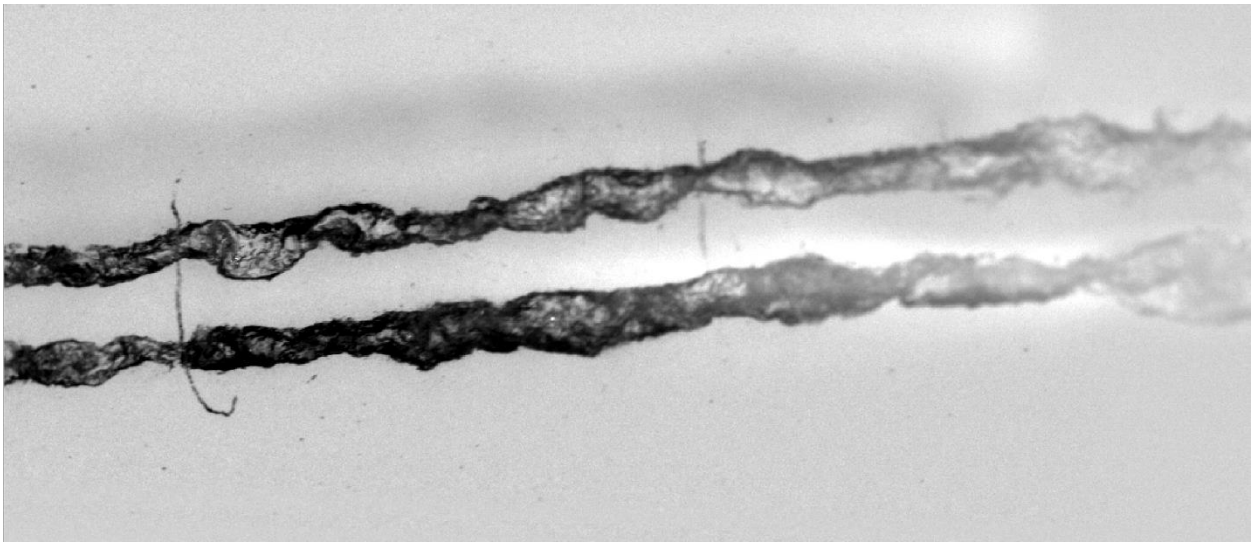


Figure 5.9 Cavitation Visualization of Case N.P2. Developed cavitation in the vortices when the non-matched secondary is set to positive 2 degrees (N.P2). In this case, the secondary is strong enough that the primary does not substantially undergo the Crow instability. The secondary here does not orbit the primary vortex. It starts above the primary vortex and stays above the primary vortex. This demonstrates that having the secondary set beyond zero degrees angle of attack does not give a case that can be studied here.

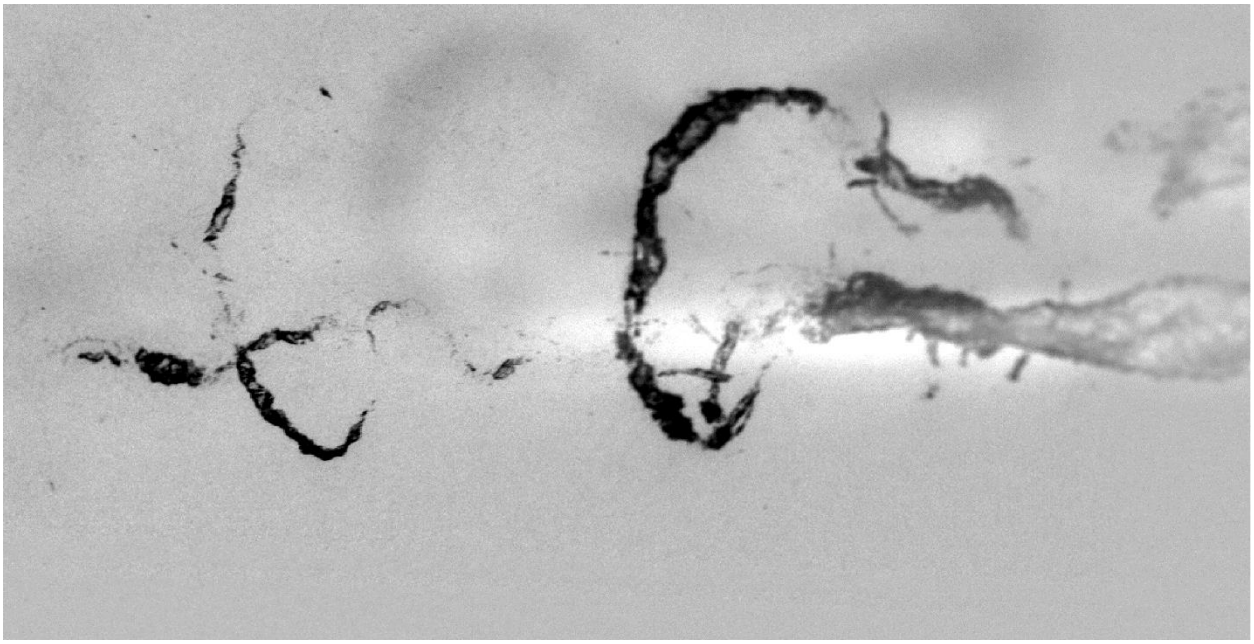


Figure 5.10 Cavitation Visualization of Case N.P4. Developed cavitation is used to visualize the vortices when the non-matched secondary is set to positive 4 degrees (N.P4). In this case, the vortices do not roll up coherently very well at all. The vertically oriented "tertiary" structures now cavitate to a comparable degree as what the primary and secondary vortices would.

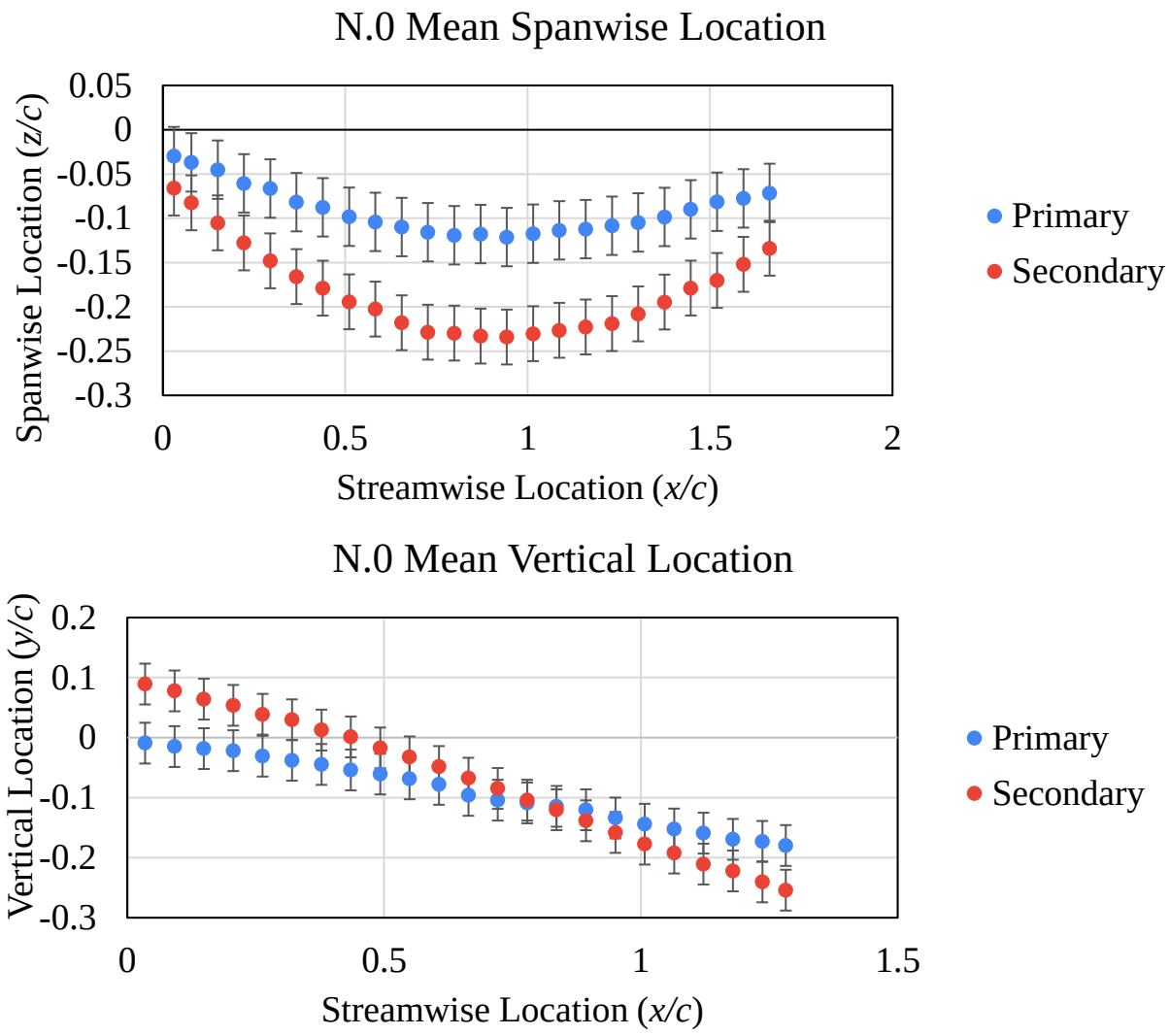


Figure 5.11 Location of Case N.0. Using the high-speed video of developed cavitation as shown in Figure 5.4, the mean locations of the vortices in Case N.0 can be found (scaled by foil chord, *c*). Note the relatively small deflections of the vortices as well as that the deflections of both vortices are comparable, although the secondary deflects somewhat more than the primary. The uncertainty primarily comes from the blurred width of the vortices in the mean.

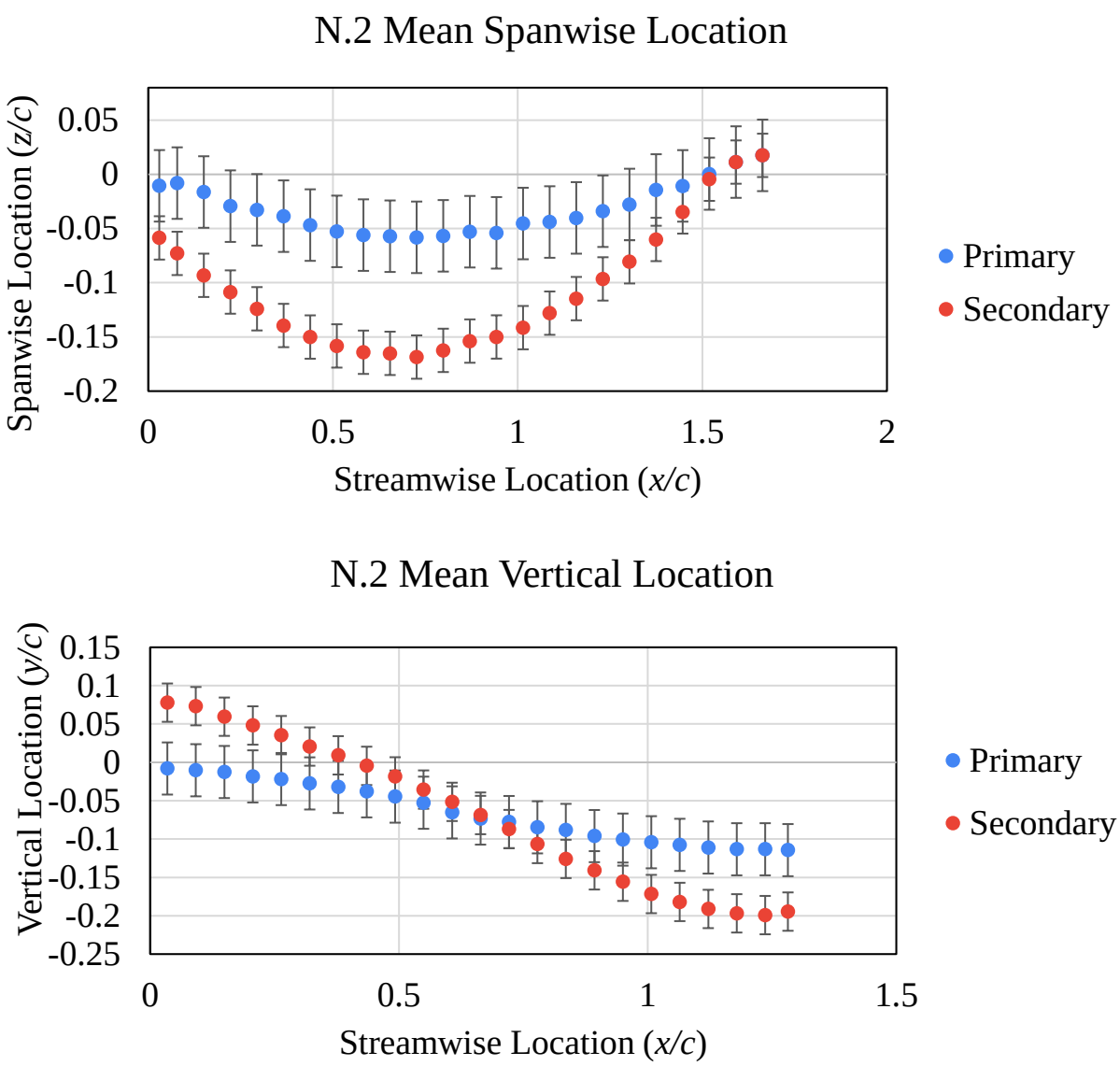


Figure 5.12 Location of Case N.2. Using the high-speed video of developed cavitation as shown in Figure 5.5, the mean locations of the vortices in Case N.2 can be found (scaled by foil chord, *c*). Note the larger deflections of the vortices then in Case N.0. Also note that the deflection of the secondary vortex is larger than that of the primary. The uncertainty primarily comes from the blurred width of the vortices in the mean.

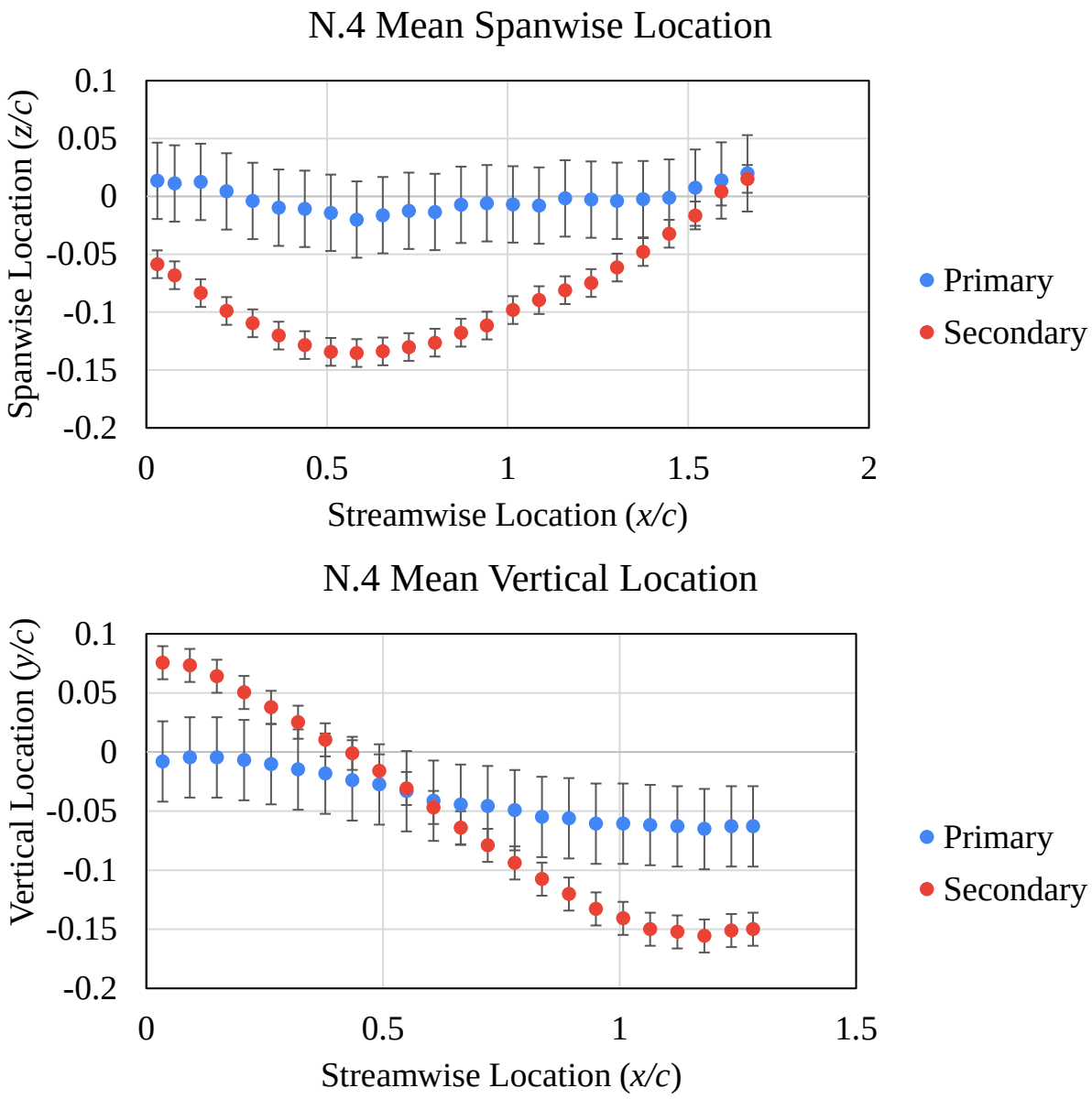


Figure 5.13 Location of Case N.4. Using the high-speed video of developed cavitation as shown in Figure 5.7, the mean locations of the vortices in Case N.4 can be found (scaled by foil chord, *c*). Note the larger deflections of the vortices then in Case N.0 and Case N.2. Also note that the deflection of the primary vortex is small compared to that of the secondary. The uncertainty primarily comes from the blurred width of the vortices in the mean.

Measurement Location	**0.7 *c*** **Upstream**	**1.2 *c*** **Midstream**	**1.7 *c*** **Downstream**
Streamwise Extent	4 (mm)	5 (mm)	7 (mm)
Spanwise Extent	38 (mm)	35 (mm)	55 (mm)
Vertical Extent	40 (mm)	40 (mm)	45 (mm)

Table 5.1 Location and Extent of Measurement Domains. The extents of the volumetric velocimetry measurement volumes at the three measurement locations (scaled by foil chord, *c*) are given here. Note that at each streamwise location, 3 separate volumes had to be set up to adequately measure the vortices as they shifted positions between different cases, but the differences in extent of those different volumes are minimal.

Case	Secondary Hydrofoil	Secondary Angle of Attack	Upstream Speed U_0 (m/s)	Midstream Speed U_0 (m/s)	Downstream Speed U_0 (m/s)
N.0	Non-matching	0	3	3	3
N.2	Non-matching	-2	3	3	3
N.4	Non-matching	-4	1, 3, 5, 7, 10	3	3
M.4	Matching	-4	1, 3, 5, 7, 10	3	3

Table 5.2 Configurations of Geometry for Different Cases. The various conditions with different foils and different angles of attack are listed here along with the freestream speeds at which they were measured.

Chapter VI

Linear Instability of Counter Rotating Vortex Pairs

Vortex Properties Upstream of Interaction

Approximately 0.7 chord lengths downstream of the trailing edge of the primary foil, the two vortices are close to completing their roll up and their axes are nearly parallel. Thus, a relatively thin volume can be used to cut through their axes and measure their properties to characterize the initial conditions of the vortex pair and the development of the Crow instability. For the non-matching foil cases, data was taken from a sweep over angles of attack of the secondary foil at a fixed speed and a sweep over speeds at fixed angle of attack. For the matched foil case, data was taken over a sweep of speeds for a fixed angle of attack. As noted above, the vortices take substantially different paths between the different conditions, so the different cases each required their own location of the measurement volumes, though the dimensions of the different measurement volumes are within a few percent of each other. Accordingly, relevant parameters such circulation, core radius, axial velocity, eccentricity, and peak vorticity were measured.

Calculations of the initial vortex properties are performed on individual velocity fields, on a plane oriented with its normal vector parallel to the local vortex axis. The computed properties from each field are then averaged. Circulation is estimated from the vorticity field, derived from the measured velocity field and integrated (considering only vorticity greater than a given threshold),

$$\Gamma = \int \omega(\omega > \omega_{threshold})\, dA.$$

This integral was performed for each vortex since the vortices have opposite sign. The threshold was 10% of the peak vorticity. An additional constraint was that the region had to be contiguous, as identified with Matlab's *bwareafilt* function. With the circulation known, the vortex centers were then calculated as

$$\boldsymbol{l}_{vortex} = \frac{1}{\Gamma}\int \boldsymbol{l}\omega dA$$

Here we consider only the region where the vorticity exceeded the threshold from above. The variable $\boldsymbol{l}$ is the *y*-, *z*- coordinate of the vortex center. With the two centers known, the separation distance between them, *b*, is found. The core radius of the vortices r_c is found by

$$r_{c,p\ or\ s}^2 = \frac{1}{\Gamma_i}\int |\boldsymbol{l} - \boldsymbol{l}_{vortex}|^2 \omega\, dA$$

where the index, *p* or *s*, is for either primary or secondary vortices. The axial velocities in the vortex cores (i.e. the region of vorticity above the threshold above) were also determined and the maximal velocity was recorded. Area moments of the identified vortex regions in the vorticity field were calculated as

$$\phi_{fg} = \int (y - \bar{y})^f (z - \bar{z})^g \omega(y, z) dA$$

where $\bar{y}$ and $\bar{z}$ are the locations of the center and *f* and *g* range from 0 to 2. The vortex centroids and radii noted above are specific cases of these area moment integrals. The integrals were discretized due to the discrete nature of the velocimetry data. Assembling a covariance matrix of these moments as

$$cov[Vortex] = \begin{bmatrix} \frac{\phi_{20}}{\phi_{00}} & \frac{\phi_{11}}{\phi_{00}} \\ \frac{\phi_{11}}{\phi_{00}} & \frac{\phi_{02}}{\phi_{00}} \end{bmatrix}$$

and calculating the eigenvalues, λ_1 and λ_2, of this two-by-two matrix, the eccentricity, ϵ, is defined as

$$\varepsilon = \sqrt{1 - \frac{\lambda_2}{\lambda_1}}$$

For all data in the upstream region, time series data was acquired and computed with STB-PTV, followed by Vortex-in-Cell # (VIC#), as implemented in LaVision's DaVis 10.2 software. The acquisition rate of the data was different for the different freestream velocities, for reasons noted in the preceding chapter. Inherent to single-frame, time series data is correlation between successive images which allows calculation of velocity fields via PIV (correlation based) or PTV (particle tracking based). To adequately capture the physically occurring variance of the vortex properties, it is necessary to sample the flow repeatedly with uncorrelated measurements. To allow for uncorrelated measurements, after acquiring the data at a rate appropriate for the freestream velocity and calculating the particle tracks with STB-PTV, only every tenth Eulerian velocity field was computed with VIC#. The resulting vorticity fields were examined at several points near the vortices and the autocorrelation between subsequent fields was between -0.1 and 0.1, indicating that the temporal subsampling of velocity fields gives independent samples. At least 1000 of these temporally subsampled fields were used for each of the cases in the data set here. However, the mean vortex properties given in this chapter did not vary more a few percent after only 100 samples.

Across the ensemble of velocity fields where vortex properties were calculated, the vortices varied significantly. It was noted with high-speed video of developed cavitation that the vortex instability was not periodic. The peaks of the instability vary in distance and amplitude, as will be discussed later. These variations are due to variations in the vortex properties themselves, which are large enough to lead to the aperiodic and nonrepeating behavior of the vortex instability. As such, the physical variability in vortex circulation and radius measured in the upstream, midstream, and downstream regions is expected. This physical variation dominates the much smaller random and bias uncertainties in the velocity fields, so the uncertainties presented in the vortex properties reflect primarily these variations.

The vortex properties are shown in Table 6.1 for the angle sweep of the non-matched foils (Cases N.0, N.2, and N.4), at a fixed freestream speed (and thus chord-based Reynolds number). Table 6.2 shows case N.4 over a range of Reynolds numbers and Table 6.3 shows case M.4 over the same range of Reynolds numbers. In all cases measured with velocimetry, the secondary foil has a negative or zero angle of attack. At the more negative limit of this range of angles of attack (Cases N.4 and M.4), it is known that this foil profile would not generate lift if isolated in the flow (Callison, personal communication, 2019, using X-Foil). However, in all cases, a pair of counter-rotating vortices is produced. This likely results from the interaction of the flows around the foils with one another as the vortices roll up. Note that as the angle of attack of the secondary foil becomes more negative, the core radius is smaller, and the vortex circulation is weaker. This change in core radius is likely also due to the complexities of the flow immediately between the two hydrofoils. If the test section were longer, the foils could be set farther apart while still observing the instability in the test section and the resulting rolling

vortices would likely have less interaction, perhaps leading to less of a change in core radius and circulation ratio with angle of attack and thus different results.

Figure 6.1 shows an instantaneous field of Case N.0. Note the presence of a tertiary vortical structure to the side of the vortices, corresponding to what was noted in the cavitation visualization section above. The typical peak vorticity in this tertiary structure is about half that of the primary vortex, and since these vortices also have a smaller radius, so the actual circulation of these tertiary vortices is much smaller than that of the primary and secondary vortices.

Figure 6.2 shows an instantaneous field from Case N.2, which demonstrates the reduced radius of the secondary vortex relative to Case N.0 in Figure 6.1. Also noticeable are the relative positions of the primary and secondary vortices compared to the Case N.0 above. As the secondary weakens, it orbits the primary at a faster speed.

Importance of Averaging Choice

As noted above, the vortex properties were individually calculated for over 1000 independent fields before averaging. Vortices in this configuration wander noticeably, on the order of their diameters in the upstream plane, so it is important to calculate quantities with independent fields, then take the average of these quantities as opposed to average the fields, then calculate vortex quantities from the averaged velocity field. This is especially important for the vortex eccentricity and peak vorticity. In the averaged field, the vortex wandering appears as higher eccentricity, and the varying location of peak vorticity leads to a lower averaged peak vorticity. As an example, the time averaged flow from Case N.2 is shown in Figure 6.3 along with an instantaneous field from Case N.2, which shows the lower peak vorticity in the averaged field as well as the falsely elongated shape of the vortex.

Scaling of Vortex Behavior

As demonstrated in the cavitation visualization section of Chapter 5, the behavior of the two vortices strongly depends on the angle of attack of the secondary hydrofoil. At positive angles of attack and the present separation distance, the Crow instability between the two vortices does not appear within the length of the test section. At higher positive angles of attack of the secondary, the closeness of the hydrofoils likely interferes with the formation of the vortices and inhibit production of two distinct counter-rotating vortices that propagate downstream. With the secondary foil at -5 degrees, cavitation in the secondary before the primary was not observed. Thus, we confine ourselves to angles of attack between -4 and 0 degrees for the secondary hydrofoil. To quantify the effect of the angle of attack of the secondary foil, a sweep over this range was done. The results are tabulated in Table 6.4. Figure 6.4 shows the circulation ratio of the vortices over this range which reveal a nearly linear dependence on the angle of attack of the secondary. The primary vortex circulation is roughly independent of the angle of attack of the secondary as shown by Figure 6.5. Figure 6.6 shows the radius of the secondary also varies with angle of attack while the primary's radius again has minimal dependence on the secondary's angle.

For reasons detailed in the preceding chapter, it is desirable to study cavitation at higher freestream speeds. In contrast, it is difficult to take velocimetry measurements at these higher speeds, but it is feasible to do so in the upstream region, so the upstream region will be used to establish scaling relationships for the vortex behavior. Table 6.5 shows the results of the sweep over speeds for the non-matched secondary foil at a fixed angle of attack of -4 degrees. Table 6.6 shows the results of the sweep over speeds for the matched secondary foil at a fixed angle of attack of -4 degrees and modest Reynolds number dependence is noted in both cases. For the

non-matching foil, the radius of the secondary vortex, scaled by the thickness of the secondary hydrofoil tip, *d*, is plotted in Figure 6.7, showing a reduction in radius with increasing Reynolds number. A reduction in core radius also occurs for the secondary vortex when produced by the matching secondary foil, but the exponent is different, as shown in Figure 6.8. This difference potentially results from the squared off tip in the case of the matching secondary foil while the non-matching secondary foil has a rounded tip to encourage the roll-up of the vortex.

The circulations of the vortices also show a Reynolds number dependence, though not as substantial as in the case of the radii. In the non-matching case, shown in Figure 6.9, both the primary and secondary vortices have a reduction in circulation strength with increasing Reynolds number, with circulation scaled by chord and freestream velocity. Similarly, Figure 6.10 shows a reduction in circulation strength for both vortices with increasing Reynolds number for the matching case. However, the circulation ratio stays approximately constant across Reynolds numbers, as shown in Figure 6.11 for the non-matching case and 6.12 for the matching case.

Also worth noting is that the average maximum vorticity in each vortex has little variation with Reynolds number when scaled with the core radius (at that Reynolds number) and the freestream velocity. Figure 6.13 shows this for the non-matching foils and Figure 6.14 shows this for the matched foils.

Linear Stability Analysis

As the vortices convect downstream, their initially nearly parallel arrangement and linear shape gives way sinuous shapes, especially for the secondary. In the midstream measurement location, at 1.2 chords downstream of the foils, the vortices are within the linear regime of this instability. Following a similar measurement approach to that used in the preceding section, STB and VIC# are performed on the vortices while they are in this linear regime.

As a first point of comparison, the vortex properties are compared to those found in the upstream regime. In the midstream, the measurements were only taken for the cases of study (M.4, N.0, N.2, and N.4) at a single freestream velocity. The results are compiled in Table 6.7. As a key criterion for comparison, within the uncertainty of the measurements, the vortices conserve their circulation from the upstream measurement location. Note the wider variability of the separation distance here than in the upstream.

For the linear stability predictions of a generalized Crow theory, we can use the upstream measurements in the prior section as an initial condition. The linear theory predicts the development of the instability by estimating a growth rate and wavelength comparable to what is observed. While the theory of Crow was acknowledged above, a basic explanation of the generalized Crow theory is detailed here, presented following that of Leweke *et al.* (2016). It is assumed that the wavelength of the instability, λ, is long relative to the size of the core radius. The general Crow instability (for equal-strength vortices) assumes that the vortex center is locally perturbed from its original axis (in sinusoidal fashion). The instability combines three elements: the self-induced rotation of a single vortex, the strain field induced by a given vortex on the other, and the mutual induction of the perturbations of both vortices on each other. Given the unequal strength of the vortices considered here, they also both rotate about their combined centroid.

While Crow (1970) originally considered a pair of equal strength and size Rankine vortices (vortices of constant vorticity across their cores) with no axial flow, subsequent efforts have generalized this. The mathematical model here follows that of Leweke, *et al.* (2016) as well as Bristol, *et al.* (2004). The goal is to determine the growth rate of the instability as a function of wavelength. To begin, the matrix representing the linear stability problem is formed

$$A = \begin{bmatrix} \eta_1 & 1+\Omega_1 & 0 & \Gamma\psi \\ -1-2\Gamma-\Omega_1 & \eta_1 & -\Gamma\chi & 0 \\ 0 & \psi & \eta_2 & \Gamma(1+\Omega_2) \\ \chi & 0 & -2-\Gamma(1+\Omega_2) & \eta_2 \end{bmatrix}$$

As above, Γ is the circulation ratio. Here Ω_i represents the self-induction of the i-th vortex, η_i is the viscous damping function, and ψ_i and χ_i are mutual induction functions

$$\Omega_i = \frac{(kb)^2}{1 + 0.995\, kr_i + 0.438(kr_i)^2}\left(\ln\left(\frac{2 + 2.151kr_i}{kr_i}\right) + 0.327\right)$$

$$\psi = (kb)^2 K_0(kb) + kbK_1(kb)$$

$$\chi = kbK_1(kb)$$

$$\eta_i = \left(-\frac{2\pi\nu}{\Gamma_1}\right)\left(\frac{r_i}{b}\right)^{-2}(1.54kr_i + (kr_i)^2)$$

where K_j is the modified Bessel functions of the second kind, and k is the wavenumber of the instability considered. The real part of the largest eigenvalue of this matrix is taken and scaled by the larger vortex strength and the separation distance,

$$\gamma = \frac{\Gamma_1}{2\pi b^2} Real(\lambda_{\max})$$

to give the growth rate, γ. Thus, the growth rate as a function of wavelength can be estimated from the upstream measurements. We assume that the maximum growth rate corresponds to the wavelength that is observed in the experiments. As the Crow instability is a displacement instability, the wavelength and amplitude can be determined by tracking the vortex centerline displacement over time. Comparing the values found in the midstream to those in the upstream gives an experimental observation of the growth rate. To relate this downstream location to the

growth rate, we note that in the linear regime, the instability grows exponentially. For a growth rate γ, an initial perturbation δ_0 grows as

$$\delta(t) = \delta_0 e^{\gamma t}$$

If we move in the reference frame of the background flow, then we can relate the downstream distance to the time of instability evolution merely *via* the speed of the flow (i.e. downstream distance $\Delta x = U_0 \Delta t$ where Δx is the distance between upstream and midstream measurement locations and Δt is the time it takes the freestream flow to travel this distance). Rearranging the terms, we have

$$\frac{\left(\ln\left(\frac{\delta_{midstream}}{\delta_0}\right) * U_0\right)}{\Delta x} = \gamma$$

where U_0 is the freestream flow speed. This can be used to estimate the growth rate, γ, from the difference in instability amplitude between the upstream (δ_0) and midstream measurement domains ($\delta_{midstream}$). We can then compare this observed growth rate with one predicted from the upstream vortex properties and the generalized Crow theory introduced above. Figure 6.15 shows the comparison between observed and predicted growth rate from theory as a function of perturbation wavelength. The magnitudes of the observed growth rate compare well to the predicted maximum growth rate, although the uncertainty in the observed growth rate measurements is considerable. Here, the large uncertainties reflect the considerable physical variability of the measured phenomena. However, the wavelength of the predicted maximum growth rate is greater than the wavelength observed in the experiments.

Discussion

Traditionally, vortex cavitation is assumed to follow the McCormick scaling with Reynolds number, which assumes a vortex core radius scaling with the boundary layer thickness. Other studies have supported this, but the exponent with Reynolds number is not completely agreed upon. Originally, the exponent was assumed to be -0.4, but some studies (Keller and Rott 1999, Gowing *et al*. 1995) find that $Re^{-0.5}$ fits the data better. The present results suggest $Re^{-0.3}$ to $Re^{-0.34}$ for the secondary vortex and $Re^{-0.1}$ for the primary. Potentially the difference from the expected McCormick exponent results due to the proximity of the two hydrofoils generating the vortices. Chesnakas and Jessup (2003) studied the tip vortices of a ducted and non-ducted propulsor and found negligible change in core size with Reynolds number for the ducted case and a typical reduction in core size for the non-ducted, open case. They suggest that the rollup of the vortex occurring in close proximity to the wall of the duct changes the dynamics and leads to no dependence of core size with Reynolds number. While in the present study the secondary core size is close to the scaling expected in McCormick scaling, the primary is quite different. The dynamics of vortex rollup with the foils so close together could lead to the differences, as suggested by the work of Chesnakas and Jessup (2003).

The peak vorticity, when unscaled, increased with Reynolds number and accompanying by decreased core radius. Having a higher vorticity in the vortex core makes the vortex less susceptible to deformation in an externally applied strain field, and this tendency was noted by Marshall *et al*. (2000) and will be discussed in the following chapter to explain the resistance of the secondary vortex to deformation in Case N.2 while the secondary deforms the stronger primary vortex.

The generalized linear theory of Crow predicts the growth rate of the instability but not the amplitude in its initial linear stage. Presumably, the wavelength of the observed instability

should match the wavelength of the maximum predicted growth rate as this would be the most unstable wavelength. Additionally, there is no deliberate forcing of the instability, so no particular wavelength is a priori assumed to cause the instability. While the Crow theory is predicated on the assumption that the separation distance is much greater than the vortex radii, the presently examined cases do not have $r_c \ll b$, so this assumption is violated. As the growth rate is more strongly dependent on Γ_p, Γ_s, and b, it is perhaps unsurprising that growth rate is predicted well. Alternatively, the wavelength of the growth rate is more sensitive to the core properties, so with r_c comparable to b, the predicted wavelength is less accurate. Notably, this difference between observed and predicted wavelength is greatest for N.0 which has the largest core radius considered.

Conclusions

The present chapter examines the initial development of the Crow instability across a range of angles of attack and a range of Reynolds numbers. The linear theory of Crow is found to reasonably predict the initial dynamics of the instability, despite the very short distance between the vortices and despite tertiary vortical structures in some cases. However, this linear prediction will not describe the long-term development of the instability, so the following chapter focuses on the non-linear regime of the vortex interaction. A scaling of vortex properties on Reynolds number is found. The dependence of vortex core sizes with Reynolds number and angle of attack of the secondary is found. The scaling developed in this chapter will be used in the following chapters to scale the downstream vortex interaction when high-speed velocimetry measurements are not feasible.

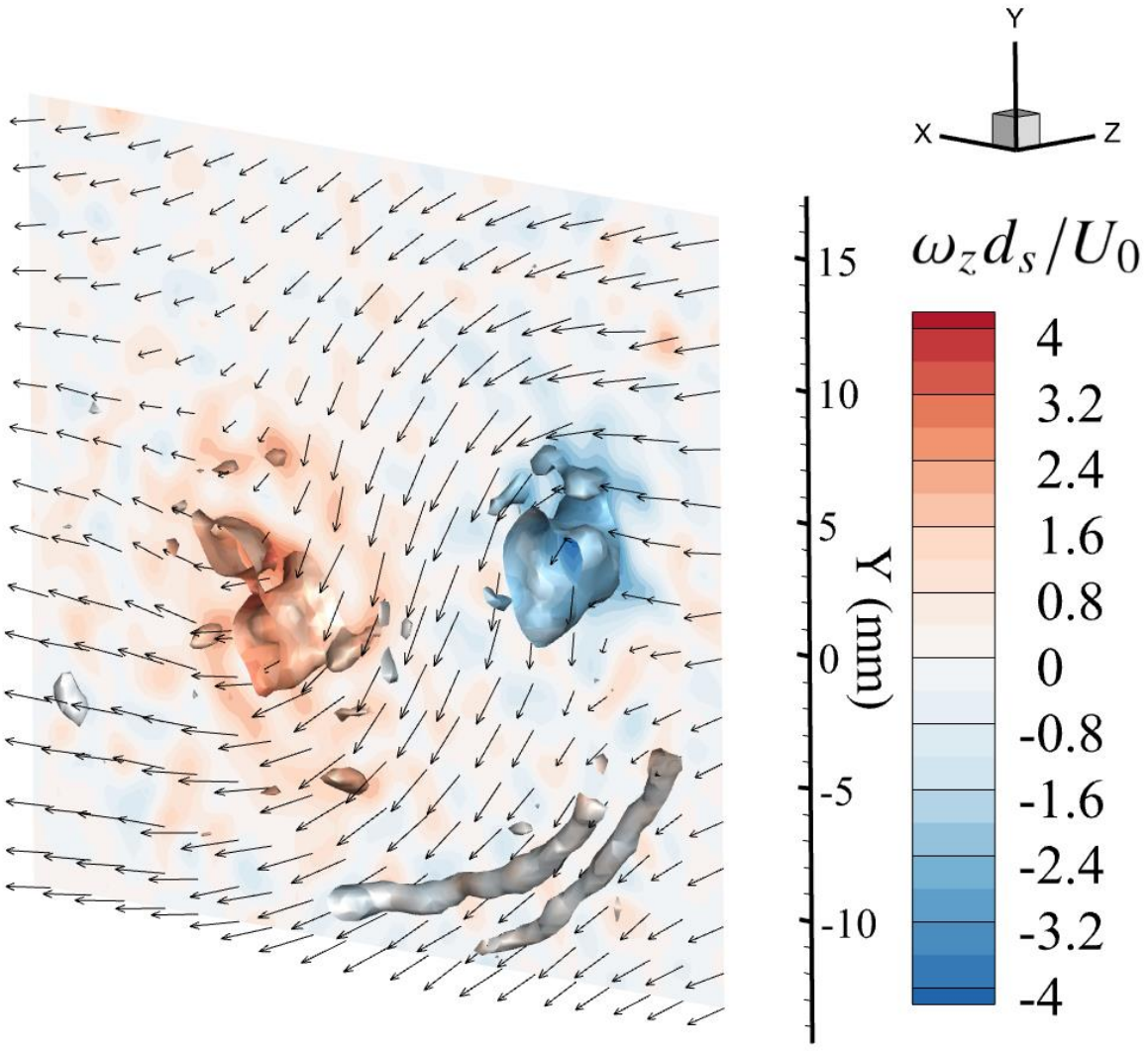


Figure 6.1 Instant of Upstream Measurement of Case N.0 with STB. An example instantaneous realization of the upstream STB-VIC# measurement of the vortices in Case N.0. ω_z is streamwise vorticity and it is scaled with d_s, the thickness of the secondary foil tip, and U_0, the freestream velocity. All cases had different measurement volumes so that the vortices would be near the center of the volume and away from the typically lower quality regions on the periphery. The vortices are visualized by λ_2 isosurfaces and colored by streamwise vorticity. Here, the secondary vortex is in blue, and the primary vortex is in red. In typical fashion for the primary vortex, it is not tightly wrapped up at this stage, and it has a somewhat multi-lobed shape. The secondary vortex has a more compact shape, likely due to the tip treatment on the secondary foil. Both vortices have relatively larger core sizes in this case as compared to the other cases. Note that the dominant structures are largely the two vortices, the primary and secondary. However, some "tertiary" vortices, generally wrapping around both the larger vortices, are also present. In this case, they are in the lower right of the flow field and correspond to the small cavitating structures in Figure 4.3.

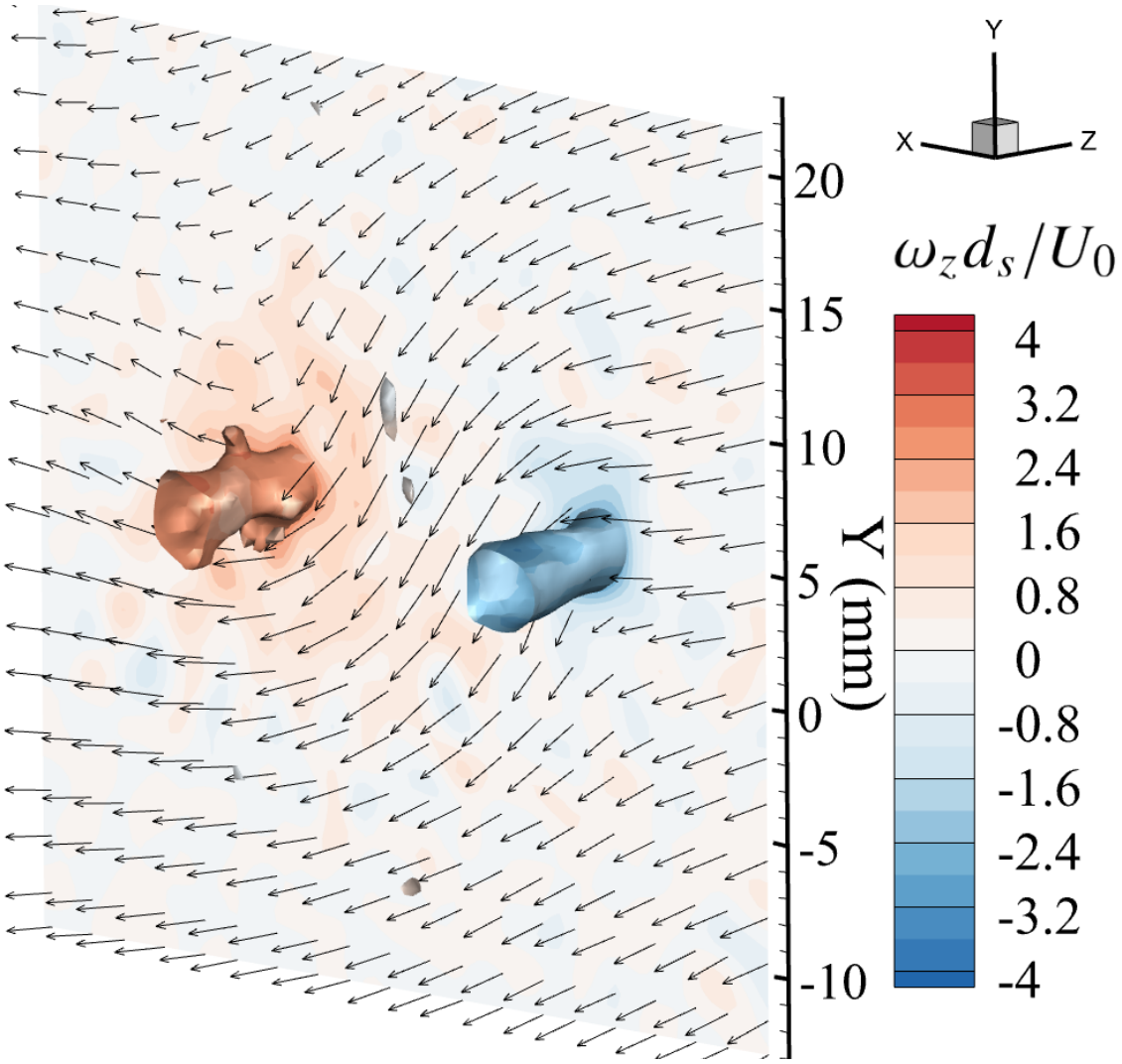


Figure 6.2 Instant of Upstream Measurement of Case N.2 with STB. An example instantaneous realization of the upstream STB-VIC# measurement of the vortices in Case N.2. ω_z is streamwise vorticity and it is scaled with d_s, the thickness of the secondary foil tip, and U_0, the freestream velocity. All cases had different measurement volumes so that the vortices would be near the center of the volume and away from the typically lower quality regions on the periphery. The vortices are visualized by λ_2 isosurfaces and colored by streamwise vorticity. Note that the dominant structures are largely the two vortices, the primary and secondary. Occasionally, small concentrations of vorticity (usually oriented vertically, not streamwise) will convect between the two vortices. The vector spacing of the velocimetry measurement is 0.42 mm, but here the vectors are spaced at 2 mm so as not to crowd the image.

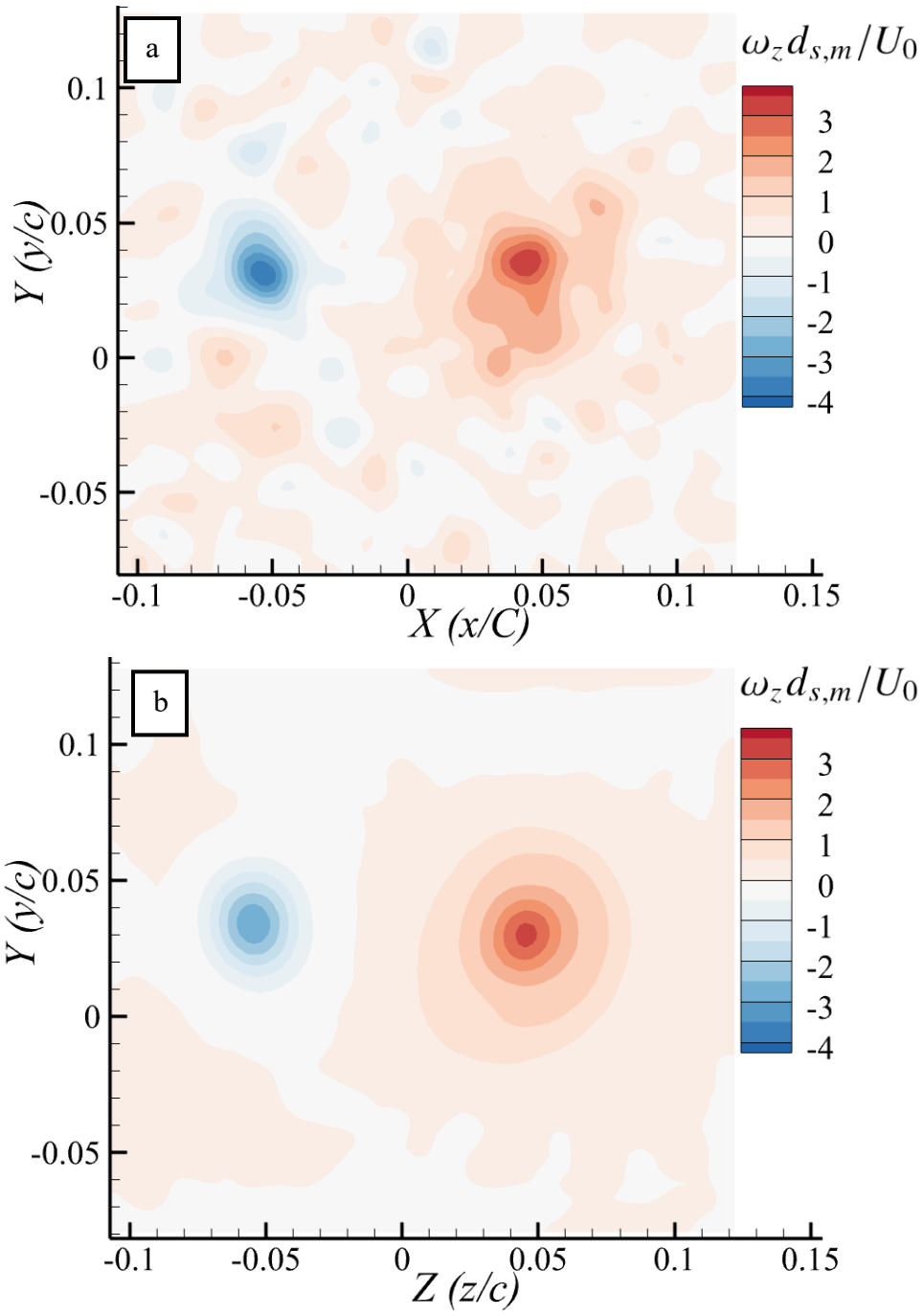


Figure 6.3 Instantaneous and Averaged 2-D Fields. An example instantaneous realization (a) and average (b) of the upstream STB-VIC# measurement of the vortices in Case N.2. ω_z is streamwise vorticity and it is scaled with $d_{s,m}$, the thickness of the matched secondary foil tip, and U_0, the freestream velocity. It is important to calculate the vortex properties from instantaneous realizations then average them. Note that the average has much lower vorticity in the secondary as it is smoothed over the averaging due to vortex wandering.

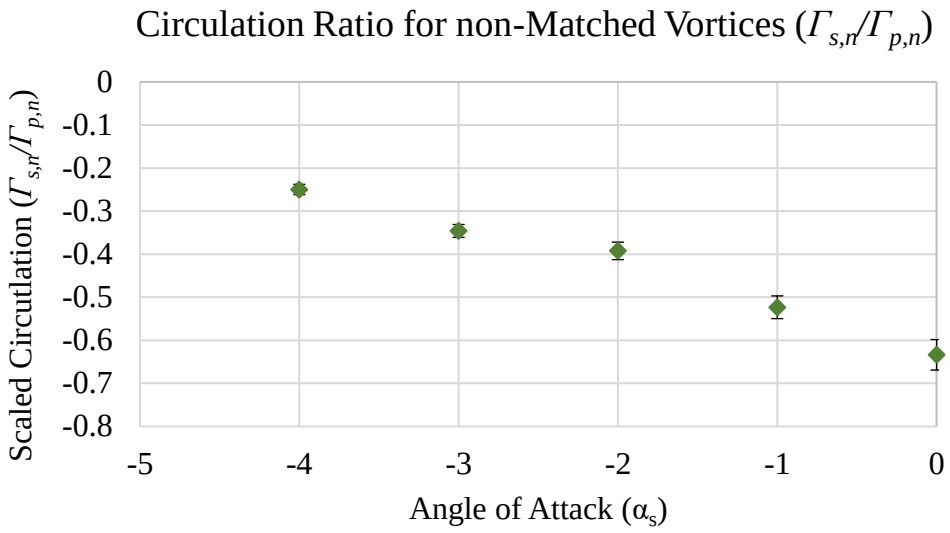


Figure 6.4 Circulation Ratio with Angle of Attack. The circulation ratio (circulation of the secondary vortex for the non-matched foils, $\Gamma_{s,n}$, divided by circulation of the primary vortex for the non-matched foils, $\Gamma_{p,n}$) of the two vortex system varies almost linearly with the angle of attack of the secondary, α_s. As also illustrated by Figure 6.5, this is due to the near linear dependence on angle of attack of circulation of the secondary vortex.

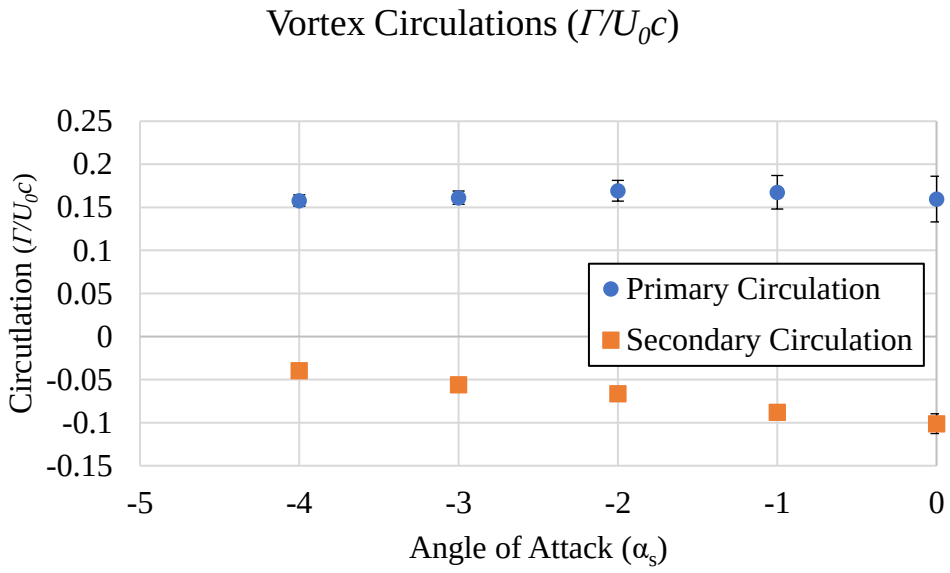


Figure 6.5 Circulations with Angle of Attack. The circulation, Γ, of the secondary vortex has a near linear dependence on the angle of attack of the secondary, α_s. It is scaled by freestream velocity, U_0, and foil chord length, c. Conversely, the primary vortex is roughly independent of the angle of attack of the secondary, which is expected. In some cases, the uncertainty bounds are too small to be seen.

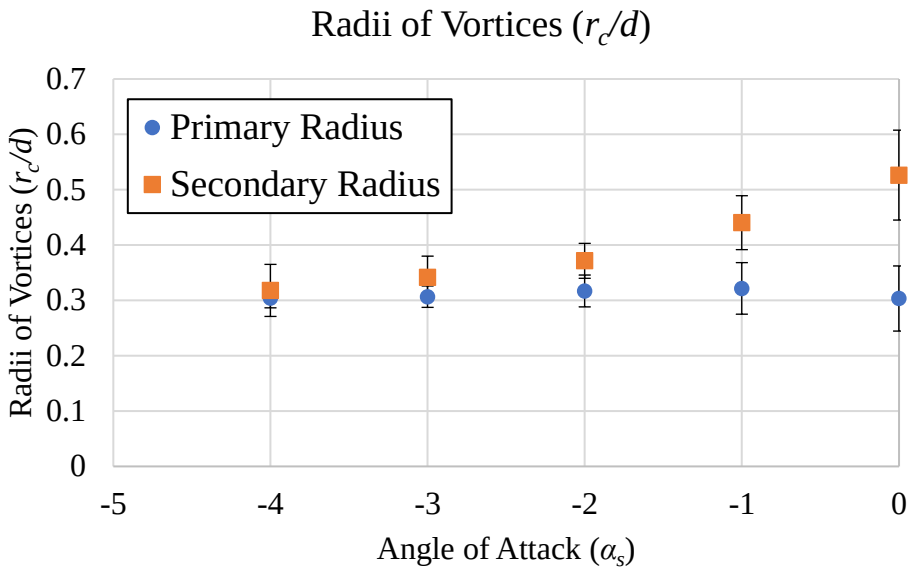


Figure 6.6 Radii of Vortices with Angle of Attack. The core radius (r_c, scaled by secondary foil tip thickness, d) of the secondary vortex increases as the angle of attack of the secondary hydrofoil (α_s)increases. With the fixed angle of attack of its generating hydrofoil, the radius of the primary vortex is roughly independent of angle of attack of the secondary.

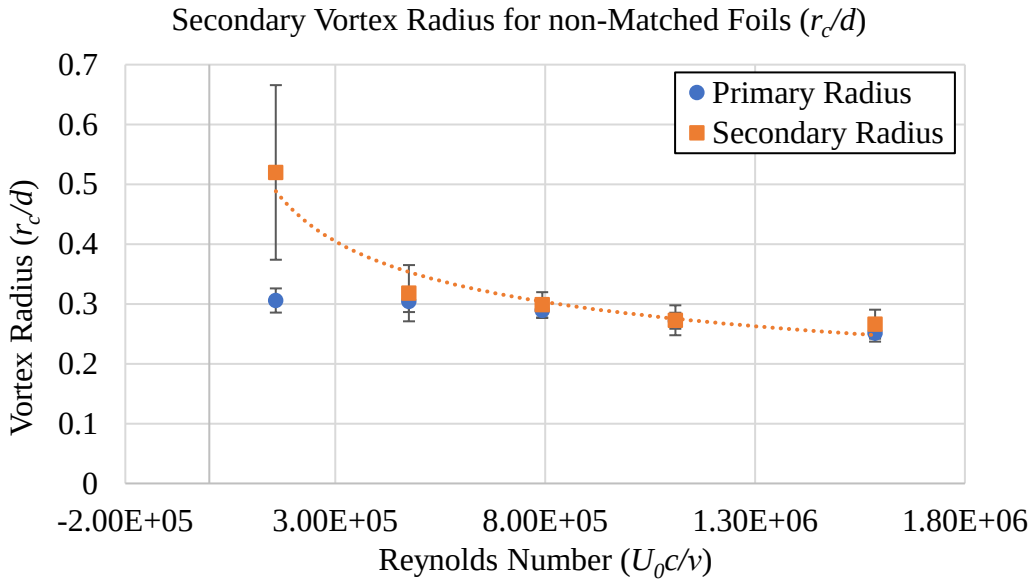


Figure 6.7 Reynolds Number Scaling of Secondary Radius. The radius of the secondary vortex (r_c, scaled by secondary foil tip thickness, d) decreases with increasing Reynolds number ($U_0 c/\nu$ with U_0 as freestream velocity, c as foil chord length, and ν as kinematic viscosity) with a scaling of around $Re^{-0.30}$. The radius of the primary vortex shows only a minimal reduction with increasing Reynolds number.

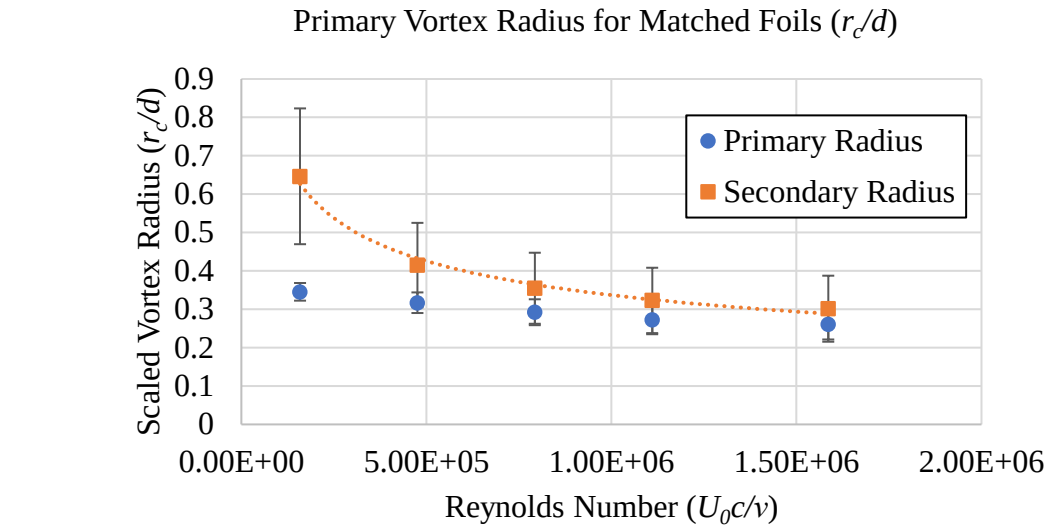


Figure 6.8 Reynolds Number Scaling of Primary Radius. The radius of the secondary vortex (r_c, scaled by secondary foil tip thickness, d) decreases with increasing Reynolds number ($U_0 c/\nu$ with U_0 as freestream velocity, c as foil chord length, and ν as kinematic viscosity) with a scaling of around $Re^{-0.34}$. The radius of the primary vortex shows only a minimal reduction with increasing Reynolds number.

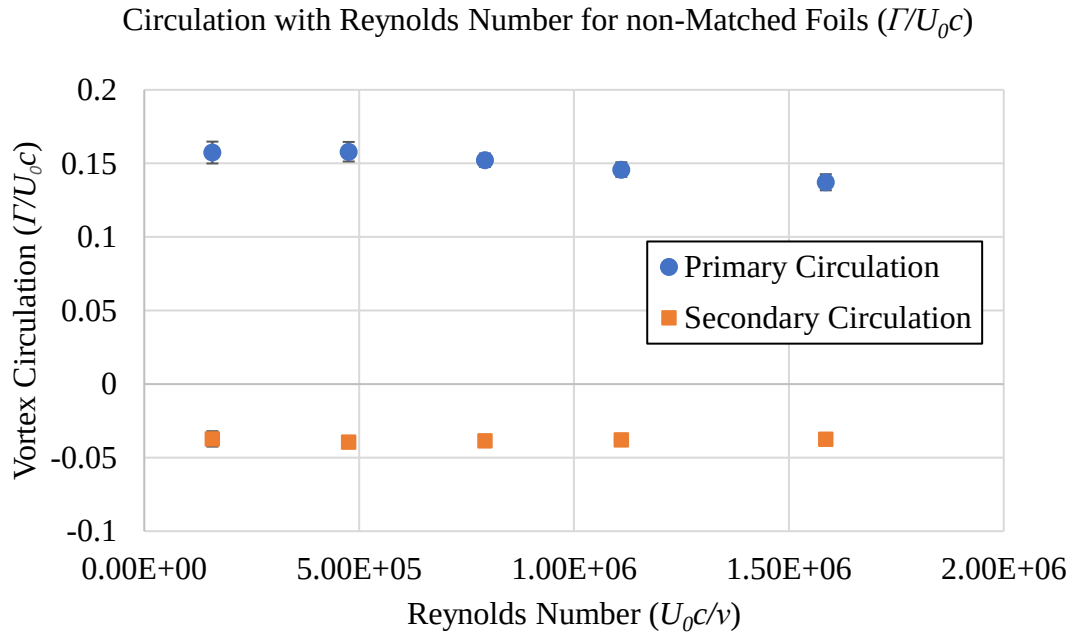


Figure 6.9 Reynolds Number Scaling of Vortex Circulations. The circulations (Γ) of both vortices show a slight reduction with increasing Reynolds number ($U_0 c/\nu$ with U_0 as freestream velocity, c as foil chord length, and ν as kinematic viscosity). In some cases, the margin of uncertainty is too small to be visible behind the markers.

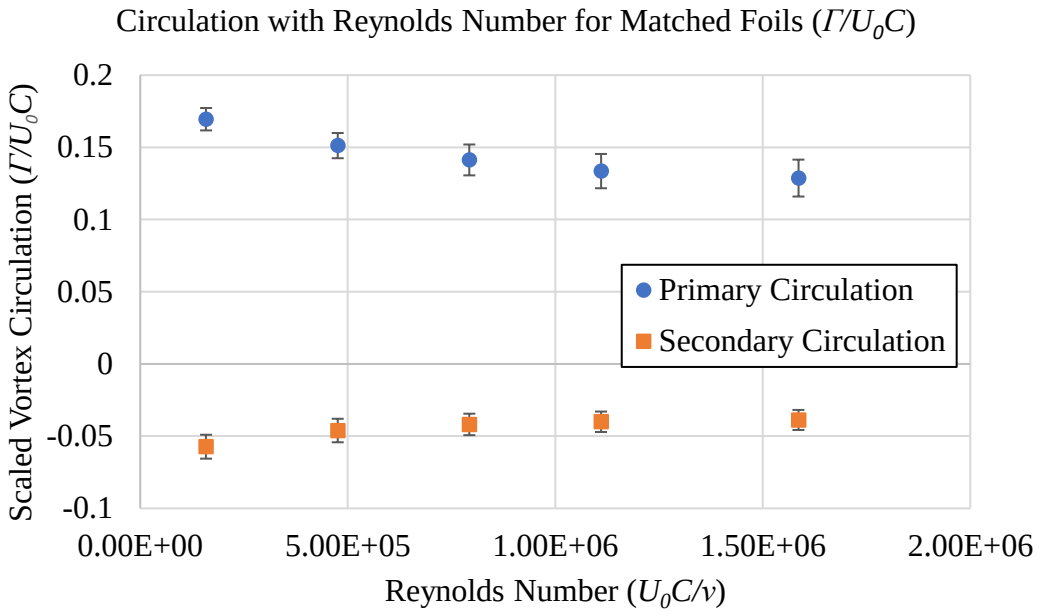


Figure 6.10 Reynolds Number Scaling of Vortex Circulations. The circulations (Γ) of both vortices show some reduction with increasing Reynolds number ($U_0 c/\nu$ with U_0 as freestream velocity, c as foil chord length, and ν as kinematic viscosity).

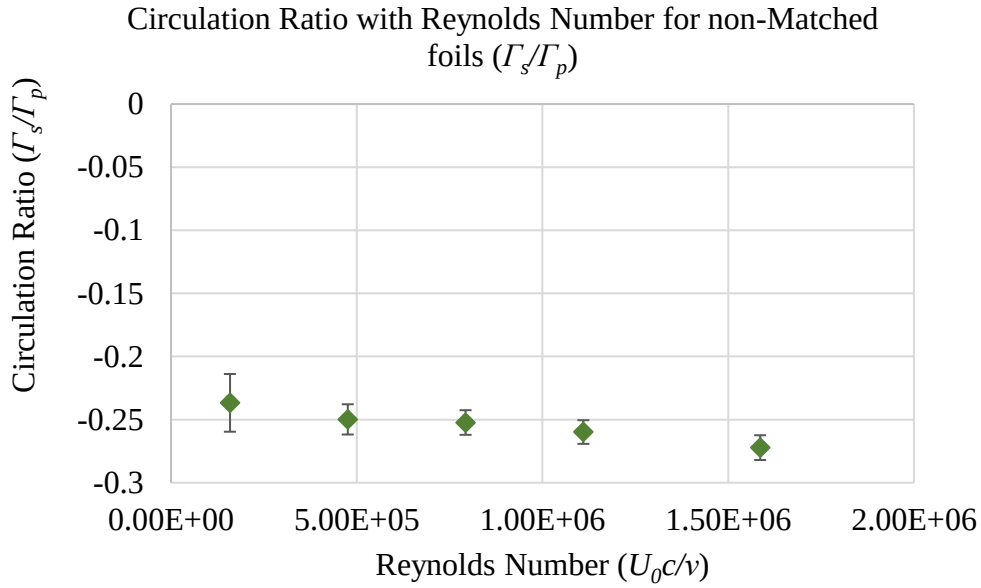


Figure 6.11 Reynolds Number Scaling of Circulation Ratio. The circulation ratio of the vortices (circulation of the secondary vortex for the non-matched foils, Γ_s, divided by circulation of the primary vortex for the non-matched foils, Γ_p) is close to constant with increasing Reynolds number ($U_0 c/\nu$ with U_0 as freestream velocity, c as foil chord length, and ν as kinematic viscosity), though it becomes slightly stronger at higher speeds.

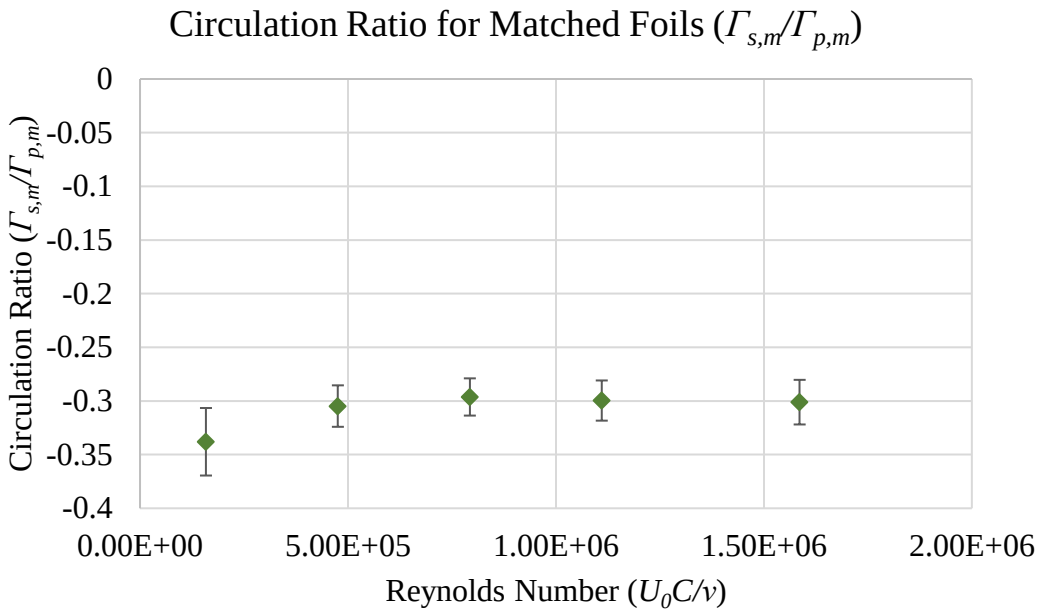


Figure 6.12 Reynolds Number Scaling of Circulation Ratio. The circulation ratio of the vortices (circulation of the secondary vortex for the non-matched foils, Γ_s, divided by circulation of the primary vortex for the non-matched foils, Γ_p) is close to constant with increasing Reynolds number ($U_0 c/\nu$ with U_0 as freestream velocity, c as foil chord length, and ν as kinematic viscosity) for the matched foils case.

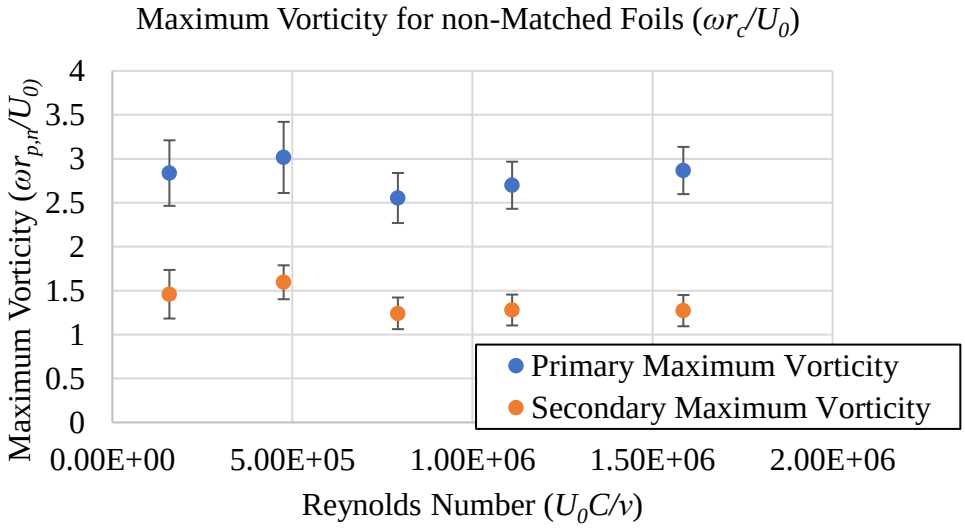


Figure 6.13 Reynolds Number Scaling of Maximum Vorticity. The maximum vorticity (ω, scaled by core radius, r_c, and freestream velocity, U_0) in the cores of the vortices remains relatively constant when scaled with the radii of the vortices.

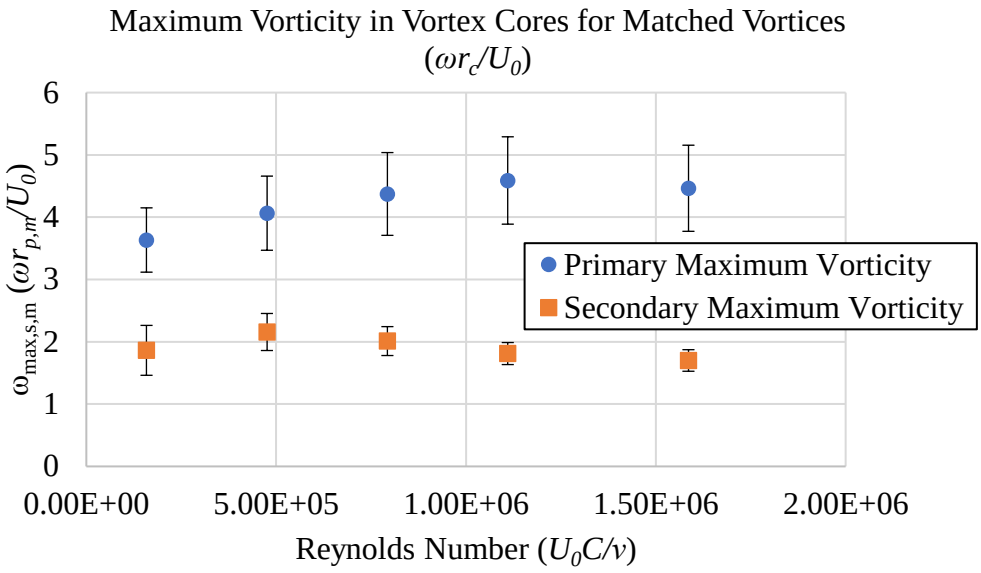


Figure 6.14 Reynolds Number Scaling of Maximum Vorticity. The maximum vorticity (ω, scaled by core radius, r_c, and freestream velocity, U_0) in the cores of the vortices remains relatively constant when scaled with the radii of the vortices.

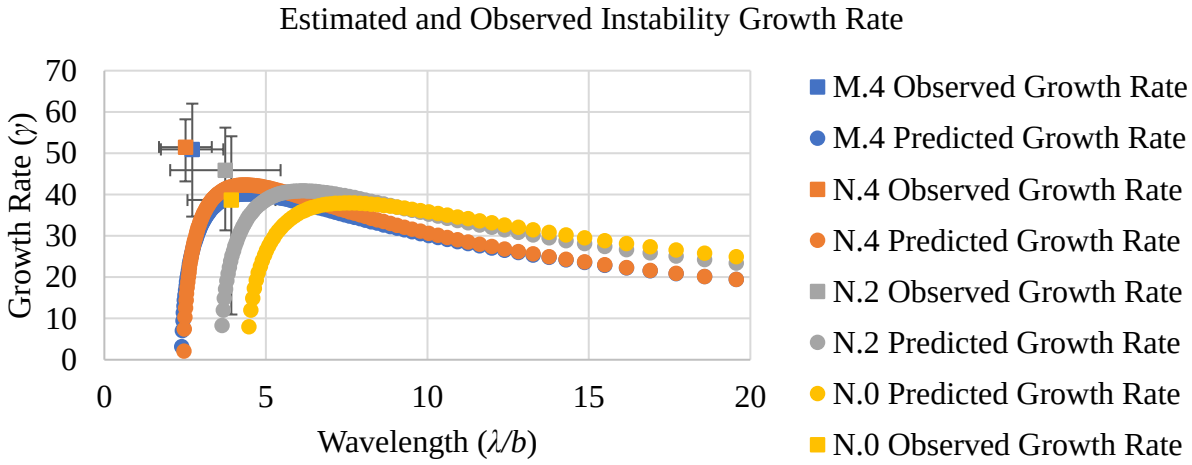


Figure 6.15 Estimated and Observed Instability Growth Rate. The growth rate (γ) observed by measuring the centerline perturbation with STB compares reasonably well to the maximum growth rate predicted by the generalized Crow instability. However, the observed wavelength (λ, scaled by vortex separation distance, b) is less than the wavelength corresponding to the predicted maximum growth rate. This likely results from the relatively high ratio of r_c/b (vortex core radius of vortex separation distance) as this violates one of the assumptions of the Crow theory. For the N.0 case, which has the largest r_c/b, the wavelength is underpredicted the most.

Secondary Angle of Attack, α_s	**-4 degrees**	**-3 degrees**	**-2 degrees**	**-1 degrees**	**0 degrees**
b/c	0.101 ± .002	0.101 ± .002	0.099 ± 0.003	0.100 ± 0.003	0.101 ± 0.004
$\Gamma_p/(U_0c)$	0.158 ± 0.007	0.161 ± 0.008	0.17 ± 0.01	0.17 ± 0.02	0.160 ± 0.03
$\Gamma_s/(U_0c)$	-0.039±0.003	-0.055±0.003	-0.066±0.04	-0.087±0.007	-0.10±0.01
r_p/d	0.30 ± 0.02	0.31 ± 0.02	0.32 ± 0.03	0.32 ± 0.05	0.30 ± 0.03
r_s/d	0.32 ± 0.03	0.34 ± 0.04	0.37 ± 0.03	0.44 ± 0.05	0.53 ± 0.08
ε_p	0.4 ± 0.1	0.4 ± 0.1	0.5 ± 0.2	0.6 ± 0.2	0.6 ± 0.2
ε_s	0.5 ± 0.2	0.5 ± 0.2	0.5 ± 0.2	0.5 ± 0.2	0.5 ± 0.2
$u_{axial,p}/(U_0)$	1.17 ± 0.08	1.18 ± 0.08	1.3 ± 0.1	1.2 ± 0.1	1.2 ± 0.2
$u_{axial,s}/(U_0)$	0.88 ± 0.06	0.87 ± 0.07	0.97 ± 0.09	1.0 ± 0.1	1.0 ± 0.2
$\omega_{max,p}/(U_0/d)$	9.9 ± 1.3	10.5 ± 1.5	12.0 ± 1.9	13.9 ± 2.6	15.8 ± 3.3
$\omega_{max,s}/(U_0/d)$	5.0 ± 0.6	5.6 ± 0.6	6.6 ± 0.8	8.1 ± 1.2	8.1 ± 1.4
$\beta_p/(U_0/d)$	-0.3 ± 0.8	-0.2 ± 0.9	-0.2 ± 1.0	-0.2 ± 1.3	0.0 ± 1.4
$\beta_s/(U_0/d)$	0.0 ± 0.4	0.0 ± 0.4	0.0 ± 0.4	-0.0 ± 0.6	-0.0 ± 0.7
Γ_s/Γ_p	-0.25 ± 0.01	-0.35 ± 0.01	-0.39 ± 0.02	-0.52 ± 0.03	-0.63 ± 0.04

Table 6.1 Vortex Properties with Angle of Attack. The properties of the vortex pair as a function of angle of attack of the secondary are given here. Separation distance, b, primary vortex circulation, Γ_p, secondary vortex circulation, Γ_s, primary vortex core radius, r_p, secondary vortex core radius, r_s, primary vortex eccentricity, ε_p, secondary vortex eccentricity, ε_s, axial velocity in primary vortex core, $u_{axial,p}$, axial velocity in secondary vortex core, $u_{axial,s}$, maximum vorticity in primary vortex, $\omega_{max,p}$, maximum vorticity in secondary vortex core, $\omega_{max,s}$, strain rate in primary vortex core, β_p, strain rate in secondary vortex core, β_s, and circulation ratio, Γ_s/Γ_p. These are scaled by foil chord length, c, foil dip thickness, d, and freestream velocity, U_0. Note that b and the primary vortex circulation strength and radius are relatively constant while the properties of the secondary vary with attack angle. The uncertainties are dominated by the inherent variability of the system of vortices.

Freestream Speed, U_0	**1 m/s**	**3 m/s**	**5 m/s**	**7 m/s**	**10 m/s**
b/C	0.102 ± 0.005	0.101 ± 0.002	0.102 ± 0.002	0.102 ± 0.002	0.103 ± 0.002
$\Gamma_p/(U_0C)$	0.157 ± 0.007	0.158 ± 0.007	0.152 ± 0.005	0.146 ± 0.005	0.137 ± 0.005
$\Gamma_s/(U_0C)$	-0.037±0.005	-0.039±0.003	-0.038±0.002	-0.038±0.002	-0.037±0.002
r_p/d	0.31 ± 0.02	0.30 ± 0.02	0.29 ± 0.01	0.27 ± 0.01	0.25 ± 0.01
r_s/d	0.52 ± 0.15	0.32 ± 0.05	0.29 ± 0.02	0.27 ± 0.02	0.27 ± 0.02
ε_p	0.3 ± 0.1	0.4 ± 0.1	0.3 ± 0.1	0.3 ± 0.1	0.3 ± 0.1
ε_s	0.6 ± 0.2	0.5 ± 0.2	0.4 ± 0.2	0.5 ± 0.2	0.5 ± 0.2
$u_{axial,p}/(U_0)$	1.16 ± 0.07	1.17 ± 0.08	1.20 ± 0.06	1.24 ± 0.07	1.28 ± 0.06
$u_{axial,s}/(U_0)$	0.87 ± 0.10	0.88 ± 0.06	0.88 ± 0.04	0.92 ± 0.04	0.93 ± 0.04
$\omega_{max,p}/(U_0/d)$	9.3 ± 1.2	9.9 ± 1.3	8.8 ± 0.9	9.9 ± 1.0	11.4 ± 1.1
$\omega_{max,s}/(U_0/d)$	2.8 ± 0.5	5.0 ± 0.6	4.6 ± 0.3	4.7 ± 0.3	4.8 ± 0.3
$\beta_p/(U_0/d)$	-0.3 ± 0.6	-0.3 ± 0.8	-0.3 ± 0.6	-0.4 ± 0.6	-0.4 ± 0.6
$\beta_s/(U_0/d)$	0.0 ± 0.4	0.0 ± 0.4	0.0 ± 0.2	0.0 ± 0.2	0.0 ± 0.2
Γ_s/Γ_p	-0.24 ± 0.02	-0.25 ± 0.01	-0.25 ± 0.01	-0.26 ± 0.01	-0.27 ± 0.01

Table 6.2 Vortex Properties with Freestream Speed. The properties of the vortex pair as a function of freestream velocity (and thus Reynolds number) for the N.4 case. Separation distance, b, primary vortex circulation, Γ_p, secondary vortex circulation, Γ_s, primary vortex core radius, r_p, secondary vortex core radius, r_s, primary vortex eccentricity, ε_p, secondary vortex eccentricity, ε_s, axial velocity in primary vortex core, $u_{axial,p}$, axial velocity in secondary vortex core, $u_{axial,s}$, maximum vorticity in primary vortex, $\omega_{max,p}$, maximum vorticity in secondary vortex core, $\omega_{max,s}$, strain rate in primary vortex core, β_p, strain rate in secondary vortex core, β_s, and circulation ratio, Γ_s/Γ_p. These are scaled by foil chord length, c, foil dip thickness, d, and freestream velocity, U_0.

Freestream Speed, U_0	**1 m/s**	**3 m/s**	**5 m/s**	**7 m/s**	**10 m/s**
b/C	0.105 ± 0.005	0.101 ± 0.003	0.099 ± 0.004	0.098 ± 0.004	0.098 ± 0.004
$\Gamma_p/(U_0C)$	0.169 ± 0.008	0.151 ± 0.009	0.141 ± 0.011	0.134 ± 0.012	0.129 ± 0.013
$\Gamma_s/(U_0C)$	-0.057±0.008	-0.046±0.008	-0.042±0.007	-0.040±0.007	-0.039±0.007
r_p/d	0.35 ± 0.02	0.41 ± 0.03	0.40 ± 0.03	0.39 ± 0.04	0.37 ± 0.04
r_s/d	0.54 ± 0.05	0.40 ± 0.07	0.35 ± 0.05	0.30 ± 0.07	0.27 ± 0.06
ε_p	0.37 ± 0.14	0.38 ± 0.15	0.40 ± 0.15	0.41 ± 0.16	0.43 ± 0.16
ε_s	0.61 ± 0.22	0.59 ± 0.21	0.61 ± 0.21	0.58 ± 0.22	0.58 ± 0.021
$u_{axial,p}/(U_0)$	1.12 ± 0.08	1.11 ± 0.10	1.15 ± 0.09	1.17 ± 0.09	1.18 ± 0.10
$u_{axial,s}/(U_0)$	0.81 ± 0.13	0.85 ± 0.09	0.84 ± 0.08	0.85 ± 0.08	0.87 ± 0.08
$\omega_{max,p}/(U_0/d)$	8.5 ± 1.2	9.8 ± 1.4	10.9 ± 1.7	11.7 ± 1.8	12.2 ± 1.9
$\omega_{max,s}/(U_0/d)$	3.4 ± 0.7	5.4 ± 0.7	5.7 ± 0.7	6.0 ± 0.6	6.3 ± 0.6
$\beta_p/(U_0/d)$	-0.3 ± 0.7	-0.2 ± 0.9	-0.1 ± 0.9	-0.1 ± 0.9	-0.1 ± 1.0
$\beta_s/(U_0/d)$	0.0 ± 0.4	0.0 ± 0.4	0.0 ± 0.4	0.0 ± 0.4	0.0 ± 0.4
Γ_s/Γ_p	-0.34 ± 0.03	-0.30 ± 0.02	-0.30 ± 0.02	-0.30 ± 0.02	-0.30 ± 0.02

Table 6.3 Vortex Properties with Freestream Speed at Upstream Point. The properties of the vortex pair as a function of freestream velocity (and thus Reynolds number) for the M.4 case. Separation distance, b, primary vortex circulation, Γ_p, secondary vortex circulation, Γ_s, primary vortex core radius, r_p, secondary vortex core radius, r_s, primary vortex eccentricity, ε_p, secondary vortex eccentricity, ε_s, axial velocity in primary vortex core, $u_{axial,p}$, axial velocity in secondary vortex core, $u_{axial,s}$, maximum vorticity in primary vortex, $\omega_{max,p}$, maximum vorticity in secondary vortex core, $\omega_{max,s}$, strain rate in primary vortex core, β_p, strain rate in secondary vortex core, β_s, and circulation ratio, Γ_s/Γ_p. These are scaled by foil chord length, c, foil dip thickness, d, and freestream velocity, U_0.

Case	M.4	N.4	N.2	N.0
b/C	0.102 ± 0.011	0.104 ± 0.006	0.100 ± 0.008	0.103 ± 0.01
$\Gamma_p/(U_0C)$	0.142 ± 0.013	0.142 ± 0.009	0.159 ± 0.009	0.163 ± 0.021
$\Gamma_s/(U_0C)$	-0.039 ± 0.010	-0.035 ± 0.004	-0.065 ± 0.004	-0.095 ± 0.015
r_p/d	0.31 ± 0.03	0.28 ± 0.03	0.32 ± 0.02	0.32 ± 0.06
r_s/d	0.36 ± 0.14	0.29 ± 0.05	0.41 ± 0.05	0.69 ± 0.18
ε_p	0.37 ± 0.15	0.36 ± 0.14	0.49 ± 0.13	0.53 ± 0.18
ε_s	0.55 ± 0.21	0.51 ± 0.19	0.52 ± 0.19	0.62 ± 0.21
$u_{axial,p}/(U_0)$	1.07 ± 0.10	1.15 ± 0.08	1.21 ± 0.10	1.09 ± 0.18
$u_{axial,s}/(U_0)$	0.85 ± 0.15	0.92 ± 0.11	0.87 ± 0.09	0.75 ± 0.17
$\omega_{max,p}/(U_0/d)$	10.8 ± 1.9	11.0 ± 1.8	9.6 ± 1.3	13.1 ± 2.9
$\omega_{max,s}/(U_0/d)$	6.9 ± 1.4	6.1 ± 1.0	4.4 ± 0.6	5.7 ± 1.3
$\beta_p/(U_0/d)$	-0.2 ± 1.0	-0.1 ± 0.8	-0.1 ± 0.6	-0.1 ± 1.0
$\beta_s/(U_0/d)$	0.0 ± 0.6	0.0 ± 0.5	0.0 ± 0.3	0.1 ± 0.6
Γ_s/Γ_p	-0.28 ± 0.03	-0.25 ± 0.04	-0.41 ± 0.02	-0.58 ± 0.04

Table 6.4 Vortex Properties for Different Cases at Midstream Point. The properties of the vortex pair in the midstream measurement location. Separation distance, b, primary vortex circulation, Γ_p, secondary vortex circulation, Γ_s, primary vortex core radius, r_p, secondary vortex core radius, r_s, primary vortex eccentricity, ε_p, secondary vortex eccentricity, ε_s, axial velocity in primary vortex core, $u_{axial,p}$, axial velocity in secondary vortex core, $u_{axial,s}$, maximum vorticity in primary vortex, $\omega_{max,p}$, maximum vorticity in secondary vortex core, $\omega_{max,s}$, strain rate in primary vortex core, β_p, strain rate in secondary vortex core, β_s, and circulation ratio, Γ_s/Γ_p. These are scaled by foil chord length, c, foil dip thickness, d, and

Chapter VII

Non-Linear Regime of Counter Rotating Vortex Pair Interaction

Topology of Non-Linear Interactions

As the secondary vortex wraps around the primary vortex, it initially forms "Ω loops" (Ortega *et al*. 2003). Eventually these loops break up and form vortex rings. Before the breakup into rings, at approximately 1.7 *c* downstream, the cores of the secondary vortex were observed to have incipient cavitation, suggesting that transient minimum pressures in the flow field are achieved as the secondary vortex undergoes these complex dynamics. The topology of the secondary vortex, in its characteristic loop shape, can be divided into three regions, as detailed in Figure 7.1. First, there is the "peak", the locations on the secondary loops roughly parallel to and nearest to the primary. Second, the "troughs", which are also parallel to and farthest away from the primary. Finally, the "legs" of the secondary are the portions of the secondary that are more vertically or spanwise oriented, and not parallel to the local primary vortex segment. On occasions, the legs are oriented nearly perfectly vertically while at other times the legs are oriented almost purely spanwise. All the while, the primary is generally oriented in the streamwise direction. To show the full loop of the secondary, in one image and display its topology, a snapshot of developed cavitation is used in Figure 7.1.

Approach for Vortex Analysis

Unlike in the midstream and upstream regions, in the downstream region, the secondary vortex is seldom oriented in the streamwise direction. The legs of the secondary loops are

generally oriented vertically and spanwise. While a Stereo-PIV plane or thin STB volume can readily be oriented perpendicular to the axes of the vortices in the upstream sections, this is not true of the downstream region. Additionally, the secondary wanders through a much larger region in the spanwise and vertical direction as the various portions of the secondary (peaks, troughs, and legs) move past this streamwise location. Accordingly, a measurement domain that is much larger in the vertical and spanwise directions is required. However, given the large vertical and spanwise extents, it is not possible to have an equivalently thick streamwise direction. A thicker streamwise direction would lead to a higher N_I and inhibit STB from tracking particles. Therefore, only a portion of the secondary loop can be measured in a given instant.

To measure the behavior of the vortices in the downstream location, at the streamwise midplane of the measurement domain, the locations of the primary and secondary are found. A small plane locally orthogonal to each vortex is interpolated. The location of these planes is recorded and the vortex properties are calculated on these planes with the same method as used in the prior chapter. Figure 7.2 shows an example section of the secondary vortex and the locally orthogonal plane.

As described in Chapter 3, STB-VIC# is used for determining the velocity fields in the vortex flows considered here. While STB offers the highest spatial resolution of PTV methods by allowing high particle concentrations, the choice of VIC# to calculate Eulerian velocity and pressure is an evolving area of study. A combination of Cost Constrained Minimization (CCM, Agarwal *et al*. 2018) and Omni-directional Integration (Omni-3D, Wang *et al*. (2018)) has been used by Agarwal *et al*. (2023) to estimate pressure drop in small secondary vortices in a backward facing step flow. In this work, VIC# based estimation of pressure drop in the core of

the secondary vortex in performed. VIC# was applied here, however, it did not offer appreciably different results from the CCM and Omni-3D approach. CCM and Omni-3D were explicitly formulated to tackle pressure calculations in turbulent flows. As the vortical flow here has only a few strong vortices as opposed to a cascade of eddies, VIC# does not give inferior results. Additionally, VIC#, as formulated in DaVis, can be used on a computing cluster, dramatically accelerating the computation.

Vortex Motion and Topology

As the vortices move in the downstream location, their postions are tracked over time when finding the locally orthogonal planes. To illustrate this, Figure 7.3 shows the separation distance in the downstream region scaled by separation distance in the upstream region, b/b_0, between the primary and secondary in Case N.2 for an arbitrary time range. With a somewhat quasiperiodic behavior, this separation distance demonstrates some of the loop behavior noted above. Another indication of the topology of the secondary loops is the vertical component of vorticity (in the global coordinate system), shown in Figure 7.4 for an arbitrary range of time. When the absolute value of the vertical component of vorticity is large, the portion of the secondary in the measurement domain is a leg region. This is also true of the spanwise component of vorticity, though the secondary legs tend to be more oriented vertically than in the spanwise direction. Together, the separation distance between the vortices and the relative local orientation of the secondary are used to define whether the secondary is at that instant in a peak, trough, or leg. In other words, from time resolved PTV measurements, vortices' properties are found at every timestrp and used to assign that instance to a category of peak, trough, or leg categories which are subsequently used in characterzing the vortex behavior along its varied topology.

Core Reduction and Straining in the Secondary Vortex

Having defined a method to categorize and measure the vortices in the downstream, the secondary vortex properties can now be analyzed. The eventual goal is to estimate the pressure reduction in the cores of the vortices, especially the secondary. When viewing high-speed video of cavitation inception in the secondary vortices, the incipient bubbles rapidly expand in the legs of the secondary vortices, as shown in the following chapter. This suggests a rapid drop in pressure leading to the inception event has occurred and this drop in pressure is due to substantial axial strain of the secondary vortex. Given that the legs of the secondary vortex are generally orthogonal to the axis of the primary vortex, they are in line with the strain field induced by the primary. This strain field of the primary is then assumed to cause significant axial straining in the secondary vortex.

With the stretching of the secondary vortex, it is possible significant that axial jetting may develop; however, our measurements suggest that the magnitude of any axial jetting in the secondary is small. Figure 7.5 shows a histogram of axial flow velocities for the legs of the secondary in Case N.2. This axial velocity is defined by considering the velocity in the core of the vortex, projected in the direction of the vortex at that point, and comparing it to the velocity of the neighboring area outside the vortex that has also been projected in the direction of the vortex. As can be seen, no substantial axial velocity is noted.

Similarly, the local strain rate tensor can be projected in the direction of the local vortex, as shown in Figure 7.6 for Case N.2. No substantial axial straining is found. While the magnitude of axial straining and jetting in the secondary is not uniquely zero at all times, it is essentially in the noise floor for our measurements of velocity gradients. As a comparison, the vorticity magnitude in the secondary, also in Figure 7.6, is several times larger than even the

outliers of the axial straining data. The other cases (N.0, N.4, and M.4) also show minimal axial jetting and straining.

The data in this section thus indicate that the effects of axial jetting and straining in the secondary vortex legs are small. As a quick check of this conclusion, it is useful to estimate the strength of the strain field generated by the primary vortex in the region of the secondary vortex. This straining should scale as

$$\beta \sim \frac{\Gamma_p}{b^2}$$

where the separation distance, b, is local, not the upstream, initial separation distance. On the other hand, the strength of the vorticity in the region of the secondary vortex should behave as

$$\beta \sim \frac{\Gamma_s}{r_{c,s}^2}$$

Using typical values for the vortex circulations and sizes and separation distance of the primary from the legs, the magnitude of axial straining is less than a tenth of the vorticity magnitude. This indicates that the local swirling motion dominates the local axial straining in the legs of the secondary vortex. The scaling of the axial straining above also comports with the growth in amplitude of the secondary vortex sinusoidal instability structures between the midstream and downstream measurements.

While the axial straining and jetting have small effects in the secondary vortex, the reduction in core size in the secondary results in significant flow effects. Table 7.1 shows the typical core size of the secondary vortex for the various cases in the upstream, midstream, and downstream locations. While the difference between upstream and midstream radii is relatively small, the radius is significantly reduced in the downstream. This results in a correspondingly

significant drop in pressure in the secondary vortex core. The effect of reduction in core radius in causing reduction in pressure in the secondary is evidenced further by the strong correlation between the pressure drop in the secondary and the secondary vortex properties. We know from a first principles analysis that for an isolated vortex,

$$P_{drop} \sim -\Gamma^2/r_c^2$$

and applying this relationship to present study, a correlation coefficient of approximately -0.85 to -0.9 between P_{drop} and Γ^2/r_c^2 for all four cases is found. The pressure used in estimated by STB-VIC#.

Estimation of Pressure in the Vortex Cores

While correlations between pressure in the secondary and the properties of the secondary are noted above, absolute value of estimates of pressure in the secondary vortex are not stated. STB-VIC# will provide a field of pressure (with a zero average) with the same temporal and spatial resolution of the velocity field measurements. If we were to manually integrate a velocity and velocity gradient field to find pressure, it would similarly only yield a solution up to a constant. It is therefore necessary to supply a boundary value to anchor this pressure field to find an absolute pressure in the core of the secondary. This gives another reason to use a larger measurement domain for these measurements. By measuring the pressure far away from where the vortices are in the domain, one can ensure that a portion of the field has only a small pressure gradient between it and the walls of the water channel and has a close to constant pressure. It was not feasible to put a pressure probe in the middle of the tunnel simultaneous to the STB measurements as this would affect the vortex interaction and pressure fields. Accordingly, by placing a pressure probe in a region that was within the measurement domain but far from where the vortices would be, an absolute pressure could be measured to supply a steady boundary value

to the pressure fields from STB-VIC#. The pressure probe used was a modified Pitot tube with epoxy in its center such that only the holes around the diameter of the probe were exposed to the flow, thus giving the static pressure at that point. This setup is detailed in Chapter 2.

It was alluded to in the previous section that the spatial resolution of the present measurements is somewhat limited. As established in Chapter 3, there is a tradeoff between spatial resolution and thickness of the measurement domain when using optical velocimetry techniques. These are simultaneously limited by the particle image density that still enables tracking. As a relatively thick volume was necessary to measure across the secondary while it is oriented nearly vertically, the spatial resolution was then limited. Further, despite the low speeds used for the downstream study, there is still some level of ejection of particles from the core of the secondary, further hindering high spatial resolution in the core of the secondary vortex. This limited spatial resolution evidently has some effect.

Circulation is expected to be conserved in this flow. However, there is a noticeable drop in circulation between the upstream and the downstream measurements, as shown in Table 7.2. Some loss can be expected due to viscosity, but at the Reynolds numbers considered here, this loss should be negligibly small, even for the slower speeds used in the downstream measurements. This can be shown by considering the Lamb-Oseen vortex as a model for the vortices. Viscous effects, while small, should simultaneously reduce the circulation of a vortex and increase its radius, yet the radii reported above showed a reduction between upstream and downstream. Further, the circulation in the primary vortex is conserved up to the uncertainty of the measurements. Together, this suggests that the limited spatial resolution in the secondary leads to an underestimation of the strength of vorticity in the core of the secondary and accordingly an underestimation of pressure drop in the secondary.

To correct for this underestimation, an additional parameter to the Reynolds number scaling used to estimate the pressure drop at full speed is applied. The pressure drop is scaled by the ratio of circulations between upstream and downstream, squared:

$$\left(\frac{\Gamma_{s,upstream}}{\Gamma_{s,downstream}}\right)^2.$$

After applying this additional correction factor, estimates for the pressure drop in the core of the secondary can be obtained. These can be subdivided and presented in several ways. First, a time series of the pressure drop in the secondary is provided for each of the different cases in Figures 7.7, 7.8, 7.9, and 7.10. Figures 7.11, 7.12, 7.13, and 7.14 show histograms of pressure drop for the legs and the rest of the secondary vortices in all the cases. The pressure drop is greater in the legs than in the other sections of the vortices. The observed trend is attributed to the reduced radii of the secondary in the legs, which is presumably due to greater stretching. Table 7.3 shows the difference in radii between the secondary vortex legs and the other segments of the secondary vortex structures. This vortex pressure will be used to estimate cavitation inception rates in the following chapter.

Vortex Strain-Out Leading to Cavitation Suppression in the Primary Vortex

Beyond the utility of STB-VIC# in estimating pressure in the cores of the secondary vortices, it also elucidates several finer points of the interaction with the primary. As noted in the prior chapter, in certain conditions, the secondary vortex suppresses cavitation in the primary vortex when the freestream pressure is low. This happens only for the N.2 case as the secondary vortex peaks draw near to the primary and wrap around it. A simple description of the process, primarily reliant upon high-speed video of developed cavitation, was in Chapter 4. Here we use

the vorticity fields from STB measurements to show quantitatively what was previously claimed from high-speed video alone.

Figure 7.15 shows a time-series of the vortical interaction as the secondary vortex wraps around the primary vortex in a plane cutting through both vortices (streamwise normal), displayed with streamwise vorticity. Initially, the secondary vortex is in a trough state (t = 0 ms). It is then drawn up so that it is at a peak (t = 3.2 ms). The previously circular cross section of the primary vortex now takes an elliptical form as it is strained out by the secondary vortex (t = 4.0 ms). As the interaction continues, this elliptically shaped primary separates out into two vortical patches with near circular cross sections (t = 4.8 ms). These patches have a connecting region of weaker vorticity. While not apparent from this view, the upper portion of the primary vortex then is peeled off and joins with the secondary vortex as that portion of the secondary vortex breaks into vortex rings. Figure 7.16 shows a plan view which illustrates this. Returning to Figure 7.15, the streamwise vorticity of both is reduced and instead spanwise oriented vorticity is present (t = 6.4 ms). Meanwhile, the lower portion of the primary then stays connected to the rest of the primary as the secondary leg passes through. Finally, the secondary is back to a trough state and the primary is back to a streamwise oriented vortex without a noticeably elliptical cross section (t = 12.0 ms).

As this process occurs, the elliptical cross section of the primary shows increasing pressure in the core region. This leads to suppression of cavitation in the primary when the vortices undergo developed cavitation. The dynamics suggested in the prior paragraph are also indicated by the high-speed video in that cavitation in the primary vortex often reinitiates after the suppression in the lower portion. In other words, the lower of the two patches of vorticity noted above has a drop in pressure as it takes a more circular cross section as opposed to the

elliptical cross section. From the velocimetry, we see that the existing lower patch of vorticity is no longer straining cross-axially so its pressure drops correspondingly. Figure 7.17 shows the eccentricity of the vortices as the secondary is in a peak state. Both vortices are strained into more elliptical shapes and thus have higher eccentricity than when the secondary is in a trough state. However, despite the primary having a greater strength, the primary also has a higher eccentricity, presumably due to the compact nature of the secondary which allows it to better resist straining deformation than the primary.

The interaction process described here was noticed first by Marshall *et al*. (2001). They used computations to examine the interaction of pairs of counter-rotating vortices of varying circulation ratios, albeit at lower Reynolds numbers than those considered here. In one case, their Case E, they prescribed a weaker vortex ($\Gamma_s/\Gamma_p = -0.25$ in our nomenclature) with a smaller radius than the primary ($r_{c,secondary}/r_{c,primary} = 0.5$ while other cases had equal core radii sizes but different vortex strengths). They noted that with a smaller radius, the secondary would have higher vorticity, potentially even higher vorticity than the primary vortex. Due to the higher vorticity, the secondary would more readily withstand straining and more able to strip vorticity from the primary. In their case, they found substantial cross-axial straining of the primary vortex. However, the secondary vortex eventually weakened due to the diffusion of vorticity between the two vortices as they were near. This allowed the primary to regain its originally circular cross section and subject the secondary to significant cross axial straining. The case noted here has a relatively stronger secondary ($\Gamma_s/\Gamma_p = -0.4$) and a slightly relatively smaller secondary radius. Accordingly, exactly the same dynamics as Marshall *et al*. (2001) are not observed. Instead, the secondary strains out the primary and evidently strips vorticity from it during the secondary's breakup into rings. Another effect that could lead to the differing results

between the present study and Marshall *et al*. (2001) is that at the lower Reynolds numbers they studied, the viscous diffusion between the two vortices would have more of an effect. This would weaken the secondary vortex more than in our case, so the secondary they consider would be more apt to strain out under the influence of the primary vortex.

Case N.4 considered in this thesis has a circulation ratio almost exactly that considered in Case E of Marshall *et al*. (2001), but the secondary core radius is smaller. Correspondingly, the peak vorticity in the secondary is generally noticeably higher than that in the primary in the N.4 case. As suggested by the physics discussed in Marshall *et al*. (2001), the secondary in the N.4 case resists cross-axial straining out better than the secondary in Case E of Marshall *et al*. (2001). The secondary does strain the primary into an elliptical cross section in both Case E and Case N.4. However, the secondary in Case N.4 is not strong enough to strain the primary to the point of suppressing cavitation in it as in Case N.2. This likely results from the weaker strength of the secondary in Case N.4 as opposed to Case N.2.

Discussion

After establishing the topology of the secondary vortex during the nonlinear phase of the Crow instability, the various portions of the secondary can then be examined individually. This allows to differentiate regions where certain dynamics are most likely to occur. Namely, the legs are expected to exhibit the most axial strain as they are oriented in the direction of the strain field of the primary vortex. Following Chang *et al*. (2012), this axial straining was expected to be a substantive driver of cavitation inception in the secondary vortex. In practice, it was found that axial straining and jetting is minimal in the secondary vortex, even in the legs of the vortical loops.

Knister *et al*. (2022) found considerable correlation between time integrated axial strain rate and pressure reduction in the secondary. The authors now acknowledge that this was an error and evidently a numerical artifact of coding of the time integration of axial strain. Independent of the fact that the present work has data with superior temporal and spatial resolution compared to that prior work, that conclusion of that prior work was not supported by the data therein.

The spatial resolution of the present measurements is not sufficient to resolve all the features needed. Given the calculated vortex radii and spatial resolutions of the VIC# fields, there are approximately only 7 vectors across the core of the secondary vortex. Typically, 8 vectors across a core is regarded as the minimum resolution necessary to accurately reconstruct pressure in a vortex. It is possible that some amount of axial jetting is accordingly smoothed out by insufficient resolution, but the vortical strain field should be similarly smoothed. Given that both are sampled with the same spatial resolution, the stronger presence of swirling as opposed to axial straining suggests it should in fact dominate the pressure drop.

Altogether, this work finds that axial jetting and straining are insubstantial for contributing to the pressure drop in this configuration. Further, a simple scaling analysis supports the reasoning that the effects of reduced core radius and swirling in the secondary are stronger than those of axial straining in the secondary. Finally, pressure in the core of the secondary is strongly correlated with Γ^2/r_c^2 for the secondary, suggesting there is not much scope for weak axial jetting to directly contribute to pressure reduction in the secondary. Additionally, this indicates that the development of the low pressure in the secondary is a relatively slow process in that it progresses in tandem with the gradual reduction in the secondary core radius. In other words, while the typical view of cavitation in weaker vortical

structures is that it is a transient process, there is not a rapid drop in pressure leading to inception. The dramatic high-speed videos of inception imply a rapid drop in pressure. Yet, the explosive growth of incipient cavitation bubbles is a consequence of the physics of cavitation and not the underlying liquid flow dynamics driving a rapid pressure reduction.

Beyond relating the pressure reduction to the vortex dynamics, the absolute pressure drop is also recovered. Using the pressures found in this chapter in combination with the scaling of Chapter 6, the pressure drops at higher speed, where cavitation was observed to occur, can be estimated. Critically, the estimate of pressure drop in the secondary indicates that fluid tension is achieved. This is significant and will be used in the following chapter to estimate inception in the secondary vortex.

The cavitation suppression in the primary that we noted in Chapter 5 can now be shown to be driven by the straining out of the primary due to the action of the secondary. This behavior was not clear with high-speed video alone; the velocity fields from STB elucidate the behavior. This can be understood with recourse to the physics examined by Marshall *et al*. (2003). They found that a weaker vortex can cause substantial straining in a stronger vortex if that weaker vortex has a smaller core radius and thus vorticity comparable to that of the stronger vortex. They did not see quite the level of straining in the stronger vortex that is observed here, which eventually led to suppression of cavitation in the primary vortex in Case N.2. Instead, they found that over a longer time, the primary would recover its initial shape and the secondary would be strained out. The vortices considered here are at higher Reynolds numbers, suggesting the secondary should lose less vorticity due to viscous effects when near the primary. Accordingly, the secondary here should more readily resist cross-axial straining. The secondary vortices in the cases considered here also had smaller radii than the weaker vortices in their study

which also leads to higher peak vorticity in the secondaries. The resulting higher vorticities in the secondary vortices also suggest that they are more resistant to straining out while enabling straining out of the primary.

Conclusions

The present efforts in estimating the pressure drop represent the best that can be done with the available velocimetry system. The system and the flow physics of the available particles necessitate a scaling argument to estimate the pressure drops in the secondary vortex cores. Admitting these efforts, pressure drops in the secondary vortex indicating fluid tensions are found. These tensions are shown to be related primarily to the reduction in the core radius of the secondary and not due to axial jetting or straining. The measured vortex dynamics then indicate that the process leading to the pressure drop in the secondary vortex core is a transient process, but not more rapid than the development of the Crow instability in the secondary.

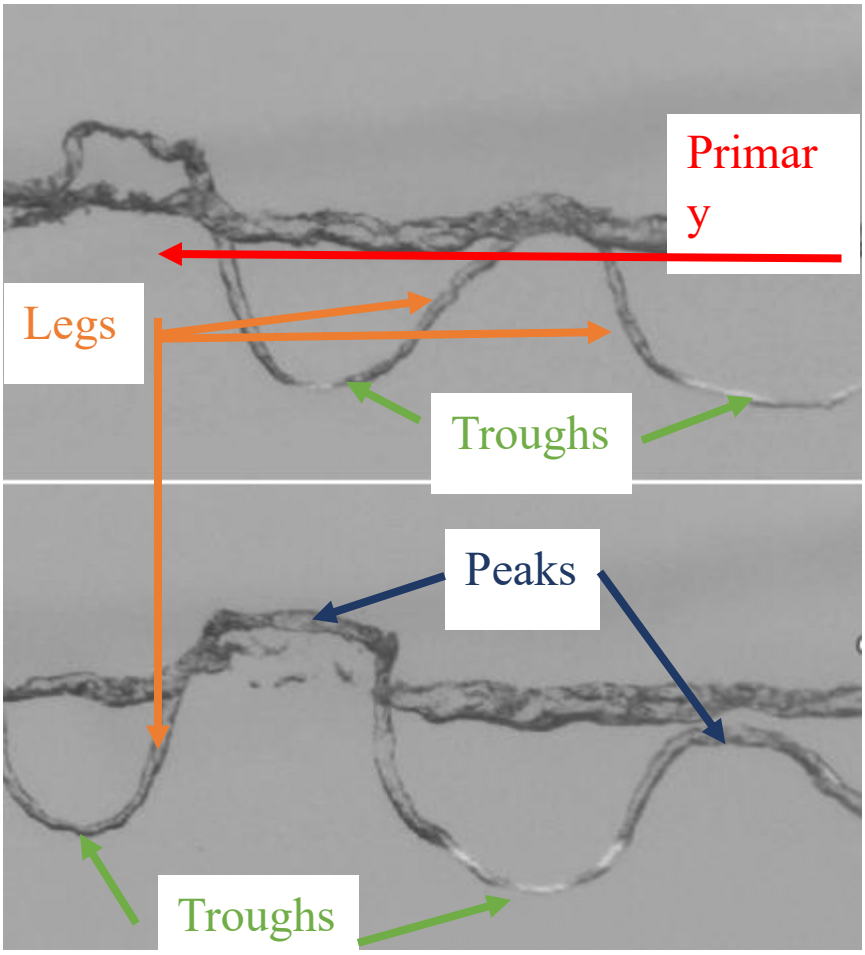


Figure 7.1 Topography of the Secondary Vortex. The shape of the secondary vortex in the downstream region, shown here in the N.2 case, can be divided into different sections. The peaks are where the instability in the secondary has the highest vertical location and is close to parallel to the primary vortex axis. The troughs are also parallel to the primary vortex, but they are the regions of the secondary that are farthest away from the primary. The legs are the portions of the secondary that are oriented mostly in the vertical and spanwise directions and connect the peaks and the troughs.

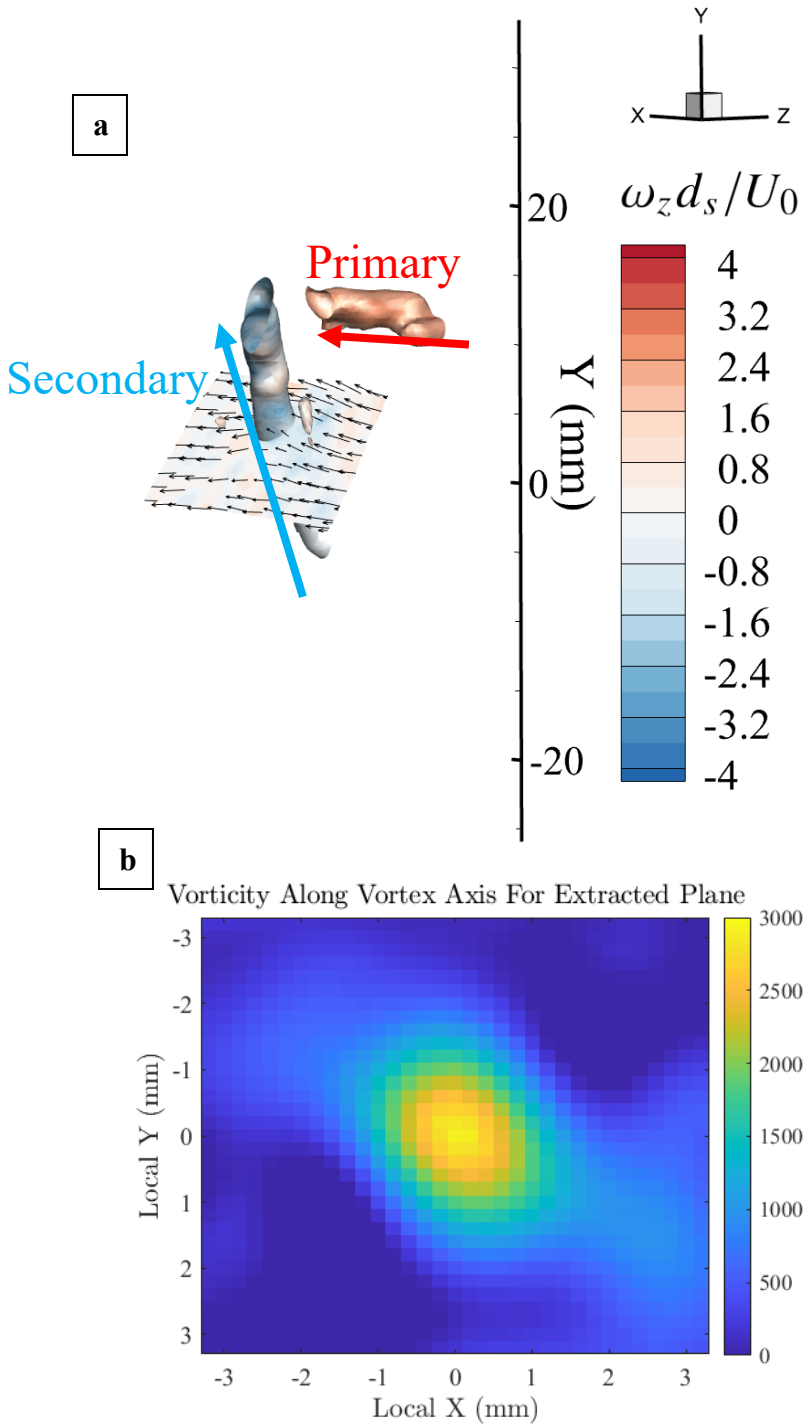


Figure 7.2 Depiction of Process of Analysis of Vortices. (a) An isometric view of a leg of the secondary vortex (nearly vertically oriented λ_2 isosurface along blue arrow, colored by streamwise vorticity, ω_z, which is scaled by foil tip thickness d_s and freestream velocity U_0) as it transits through the measurement domain near the primary vortex (horizontally oriented isorsurface near red arrow). The plane bisecting the secondary vortex is normal to the secondary vortex at that location, and the data on that plane are extracted and examined independently as in (b). On this plane, the vortex circulation, radius, velocity, strain rate, pressure, and other properties are calculated and recorded.

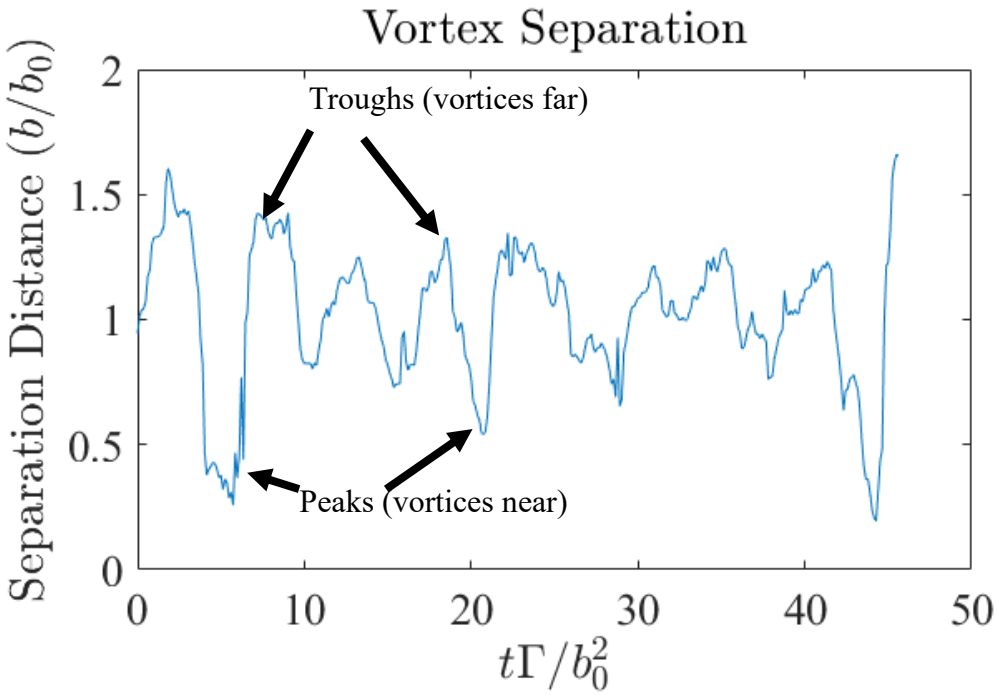


Figure 7.3 Separation of Vortices Over Time. The distance (b, scaled by upstream vortex separation, b_0) between the secondary vortex and primary vortex in the midplane of the downstream measurement domain over time (scaled by the circulation of the primary vortex, Γ, and the (upstream) separation distance for Case N.2). The secondary vortex is at a peak when the separation is low and a trough when the separation is far. A middling distance would typically indicate a "leg" in the secondary, a division made in conjunction with the vertical component of vorticity at that point.

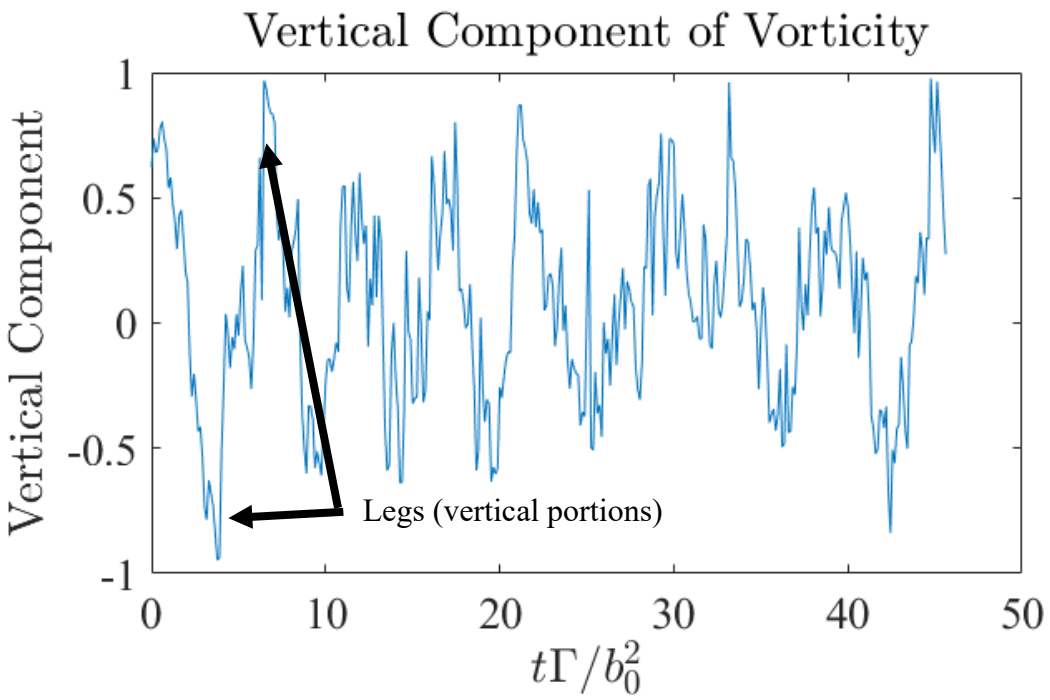


Figure 7.4 Vertical Component of Vorticity Over Time. The vertical component of the vorticity unit vector for the secondary vortex in Case N.2 over an arbitrary timespan (time is scaled by the circulation of the primary vortex, Γ, and the (upstream) separation distance for Case N.2. A vertical component of near 1 indicates that that portion of the secondary is a "leg" of the secondary. This can be used in combination with vortex separation to determine whether the secondary is in a peak, trough, or leg.

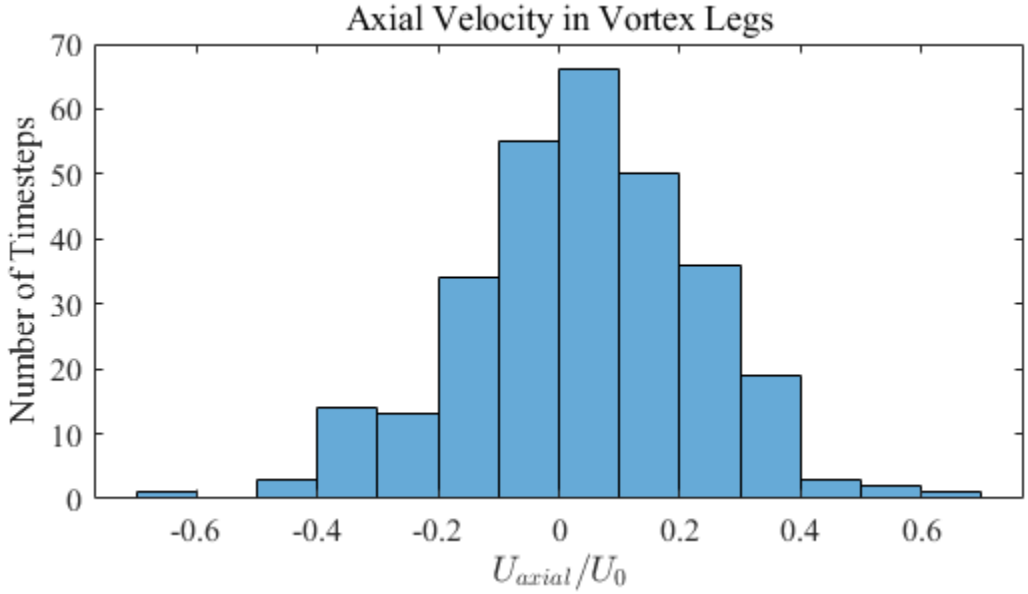


Figure 7.5 Axial Velocity in Secondary Vortex Legs. The axial velocity (U_{axial}, scaled by freestream velocity, U_0) in the secondary vortex legs for Case N.2. There is generally minimal axial flow relative to the surrounding fluid indicating that axial jetting is not present here.

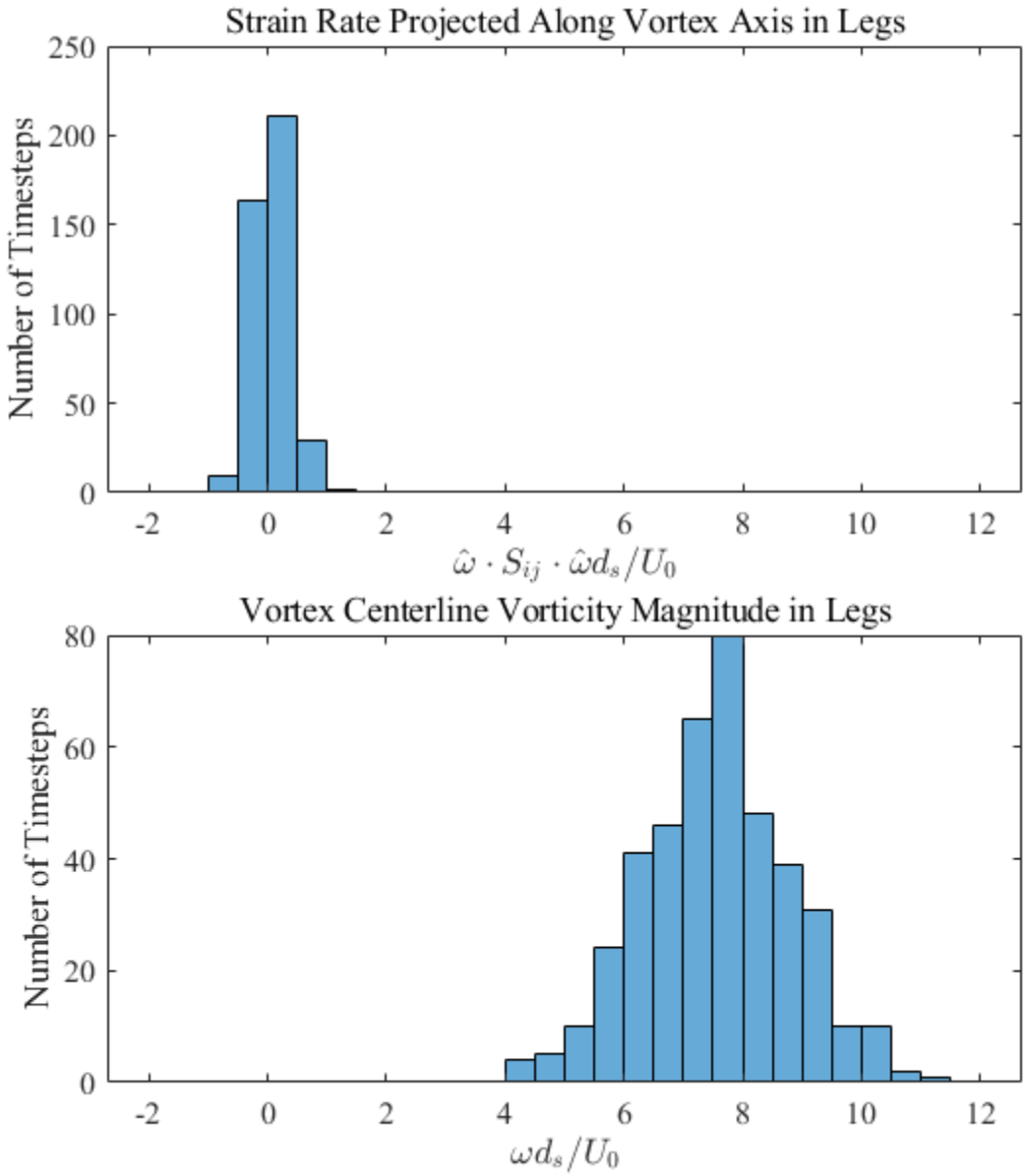


Figure 7.6 Strain Rate Projected Along Vortex Legs. (a) The axial strain rate projected along the axis of the secondary vortex legs ($\hat{\omega} \cdot S_{ij} \cdot \hat{\omega}$ where the hat indicates a unit vector in the direction of the vortex, scaled by secondary foil tip thickness, d_s, and freestream velocity U_0) for Case N.2 is relatively small. (b) The vorticity in the center of the vortex (ω) is much greater than the strain rate along the axis, indicating that the swirling velocity gradients are more important than axial straining gradients for pressure drop in the secondary vortex core.

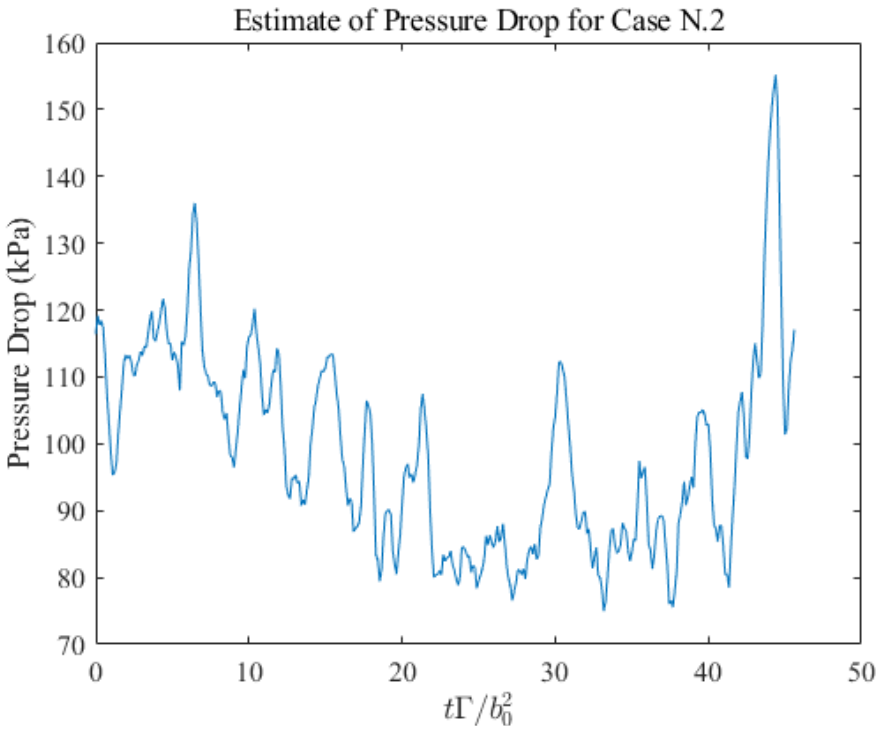


Figure 7.7 Estimate of Vortex Pressure Drop for Case N.2. A trace of the estimated pressure drop in the secondary for Case N.2 over time (scaled by the circulation of the primary vortex, Γ, and the (upstream) separation distance, b_0, for Case N.2).

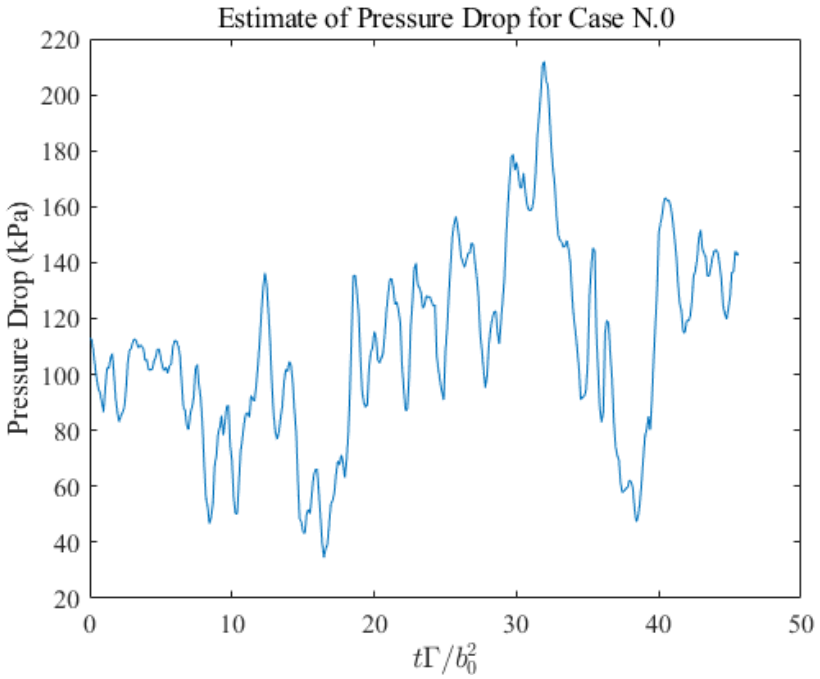


Figure 7.8 Estimate of Vortex Pressure Drop for Case N.0. A trace of the estimated pressure drop in the secondary for Case N.0 over time (scaled by the circulation of the primary vortex, Γ, and the (upstream) separation distance, b_0, for Case N.0).

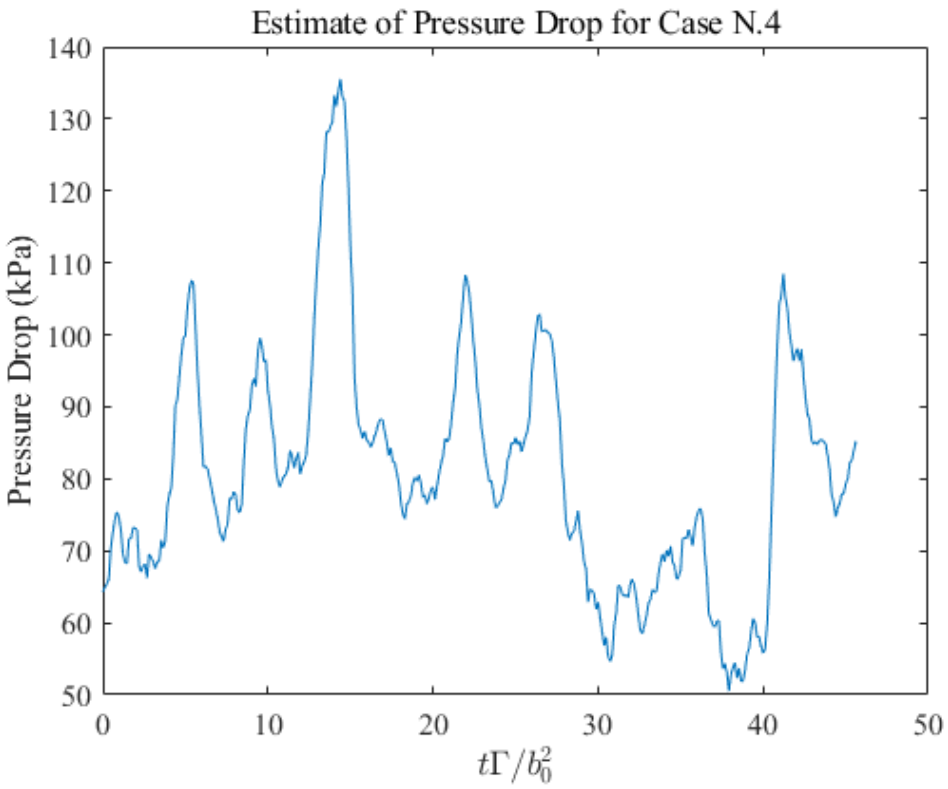


Figure 7.9 Estimate of Vortex Pressure Drop for Case N.4. A trace of the estimated pressure drop in the secondary for Case N.4 over time (scaled by the circulation of the primary vortex, Γ, and the (upstream) separation distance, b_0, for Case N.4).

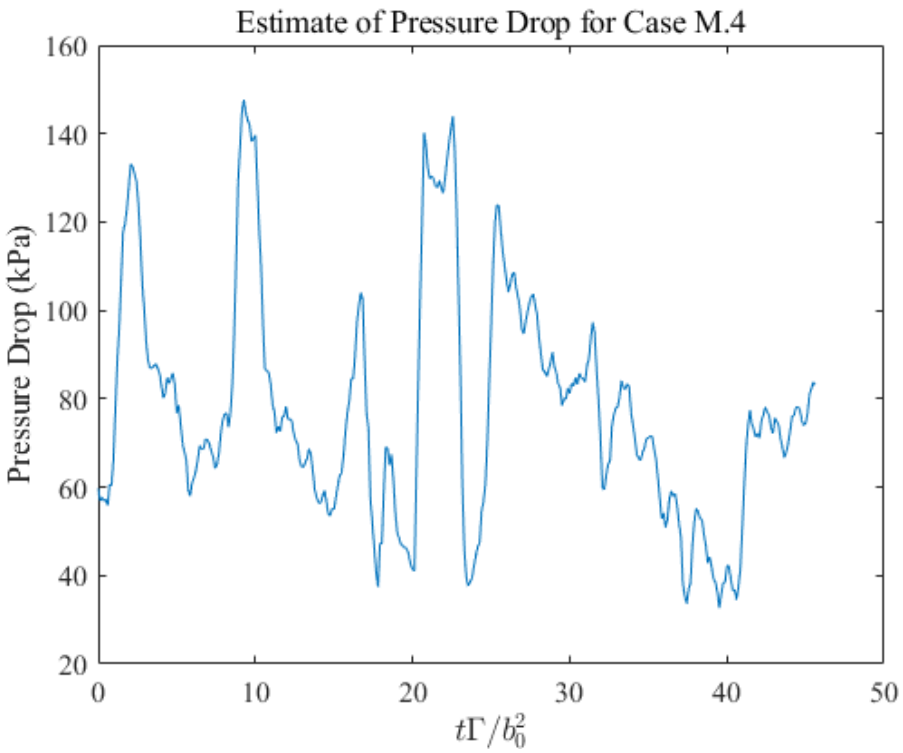


Figure 7.10 Estimate of Vortex Pressure Drop for Case M.4. A trace of the estimated pressure drop in the secondary for Case M.4 over time (scaled by the circulation of the primary vortex, Γ, and the (upstream) separation distance, b_0, for Case M.4).

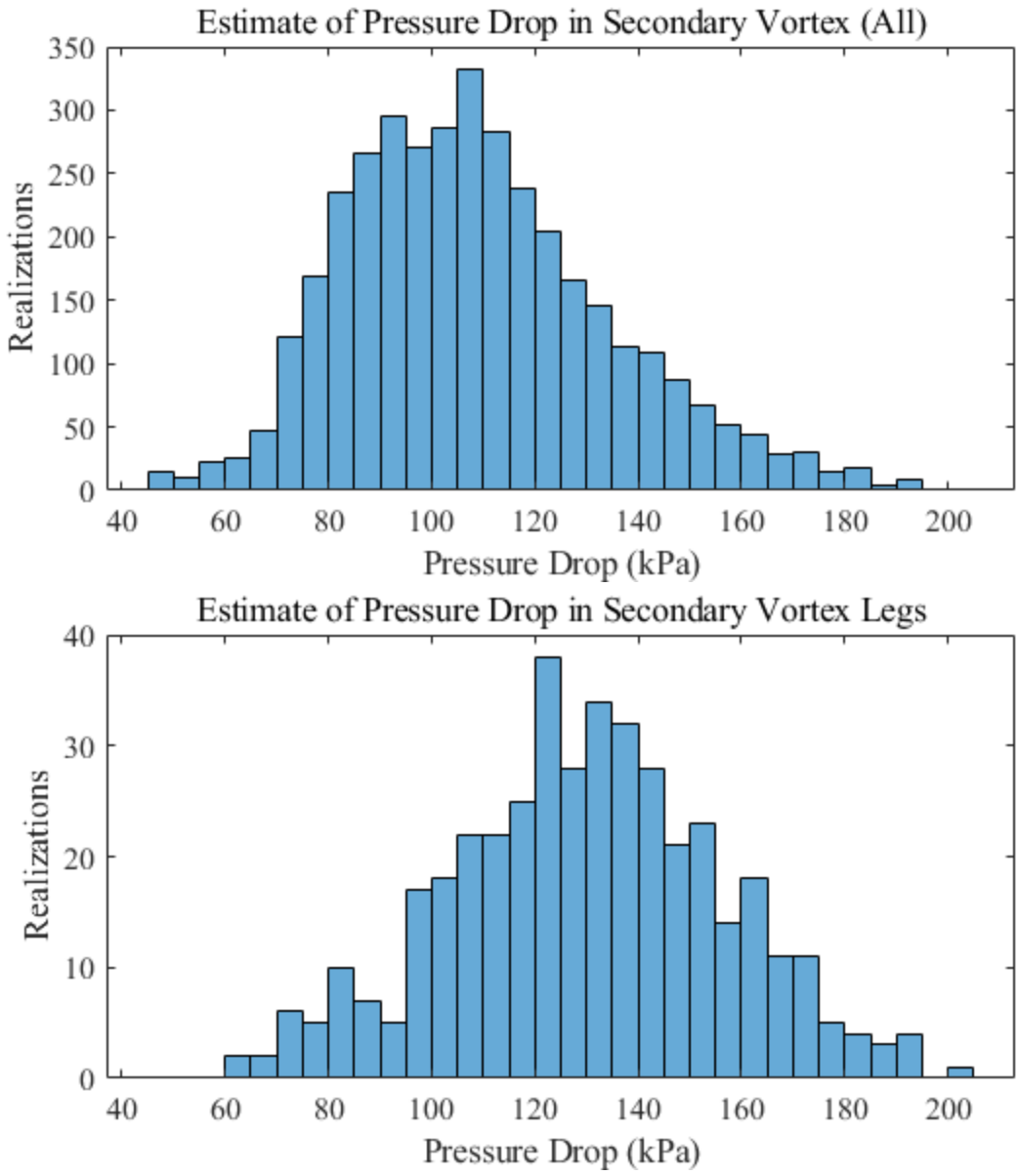


Figure 7.11 Pressure Drop in the Legs of Case N.2. The pressure drop, the reduction in core pressure in the secondary relative to the freestream pressure far from the vortices, is estimated to be greater in regions identified as the legs of the secondary in Case N.2.

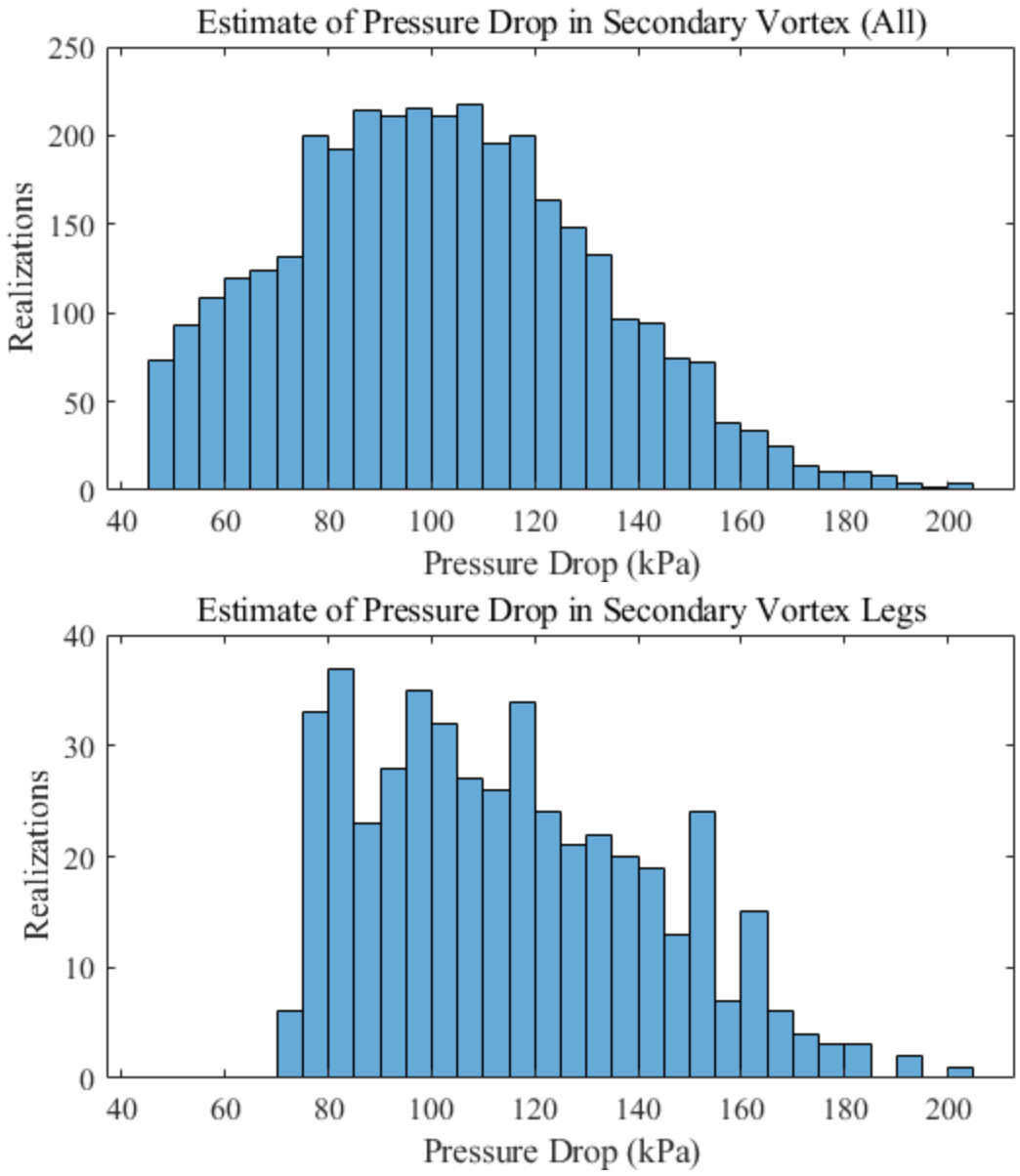


Figure 7.12 Pressure Drop in the Legs of Case N.0. The estimated pressure drop, the reduction in core pressure in the secondary relative to the freestream pressure far from the vortices, is greater in the legs of the secondary vortex than for the secondary vortex overall for Case N.0. However, the difference is lesser for Case N.0 than for Case N.2. This is likely due to the legs in Case N.0 not persisting as long as in Case N.2 or N.4.

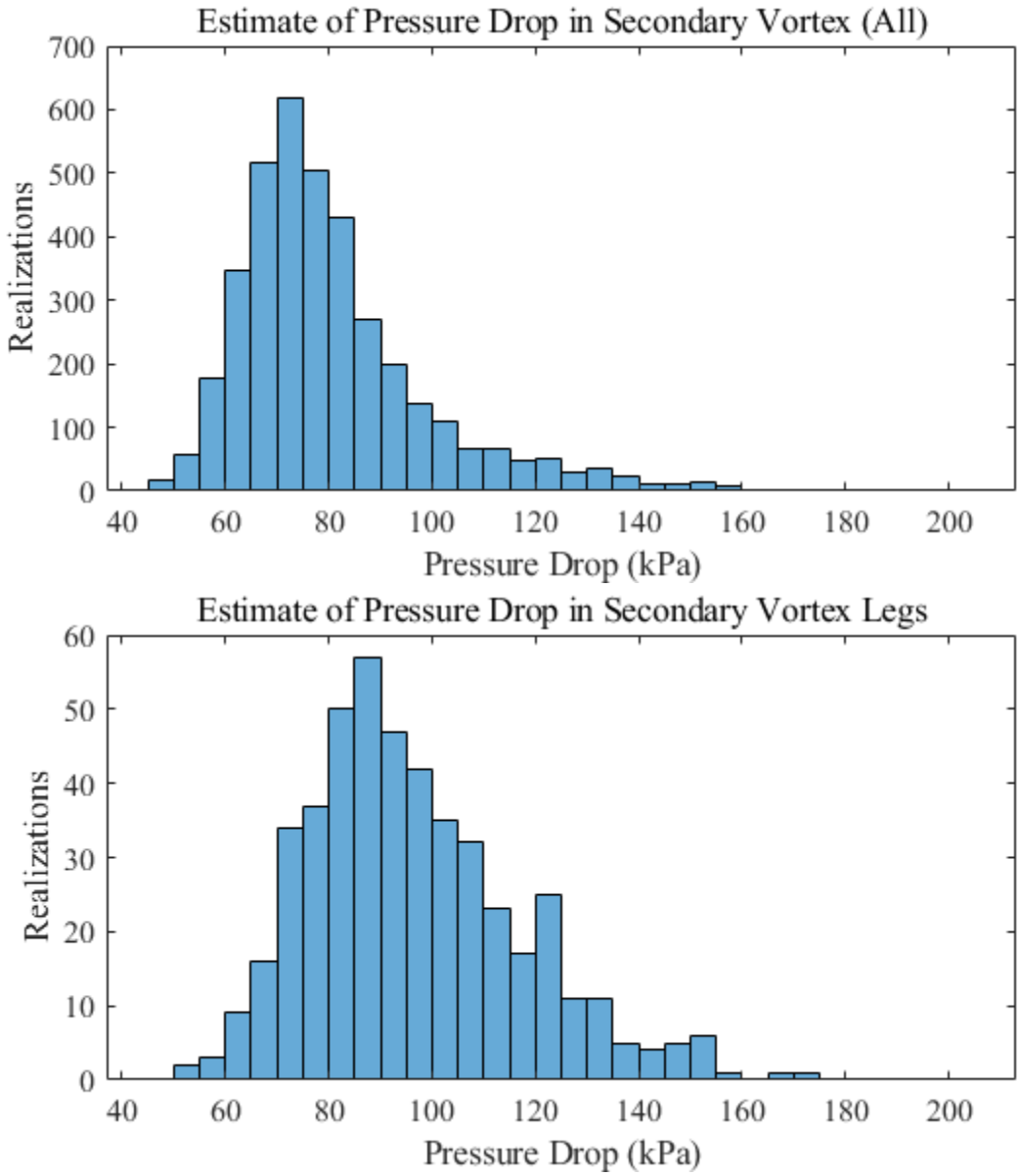


Figure 7.13 Pressure Drop in the Legs of Case N.4. The estimated pressure drop, the reduction in core pressure in the secondary relative to the freestream pressure far from the vortices, over multiple realizations is greater in the legs of the secondary vortex than in the secondary vortex overall for Case N.4, similar to what was noted above for Case N.2.

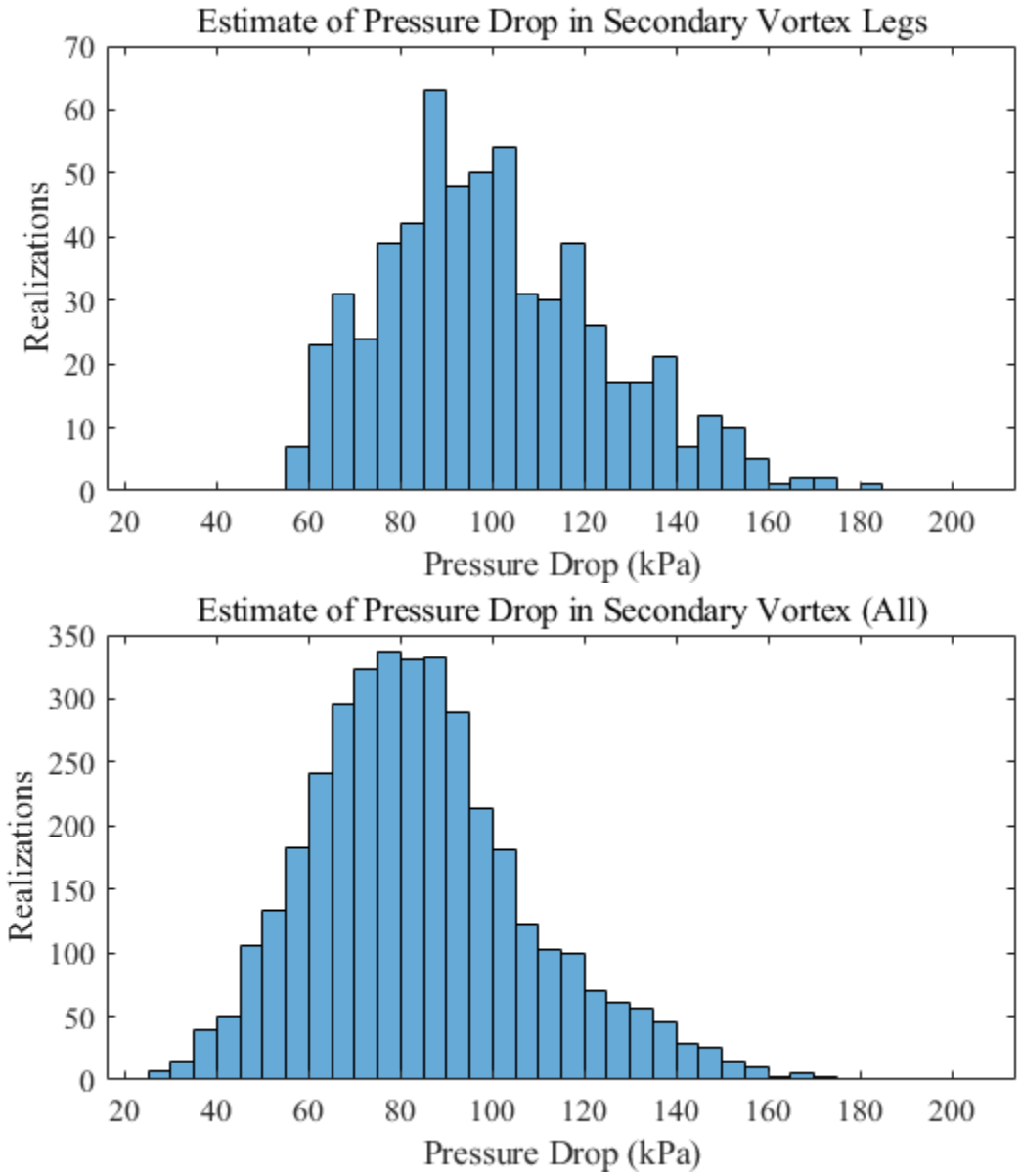


Figure 7.14 Pressure Drop in the Legs of Case M.4. The estimated pressure drop, the reduction in core pressure in the secondary relative to the freestream pressure far from the vortices, over multiple realizations is greater in the legs of the secondary vortex than in the secondary vortex overall for Case M.4, similar to what was noted for Case N.2 and N.4 above.

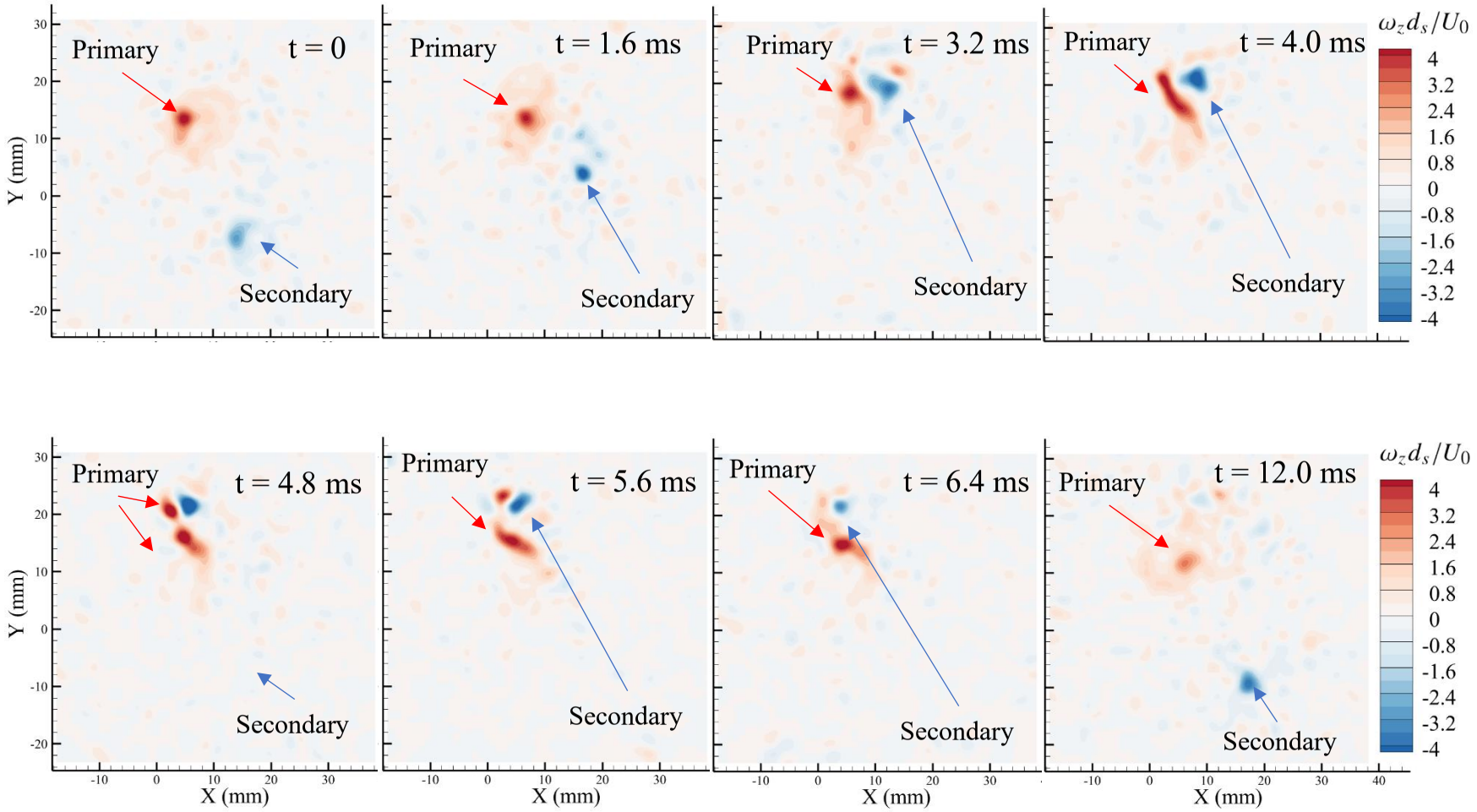
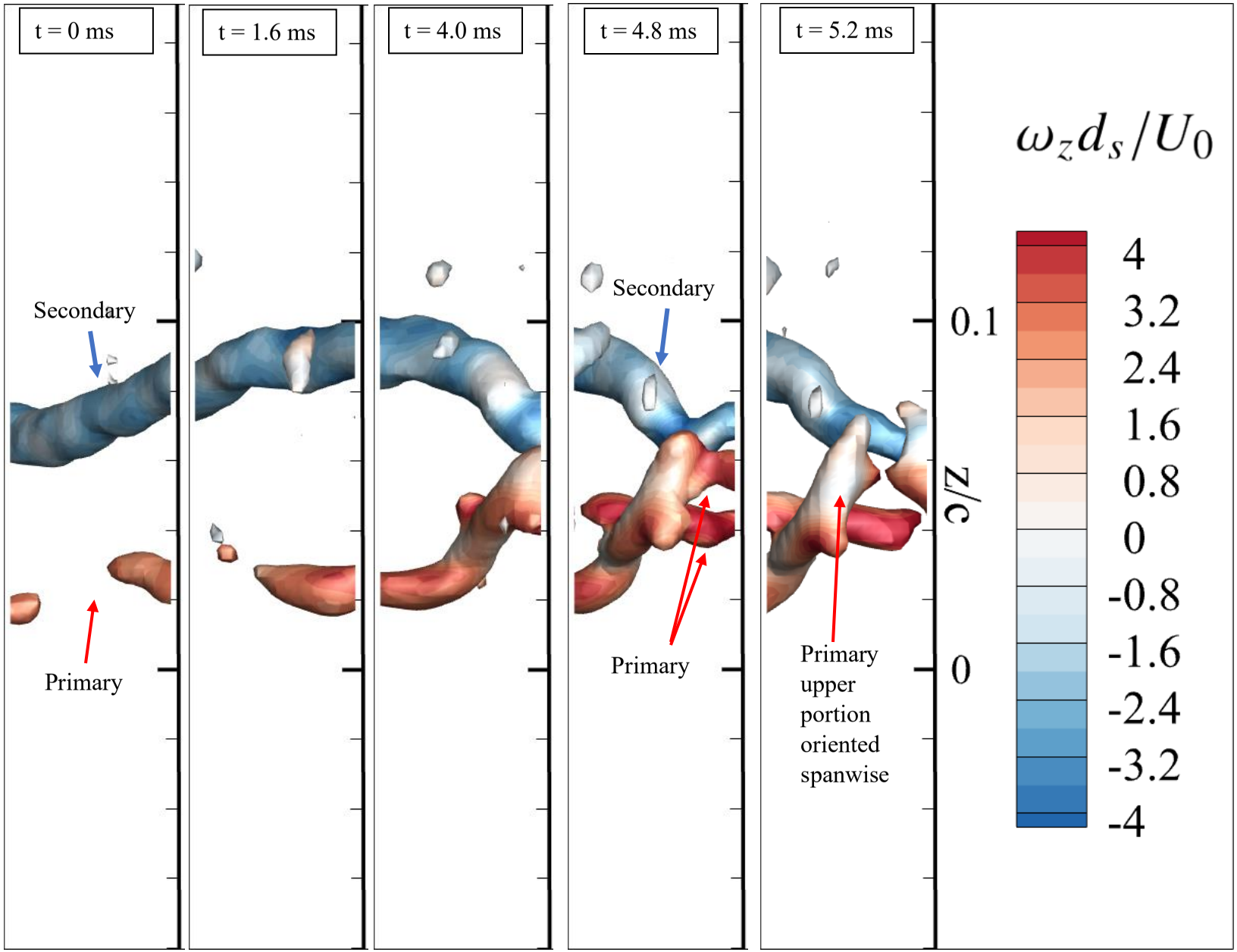

Primary
t = 0
Secondary
Primary
t = 1.6 ms
Secondary
Primary
t = 3.2 ms
Secondary
Primary
t = 4.0 ms
Secondary
$\omega_z d_s/U_0$
4
3.2
2.4
1.6
0.8
0
-0.8
-1.6
-2.4
-3.2
-4
Y (mm)
Primary
t = 4.8 ms
Secondary
Primary
t = 5.6 ms
Secondary
Primary
t = 6.4 ms
Secondary
Primary
t = 12.0 ms
Secondary
$\omega_z d_s/U_0$
X (mm)
X (mm)
X (mm)
X (mm)

Figure 7.15 Vortex Strain-out for Case N.2. (Previous page) A cross section (streamwise normal) of the time evolution of the secondary and primary vortices as the peak of the secondary vortex is drawn near the primary vortex and colored by streamwise vorticity. Shown here for Case N.2, the compact core of the secondary allows it to strain out the primary vortex. Initially, at t = 0, the secondary is in a trough and far away from the primary at this location. As it is drawn near, at t = 3.2 ms and after, the previously near circular cross section of the primary vortex is then deformed to take an elongated shape. By t = 4.8 ms, the primary is strained to the point of almost breaking into two distinct vortex patches. The upper patch is effectively peeled off and apparently merges with the secondary vortex as the secondary vortex breaks apart and orients itself spanwise, although this cannot be seen in this view. This straining out of the primary leads into a reduction in pressure drop in the primary vortex and thus a rise in core pressure, suppressing cavitation. After this interaction, the secondary and primary have a configuration similar to their initial state (as shown at t = 12.0


t = 0 ms
t = 1.6 ms
t = 4.0 ms
t = 4.8 ms
t = 5.2 ms
Secondary
Primary
Secondary
Primary
Primary upper portion oriented spanwise
0.1
z/c
0
$\omega_z d_s / U_0$
4
3.2
2.4
1.6
0.8
0
-0.8
-1.6
-2.4
-3.2
-4

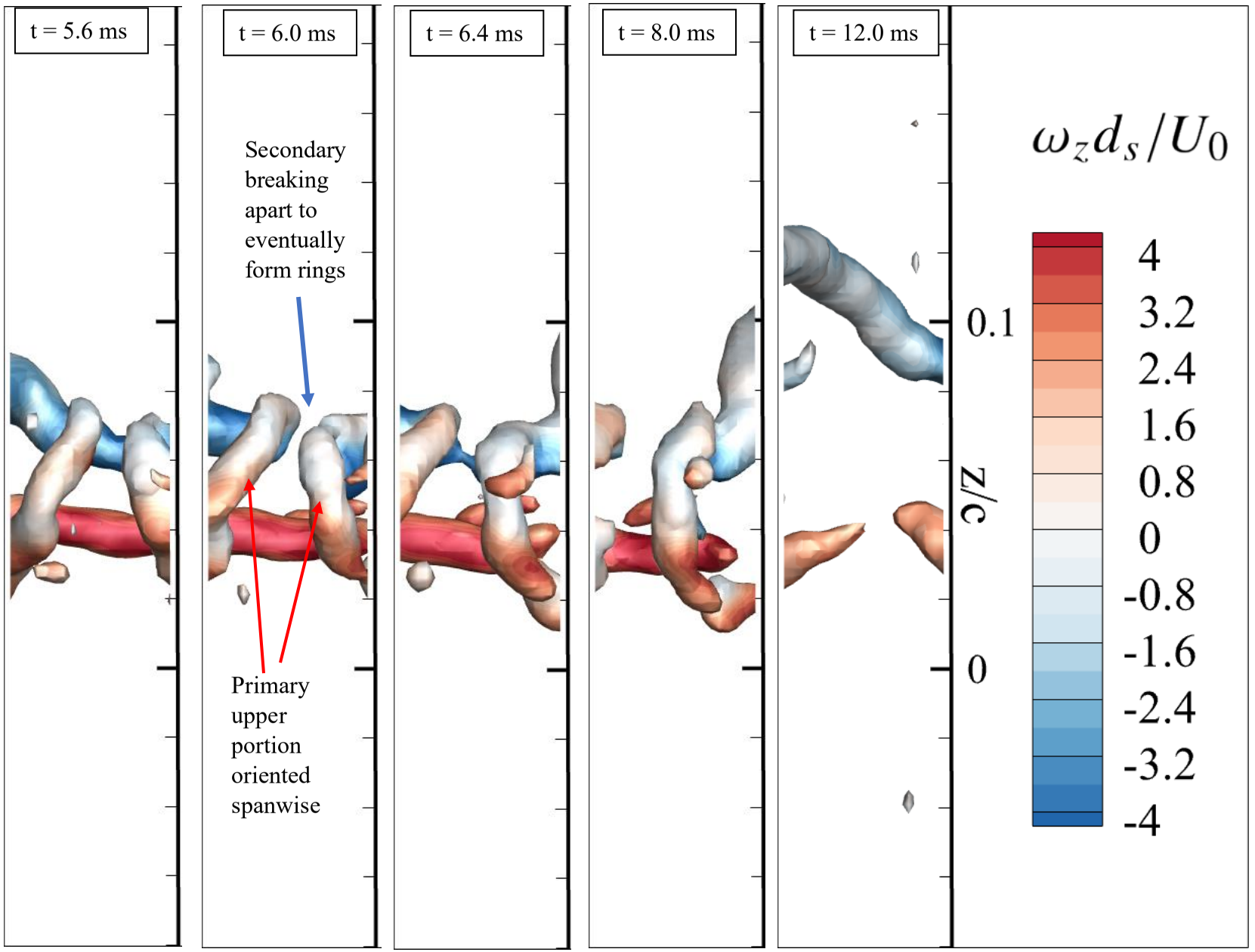

t = 5.6 ms
t = 6.0 ms
t = 6.4 ms
t = 8.0 ms
t = 12.0 ms
Secondary breaking apart to eventually form rings
Primary upper portion oriented spanwise
$\omega_z d_s / U_0$
4
3.2
2.4
1.6
0.8
0
-0.8
-1.6
-2.4
-3.2
-4
0.1
z/c
0

Figure 7.16 Top View of Vortex Strain-out for Case N.2. (Previous pages) A top down view of the time evolution of the secondary and primary vortices as the peak of the secondary vortex is drawn near the primary vortex. Shown here with λ_2 isosurfaces, colored by streamwise vorticity, ω_z (scaled by secondary foil tip thickness, d_s, and freestream velocity U_0), for Case N.2, the compact core of the secondary allows it to strain out the primary vortex. Initially, at t = 0, the secondary is in a trough and far away from the primary at this location. The secondary is drawn up near the primary by its own self induced motion (t = 4.0 ms). By t = 4.8 ms, the primary is strained to the point of almost breaking into two distinct vortex patches, though this appearance is somewhat influenced by the isosurface level. At t = 5.2 ms, the primary upper patch has separated and is now oriented as two spanwise oriented sections. This continues into t = 5.6 ms, and by t = 6.0 ms and after, the secondary has also broken apart as it will begin to form vortex rings. By t = 8.0 ms, it continues to appear that the upper section of the primary has been stripped off and joined to the secondary in spanwise oriented structures. As the vortices convect downstream, they recover back to similar to their prior compact shapes (t = 12.0 ms).

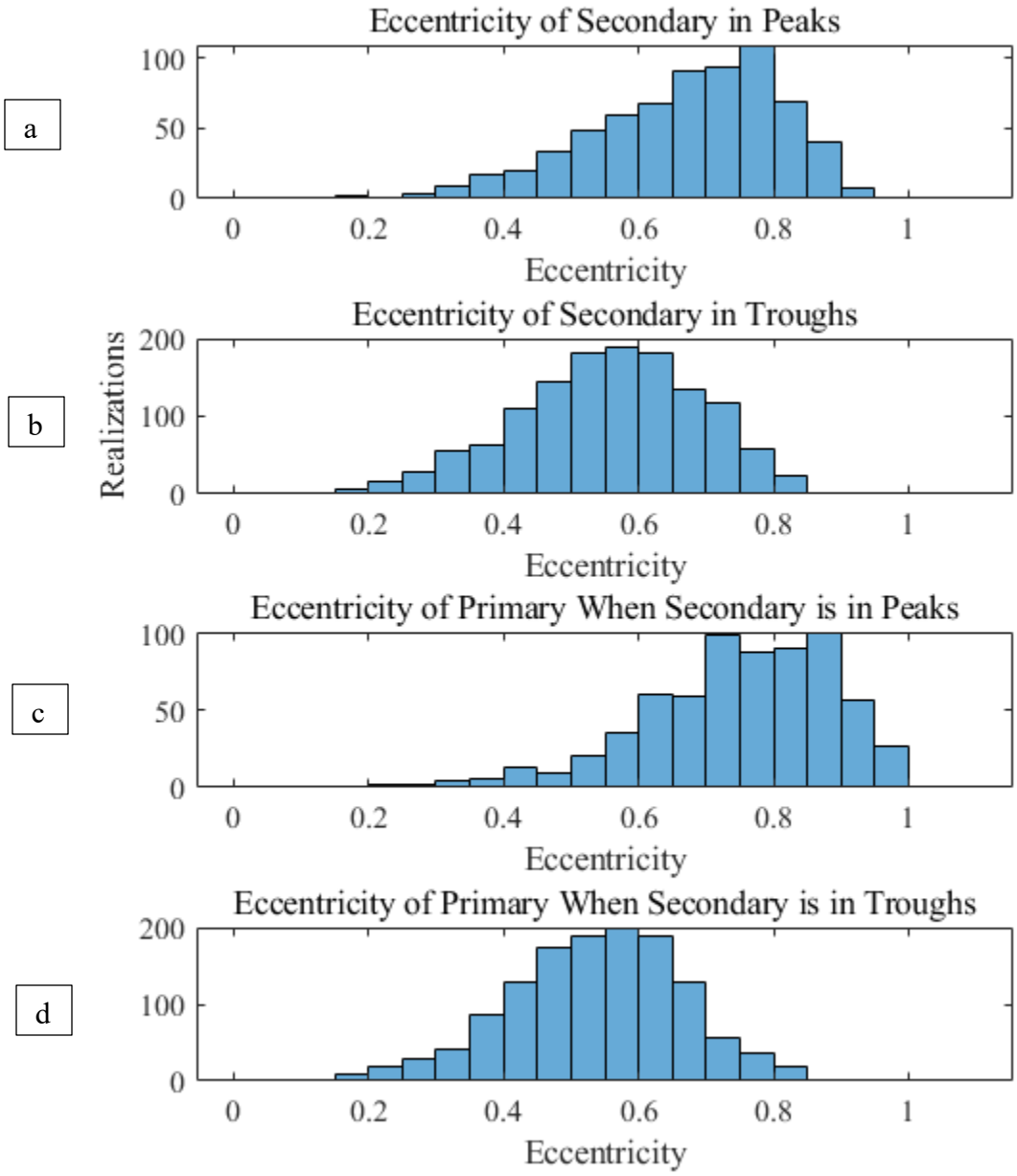


Figure 7.17 Eccentricity of Vortex Components. The eccentricity of the secondary and primary vortices depends on how close they are to each other, as shown here with Case N.2. The eccentricity of both is increased as they draw near to each other (when the secondary is in the peaks (a) and (c)) relative to when they are far from each other (when the secondary is in troughs (b) and (d)). Notably, the primary (c) is made more eccentric than the secondary (a) when the secondary is in a peak even though the secondary is weaker. This is due to the smaller core radius of the secondary.

$r_{c,secondary}/d_s$	M.4	N.4	N.2	N.0
Upstream	0.42 ± 0.03	0.32 ± 0.05	0.37 ± 0.03	0.53 ± 0.08
Midstream	0.36 ± 0.03	0.29 ± 0.05	0.41 ± 0.05	0.69 ± 0.18
Downstream	0.24 ± 0.05	0.23 ± 0.04	0.29 ± 0.04	0.32 ± 0.06

Table 7.1 Radius of the Secondary Vortex at Different Locations and Cases. The radius of the secondary vortex is given across the conditions at the various locations. There is a dramatic decrease in the radius between the midstream and downstream due to the substantive stretching between the midstream and downstream measurement locations.

$\Gamma_s/(U_0C)$	M.4	N.4	N.2	N.0
Upstream	-0.046 ± 0.008	-0.039 ± 0.003	-0.066 ± 0.04	-0.10 ± 0.01
Midstream	-0.039 ± 0.010	-0.035 ± 0.004	-0.065 ± 0.004	-0.095 ± 0.015
Downstream	-0.028 ± 0.006	-0.029 ± 0.003	-0.049 ± 0.007	-0.046 ± 0.013

Table 7.2 Circulation of the Secondary Vortex at Different Locations and Cases. The circulation of the secondary vortex is given across the conditions at the various locations. While circulation should be conserved due to the minimal effects of viscosity, it does not appear to be conserved here. This is likely due to an imperfect spatial resolution to capture the high vorticity in the core of the secondary.

$r_{c,secondary}/d_s$	M.4	N.4	N.2	N.0
Legs	0.21 ± 0.04	0.21 ± 0.04	0.27 ± 0.04	0.30 ± 0.06
Troughs	0.24 ± 0.05	0.24 ± 0.04	0.30 ± 0.04	0.35 ± 0.04
Overall	0.24 ± 0.05	0.24 ± 0.04	0.29 ± 0.04	0.32 ± 0.06

Table 7.3 Radius of the Secondary Throughout the Topography. The radius of the secondary in the downstream varies depending on where in the secondary vortex it is measured. The legs of the secondary have the smallest radius as they are stretched the most.

Chapter VIII

Cavitation Inception in the Interaction of a Pair of Counter-Rotating Vortices

Characterization of Freestream Nuclei

Incipient cavitation in the freestream is generally dependent on the local pressure magnitude below the liquid vapor pressure and the presence of nuclei that initiate the phase change of cavitation. Depending on the nuclei strength (size), liquid tensions (i.e. negative absolute pressures) may be necessary for cavitation inception. Treating cavitation nuclei as spherical bubbles of contaminant gas in the liquid, the critical threshold of pressure required for cavitation can be related to the bubble radius as

$$P_{critical} = P_{vap} - \frac{4S}{3r_{critical}}$$

where *S* is the surface tension, as discussed above. This is known as the Blake critical radius, and we shall use that later to evaluate behavior of the range of nuclei.

Recall that the natural nuclei distributions exist as an equilibrium between dissolved gas and nuclei. Subjecting a bolus of water to lower pressure will reduce the saturation concentration of the dissolved gas and lead to the outgassing of the water. Outgassing here refers to the generation of nuclei as dissolved gas comes out of the solution. The relation between saturation concentration and pressure is given by Henry's law

$$p_{gas} = H\chi_0$$

where p_{gas} is the partial pressure of the gas, H is the Henry's law constant, and χ_0 is the concentration of the gas dissolved in the liquid.

In a natural nuclei population, not all nuclei are of the same size. To characterize the distribution of nuclei sizes and their concentrations, a cavitation susceptibility meter (CSM) was employed in this study, and a detailed description of the CSM used here is offered in Chapter 2. For the inception experiments done in the present study, four different nuclei concentrations were used. High and low nuclei concentration experiments were performed for each foil configuration for a range of freestream pressures. As the foils needed to be switched between matching and non-matching cases, the nuclei could not be perfectly matched between the matching and non-matching cases which gives rise to the two sets of "high" and "low" concentration measurements. These "high" and "low" concentrations were roughly approximated by the dissolved oxygen concentration with high being 35% (± 2%) and low being 13% (± 2%) of saturation at atmospheric pressure. The nuclei concentrations were measured before and after each inception run, so the small differences between the matching and non-matching nuclei concentrations are known and can be accounted for. To ensure that the effects of nuclei outgassing and drifting are represented in the measurements, the tunnel was allowed to run at full experimental speed and low enough pressure to cause developed cavitation in the vortices before the initial CSM measurements were made. Ideally, this should set the nuclei distribution in the appropriate point of equilibrium such that it does not change due to the cavitation inception measurements. Figures 8.1 and 8.2 show the nuclei measurements for the non-matched and matched foil inception experiments.

Combined High-Speed Video and Acoustic Characterization of Inception

While prior chapters made extensive use of volumetric velocimetry techniques, such methods were not feasible for the study of inception. First, a near spherical cavitation bubble with a radius on the order of the typical vortex radius here can scatter far more light than a typical PIV particle and has the potential to damage the cameras used. For the cavitating flows considered here, the cavitation bubbles generally take an oblong shape, matching the topography of the secondary vortex. With this shape, the scattering of light is reduced relative to a spherical bubble, but such a large structure could potentially still scatter enough light to damage the imaging equipment. To mitigate this issue, using fluorescent particles and filtering out the wavelength of the laser light will prevent such bright reflections from striking the camera sensor. However, as noted in Chapter 3, appropriate fluorescent particles were not available in sufficient quantity to be used for the present study. Beyond concerns about damaging the cameras used, accounting for the change in the index of refraction between the vapor phase cavitation bubble and surrounding liquid water is non-trivial. While a particle tracking approach such as STB may be less likely to generate false tracks inside a bubble, the robustness of Tomo-PIV means velocity fields through a cavitating vortex will be found, as in Ye *et al*. (2023).

Instead of volumetric velocimetry, a combination of high-speed video and acoustic measurements are used here to characterize the inception in the secondary vortex. These two measurement devices can be synchronized, however, the amount of data generated by a camera is orders of magnitude more than that generated by a hydrophone, so the cameras only recorded for a portion of the length of hydrophone measurements. The video measurements confirm that inception occurs first in the secondary for the vortex configurations considered. This is shown by the observed matching in topography of the incipient cavitation with topography of the secondary vortex and not the primary vortex. Figure 8.3 and Figure 8.4 show examples of

cavitation inception in the secondary vortex from Case N.4. Figure 8.3 shows a rapid expansion of a cavitation bubble in a leg of a secondary vortex instability loop. After its rapid growth, the bubble persists for several milliseconds, but only weakly oscillates before collapsing again. Figure 8.4 shows a similar process, but the cavitation bubble does not expand as much and collapses more rapidly than the bubble in Figure 8.3. Figure 8.5 shows an example of inception in the secondary vortex with simultaneous hydrophone and video measurements.

After the first CSM runs, for the four different foil configurations detailed in this thesis, the inception event rate was counted acoustically at a range of freestream pressures. Freestream speed was held fixed at 10 m/s, so the varying pressure was the sole variable in changing cavitation number. While the uncertainty in the measurement of freestream static pressure is less than 1%, the pressure for the following experiments was controlled manually, and the uncertainty for freestream pressure in these measurements is ±0.5 kPa. A hydrophone was used to detect inception events over 150 seconds at each condition. As mentioned earlier, due to the amount of storage required by video, long time measurements were only feasible acoustically. The number of inception events was divided by this time span to give the event rate. The acoustic signal of the hydrophone was continuously sampled at 500 kHz over the measurement duration. Counting and characterizing the inception events was processed using a algorithm in Matlab.

To process the acoustic data, a high pass filter was used (cutoff frequency 500 Hz) to eliminate noises emanating from the tunnel and motor, and peak amplitudes above a threshold were found. This threshold was varied as certain cases were generally quieter than others. Around these peak amplitudes, a spectrogram was taken. If the acoustic event had a sharp peak (i.e. broadband in frequency and short in duration on the spectrogram), the event was recorded as a “pop”. An example pop from Case N.4 at a freestream pressure of 100 kPa is shown in Figure

8.6. If the event had a consistent dominant frequency and a measurable duration of several milliseconds, the event was recorded as a “chirp”, of which an example from Case N.4 at a freestream pressure of 100 kPa is given in Figure 8.7. Some events had pops that lead into or followed chirps, as shown in Figure 8.8 and Figure 8.9, again from Case N.4 at 100 kPa. These events were regarded as chirps as well. The pop may lead or lag the chirp depending on whether the initial expansion of the bubble or eventual collapse is more rapid. If none of the above were not true, the acoustic event was labeled as falsely indicated by the peak amplitude and therefore ignored.

Accumulating all events, pops and chirps, the resulting event rates are found for a given foil configuration and freestream cavitation number. The results are plotted in Figure 8.10 for Case N.0. In this and the following cases, the background nuclei concentration is plotted as well with the modification that it is multiplied by the volume flux of the secondary vortex to give a nuclei flux instead of nuclei concentration. Given the rather strong secondary in this case, only a small range of freestream cavitation numbers could be measured for Case N.0 and only at low freestream nuclei concentrations. At lower pressures, the vortices had developed cavitation as opposed to incipient cavitation. Significant leakage of water from the cavitation channel made higher pressures than those shown infeasible. With higher dissolved gas concentration, the occurrence of developed cavitation or pseudo cavitation in the secondary vortex at a feasible range of pressures was exacerbated, so measurements were not taken at the higher dissolved gas concentration.

The inception rates and nuclei (flux rate) for Case N.2 are shown in Figure 8.11. A larger range of freestream pressures is possible here, and accordingly, a larger range of inception event rates is documented as well. Note that again, the nuclei flux is on the same order of magnitude

as the inception event rate, suggesting that the key element for relating the nuclei and inception events is the pressures (or specifically, tensions) that the nuclei undergo in the cores of the secondary vortices. Similar results are shown for Case N.4 and Case M.4 in Figures 8.12 and 8.13.

Relating Nuclei Content to Observed Cavitation Event Rate

The prior chapter detailed the range of pressure drops measured in the secondary vortex in the downstream region. Using these to estimate the inception event rate requires the knowledge of nuclei detailed earlier in this chapter. However, additional modeling assumptions and decisions must be considered to use these nuclei distributions.

First, it is initially assumed that the nuclei present in the secondary are the only nuclei available to incept due to the pressure drops in the secondary. The nuclei available for cavitation can then be assumed to be equivalent to the nuclei distribution multiplied by the volume flux of liquid in the core of the secondary. This assumption could be modified slightly to account for the ability of the secondary to capture nuclei. Just as the seeding particles are expelled from the vortex due to their higher density than the surrounding water, buoyant nuclei bubbles may be captured from the surrounding flow and brought into the secondary cores. Oweis *et al*. (2005) examined this situation in detail with a combination of computational modeling and experiments on nuclei generated a small distance from a vortex. Using their approach, the effects of nuclei capture can be estimated, considering nuclei as individual bubbles of non-condensable gas.

A one-way coupled model, with the bubble transported by the flow but the flow unaffected by the bubble, was created. The model developed assumes that the bubbles experience small radial accelerations and that the Basset history term, gravitational effects, and volume variation effects are small. This then leads to a balance between pressure gradient forces

and drag forces on the bubble. Assuming a Gaussian vortex, this then leads to an estimate for capture time for a bubble. By setting this capture time to be equal to the time required for the vortex to transit from the foils to the location of most likely inception, $\tau_{transit}$, the capture radius of the vortex can then be estimate by

$$r_{capture} = \sqrt[4]{\tau_{transit} \cdot \frac{2}{9\pi^2} \cdot \frac{r_{nuclei}^2 \Gamma^2}{\nu}}$$

where none of the terms are non-dimensionalized and r_{nuclei} is the radius of the contaminant gas bubble considered. This radius is estimated by the Blake's critical radius introduced above (so, $r_{nuclei} = r_{critical}$ over a range of critical tensions). Figure 8.14 shows the increase in capture radius for nuclei between 1 and 10 micron. These effects depend on the critical radius of the nuclei, so the differences between capture radius must accordingly be weighted by the prevalence of nuclei of that size in the eventual event rate calculation. Using the Blake's critical radius and CSM measurements of the present study, it is found that the prevalence of nuclei of 1 micron radius is approximately 5 orders of magnitude greater than nuclei of 10 micron radius. While the apparent increase in capture radius is significant for larger bubbles, the larger bubbles are uncommon, so the overall effect of capture effects is generally less than doubling the effective radius of the vortex.

Another assumption to consider is whether growth of the nuclei due to diffusion of dissolved gas is negligible or significant. As the nuclei are in the cores of the secondary, they are at reduced pressure, perhaps even tension. In such a case, the water is locally supersaturated, and dissolved gas will tend to diffuse into the nuclei. With more non-condensable gas inside them, the nuclei will be larger and therefore require less tension to incept. This effectively could shift the nuclei distribution curve to the right in Figure 8.1. These effects can be estimated by

examining the timescale of diffusion relative to the time it takes the flow to travel between the vortex generation at the foils and the most likely point of cavitation inception. Following Brennen (1995), we estimate the timescale of significant bubble growth via diffusion with

$$\tau_{diffusion} = \frac{\rho_{gas} r_{bubble}^2}{D_{gas} \Delta\chi}$$

where D_{gas} is the diffusion coefficient of air in water and $\Delta\chi$ is the concentration differential between the bubble and the far field. The value of D_{gas} is generally accepted to be around $2 \cdot 10^{-9}\ m^2/s$ (Brennen 1995). Gowing (1992) examined this coefficient over a decade of Reynolds number in turbulent pipe flow, a situation where diffusion is likely higher than the present vortical flow and found only a modest increase. Using the higher values reported by Gowing (1992), overestimating the speed of diffusion, the timescale for diffusion is still substantially greater than the time the nuclei spend traveling in the vortex before inception

$$\frac{\tau_{diffusion}}{\tau_{transit}} \gg 1.$$

The effects of dissolved gas diffusion then can be neglected in the model of cavitation inception.

With the noted inclusion of the effects of vortex capture of nuclei and exclusion of the effects of nuclei growth due to diffusion, an estimate of inception event rate can now be found. This estimate involves considering the nuclei flux through the secondary vortex core and determining what portion of those nuclei are likely to cavitate given the tensions in the secondary vortex. These tensions are obtained from the estimations of pressure drop discussed in the prior chapter subject to the varied freestream pressures used in the inception study. The resulting estimation of the inception event rate, *e*, follows the relationship

$$e = \sum \dot{q}_{nuclei}(P_{critical}) \cdot prob(P_{core} < P_{critical}) \Delta P_{critical}$$

where the summation is taken over the range of critical pressures measured with the CSM. The nuclei flux rate, $\dot{q}_{nuclei}$, is a function of the critical pressure as well as the volumetric flux of carrier liquid through the secondary. $prob(P_{core} < P_{critical})$ is the probability that the pressure in the core is below the critical pressure of the nuclei considered, which depends on the freestream pressure and distribution of pressure depressions (for P_{core}) and on the size of the nuclei (for critical pressure). This summation is repeated for the different vortex configuration cases and different freestream pressures.

Using the estimates of event rates from above, the results can then be compared to the event rates observed with acoustics measurements. Case N.0 shows good agreement over a limited range of conditions, as demonstrated in Figure 8.15. Case N.2 shows some agreement between the predicted inception event rate and the observed rate over a significantly larger range than what was available for Case N.0, as shown in Figure 8.16. Case N.4 similarly shows some agreement between the predicted and observed event rates over a large range, as shown by Figure 8.17. The uncertainty bands for all the predicted cases are dominated by the uncertainty in the nuclei distribution as described in Chapter 2. *Given the reasonable agreement between the predicted and observed rates of cavitation inception, these results imply that the simple model of cavitation inception in a stretched secondary vortex captures the essential physics connecting the nuclei population, the underlying dynamic flow field, and the resulting observed inception rates.*

Nuclei Content, Vortex Minimum Pressure, and Acoustic Emission

As has been shown by the works of Oweis *et al*. (2004), Chang and Ceccio (2011), and Choi *et al*. (2008), the acoustic emissions of incipient cavitation in vortices depend on the

properties of the vortices themselves as well as the properties of the nuclei. The following description of inception physics in vortices coalesces the conclusions of those papers.

Smaller nuclei require greater tensions to incept. After the critical tension is reached, the pressure differential driving bubble growth is large, so the bubble's volumetric acceleration is correspondingly large. This large acceleration makes the bubble likely to overshoot its equilibrium radius at the surrounding pressure, so after overshooting, it collapses rapidly. This rapid expansion and collapse lead to broadband pops. Peak acoustic amplitude is driven by the volumetric acceleration of the bubble, which is greater for smaller nuclei. Thus, smaller nuclei should lead to louder events that are more likely to pop.

In contrast, larger nuclei require lesser tensions to incept. For a very large nucleus (O(100 μm)), just reaching vapor pressure will lead to inception. In such a case, there is less of a pressure differential driving bubble growth. Accordingly, the volumetric acceleration of the bubble is smaller, making the acoustic emissions quieter. With the slower expansion of the bubble, the overshoot is less, and the rebound is correspondingly slower. This leads to an exchange of angular momentum between the bubble and the liquid. As the bubble expands, its moment of inertia increases, and its angular velocity slows. The pressure drop in the core of the vortex is proportional to this angular velocity, squared, so the pressure rises, and the bubble shrinks down accordingly. This leads to an increase in angular velocity as the moment of inertia decreases again. Oscillations between the interplay of these effects leads to an oscillating bubble radius and a corresponding chirp at a consistent frequency related to the vortex properties. While the frequency of the chirp is governed by the vortex properties, the likelihood of this chirping process occurring as opposed to popping is a function of the critical tension of a given nucleus as

well as the vortex properties. The typical timescale for oscillations of vortex cavitation bubbles of Choi *et al*. (2009) follows from the vortex time-scale

$$\tau_{vortex} = \frac{4\pi r_c^2}{0.715 \cdot \Gamma}$$

and they observed the period of volume oscillations to be within a range of 40% of this time scale.

Overall, smaller nuclei, corresponding to lower dissolved gas concentrations, require greater tensions to incept and therefore are more likely to pop. Larger nuclei, present in higher dissolved gas concentration situations, are more likely to chirp, since they require much less tension to incept (Choi *et al*. (2009)). This is also observed in the present inception experiments. Figure 8.18 shows the percentage of popping of cases for Case N.2, where the low DO case (with smaller nuclei) is more likely to pop than the high DO case (with larger nuclei). There is also a slight U-shaped trend wherein a lower freestream pressure and a higher freestream pressure tend to lead to more pops while pressures in between lead to more chirps. This reflects the balance between the interplay of the vortex dynamics and nuclei. At the lowest freestream pressures, very small nuclei can now be activated. As these are small, once these nuclei incept, they overshoot an equilibrium radius and thus pop. With higher freestream pressures, the typical nuclei that cavitate are of a larger size. These do not experience as explosive of growth and thus are more likely to chirp. As the freestream pressure is further raised, it is likely these same larger nuclei that incept. However, with a higher far field pressure, they then can no longer sustain the dynamic equilibrium involved in chirping and instead collapse readily. This U-shaped trend is present in the prior work of Chang and Ceccio (2011), though that did not consider as large a range of cases of vortex configurations.

Case N.4 also displays this U-shaped trend, as shown in Figure 8.19. Again, the inception events are more likely to pop for the lower DO content case because the nuclei present are smaller. This holds still for Case M.4, demonstrated in Figure 8.20, though the differences are reduced and the system generally tends to pop more so than for the non-matched cases. Case N.0 is not shown by itself as there was little room to make comparisons with the limited data available. Figure 8.21 shows the percentage of pops for all non-matched cases (N.0, N.2, and N.4) at low DO content. With the widest range of freestream pressures, this demonstrates that U-shaped trend again. It should be noted that at higher pressures for the low DO cases, there are very few inception events (<10).

Beyond the likelihood of chirping as opposed to popping, there is some reduction in the length of chirps with increasing freestream pressure, as noted in Figure 8.22 for the low DO non-matched cases and Figure 8.23 for the high DO non-matched cases. Figure 8.24 shows the duration of chirps for both DO contents for the matched cases. The uncertainty in chirp duration depends primarily on the variability of the distribution of the chirps themselves. As there are significantly fewer inception events with the low DO tests, the uncertainties in those cases are much higher. The chirping frequency does not show clear trends relating to freestream pressure nor does chirping frequency vary significantly across the different vortex cases. In all cases, the mean chirping frequencies were around 3 to 4 kHz with standard deviations of between 0.5 and 1 kHz with the higher standard deviations for cases with limited events due to elevated freestream pressures. These frequencies agree with what was observed by Chang and Ceccio (2011) and predicted by Choi *et al*. (2009). For example, $\frac{1}{\tau_v} = 0.715 \cdot \Gamma/(4\pi r_c^2)$ is 3.1 kHz for both cases M.4 and N.4 while it is 3.3 kHz for Case N.2. That M.4 and N.4 would have the same frequency is unexpected from the upstream measurements as their core radii are rather different and their

circulations are close. However, in the downstream region where inception is most likely, their core radii are close, so by theory they should have comparable frequencies.

Conclusions

This chapter unites the estimation of pressure of the prior chapter with the measurements of nuclei in the channel to estimate cavitation inception in the secondary vortex. The results are comparable to the acoustically measured rates of inception. The uncertainty of the estimates is significant, largely due to the uncertainty of knowing the underlying nuclei distribution. Nevertheless, the results suggest that the underlying assumptions in estimating the inception event rate are valid and that the physics represented are the essential physics. These results show that the simple model of cavitation inception in a stretched secondary vortex captures the essential physics connecting the nuclei population, the underlying dynamic flow field, and the resulting observed inception rates.

Further, these results provide additional support for the conclusions regarding the acoustic emissions of stretched vortices in Chang and Ceccio (2011). The likelihood of chirping as opposed to popping depends on the freestream pressure and the nuclei present. The model for inception chirping frequency as noted by Choi *et al*. (2009) predicts the observed frequency well.

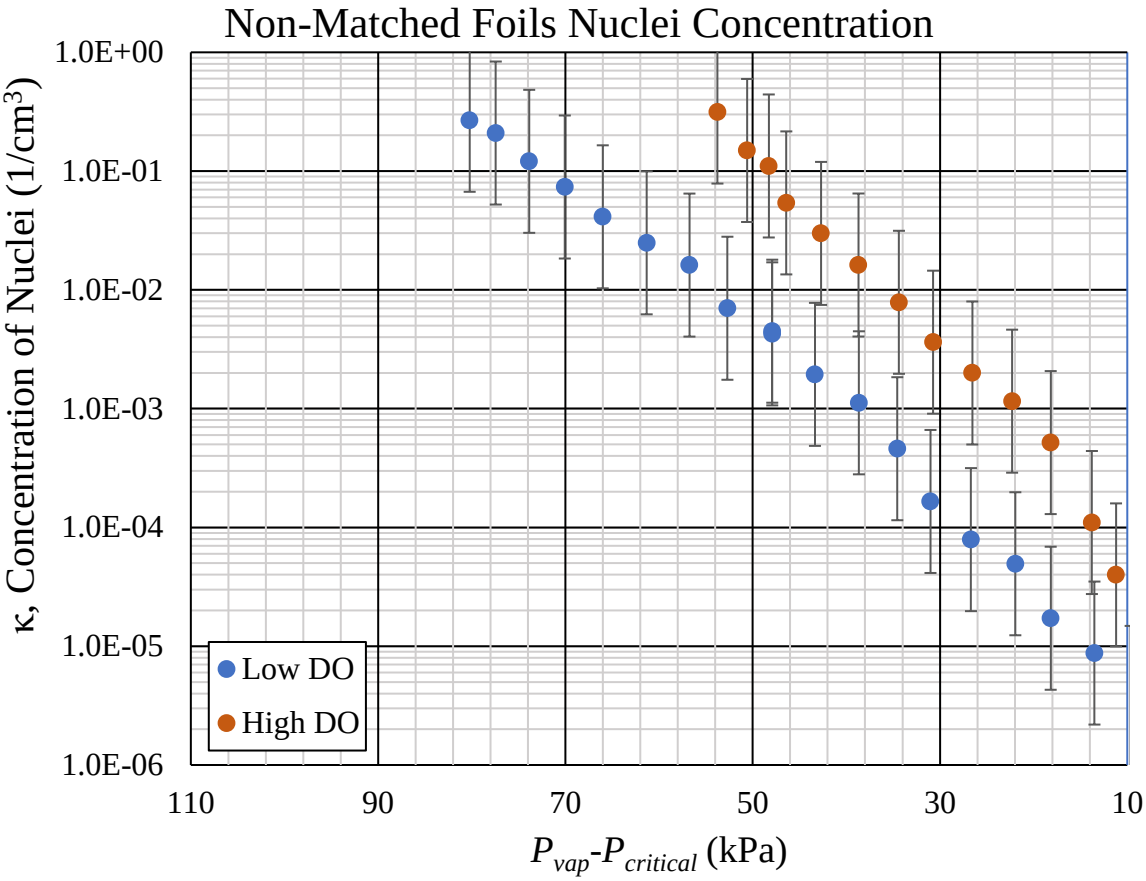


Figure 8.1 Non-Matched Foil Nuclei Concentration. The inception experiments in this thesis were conducted at two different dissolved gas contents, approximated by dissolved oxygen (DO). The Low DO case corresponds to 13% (+/- 2%) of saturation at atmospheric pressure. The High DO case corresponds to 35% (+/- 2%) of saturation at atmospheric pressure. At each dissolved gas content, the nuclei content was measured with a CSM to give the nuclei concentration shown here. The data here was for experiments taken with the non-matched foils conditions N.0, N.2, and N.4.

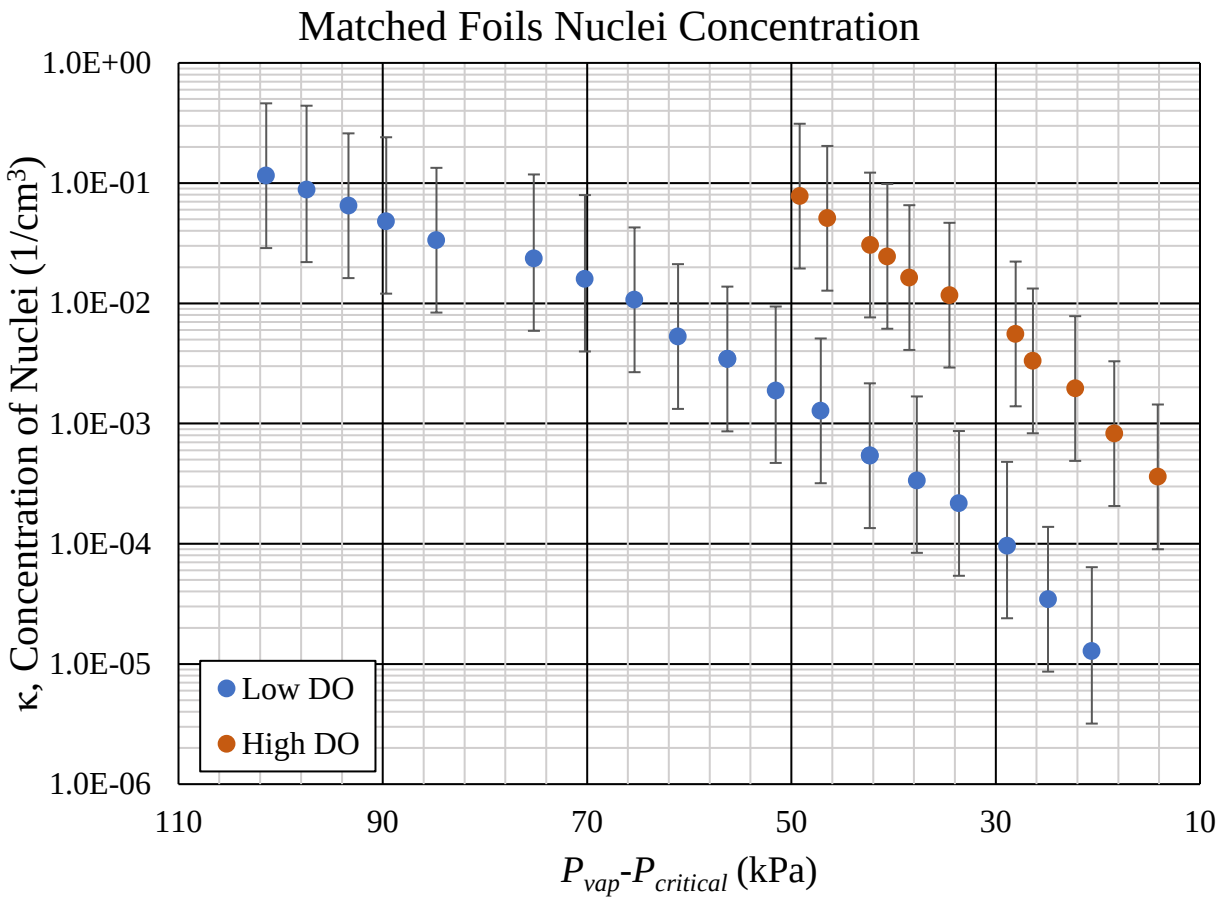


Figure 8.2 Matched Foil Nuclei Concentration. The inception experiments in this thesis were conducted at two different dissolved gas contents, approximated by dissolved oxygen (DO). The Low DO case corresponds to 13% (+/- 2%) of saturation at atmospheric pressure. The High DO case corresponds to 35% (+/- 2%) of saturation at atmospheric pressure. At each dissolved gas content, the nuclei content was measured with a CSM to give the nuclei concentration shown here. The data here was for experiments taken with the matched foils condition (M.4).

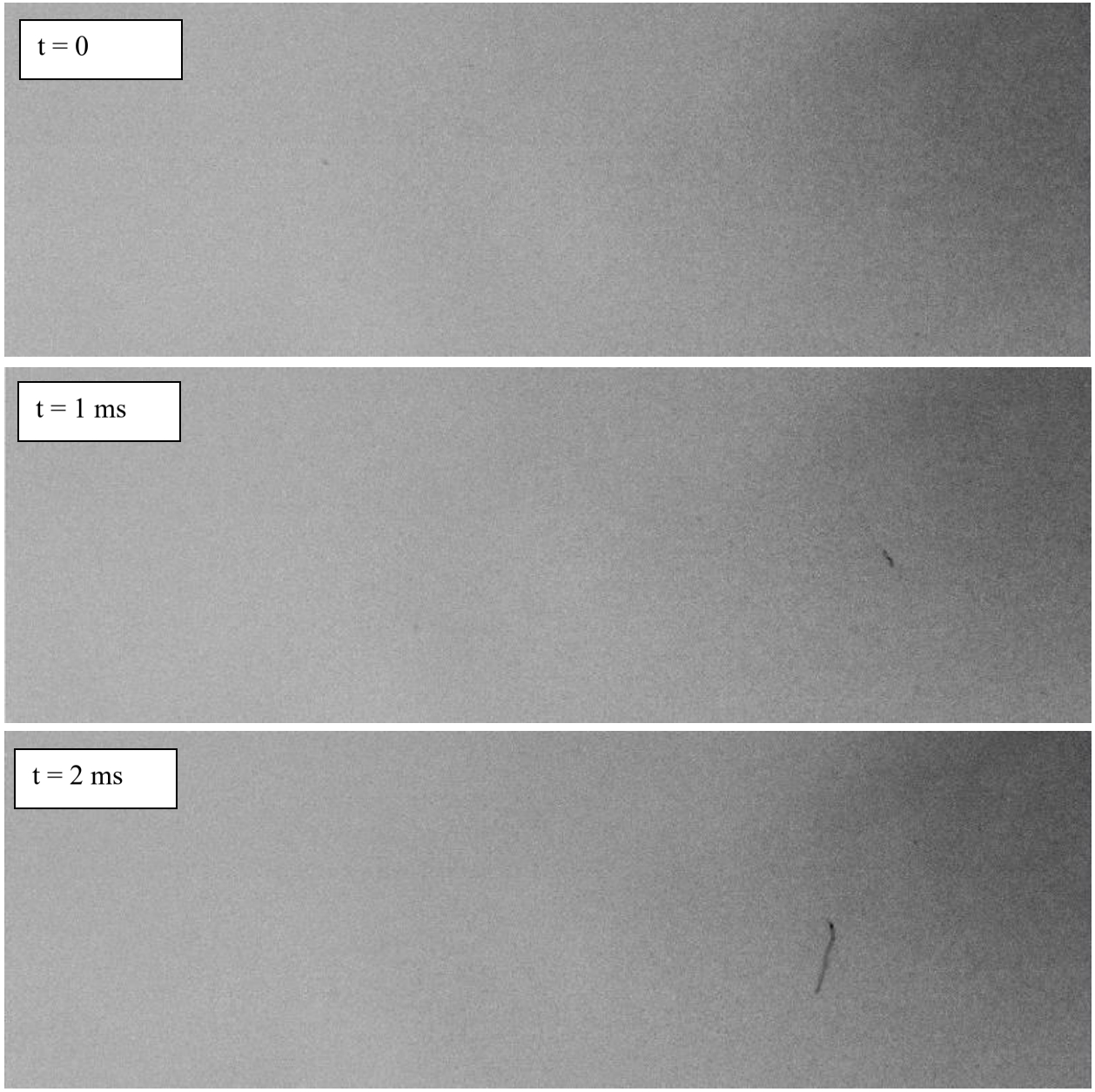


Figure 8.3 Example Inception Event. (This and following page) An inception event in the secondary vortex is shown with high-speed video. The event shown demonstrates inception in a leg of the secondary vortex, fitting with the vortex topography discussed in Chapter 7. The initial expansion and eventual collapse of the cavitation bubble are rapid, but it persists for several milliseconds in between expansion and collapse.

t = 5 ms
t = 7 ms
t = 10 ms

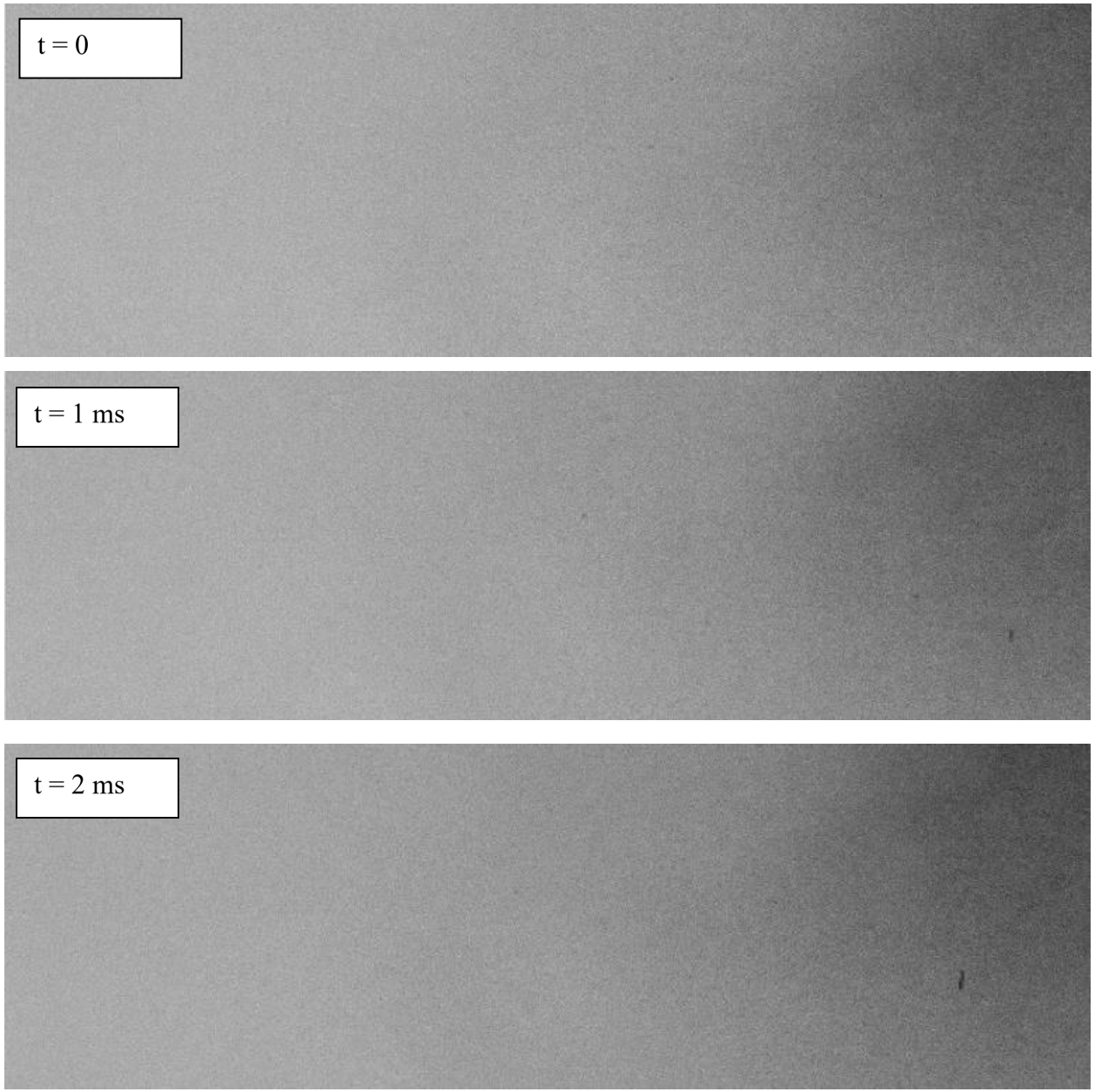
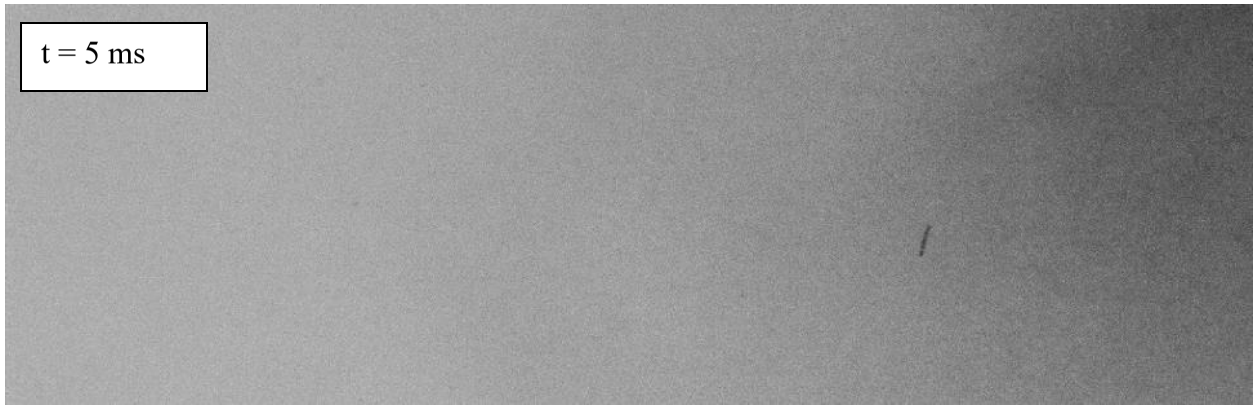
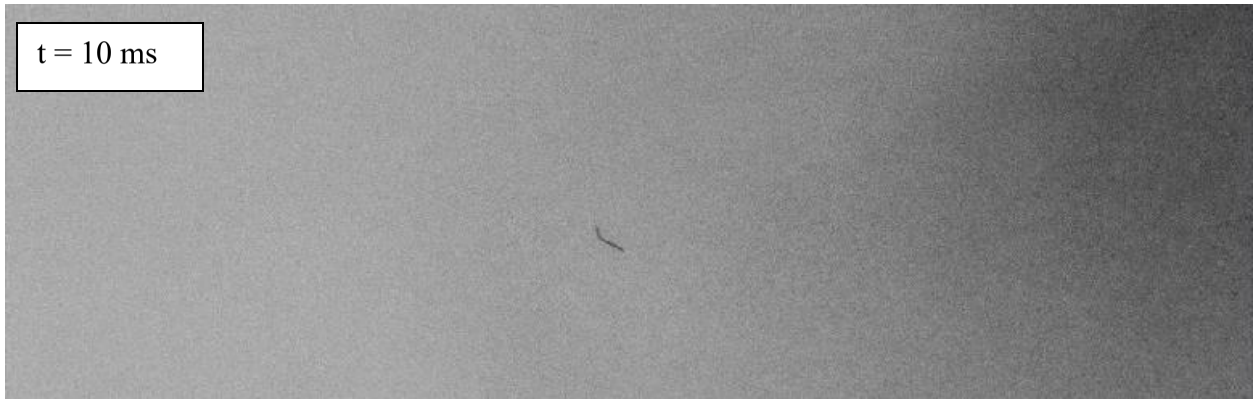
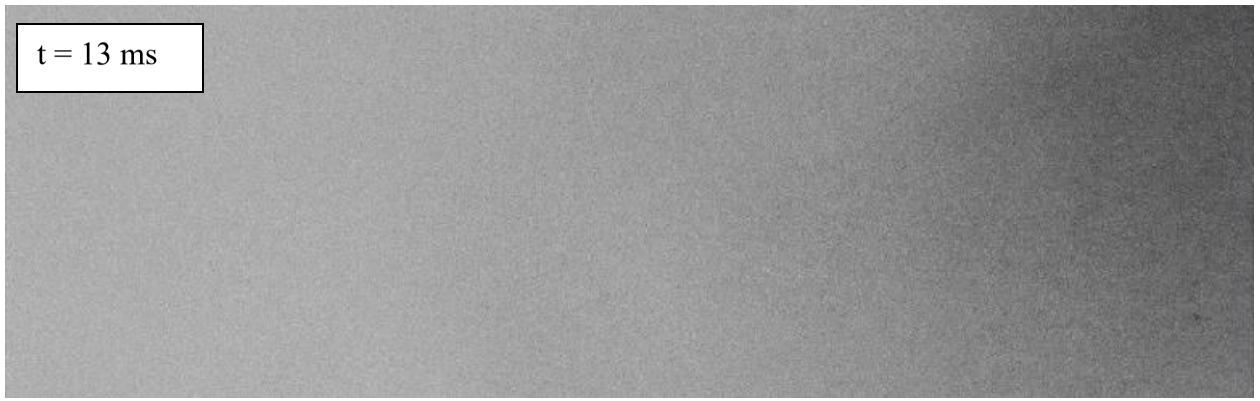
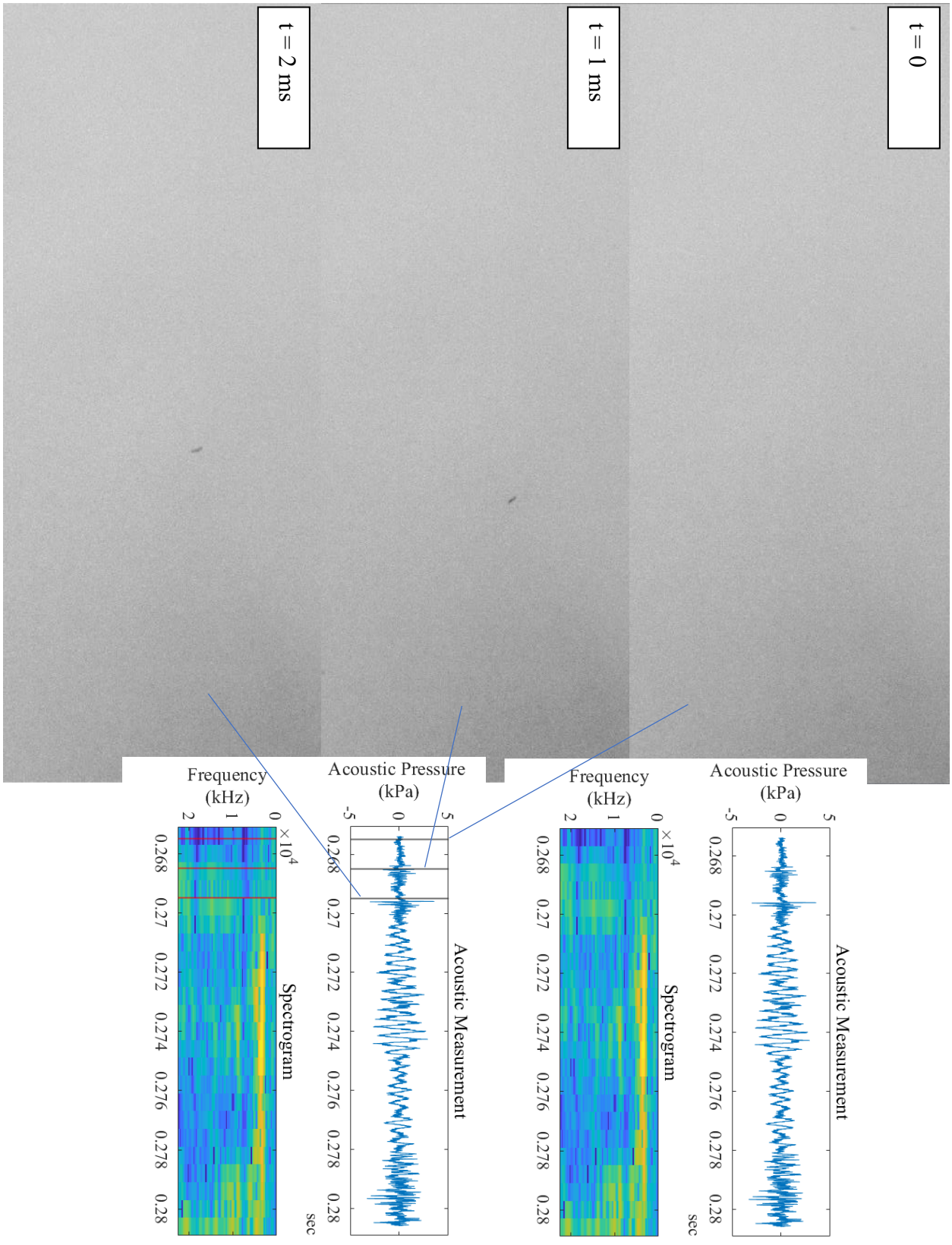


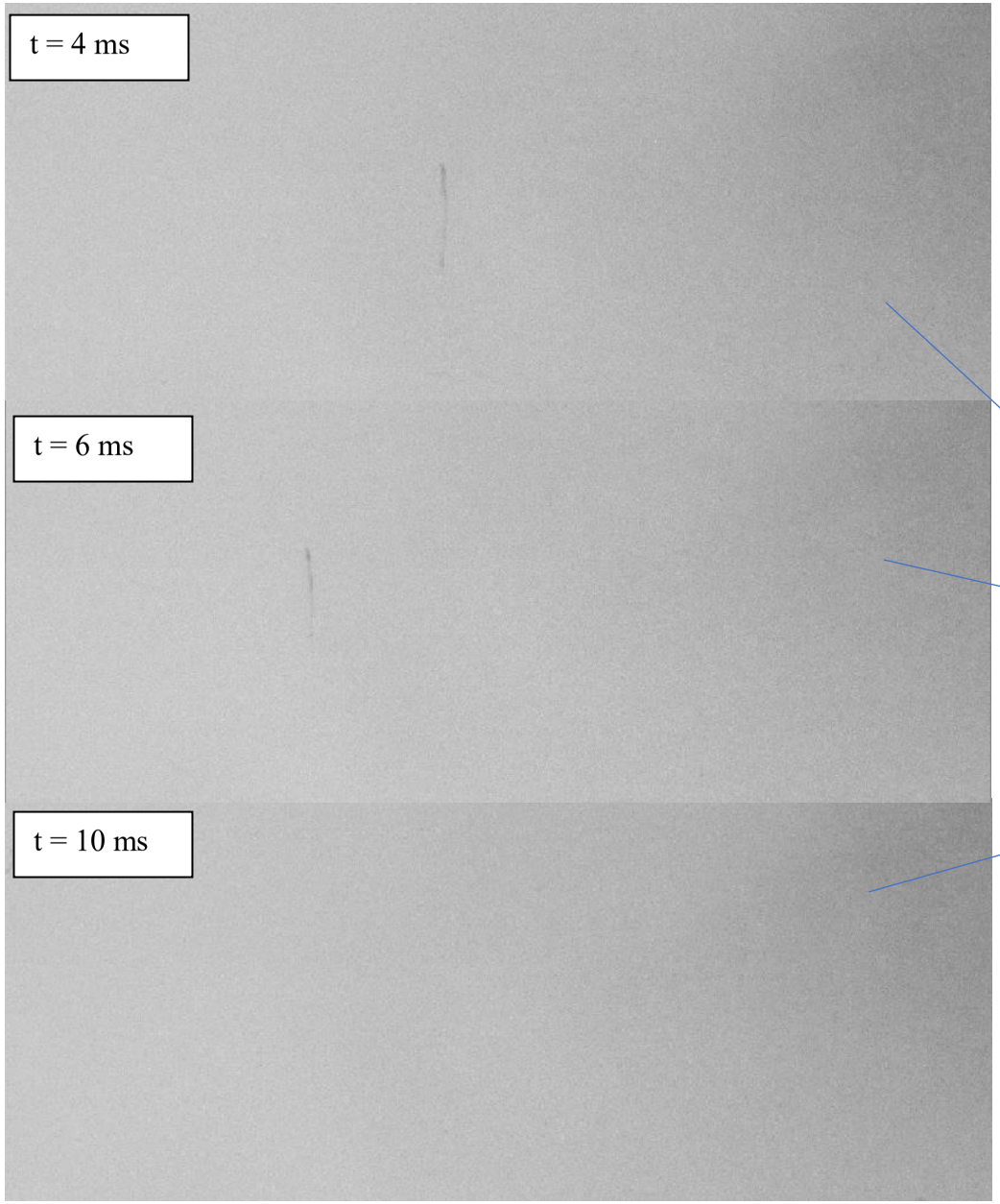
Figure 8.4 Example Inception Event. (This and following page) An inception event in the secondary vortex is shown with high-speed video. The event shown demonstrates inception in a leg of the secondary vortex, fitting with the vortex topography discussed in Chapter 7. The initial expansion and eventual collapse of the cavitation bubble are rapid, but it does not expand as much as the inception event in Figure 8.3.


t = 5 ms


t = 10 ms


t = 13 ms


t = 0
t = 1 ms
t = 2 ms
Acoustic Pressure (kPa)
Acoustic Measurement
Frequency (kHz)
Spectrogram
sec


t = 4 ms
t = 6 ms
t = 10 ms

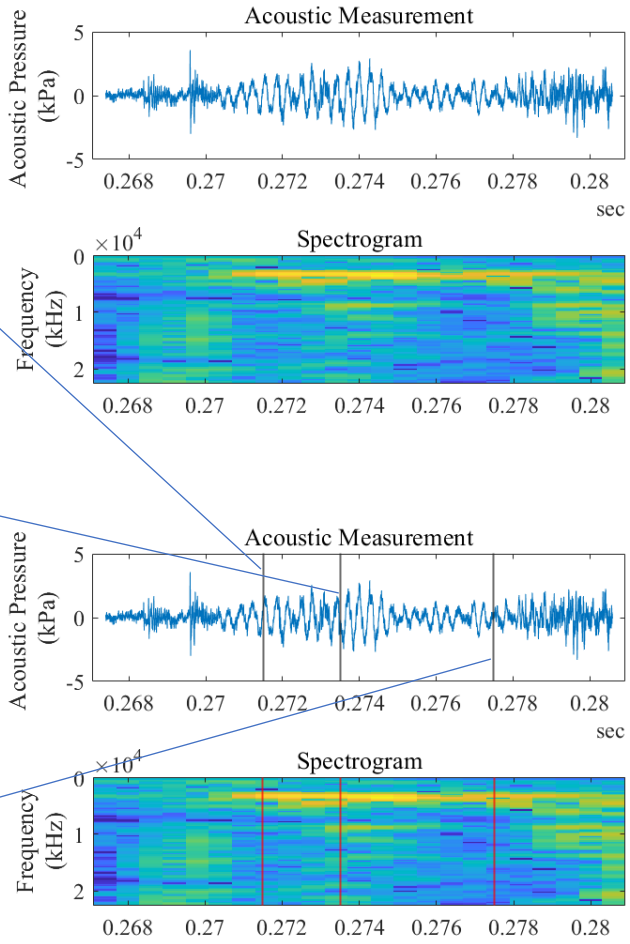

Acoustic Measurement
Acoustic Pressure (kPa)
5
0
-5
0.268
0.27
0.272
0.274
0.276
0.278
0.28
sec
Spectrogram
×10^4
Frequency (kHz)
0
1
2
Acoustic Measurement
Acoustic Pressure (kPa)
Spectrogram
Frequency (kHz)

Figure 8.5 Example Inception Event with Acoustics and Video. (Previous pages) An inception event in the secondary vortex with synchronous high-speed video (black and white images) and acoustic measurements (plotted data) is shown. The instances shown in the images are highlighted in the acoustic data with vertical lines. The acoustic data is repeated with and without the lines for clarity. It initially expands rapidly, leading to a loud pop and showing up as a dark patch in the video (at t = 1 and t = 2 ms). The high volumetric acceleration is noticeable by comparing the video images at t = 2 ms and t = 4 ms. This high acceleration leads to a loud acoustic pulse. However, after the bubble reaches its new, larger volume it grows fainter in the video and weakly oscillates (from around t = 3 ms to t = 8 ms) before eventually collapsing weakly and quietly such that it is no longer apparent in the video at t = 10 ms.

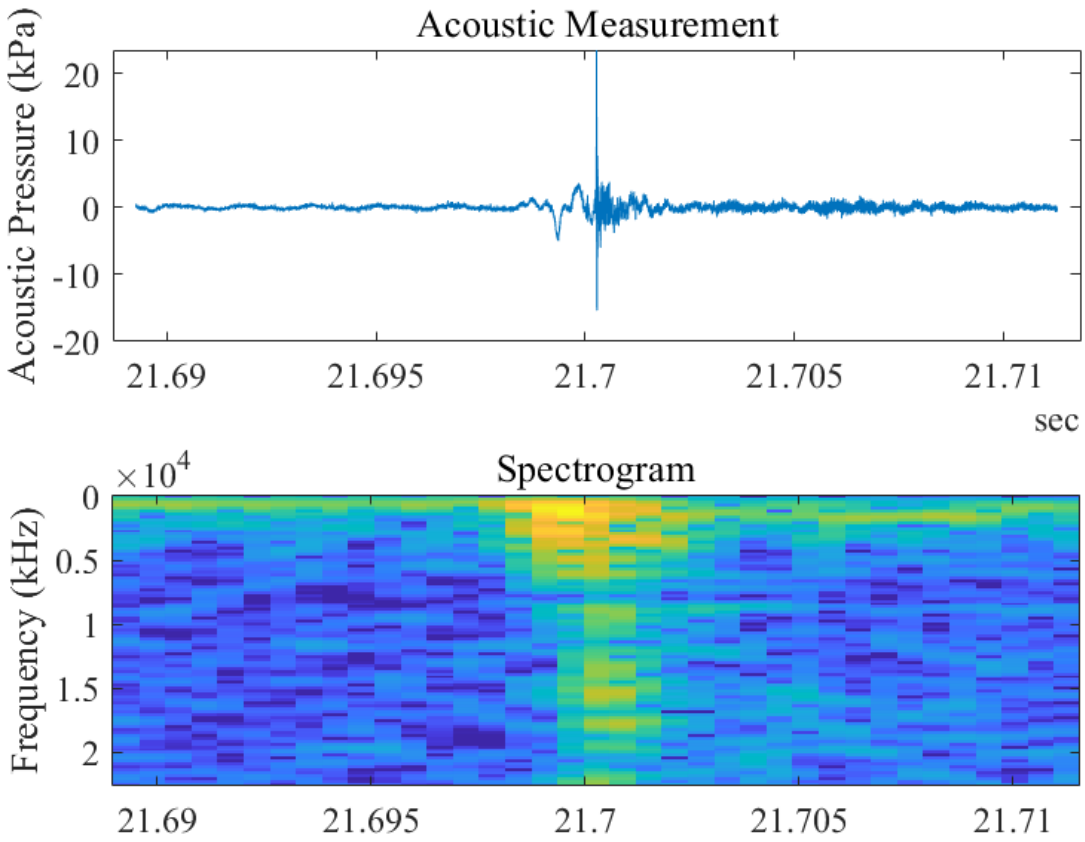


Figure 8.6 Example Pop Event. An example of a popping inception event is shown here in both the time domain and frequency domain. Due to the rapid collapse of the bubble, the pop is broadband in frequency as shown by the spectrogram.

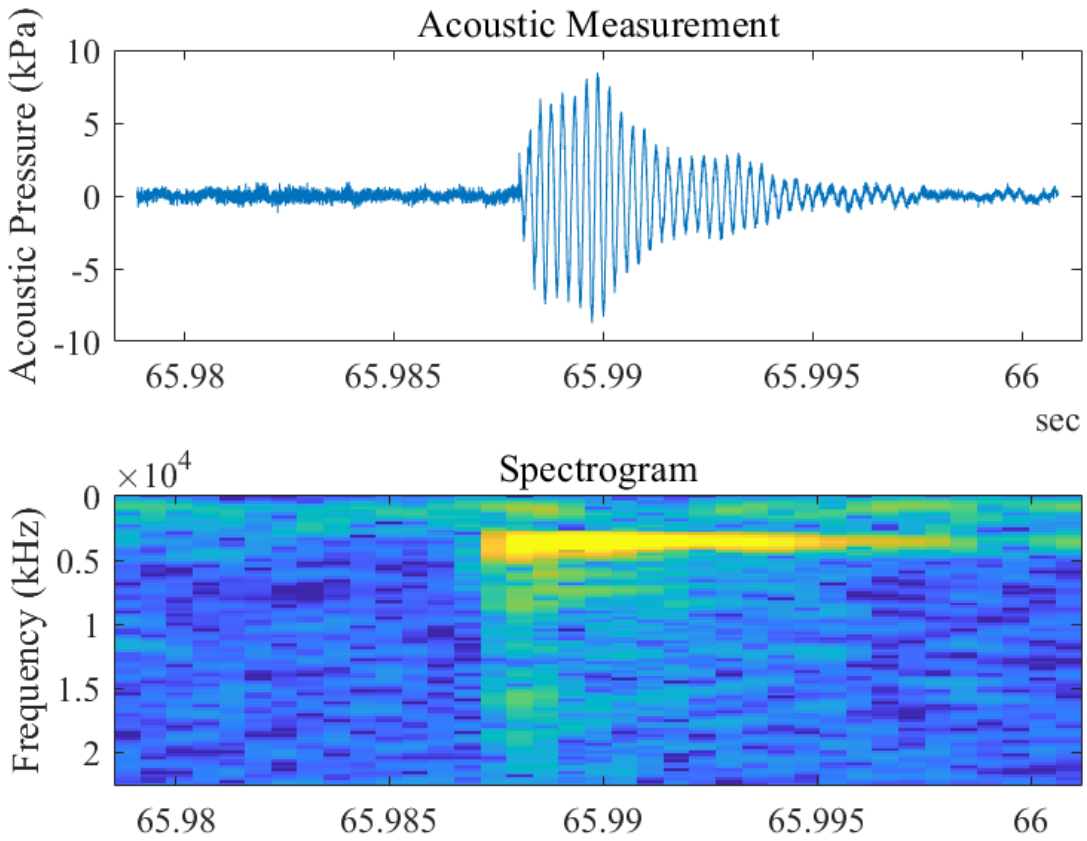


Figure 8.7 Example Chirp Event. An example of a chirping inception event is shown here in both the time domain and frequency domain. As the bubble's initial expansion is slow (due to it being a large nucleus), it chirps with a consistent frequency (here, approximately 3 kHz) as opposed to the broadband pop.

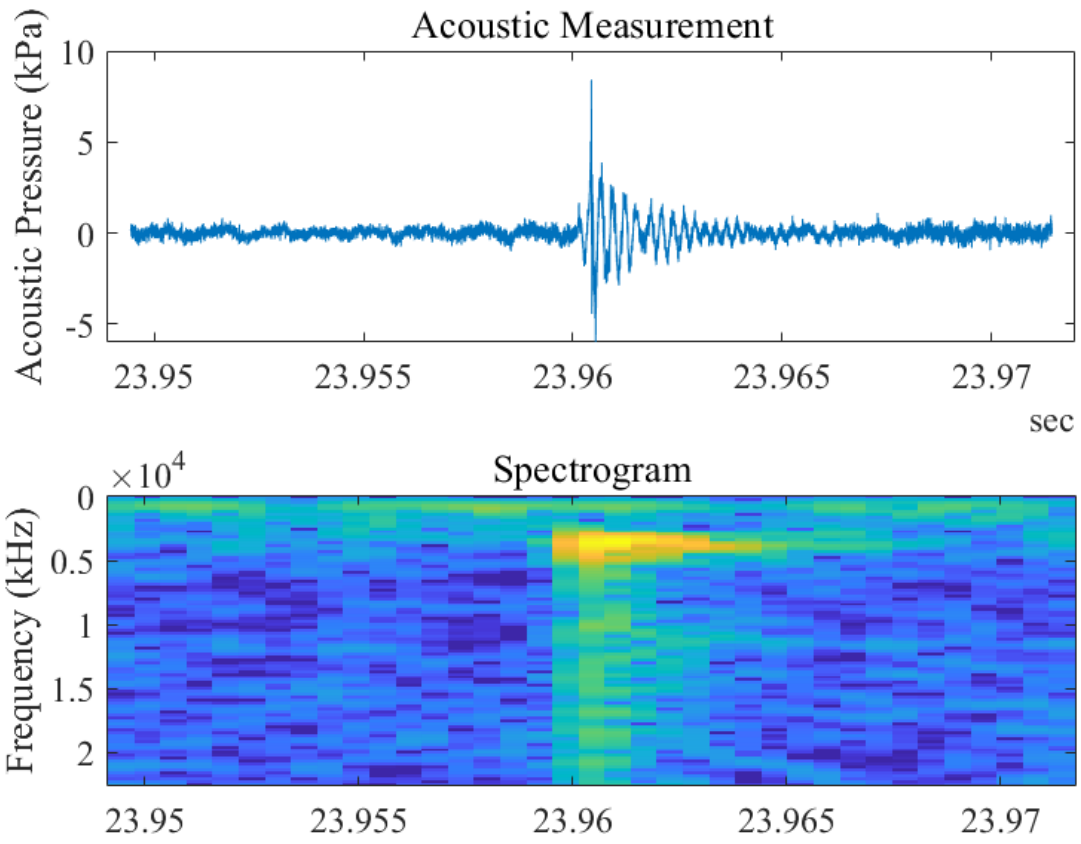


Figure 8.8 Example Chirpy Pop Event. An example of a "chirpy pop" inception event is shown here in both the time domain and frequency domain. As the bubble initially expands rapidly, it pops before settling into an oscillation and chirp.

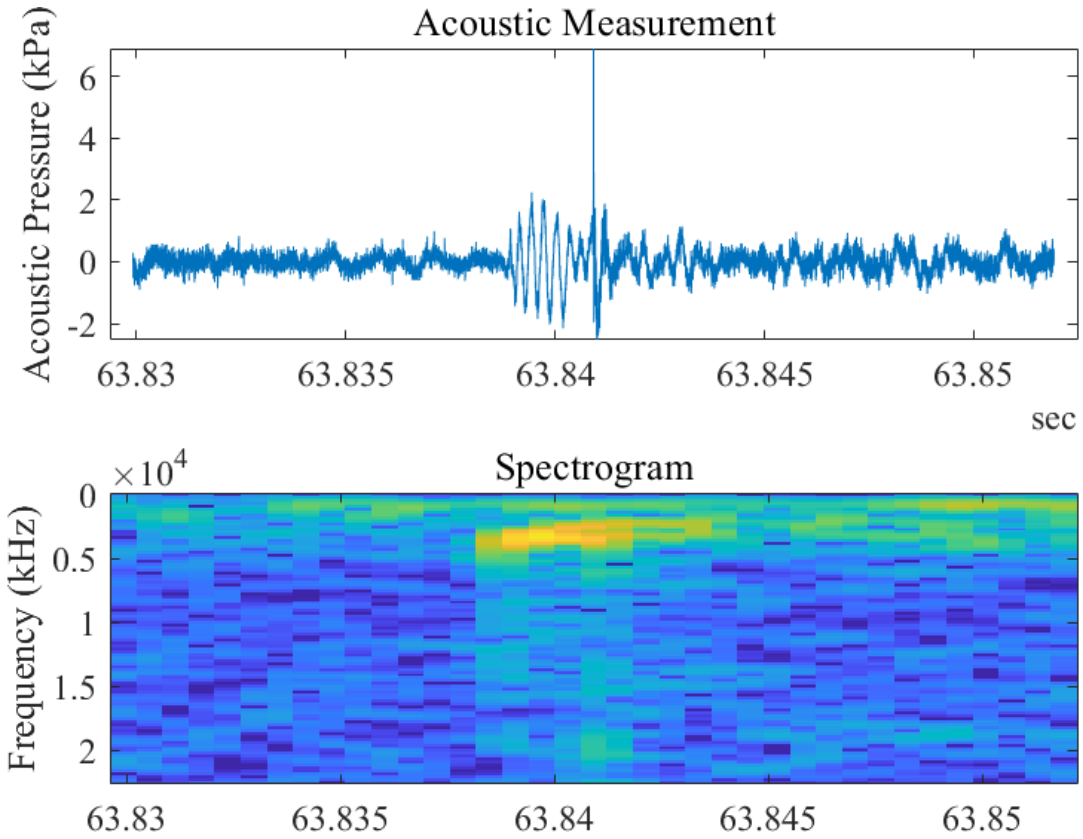


Figure 8.9 Example Chirpy Pop Event. An example of a "chirpy pop" inception event is shown here in both the time domain and frequency domain. In contrast to the prior example, the bubble initially experiences a slow growth and consequently chirps at the beginning of inception. However, its eventual collapse is rapid, and it pops.

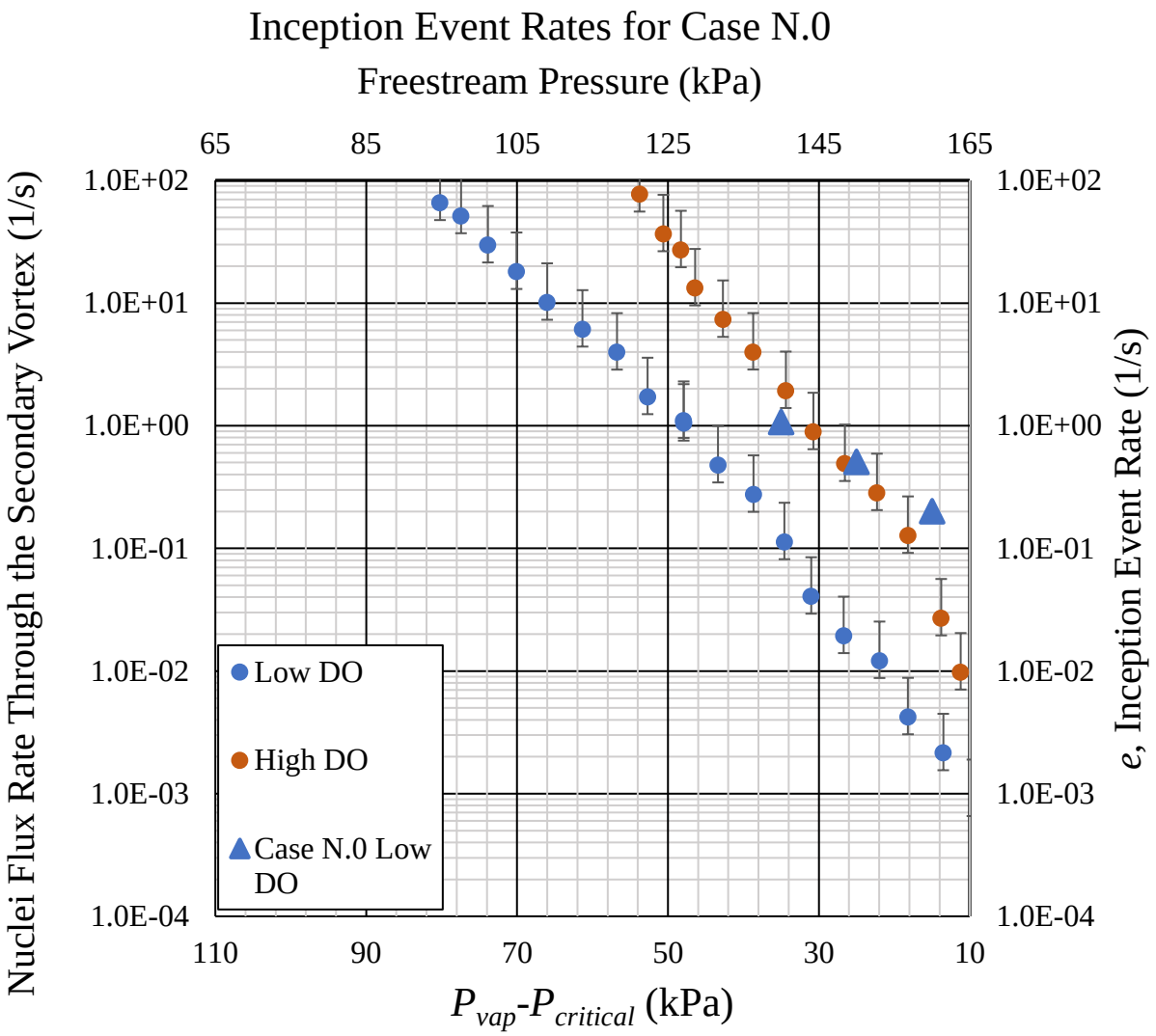


Figure 8.10 Inception Event Rates for Case N.0. The CSM measurements of Figure 8.1 are repeated used to estimate the nuclei flux rate through the secondary in Case N.0, as shown on the left side and circular symbols. The right side and triangular symbols give the acoustically measured inception event rate. Note that these are on the same scale, suggesting that the matching of them depends on the relation of the pressure drop in the vortices to the critical pressure of the nuclei. For Case N.0 as shown here, only a limited range of freestream pressures for the low dissolved gas content could be studied as at higher nuclei concentrations and lower pressures, pseudo-cavitation and developed cavitation in the secondary were prevalent.

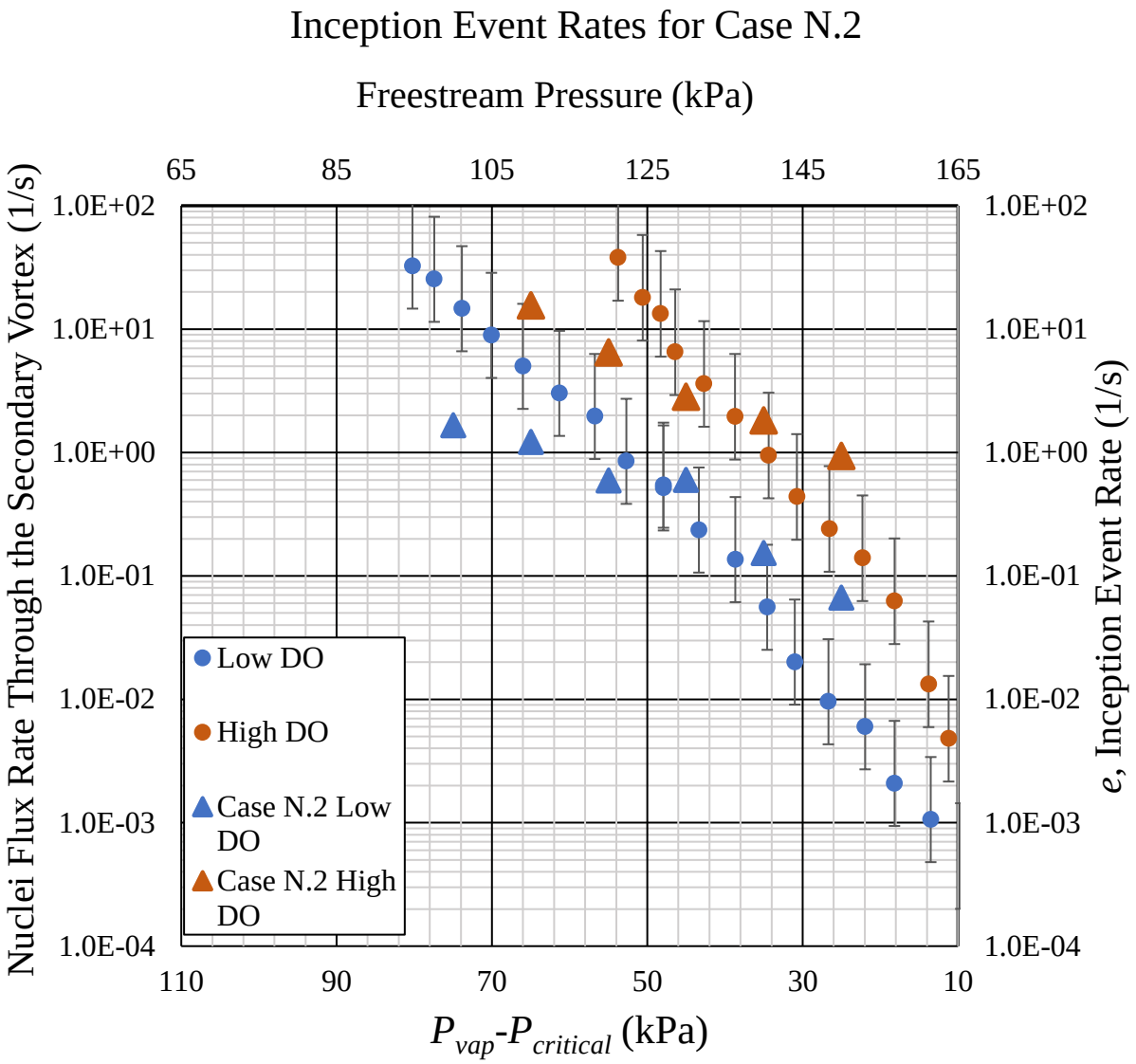


Figure 8.11 Inception Event Rates for Case N.2. The CSM measurements of Figure 8.1 are repeated used to estimate the nuclei flux rate through the secondary in Case N.2, as shown on the left side and circular symbols. The right side and triangular symbols give the acoustically measured inception event rate. Note that these are on the same scale, suggesting that the matching of them depends on the relation of the pressure drop in the vortices to the critical pressure of the nuclei. In comparison to N.0 above, the event rate is shifted left or down, showing the weaker pressure drop in this case.

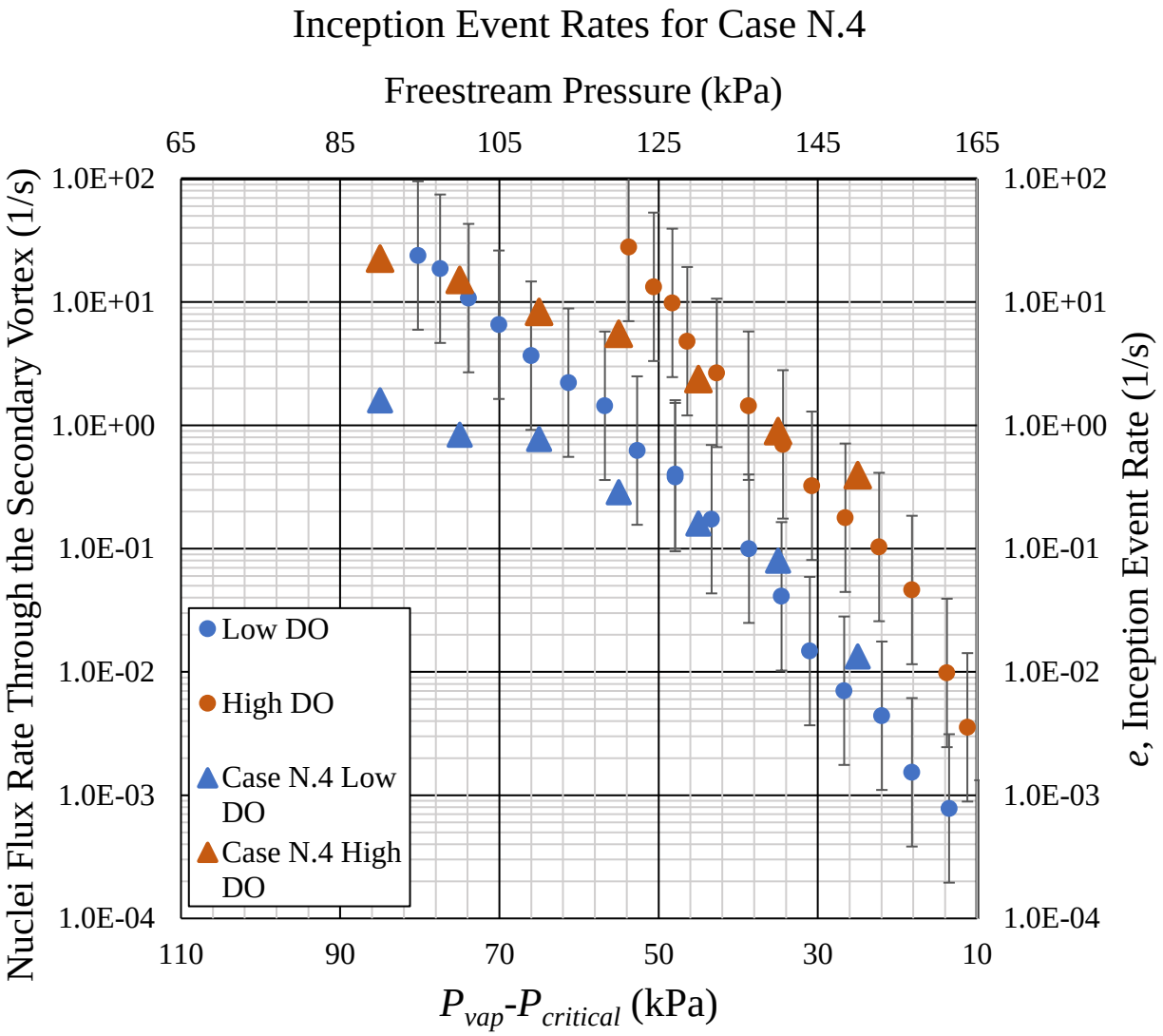


Figure 8.12 Inception Event Rates for Case N.4. The CSM measurements of Figure 8.1 are repeated used to estimate the nuclei flux rate through the secondary in Case N.4, as shown on the left side and circular symbols. The right side and triangular symbols give the acoustically measured inception event rate. Note that these are on the same scale, suggesting that the matching of them depends on the relation of the pressure drop in the vortices to the critical pressure of the nuclei. In comparison to N.2 above, the nuclei flux rate and event rate are shifted left or down, showing the lower presence of available nuclei for cavitation due to the smaller radius for N.4 as well as the somewhat weaker pressure drop in N.4 relative to N.2.

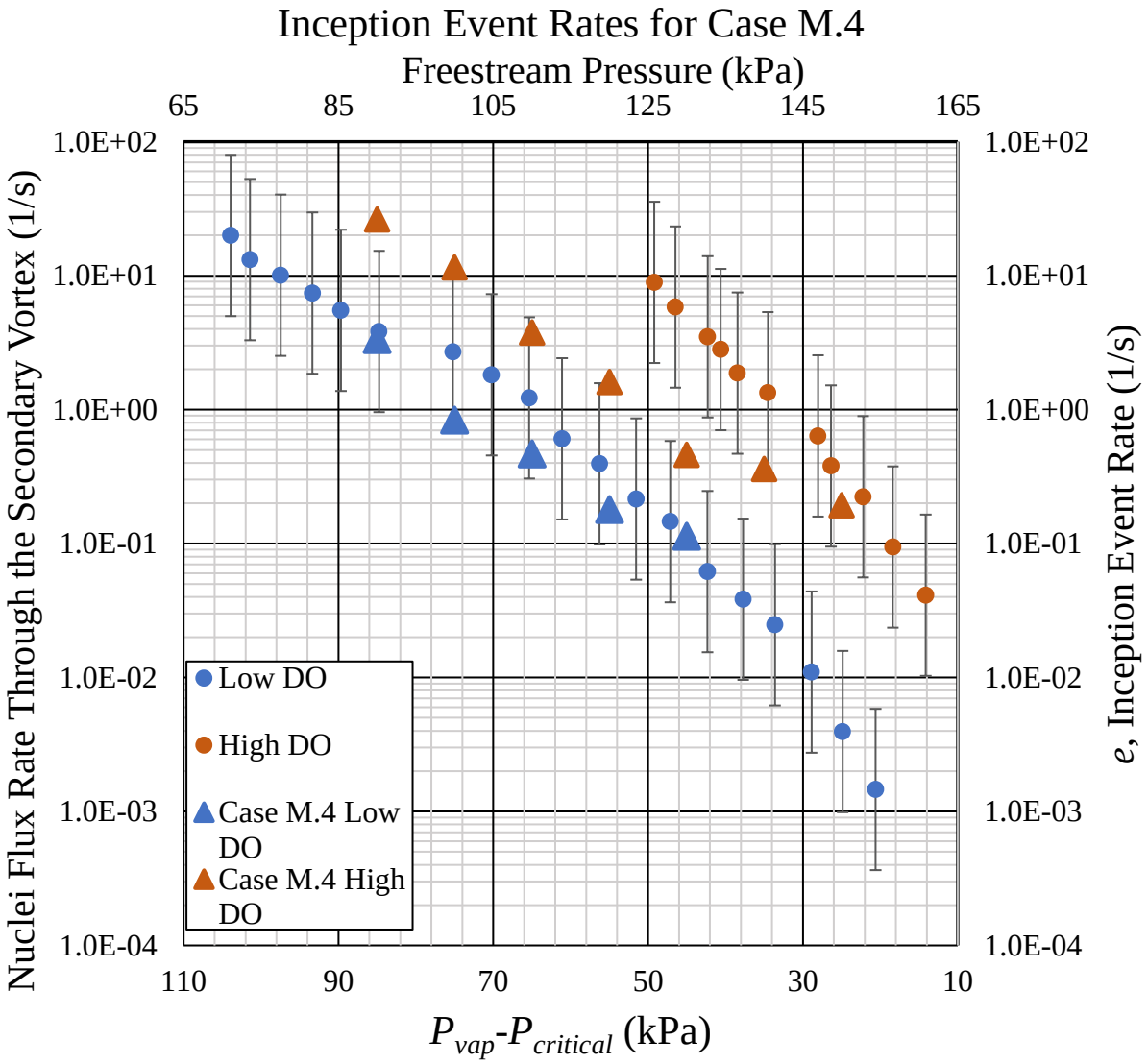


Figure 8.13 Inception Event Rates for Case M.4. The CSM measurements of Figure 8.2 are repeated used to estimate the nuclei flux rate through the secondary in Case M.4, as shown on the left side and circular symbols. The right side and triangular symbols give the acoustically measured inception event rate.

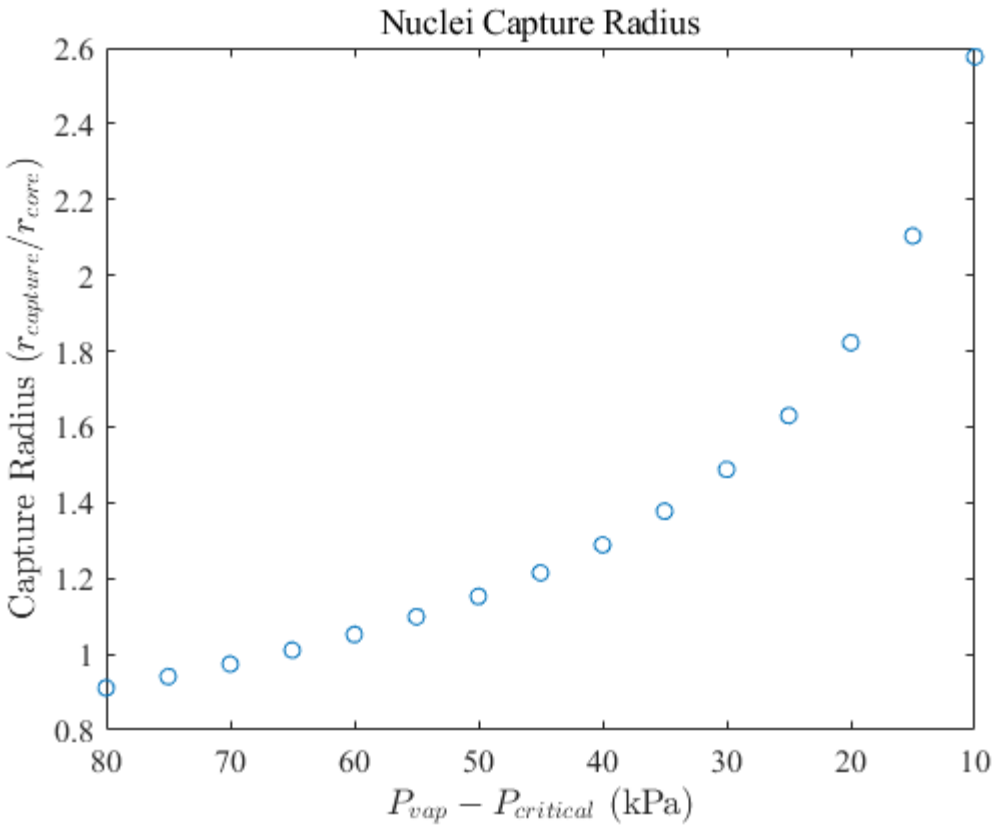


Figure 8.14 Nuclei Capture Radius. The ability of the secondary vortex to capture nuclei outside of it for inception depends strongly on the size of the nuclei and thus their critical pressure for inception. The effects of capture are modest for the smaller nuclei that dominate the population of available nuclei. As shown in Figures 8.1 and 8.2, the concentration of nuclei considered over the range of critical pressures displayed here varies by approximately 5 orders of magnitude.

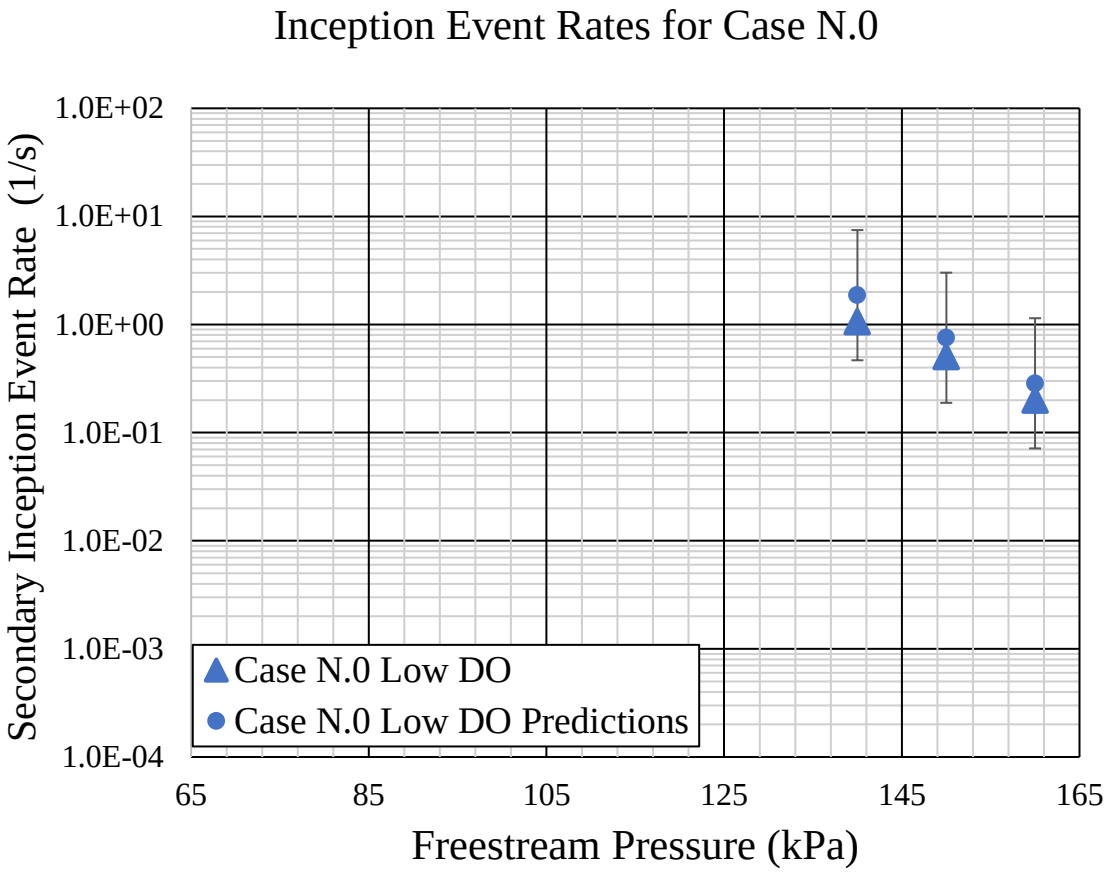


Figure 8.15 Estimated Inception Rates for Case N.0. The observed and predicted inception event rates for the secondary vortex in Case N.0 are shown above. There is good agreement between the observed and predicted rates, but this represents only a narrow range of study.

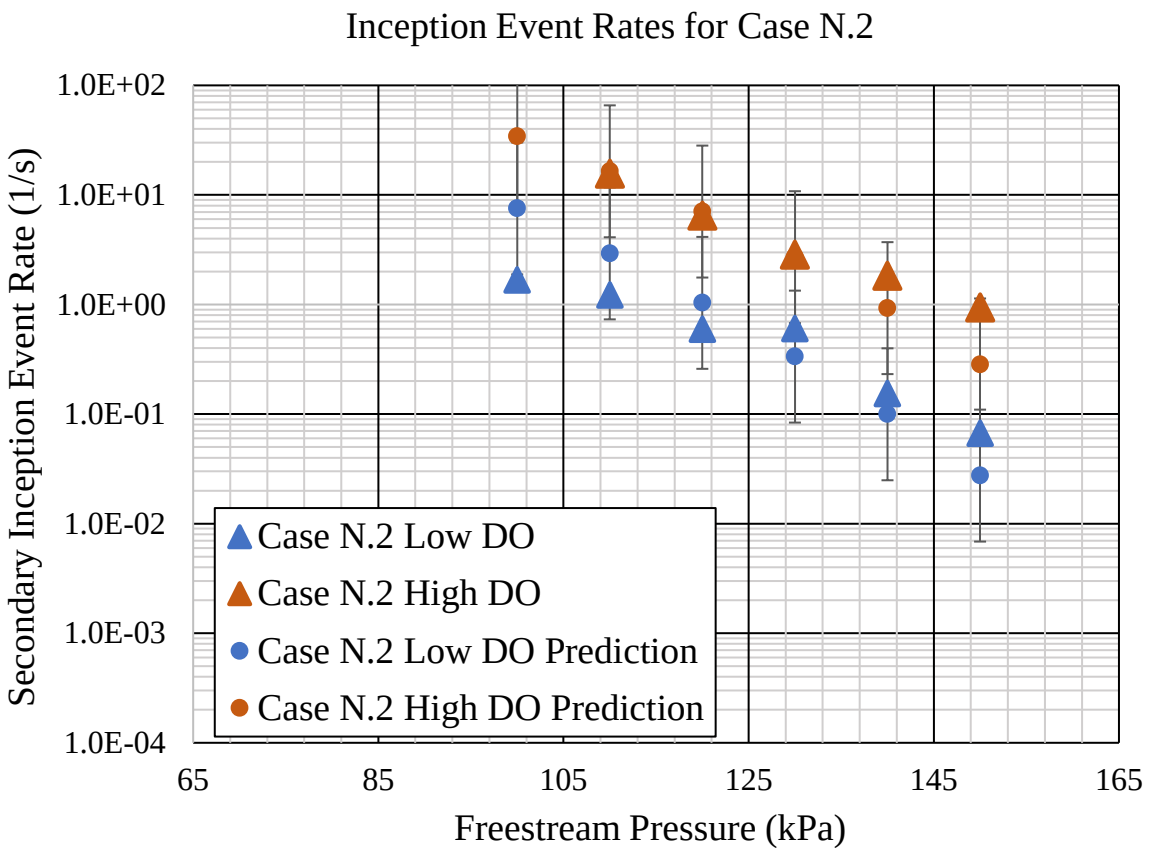


Figure 8.16 Estimated Inception Rates for Case N.2. The observed and predicted inception event rates for the secondary vortex in Case N.2 are shown above. There is some agreement between the observed and predicted rates over a wider range than for Case N.0 above, indicating that the model for cavitation inception in the stretched secondary vortex captures the essential physics.

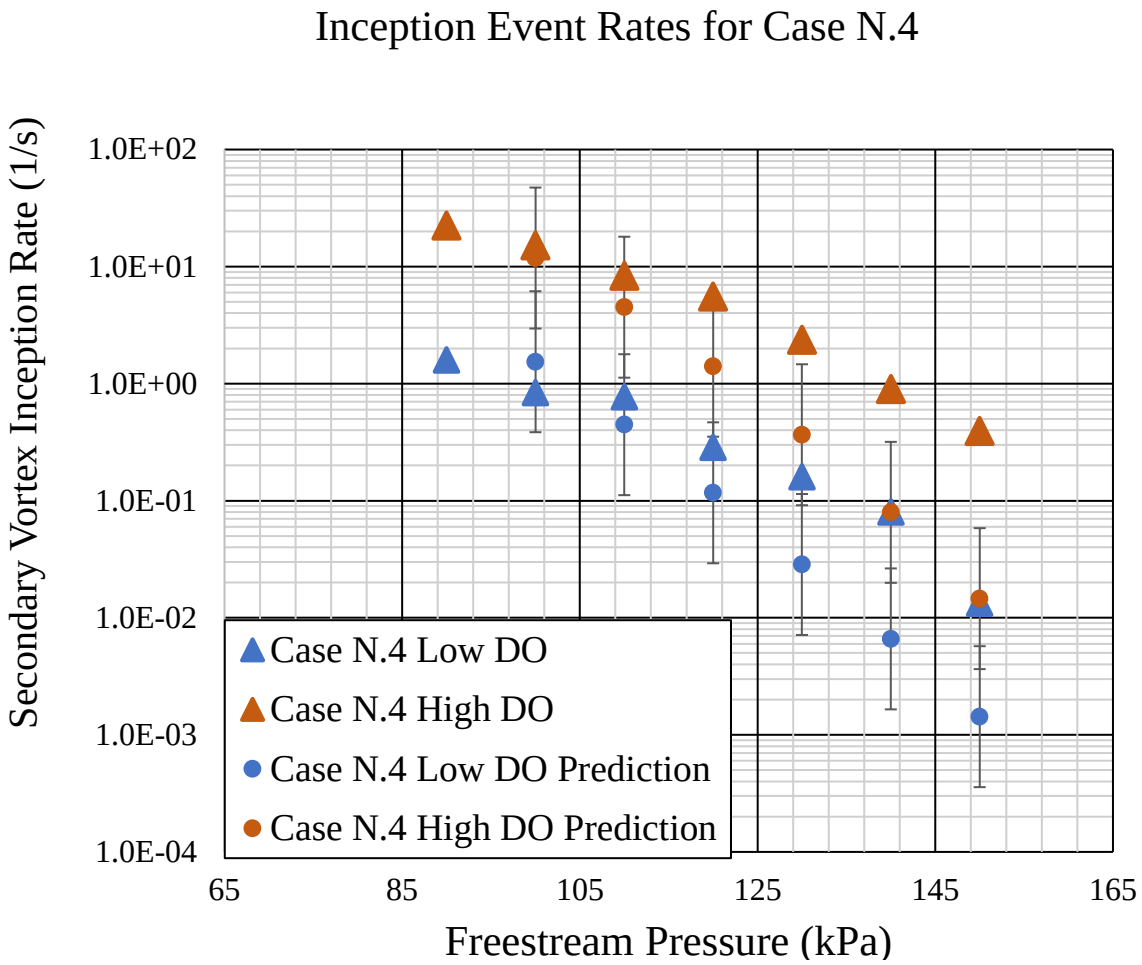


Figure 8.17 Estimated Inception Rates for Case N.4. The observed and predicted inception event rates for the secondary vortex in Case N.4 are shown above. There is some agreement between the observed and predicted rates over a wider range than for Case N.0 above, indicating that the model for cavitation inception in the stretched secondary vortex captures the essential physics.

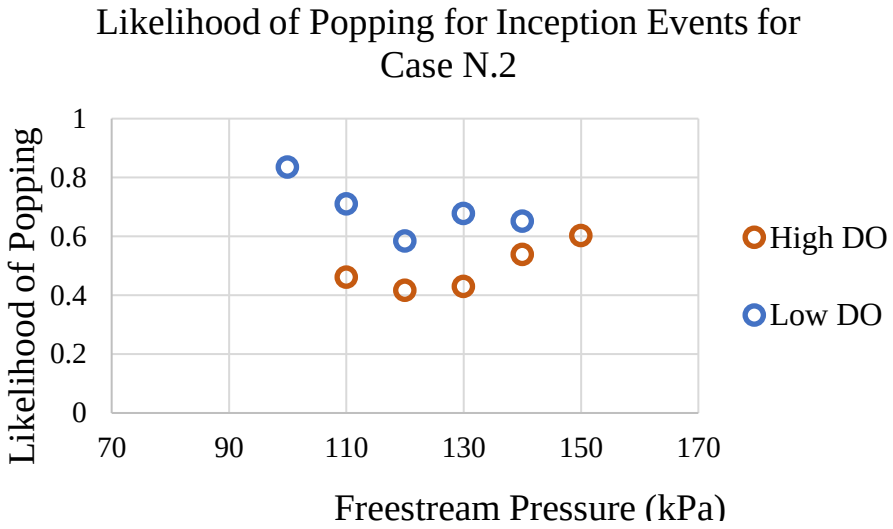


Figure 8.18 Likelihood of Popping for Case N.2. The likelihood of the secondary popping as opposed to chirping is higher for the low DO case for Case N.2. The low DO case has smaller nuclei that require greater tension to incept. When these smaller nuclei incept, they have a greater volumetric acceleration due to the larger pressure differential driving their inception. Accordingly, they overshoot their equilibrium radius and pop as opposed to chirp.

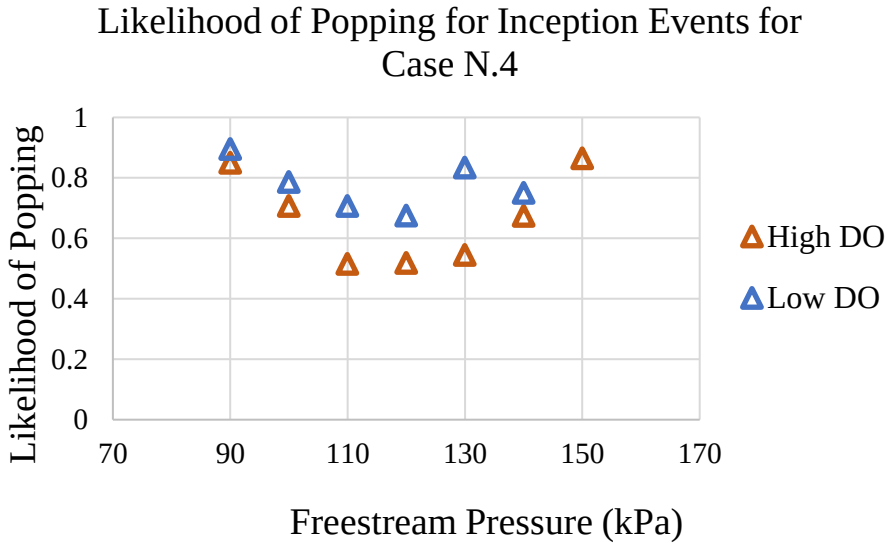


Figure 8.19 Likelihood of Popping for Case N.4. The likelihood of the secondary popping as opposed to chirping is higher for the low DO case for vortex configuration Case N.4. The low DO case has smaller nuclei that require greater tension to incept. When these smaller nuclei incept, they have a greater volumetric acceleration due to the larger pressure differential driving their inception. Accordingly, they overshoot their equilibrium radius and pop as opposed to chirp.

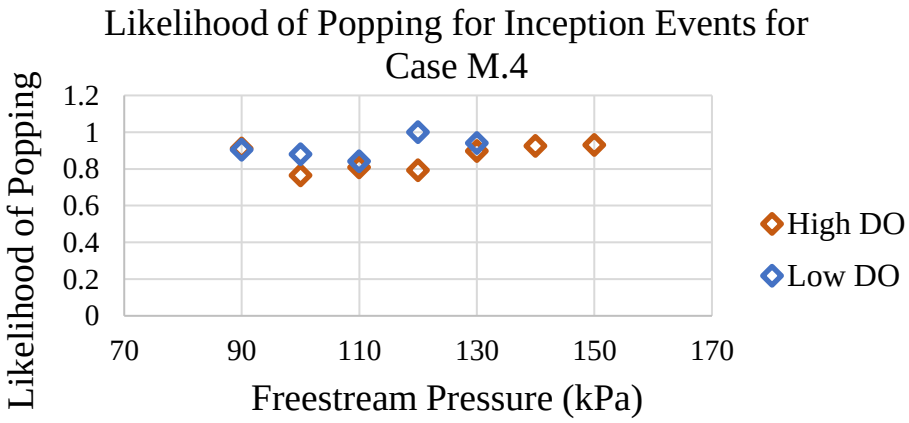


Figure 8.20 Likelihood of Popping for Case M.4. The likelihood of the secondary popping as opposed to chirping is higher for the low DO case for vortex configuration Case M.4. The low DO case has smaller nuclei that require greater tension to incept. When these smaller nuclei incept, they have a greater volumetric acceleration due to the larger pressure differential driving their inception. Accordingly, they overshoot their equilibrium radius and pop as opposed to chirp.

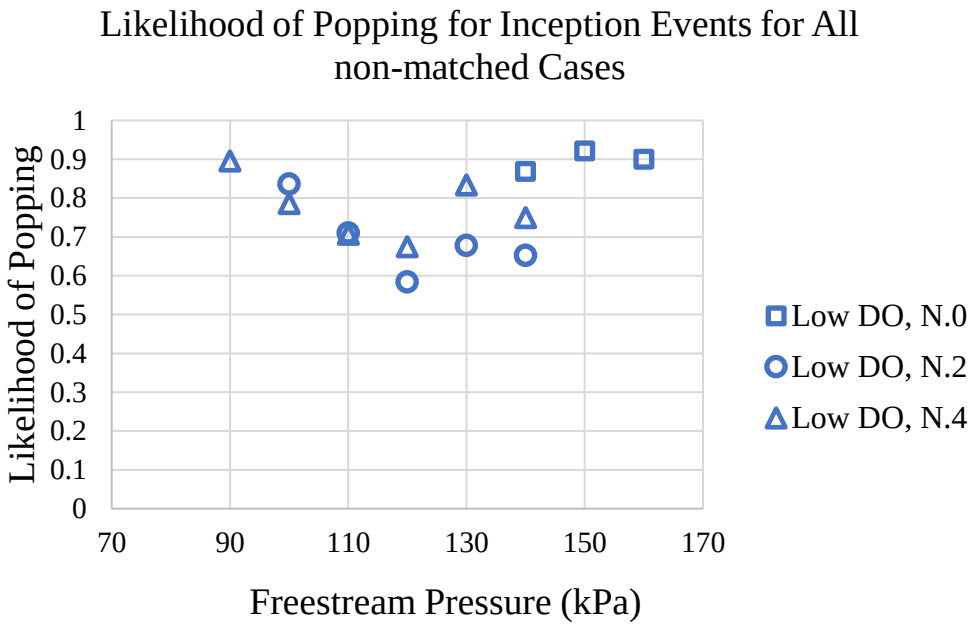


Figure 8.21 Likelihood of Popping for All Cases. For all the non-matched foil configurations considered, the likelihood of popping with the low DO content is plotted here. Note the apparent "U-shape" over this range. This is due to the balance of the effects of nuclei size and applied tension on acoustic emissions.

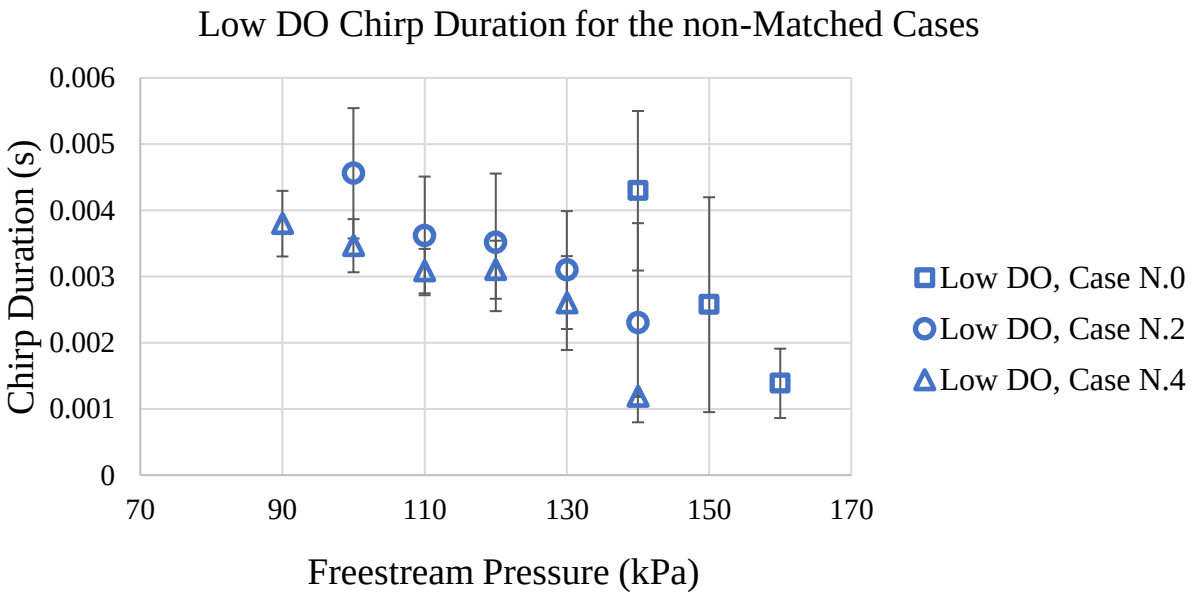


Figure 8.22 Low DO Chirp Duration for All Cases. The chirp duration is decreased with increasing pressure as the vortices cannot sustain tensions for as long with higher surrounding pressure.

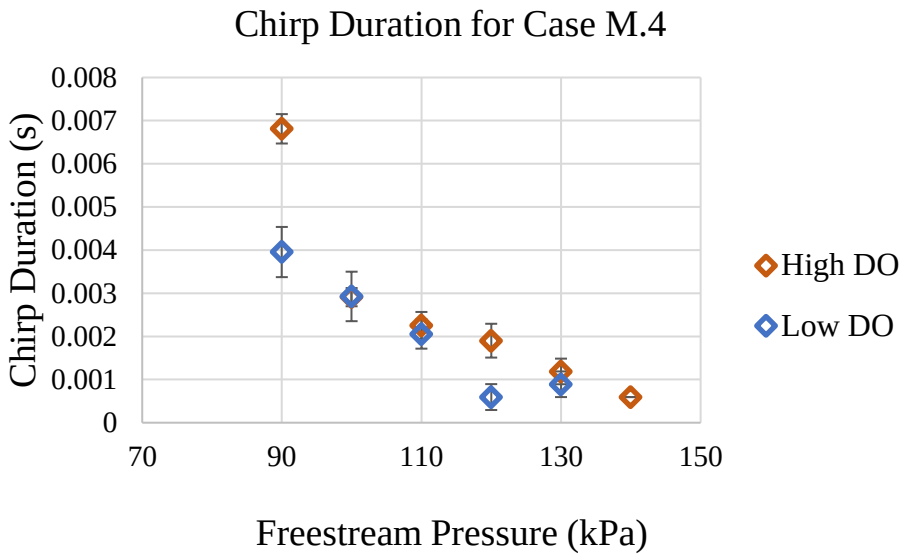


Figure 8.23 Chirp Duration for Case M.4. The chirp duration for the matched foil case is decreased with increasing pressure as the vortices cannot sustain tensions for as long with higher surrounding pressure. This effect is more dramatic for higher DO content as the larger nuclei present cavitate with weaker tensions which cannot be sustained with higher surrounding pressures.

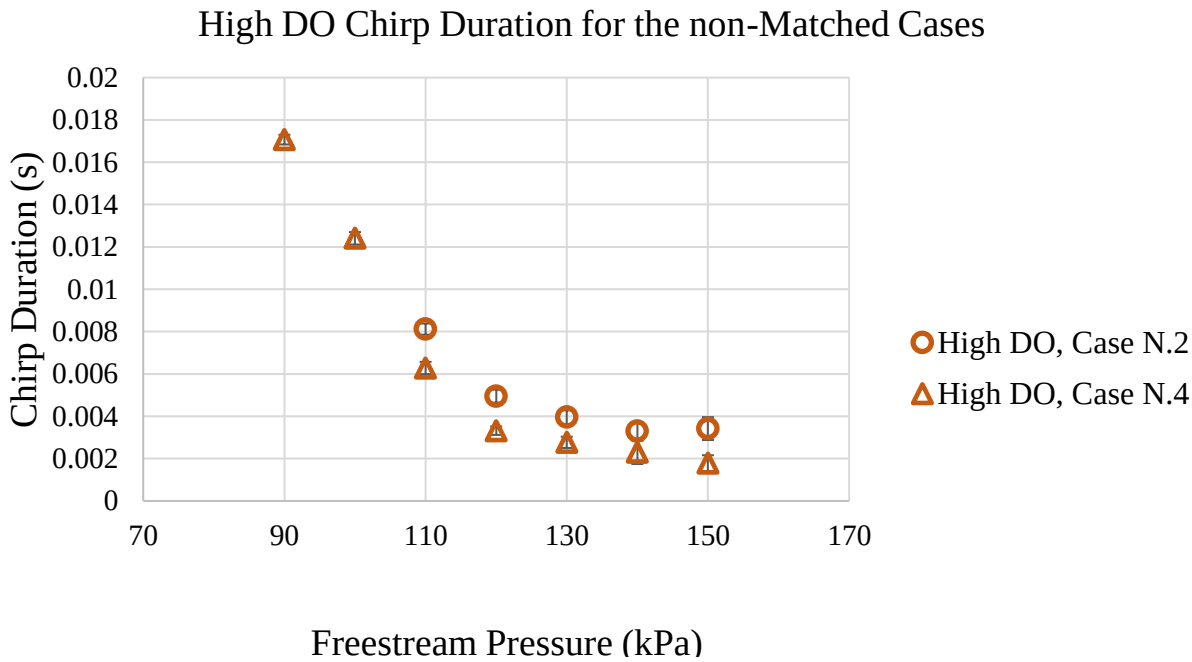


Figure 8.24 High DO Chirp Duration for All Cases. The chirp duration is decreased with increasing pressure as the vortices cannot sustain tensions for as long with higher surrounding pressure. This effect is more dramatic for higher DO content as the larger nuclei present cavitate with weaker tensions which cannot be sustained with higher surrounding pressures.

Chapter IX

Contributions

Study of Artificially Constrained Velocimetry as a Proxy for Coaxial Measurements

The present work directly compares the tomographic reconstruction of particles in an ideal setup with an artificially constrained approach, a study not undertaken before. The main findings are,

- This showed that the effects of the tomographic reconstruction in a non-idealized case were as initially expected in that the reconstruction falsely reconstructed image intensity within the constrained domain and this affected the subsequent PIV calculation.
- However, the effect on eventual velocity fields was small relative to other sources of uncertainty (e.g., misalignment of laser heads), which was unexpected prior to the study.
- Comparison of the Reynolds stress fields and other ensemble averaged flow quantities between Tomo-PIV, STB, and Stereo-PIV, a study not performed before, showed notable differences, particularly for out of plane quantities in Stereo-PIV. Additionally, the naïve binning approach to STB performed poorly in the shear layer of the wedge.
- Tomo-PIV performed reasonably well even in an artificially constrained approach. These results suggest that a Tomo-PIV approach in a coaxially illuminated arrangement can provide acceptable measurements.

Accordingly, future investigators should examine the use of Tomo-PIV in a coaxially illuminated system over a range of seeding densities to compare with STB. The present results

indicate that such an experiment may succeed, however the present results are limited by the use of only a singular seeding density. Additionally, the effect of out of focus particles on a noise background is not tested here.

Study of Vortex Interaction Leading to Cavitation Inception

This work expanded upon a similar flow regime to Chang *et al*. (2012) and Chang and Ceccio (2011) and similarly examined the underlying liquid flow, nuclei content, acoustic emissions, and cavitation inception event rate in two line vortices experiencing the Crow instability. The main outcomes and the findings of the present study are,

- The present work obtained 3-D velocity measurements at multiple locations across a systematic range of two-vortex configurations, a measurement never performed before at the reported temporal and spatial resolution. These data yielded a scaling relationship for vortex development in the very near configuration of the hydrofoil tips as well as prediction of the linear instability of a pair of counter-rotating vortices via the generalized Crow instability theory.
- Despite violating one of the assumptions of Crow instability theory, the present study showed that linear stability theory can predict the linear stage of instability. The novelty of this prediction was in the very close formation of the vortices, in a case where one of the underlying assumptions of the Crow instability was tenuous, so that this study showed one of the limits of such predictions.
- The non-linear, downstream development of this instability was measured, and these measurements demonstrated that the reduction in core pressure of the secondary vortex primarily resulted from the reduction in core radius. In addition, high fidelity volumetric

velocimetry measurements showed lack of substantive axial jetting and straining in secondary vortices, contrary to the theory of Chang *et al*. (2012).

- The velocity fields in the downstream non-linear region were used to estimate pressure drop (magnitude) in the secondary, a measurement not done before. This pressure drop was then used in combination with the CSM measurements of freestream nuclei to estimate cavitation inception rates with considerable success.
- These results show that the simple model of cavitation inception in a stretched secondary vortex captures the essential physics connecting the nuclei population, the underlying dynamic flow field, and the resulting observed inception rates. Estimation of pressure drop in the stretched secondary vortex and subsequent estimation of cavitation inception event rates was previously infeasible.

While the present results capture the essential physics of the inception process, several areas of research remain. First, this study examined the vortex interaction over only a small range of Reynolds number. Experiments at higher Reynolds number will be more difficult as they will likely require illuminating a larger volume at higher speeds, but these could better reflect the Reynolds number of actual naval vessels. Second, a significant limitation on this study was the lack of precise control over the nuclei in the water channel. Further experiments with more precise control over nuclei, perhaps with intentional generation of nuclei at specific sizes, could better elucidate the effects of nuclei on acoustic emissions. The present experiments can only identify general trends toward chirping and popping while use of monodisperse nuclei of different sizes could give more insight. A final avenue for future researchers is examining the behavior of the vortex after inception and after collapse of the cavitation bubbles. This portion of the vortex interaction and cavitation process was not studied due to concerns over cavitation

bubbles reflecting too much light into the cameras and damaging their sensors. To mitigate this, fluorescent particles could be used. Filtering out the green light of the laser would then protect the cameras from reflections from the bubble. Use of fluorescing particles was initially done in this project, but as stated before, it was not feasible to wait for an adequate supply of fluorescent particles to complete this study. When fluorescing particles were used, however, the placement of cameras on both sides of the tunnel allowed STB to track particles around the cavitating vortices which therefore allowed determination of the liquid flow around the bubbles. The seeding was insufficiently dense to determine the velocity field to the desired accuracy, but the success suggests that use of fluorescing particles could allow the study of the flow during and after the inception process as at present the remnants of the vortical flow after bubble collapse are unknown.

APPENDIX

Drawings of Foils and Foil Configurations

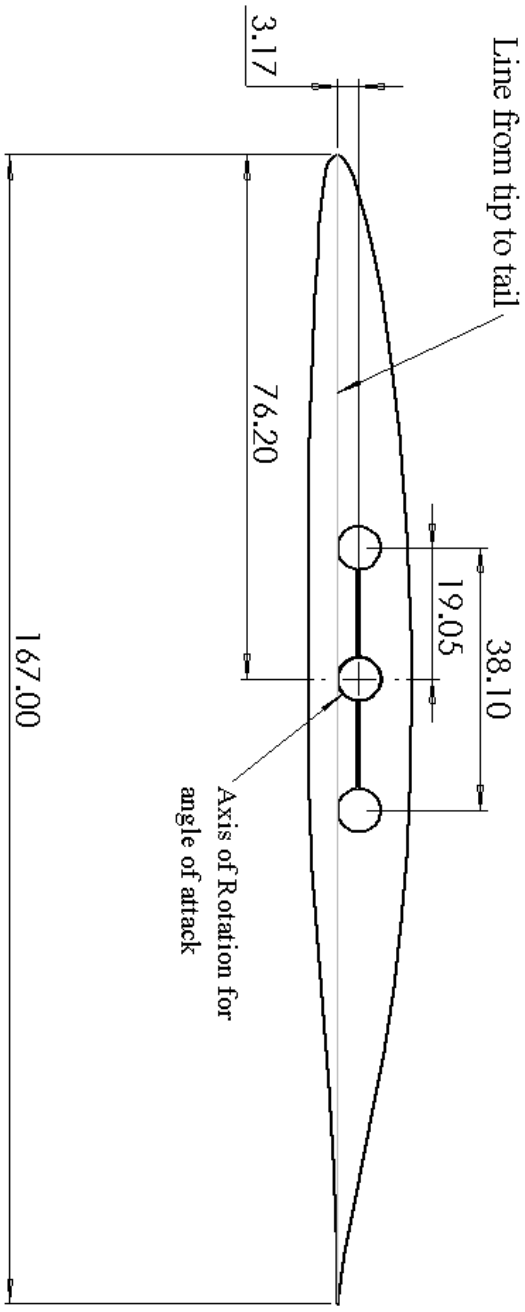


Figure A.1 Large Foil Schematic. Geometry of matched foils (both primary and secondary) follows 2-D Modified NACA 66 Profile. Dimensions are in mm.

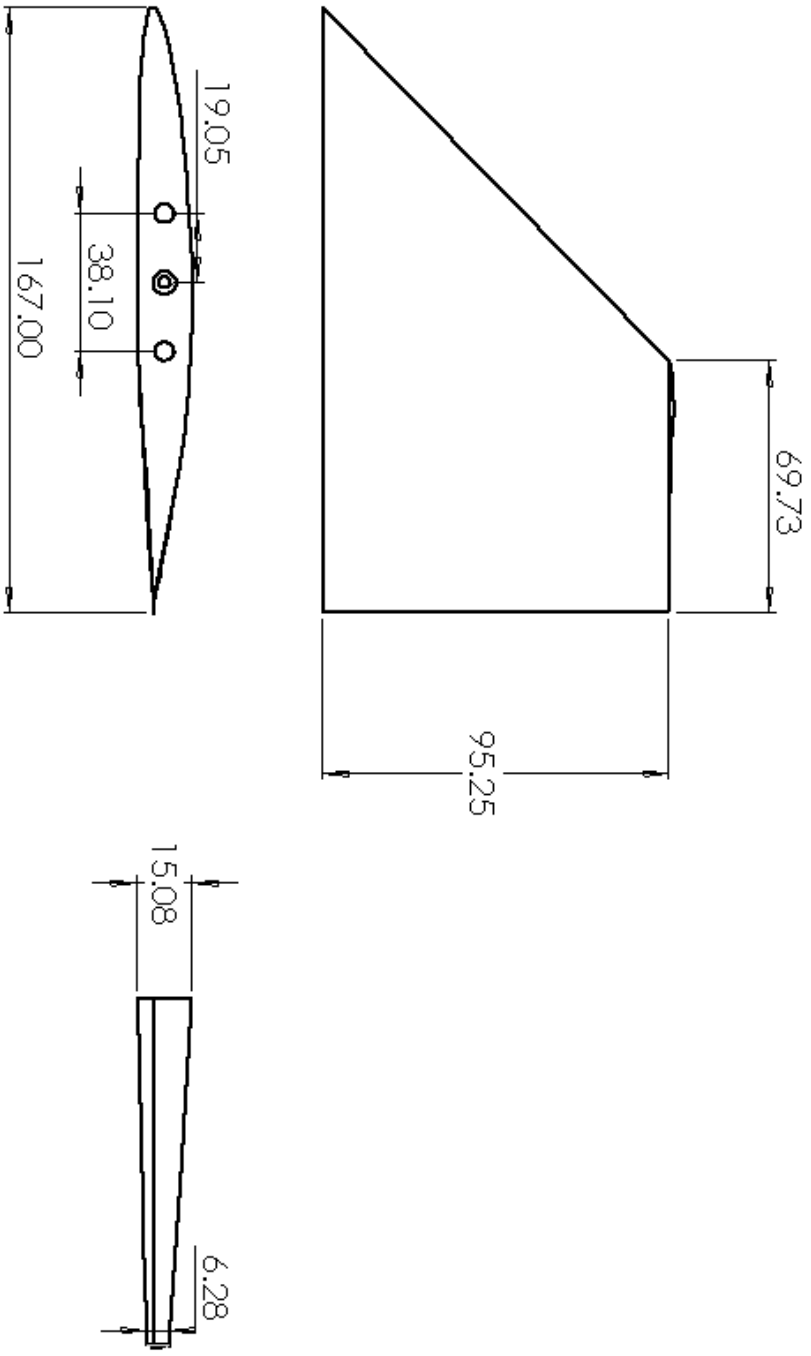


Figure A.2 Small Foil Schematic. Geometry of non-matched secondary foil follows modified NACA 66 Profile with tapering. Dimensions are in mm.

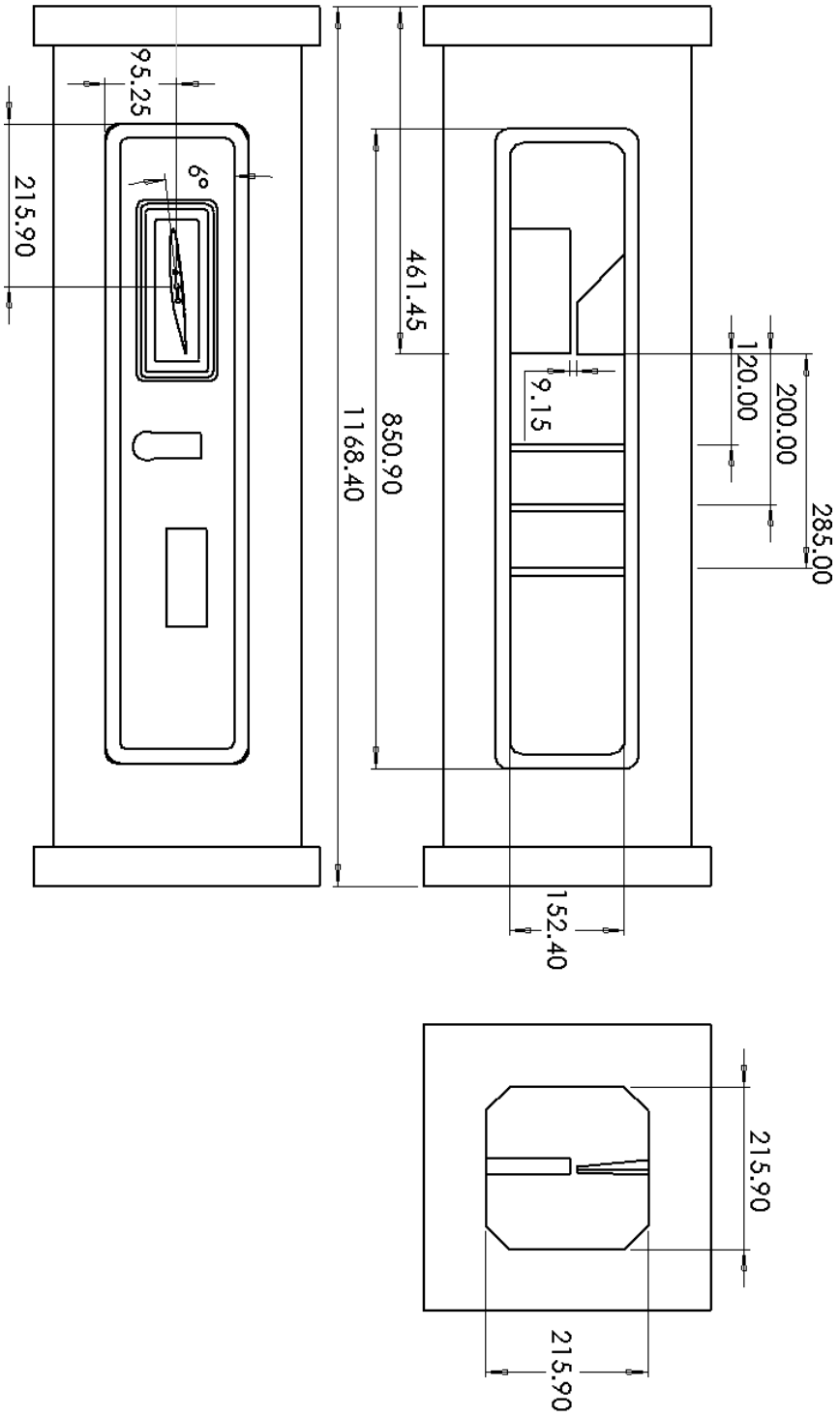


Figure A.3 Water Tunnel Layout Drawing. Geometry of water tunnel from side, top, and streamwise views showing location of foils within the test section as well as the streamwise location of the three STB measurement domains.

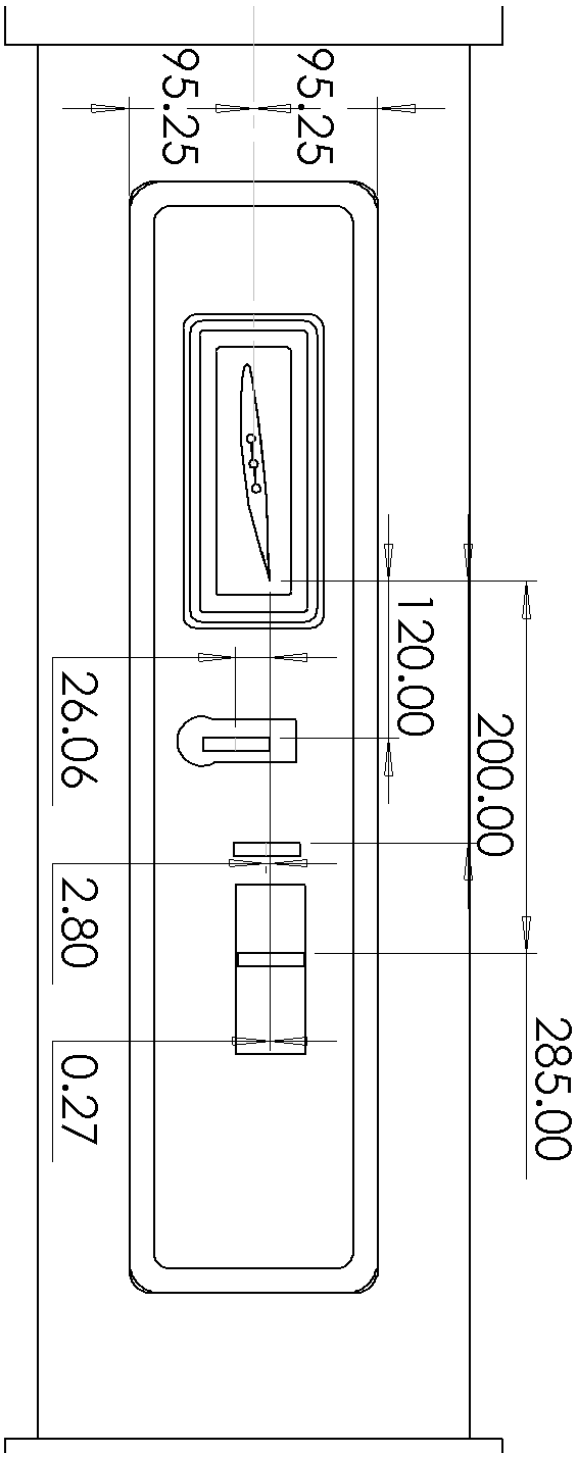


Figure A.4 Water Tunnel Layout Drawing. Additional detail of the test section viewed from the top, showing the locations of the measurement domains.

BIBLIOGRAPHY

Agarwal, K., Ram, O., Lu, Y., & Katz, J. (2023). On the pressure field, nuclei dynamics and their relation to cavitation inception in a turbulent shear layer. *Journal of Fluid Mechanics*, *966*. https://doi.org/10.1017/jfm.2023.368

Agarwal, K., Ram, O., Wang, J., Lu, Y., & Katz, J. (2021). Reconstructing velocity and pressure from noisy sparse particle tracks using constrained cost minimization. *Experiments in Fluids*, *62*(4). https://doi.org/10.1007/s00348-021-03172-0

Atkinson, C., Coudert, S., Foucaut, J. M., Stanislas, M., & Soria, J. (2011). The accuracy of tomographic particle image velocimetry for measurements of a turbulent boundary layer. *Experiments in Fluids*, *50*(4), 1031–1056. https://doi.org/10.1007/s00348-010-1004-z

Belahadji, B., Franc, J. P., & Michel, J. M. (1995). Cavitation in the rotational structures of a turbulent wake. *Journal of Fluid Mechanics*, *287*, 383–403. https://doi.org/10.1017/S0022112095000991

Brandao, F. L., Madabhushi, A., Bhatt, M., & Mahesh, K. (n.d.). *Large eddy simulation for the investigation of different regimes of cavitation*.

Brandner, P. A. (n.d.). *Microbubbles and Cavitation: Microscales to Macroscales*. http://asmedigitalcollection.asme.org/book/chapter-pdf/3823146/861851_ch136.pdf

Bristol, R. L., Ortega, J. M., Marcus, P. S., & Savaş, Ö. (2004). On cooperative instabilities of parallel vortex pairs. *Journal of Fluid Mechanics*, *517*, 331–358. https://doi.org/10.1017/S0022112004001016

Chang, N. A., & Ceccio, S. L. (2011). The acoustic emissions of cavitation bubbles in stretched vortices. *The Journal of the Acoustical Society of America*, *130*(5), 3209–3219. https://doi.org/10.1121/1.3626121

Chang, N. A., Choi, J., Yakushiji, R., & Ceccio, S. L. (2012). Cavitation inception during the interaction of a pair of counter-rotating vortices. *Physics of Fluids*, *24*(1). https://doi.org/10.1063/1.3674299

Charonko, J. J., & Vlachos, P. P. (2013). Estimation of uncertainty bounds for individual particle image velocimetry measurements from cross-correlation peak ratio. *Measurement Science and Technology*, *24*(6). https://doi.org/10.1088/0957-0233/24/6/065301

Chesnakas, C. J., & Jessup, S. D. (n.d.). *FEDSM2003-45320 TIP-VORTEX INDUCED CAVITATION ON A DUCTED PROPULSOR*.

http://asmedigitalcollection.asme.org/FEDSM/proceedings-pdf/FEDSM2003/36967/257/2594573/257_1.pdf

Choi, J., & Ceccio, S. L. (2007). Dynamics and noise emission of vortex cavitation bubbles. *Journal of Fluid Mechanics*, *575*, 1–26. https://doi.org/10.1017/S0022112006003776

Choi, J., Hsiao, C. T., Chahine, G., & Ceccio, S. (2009). Growth, oscillation and collapse of vortex cavitation bubbles. *Journal of Fluid Mechanics*, *624*, 255–279. https://doi.org/10.1017/S0022112008005430

Crouch, J. D. (1997). Instability and transient growth for two trailing-vortex pairs. *Journal of Fluid Mechanics*, *350*, 311–330. https://doi.org/10.1017/S0022112097007040

Crow, S. C. (1970). Stability theory for a pair of trailing vortices. *AIAA Journal*, *8*(12), 2172–2179. https://doi.org/10.2514/3.6083

Etter, R. J., Cutbirth, J. M., Ceccio, S. L., Dowling, D. R., & Perlin, M. (2005). High Reynolds number experimentation in the US Navy's William B Morgan large cavitation channel. *Measurement Science and Technology*, *16*(9), 1701–1709. https://doi.org/10.1088/0957-0233/16/9/001

Jeon, Y. J., Müller, M., & Michaelis, D. (2022). Fine scale reconstruction (VIC#) by implementing additional constraints and coarse-grid approximation into VIC+. *Experiments in Fluids*, *63*(4). https://doi.org/10.1007/s00348-022-03422-9

Jimenez, J. (1975). Stability of a pair of co-rotating vortices. *Physics of Fluids*, *18*(11), 1580–1581. https://doi.org/10.1063/1.861056

Jux, C., Sciacchitano, A., Schneiders, J. F. G., & Scarano, F. (2018). Robotic volumetric PIV of a full-scale cyclist. *Experiments in Fluids*, *59*(4). https://doi.org/10.1007/s00348-018-2524-1

Khoo, M. T., Venning, J. A., Pearce, B. W., & Brandner, P. A. (2020). Statistical aspects of tip vortex cavitation inception and desinence in a nuclei deplete flow. *Experiments in Fluids*, *61*(6). https://doi.org/10.1007/s00348-020-02967-x

Leweke, T., Le Dizès, S., & Williamson, C. H. K. (2016). Dynamics and Instabilities of Vortex Pairs. In *Annual Review of Fluid Mechanics* (Vol. 48, pp. 507–541). Annual Reviews Inc. https://doi.org/10.1146/annurev-fluid-122414-034558

Leweke, T., & Williamson, C. H. K. (2011). Experiments on long-wavelength instability and reconnection of a vortex pair. *Physics of Fluids*, *23*(2). https://doi.org/10.1063/1.3531720

Lynch, K. P., & Scarano, F. (2014). Experimental determination of tomographic PIV accuracy by a 12-camera system. *Measurement Science and Technology*, *25*(8). https://doi.org/10.1088/0957-0233/25/8/084003

Marshall, J. S., Brancher, P., & Giovannini, A. (2001). Interaction of unequal anti-parallel vortex tubes. *Journal of Fluid Mechanics*, *446*, 229–252. https://doi.org/10.1017/s0022112001005754

Michaelis, D., & Wieneke, B. (2008). *Comparison between Tomographic PIV and Stereo PIV*.

Neal, D. R., Sciacchitano, A., Smith, B. L., & Scarano, F. (2015). Collaborative framework for PIV uncertainty quantification: The experimental database. *Measurement Science and Technology*, *26*(7). https://doi.org/10.1088/0957-0233/26/7/074003

Novara, M., Schanz, D., & Schröder, A. (2023). Two-Pulse 3D particle tracking with Shake-The-Box. *Experiments in Fluids*, *64*(5). https://doi.org/10.1007/s00348-023-03634-7

Ortega, J. M., Bristol, R. L., & Savaş, Ö. (2003). Experimental study of the instability of unequal-strength counter-rotating vortex pairs. *Journal of Fluid Mechanics*, *474*, 35–84. https://doi.org/10.1017/S0022112002002446

Oweis, G. F., Choi, J., & Ceccio, S. L. (2004). Dynamics and noise emission of laser induced cavitation bubbles in a vortical flow field. *The Journal of the Acoustical Society of America*, *115*(3), 1049–1058. https://doi.org/10.1121/1.1646402

Oweis, G. F., van der Hout, I. E., Iyer, C., Tryggvason, G., & Ceccio, S. L. (2005). Capture and inception of bubbles near line vortices. *Physics of Fluids*, *17*(2), 1–14. https://doi.org/10.1063/1.1834916

Park, J. T., Morgan, W. B., Cutbirth, J. M., & Brewer, W. H. (n.d.). *FEDSM2003-45599 HYDRODYNAMIC PERFORMANCE OF THE LARGE CAVITATION CHANNEL (LCC)*. http://asmedigitalcollection.asme.org/FEDSM/proceedings-pdf/FEDSM2003/36975/87/2593175/87_1.pdf

Raffel, M., Willert, C. E., Scarano, F., Kähler, C. J., Wereley, S. T., & Kompenhans, J. (n.d.). *Particle Image Velocimetry A Practical Guide Third Edition*.

Ran, B., & Katz, J. (1994). Pressure fluctuations and their effect on cavitation inception within water jets. *Journal of Fluid Mechanics*, *262*(1), 223–263. https://doi.org/10.1017/S0022112094000492

Scarano, F. (2013). Tomographic PIV: Principles and practice. In *Measurement Science and Technology* (Vol. 24, Issue 1). Institute of Physics Publishing. https://doi.org/10.1088/0957-0233/24/1/012001

Schneiders, J. F. G., Scarano, F., Jux, C., & Sciacchitano, A. (2018). Coaxial volumetric velocimetry. *Measurement Science and Technology*, *29*(6). https://doi.org/10.1088/1361-6501/aab07d

Schröder, A., & Schanz, D. (2022). Annual Review of Fluid Mechanics 3D Lagrangian Particle Tracking in Fluid Mechanics. *Annu. Rev. Fluid Mech. 2023*, *55*, 511–540. https://doi.org/10.1146/annurev-fluid-031822

Sciacchitano, A. (2019). Uncertainty quantification in particle image velocimetry. In *Measurement Science and Technology* (Vol. 30, Issue 9). Institute of Physics Publishing. https://doi.org/10.1088/1361-6501/ab1db8

Sciacchitano, A., Neal, D. R., Smith, B. L., Warner, S. O., Vlachos, P. P., Wieneke, B., & Scarano, F. (2015). Collaborative framework for PIV uncertainty quantification: Comparative

assessment of methods. *Measurement Science and Technology*, *26*(7). https://doi.org/10.1088/0957-0233/26/7/074004

Sciacchitano, A., Wieneke, B., & Scarano, F. (2013). PIV uncertainty quantification by image matching. *Measurement Science and Technology*, *24*(4). https://doi.org/10.1088/0957-0233/24/4/045302

Shen, Y. T., & Dimotakis, P. E. (1989). *Viscous and Nuclei Effects on Hydrodynamic Loadings and Cavitation of a NACA 66 (MOD) Foil Section*. http://asmedigitalcollection.asme.org/fluidsengineering/article-pdf/111/3/306/5711300/306_1.pdf

Smith, B. L., Neal, D. R., Feero, M. A., & Richards, G. (2018). Assessing the limitations of effective number of samples for finding the uncertainty of the mean of correlated data. *Measurement Science and Technology*, *29*(12). https://doi.org/10.1088/1361-6501/aae91d

Timmins, B. H., Wilson, B. W., Smith, B. L., & Vlachos, P. P. (2012). A method for automatic estimation of instantaneous local uncertainty in particle image velocimetry measurements. *Experiments in Fluids*, *53*(4), 1133–1147. https://doi.org/10.1007/s00348-012-1341-1

Theophrastus. *Meteorology*, translated from the Arabic recension in Daiber, H. (2018). The meteorology of Theophrastus in Syriac and Arabic translation. In *Theophrastus* (pp. 166-293). Routledge.

Tsai, C. Y., & Widnall, S. E. (1976). The stability of short waves on a straight vortex filament in a weak externally imposed strain field. *Journal of Fluid Mechanics*, *73*(4), 721–733. https://doi.org/10.1017/S0022112076001584

Wang, J., Zhang, C., & Katz, J. (2019). GPU-based, parallel-line, omni-directional integration of measured pressure gradient field to obtain the 3D pressure distribution. *Experiments in Fluids*, *60*(4). https://doi.org/10.1007/s00348-019-2700-y

Widnall, S. E. (1975). *THE STRUCTURE AND DYNAMICS OF VORTEX FILAMENTS*. www.annualreviews.org

Wieneke, B. (2008). Volume self-calibration for 3D particle image velocimetry. *Experiments in Fluids*, *45*(4), 549–556. https://doi.org/10.1007/s00348-008-0521-5

Wieneke, B. (2015). PIV uncertainty quantification from correlation statistics. *Measurement Science and Technology*, *26*(7). https://doi.org/10.1088/0957-0233/26/7/074002

Yakushiji, R. (2010). *MECHANISM OF TIP VORTEX CAVITATION SUPPRESSION BY POLYMER AND WATER INJECTION*.

Ye, Q., Wang, Y., & Shao, X. (2023). Dynamics of cavitating tip vortex. *Journal of Fluid Mechanics*, *967*. https://doi.org/10.1017/jfm.2023.465